Neuro-chemical analysis of cortical spreading depolarizations after severe traumatic brain injury : a continuum from a physiologic response to a metabolic crisis?

Baptiste Balanca

UNIVERSITÉ DE LYON

Lyon 1

N°:205-2015

Anneé: 2015

THESE DE L'UNIVERSITE DE LYON

Délivrée par

L'UNIVERSITE CLAUDE BERNARD LYON 1

ECOLE DOCTORALE: Neuroscience et Cognition

DIPLOME DE DOCTORAT

(arrêté du 7 août 2006)

Soutenue publiquement le 6 Novembre 2015
par
Mr BALANCA Baptiste

TITRE:

Analyse neurochimique des dépolarisations corticales envahissantes après un traumatisme crânien sévère: existe-il un continuum entre une réponse physiologique et une crise métabolique?

Directeur de thèse: Dr Stéphane MARINESCO

Co-directeur: Dr Thomas LIEUTAUD

JURY:

Rapporteurs	Pr Martin LAURITZEN
	Dr Pierre BOUZAT
Examinateur	Pr Jens DREIER
Président	Pr Luc ZIMMER

Lyon University

PhD thesis

Discipline : Neurosciences

Doctoral school : Neuroscience and cognition

Neuro-chemical analysis of cortical spreading depolarizations after severe traumatic brain injury: a continuum from a physiologic response to a metabolic crisis?

Author:
Baptiste Balança

Supervisor: Dr Stéphane Marinesco
Co-supervisor: Dr Thomas Lieutaud

Public Defence : 6^{th} November 2015

Jury :

Referee	Pr Martin Lauritzen
	Dr Pierre Bouzat
External member	Pr Jens Dreier
President	Pr Luc Zimmer

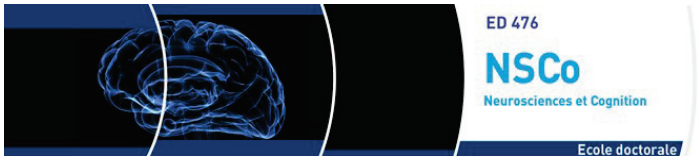

UNIVERSITE CLAUDE BERNARD - LYON 1

Président de l'Université	**M. François-Noël GILLY**
Vice-président du Conseil d'Administration	M. le Professeur Hamda BEN HADID
Vice-président du Conseil des Etudes et de la Vie Universitaire	M. le Professeur Philippe LALLE
Vice-président du Conseil Scientifique	M. le Professeur Germain GILLET
Directeur Général des Services	M. Alain HELLEU

COMPOSANTES SANTE

Faculté de Médecine Lyon Est - Claude Bernard	Directeur : M. le Professeur J. ETIENNE
Faculté de Médecine et de Maïeutique Lyon Sud - Charles Mérieux	Directeur : Mme la Professeure C. BURILLON
Faculté d'Odontologie	Directeur : M. le Professeur D. BOURGEOIS
Institut des Sciences Pharmaceutiques et Biologiques	Directeur : Mme la Professeure C. VINCIGUERRA
Institut des Sciences et Techniques de la Réadaptation	Directeur : M. le Professeur Y. MATILLON
Département de formation et Centre de Recherche en Biologie Humaine	Directeur : Mme. la Professeure A-M. SCHOTT

COMPOSANTES ET DEPARTEMENTS DE SCIENCES ET TECHNOLOGIE

Faculté des Sciences et Technologies	Directeur : M. F. DE MARCHI
Département Biologie	Directeur : M. le Professeur F. FLEURY
Département Chimie Biochimie	Directeur : Mme Caroline FELIX
Département GEP	Directeur : M. Hassan HAMMOURI
Département Informatique	Directeur : M. le Professeur S. AKKOUCHE
Département Mathématiques	Directeur : M. le Professeur Georges TOMANOV
Département Mécanique	Directeur : M. le Professeur H. BEN HADID
Département Physique	Directeur : M. Jean-Claude PLENET
UFR Sciences et Techniques des Activités Physiques et Sportives	Directeur : M. Y.VANPOULLE
Observatoire des Sciences de l'Univers de Lyon	Directeur : M. B. GUIDERDONI
Polytech Lyon	Directeur : M. P. FOURNIER
Ecole Supérieure de Chimie Physique Electronique	Directeur : M. G. PIGNAULT
Institut Universitaire de Technologie de Lyon 1	Directeur : M. le Professeur C. VITON
Ecole Supérieure du Professorat et de l'Éducation	Directeur : M. le Professeur A. MOUGNIOTTE
Institut de Science Financière et d'Assurances	Directeur : M. N. LEBOISNE

Acknowledgements

To Martin Lauritzen, Pierre Bouzat and Luc Zimmer, for accepting to serve on my thesis jury. I will benefit your critical insight on my work.

To Jens Dreier who gave me wise advices and great opportunities in many occasions. I am very lucky to have met you.

À Stéphane Marinesco et Thomas Lieutaud pour leur encadrement de qualité durant ces trois années de doctorat, toujours avec beaucoup de respect et d'humanité. J'espère que l'on va pouvoir continuer à travailler ensemble dans l'avenir.

À l'ensemble des membres des équipes WAKING et TIGER qui m'ont agréablement accueilli parmi eux, et se sont toujours montrés disponibles pour m'aider.

À Anne Meiller qui a beaucoup participé à l'aboutissement de ce travail. C'est toujours un plaisir de travailler avec toi dans la bonne humeur !

À toute l'équipe de l'école de l'INSERM, qui m'a donné ce goût pour la recherche. Vous avez fait un pari remarquable en croyant et soutenant de jeunes étudiants tout juste sortis de la première année de médecine. Merci, sans vous et votre dynamisme, rien de cela n'existerait.

À Noémie qui sans le savoir m'a donné de précieux instants de pur bonheur et d'insouciance dans ces derniers moments de stress. Quel plaisir de te voir grandir !

À Kathleen qui m'a toujours supporté et soutenu durant ces années passées ensembles. Il est bon de connaitre ses attaches afin de ne pas perdre de vue l'objectif de tout dépassement de soi : revenir grandi auprès des siens. Merci pour tous ces moments passés et à venir.

À mes parents et ma famille, qui m'ont appris à être curieux de ce qui m'entoure. Si vous n'avez pas toujours compris mes choix, vous m'avez toujours soutenu. Merci pour les valeurs que vous m'avez apportées et qui font de moi ce que je suis aujourd'hui.

À mes amis : eh oui, je finis malgré tout par passer ma thèse ! C'est un plaisir de vous avoir tous rencontré à différentes occasions. J'apprécie votre soutien ainsi que les réflexions morales, médicales, culturelles, sportives ou spirituelles que nous avons eu. La vie est faite de rencontres et je suis heureux d'avoir croisé votre chemin.

"Je me méfie des théories qui voudraient réduire l'être humain à un mécanisme d'horlogerie. Je crois que l'être humain est beaucoup plus composite, en mouvement. Ne l'enfermons pas, ne nous enfermons pas dans une case. Il nous en manquerait une."
Josef Schovanec, *Je suis à l'est, 2012.*

"On ne repousse pas ses limites, on les découvre".
Jean-Louis Étienne, *Persévérer, 2015*

Abstract

"Traumatic brain injury" (TBI) encompasses a heterogeneous group of physio-pathological phenomenon. Prognosis, clinical course evaluation and treatment of brain trauma remain challenging. Brain damage results from both the initial physical insult (primary injury), and also continues to occur in the ensuing hours to days because of secondary brain aggressions. Among secondary injuries following TBI, Cortical Spreading Depolarizations (CSD) have emerged since the mid-90s. CSD are waves of depolarization propagating along the cortex at a speed of 1-5 mm/min that induced a massive energetic demand to repolarize the cells. CSD are participating to prognosis because their occurrence and duration are related to outcome in different acute brain injuries (TBI, sub-arachnoid hemorrhage and ischemic stroke). During my thesis, our main goal was to determine whether the CSD reinforced neuronal death following brain trauma that can explain the poor prognosis. In a first study we delineated brain regions where neuronal death occurs following lateral fluid percussion injury (LFPI) in order to record CSDs in this area. Then, as we wanted to assess the energetic balance of this tissue during CSD using biosensors, we had primarily to check for the biosensor reliability to oxygen (O_2) and temperature (T^o). As oxygen and temperature were different from bench (in vitro) to bedside (in vivo) monitoring, we developed algorithms to compute offline the in vivo values obtained for glucose, lactate or glutamate brain concentrations respecting the local O_2 concentrations and T^o measured in the cortex. Finally, using the biosensors, we described the dynamic real time metabolic changes occurring after CSDs in 3 conditions: A healthy cortex, an injured cortex after LFPI, and when CSD occurred in cluster after LFPI. Although the normal brain displayed a hyper-glycolytic state following CSD (transient low glucose concentrations + prolonged elevated lactate concentrations), TBI tissue exhibited a different pattern that could be metabolic crisis (very low glucose concentrations + normal to low lactate concentrations). However, as pyruvate was not monitored, these results might also parallel the "low pyruvate state" described in humans. Finally, preliminary results showed that neither glutamate excitotoxicity, nor H2O2 overproduction are candidate to sustain the mechanisms by which CSD might participate to secondary injury. Understanding CSDs patho-physiology gave us new insights about their implications in secondary brain aggressions and rose further questions about their toxicity.

Key words: Cortical spreading depolarizations, traumatic brain injury, brain metabolism, biosensors

Résumé

Les traumatismes crâniens (TC) représentent la première cause de décès ou de handicap avant l'âge de 45 ans, avec une incidence en Europe de 235/100 000 habitants. Chez les patients survivant à un TC, les séquelles sont fréquentes allant de l'état végétatif chronique au syndrome post-concussionnel compliquant principalement la réinsertion socio-professionnelle et familiale des victimes. Cependant la nature des lésions cérébrales provoquées par un TC est encore mal connue et les thérapies susceptibles d'empêcher la progression des lésions neurologiques sont très limitées. Un TC provoque d'abord des lésions directement dues à l'impact (lésions primaires). D'autres mécanismes secondaires vont avoir lieu dès les premières minutes suivant le TC et peuvent évoluer sur plusieurs jours. Elles sont susceptibles d'être atténuées par une thérapeutique appropriée et sont donc l'objet de la plupart des efforts de recherche actuels. Néanmoins, notre connaissance de ces phénomènes d'agression primaires et secondaires, est

incomplète et ne permet pas d'expliquer correctement l'évolution des TC.
Les dépolarisations corticales envahissantes (DCE) ou "cortical spreading depolarizations""sont un des événements délétères contribuant aux lésions secondaires consécutives au TC. Les DCE sont des vagues de dépolarisation massive associées à un mauvais pronostic. Elles sont caractérisées par une dépression de l'activité électrocorticographique et une dépolarisation des neurones corticaux et des astrocytes qui se propagent sur le cortex. Les DCE s'accompagnent d'une augmentation des besoins métaboliques visant à restituer au tissu son état d'homéostasie neurochimique et de polarisation cellulaire. Les conséquences des DCE sur le métabolisme cérébral sont encore mal connues aussi bien sur un tissu sain qu'après agression cérébrale. Il existe des arguments pour penser que l'incidence, le nombre et la durée des DCE sont associés à un moins bon pronostic chez l'homme après agression cérébrale. Cependant, les mécanismes par lesquels ces DCE auraient une toxicité directe reposent encore sur des arguments le plus souvent indirects et sont mal compris.
L'objectif principal de ce travail de thèse a été de caractériser les conséquences neurochimiques et micro-vasculaires des DCE afin de mieux comprendre leur physiopathologie dans un cortex sain ou agressé par un TC sévère.
Dans une première étude nous avons caractérisé les dommages cellulaires engendrés par un TC sévère expérimental chez le rat. Le modèle de percussion latérale de fluide (LFP) est le plus utilisé et reproduit une partie des conséquences d'un TC modéré ou sévère chez l'homme. Dans cette étude nous avons déterminé la perte de neurones engendrée par un LFP sévère en utilisant une méthode automatisée de comptage des neurones. Nous avons ainsi mis en évidence une diminution de la densité neuronale dans le cortex temporal, le thalamus dorsal et dans l'aire CA3 de l'hippocampe. Cette perte de neurone était associée avec une augmentation de la densité totale de cellules suggérant la présence d'une gliose réactionnelle. Dans un second temps nous avons étudié les conséquences du LFP sur les cellules gliales et observé une augmentation de la densité de cellules microglies dans ces mêmes régions (thalamus, cortex temporal et CA3). Ces cellules microgliales étaient pourvues d'un phénotype activé. Cette première étude nous a permis de définir les régions où la perte neuronale était la plus importante après un LFP et de définir le cortex temporal comme une zone de « pénombre traumatique » où nous avons avons considéré que les conséquences neurochimiques et microvasculaires des DCE pouvaient être les plus importantes.
Dans une deuxième étude nous avons validé la technique de mesure par différents biocapteurs enzymatiques (glucose, lactate, glutamate). Ceux-ci génèrent un signal qui repose sur une réaction enzymatique d'oxydation qui est dépendante de la température et de la concentration d'oxygène. Comme les conditions de calibration des biocapteurs et les conditions d'enregistrement in vivo sont différentes, nous avons fait varier in vitro les conditions de température et d'oxygène afin de reproduire les conditions dynamiques observées au cours des DCE. Nous avons étudié séparément l'influence des deux paramètres (O_2 et T^o) sur le signal des biocapteurs et développé des algorithmes pour corriger les mesures des concentrations cérébrales de glucose, lactate ou glutamate déterminées par les biocapteurs.
Enfin dans une troisième étude, nous avons étudié les effets des DCE sur la micro vascularisation cérébrale, sur les concentrations cérébrales d'oxygène, de glucose et de lactate sur cerveau non agressé, après LFP et en déclenchant les DCE par cluster. Au cours de ces travaux nous avons montré que les DCEs isolées sur un cortex non agressé conduisaient à une hyper-glycolyse aérobie (glucose bas, élévation du lactate, élévation de la CMRO2). Au contraire après un LFP sévère, où les concentrations cérébrales de glucose sont déjà abaissées par rapport aux conditions dans les cerveaux non agressé, les DCE entrainaient un effondrement du glucose, sans augmentation compensatrice du lactate et une diminution de l'oxygène tissulaire. La répétition de ces DCEs sous forme de clusters après un LFP conduisait à une réponse métabolique plus marquée encore en termes de diminution du glucose évoquant une la crise métabolique.

Sur le plan de la réponse vasculaire à la demande métabolique induite par les DCE, sur tissu cérébral non agressé, celles-ci induisaient une augmentation du débit sanguin cérébral (CBF) local. Par contre, en situation pathologique, il est montré qu'on assiste à un découplage vasculo-métabolique avec une moindre réponse hyperhémique aux DCEs jusqu'à une ischémie terminale en passant par des réactions oligémiques intermédiaires. Dans notre modèle de LFP sévère, les DCEs conduisaient à une réaction hyperhémique, significativement réduites par rapport aux animaux non traumatisés. Nous n'avons pas observé d'évènements ischémiques, ce qui concorde avec le fait que le CBF dans ce modèle est diminué mais sans atteindre les seuils ischémiques observés dans les modèles d'ischémie cérébrale. Enfin, lors de la répétition de DCEs en cluster, nous avons mis en évidence une augmentation progressive et compensatrice du CBF. Ainsi nous pouvons raisonnablement penser que les clusters de DCE peuvent participer à la génération d'oedèmes vasogéniques observés en pathologie humaine. Pour conclure, il apparait que les DCE constituent un challenge énergétique majeur pour le parenchyme cérébral, avec des conséquences différentes en fonction de l'état du cortex sous-jacent. Cependant la toxicité directe des DCE sur le parenchyme cérébral nécessite de plus amples expérimentations.

Mots clés: traumatismes crâniens, dépolarisations corticales envahissantes, métabolisme cérébral, biocapteurs

Contents

I Introduction **9**

1 Traumatic brain injury: repercussion and evaluation **11**
1.1 Epidemiology . . . 11
1.2 Classification and scores . . . 12
1.2.1 Early evaluation . . . 12
1.2.2 Post-acute and follow-up evaluation . . . 13
1.3 Traumatic brain injury sequels . . . 14
1.3.1 Mortality . . . 14
1.3.2 Post traumatic seizure . . . 15
1.3.3 Sensory and motor disability . . . 15
1.3.4 Cognitive dysfunction . . . 16
1.3.5 Chronic traumatic encephalopathy . . . 16
1.3.6 Social rehabilitation . . . 17

2 Secondary brain aggressions patho-physiology **18**
2.1 Systemic insults to the brain . . . 18
2.2 Brain metabolism . . . 19
2.2.1 General physiology . . . 19
2.2.2 Neuronal activity, metabolism and vascular coupling . . . 19
2.2.2.1 Neuro-vascular coupling . . . 19
2.2.2.2 Neuronal activity and brain metabolism . . . 21
2.2.2.3 Glucose metabolism . . . 21
2.2.2.4 Other substrates . . . 23
2.2.3 Modelling brain metabolism . . . 25
2.2.3.1 Astrocyte-to-neuron shuttle . . . 25
2.2.3.2 Redox switch/redox coupling . . . 26
2.3 Cerebral perfusion and blood flow alterations . . . 28
2.4 Excitotoxicity . . . 29
2.5 Inflammation . . . 30
2.6 Abnormal brain activity . . . 30

3 Monitoring techniques and their implication in clinical course evaluation **32**
3.1 Usual monitoring techniques . . . 32
3.1.1 Intra-cranial pressure . . . 32
3.1.2 Trans-cranial Doppler . . . 34
3.1.3 Pupil reactivity . . . 35
3.2 Brain metabolism assessment methods . . . 36
3.2.1 Global assessment . . . 36
3.2.1.1 Oxygen . . . 36
3.2.1.2 Glucose and lactate . . . 36

3.2.2 Local measures . . . 38
3.2.2.1 Brain oxygen partial pressure . . . 38
3.2.2.2 Carbohydrate brain concentrations . . . 39
3.3 Electro-physiology . . . 41

4 Cortical spreading depolarization 43
4.1 From bench to bedside . . . 43
4.2 CSD in brain pathology . . . 44
4.3 Mechanisms of spreading depolarization . . . 46
4.4 Brain homoeostasis modifications during CSD . . . 48
4.4.1 Micro-vascularization changes during CSD . . . 48
4.4.2 Oxygen concentration changes during CSDs . . . 49
4.4.3 Glucose and lactate changes during CSDs . . . 50
4.4.4 Excitotoxicity and CSDs . . . 51

II Aims and hypothesis 52

III Methods 55

1 Modeling traumatic brain injury: Choosing the right model 56
1.1 Different animal models . . . 56
1.1.1 Closed head injury models . . . 56
1.1.2 Open skull experimental models . . . 58
1.1.2.1 Lateral fluid percussion injury . . . 58
1.1.2.2 Control cortical impact . . . 59
1.1.2.3 Weight drop injury . . . 59
1.1.2.4 Penetrating ballistic-like brain injury . . . 59
1.2 Which model suits best our needs? . . . 59
1.3 Lateral fluid percussion injury (LFPI) experimental setup . . . 60

2 Mapping brain cells injury 62
2.1 How to assess cells injury after TBI? . . . 62
2.2 Immuno-fluorescence . . . 63
2.3 Imaging brain slices . . . 65
2.3.1 Whole slide imaging . . . 65
2.3.2 Confocal microscopy . . . 65
2.4 Cell counts . . . 66

3 Brain metabolism recordings during CSDs 68
3.1 Cortical spreading depolarization . . . 68
3.1.1 Recording techniques . . . 68
3.1.2 How to trigger CSDs? . . . 69
3.2 Cerebral blood flow . . . 70
3.3 Tissue oxygen concentration . . . 71
3.4 Glucose, lactate and glutamate concentrations . . . 72
3.4.1 Imaging . . . 72
3.4.2 Tissue measurements . . . 72
3.4.2.1 Microdialysis . . . 72
3.4.2.2 Microelectrode biosensors . . . 73

3.5 Cerebral metabolic rate calculations . . . 75
3.5.1 $CMRO_2$ calculation . . . 75
3.5.2 $CMR_{glucose}$ calculation . . . 76

4 Statistical analysis and signal processing 82

IV Anatomical modifications following severe Lateral fluid percussion injury 83

1 Neuronal loss - Accepted article 84

2 Glial modification 121
2.1 Methods . . . 121
2.1.1 Animals . . . 121
2.1.2 Brain fixation and removal . . . 121
2.1.3 Glial cells labelling . . . 121
2.1.4 Whole slide images . . . 122
2.1.5 Confocal microscopy . . . 122
2.2 Results . . . 122
2.2.1 Astrocyte modification . . . 122
2.2.2 Microglia modification . . . 123
2.3 Conclusion . . . 125

V Electrochemical measurement validation 126

1 Micro-electrode biosensors 127
1.1 Biosensor manufacturing . . . 127
1.2 Recordings set-up . . . 128

2 Biosensor reliability in changing conditions 129
2.1 Effect of temperature variations on biosensors oxidative currents . . . 131
2.2 Effect of oxygen concentration variations on biosensor oxidative current . . . 132

3 Implication for *in vivo* experiments 137

VI Metabolic and micro-vascular consequences of cortical spreading depolarizations, in a normal or injured brain. 139

1 Introduction 140

2 Methods 141
2.1 Animals . . . 141
2.2 Experimental design . . . 141
2.3 Recordings set-up . . . 142
2.3.1 CSDs detection . . . 142
2.3.2 Neuro-chemical and Micro-vascular recordings . . . 143
2.3.2.1 Microvascular recording . . . 143
2.3.2.2 brain tissue oxygen partial pressure ($PbtO_2$) recordings . . . 143
2.3.2.3 Biosensors for glucose and lactate recordings . . . 143

3 Effect of severe LFPI on systemic and brain hemodynamic and metabolic parameters 144
3.1 Vascular modifications . . . 144
3.2 Metabolic modifications . . . 144
3.2.1 Systemic blood concentrations . . . 144
3.2.2 Brain concentrations . . . 144

4 Cortical spreading depolarizations consequences in a normal or injured brain. 146
4.1 Micro-vascular changes . . . 146
4.1.1 LDF recordings during isolated CSDs . . . 146
4.1.2 LDF recordings during clusters of CSDs . . . 146
4.2 Oxygen concentration ($PbtO_2$) and consumption ($CMRO_2$) modifications . . . 149
4.2.1 $PbtO_2$ recordings during isolated CSDs . . . 149
4.2.2 $PbtO_2$ recordings during clusters of CSDs . . . 149
4.3 Glucose, Lactate and $CMR_{glucose}$ modifications . . . 149
4.3.1 Biosensors recordings during isolated CSDs . . . 149
4.3.2 Biosensors recordings during clusters of CSDs . . . 151

5 Discussion 154
5.1 How severe LFPI affected brain tissue . . . 154
5.2 Micro-vascular modifications . . . 155
5.3 $PbtO_2$ modifications . . . 155
5.4 Glucose and lactate metabolism . . . 156

6 Conclusion 159

VII Conclusion and perspectives 160

1 General conclusion 161

2 Perspectives 163
2.1 Does CSD lead to neuronal damage? . . . 163
2.2 What about glutamate and ROS during CSDs? . . . 163
2.2.1 Introduction . . . 163
2.2.2 Methods . . . 164
2.2.3 Reactive oxygen species release . . . 164
2.2.4 Glutamate release . . . 165
2.3 Fuelling the injured brain? . . . 166

VIII R package documentation 168

IX Communications and publication 181

Bibliography 183

List of Figures

1 Neuro-vascular coupling . . . 22
2 Brain Nutriment transport . . . 23
3 Glucose metabolic pathway . . . 24
4 Brain metabolism hypothesis . . . 25
5 NADH-NAD+ and lactate coupling . . . 27
6 NMDA receptor binding sites . . . 29

7 Intra cranial pressure threshold . . . 33

8 Cortical spreading depolarization patterns . . . 45
9 Cortical spreading depolarization mechanism . . . 47
10 Vascular responses to CSDs . . . 49
11 CSD induce PtO_2 modification . . . 50

12 Animal models of TBI . . . 57
13 Lateral fluid percussion device . . . 60

14 Fluorescent dye excitation and emission spectrum . . . 64
15 Confocal microscopy principle . . . 66
16 Schematic representation of neuronal density quantification . . . 67

17 Local field potential recording during a CSD . . . 70
18 Rapid-sampling microdialysis system principle . . . 73
19 Biosensor principle . . . 75
20 Glucose transport models . . . 80

21 LFPI induce glial modifications, whole tissue . . . 123
22 Glial cells morphology after LFPI . . . 124

23 Glass chamber for temperature and O_2 calibration . . . 129
24 Sensor temperature and O_2 calibration, raw data . . . 130
25 Sensors temperature calibrations . . . 135
26 Sensors PO_2 calibrations . . . 136

27 Vascular, $PbtO_2$ and $CMRO_2$ modifications after a CSD . . . 147
28 vascular response during a cluster of CSDs . . . 148
29 $PbtO_2$ and $CMRO_2$ modifications during a cluster of CSDs . . . 150
30 Glucose, lactate and $CMR_{glucose}$ modifications during a CSD . . . 152
31 Glucose and lactate modifications during a cluster of CSDs . . . 153

32 Hydrogen peroxide and nitric oxide sensors signals . . . 165
33 Glutamate release following isolated CSDs . . . 166
34 Glutamate release modifications during a cluster of CSDs . . . 167

List of Tables

1 Glasgow coma score 12
2 Marshall computerized tomography classification 13
3 Glasgow outcome scale 15

4 Systemic insult to the brain 19

5 Carbohydrate metabolic rate 37
6 Cerebral Microdialysis parameters 39
7 Brain metabolism states 40
8 Prognostic value of EEG and EP patterns 42

9 Values of CBF and $CMRO_2$ 77
10 Glucose kinetic parameters 79

11 Parameters of temperature dependency model 132
12 Parameters of oxygen sensitivity model 133

Acronyms

20-HETE 20-hydroxyeicosatetraenoic acid. 20

AIC Akaike's Information Criterion. 131, 132, 133
AIS abbreviated injury scale. 11
AUC area under the curve. 146
avD$_{gluc}$ arterio-venous difference in glucose blood content. 36, 76
avDL arterio-venous difference in lactate blood content. 36
avDO$_2$ arterio-venous difference in oxygen content. 36, 74

BBB blood–brain barrier. 21, 30, 58, 70, 76, 78, 155, 166
BPU blood perfusion unit. 70, 71, 76, 142
BSA bovine serum albumin. 127, 164

CBF cerebral blood flow. 19, 21, 28, 30, 34, 36, 37, 38, 39, 41, 44, 48, 62, 68, 70, 74, 75, 76, 78, 140, 141, 146, 154, 155, 159, 161
CCI controlled cortical impact. 58, 59
CHI controlled head injury. 56, 59
cMD cerebral micro-dialysis. 18, 28, 36, 37, 39, 50, 51, 72, 140, 156, 157, 159, 161, 163, 164, 166
CMR$_{glucose}$ glucose cerebral metabolic rate. 19, 21, 35, 36, 37, 39, 72, 76, 78, 79, 81, 82, 149, 151, 156, 157, 161
CMRO$_2$ oxygen cerebral metabolic rate. 19, 21, 36, 38, 39, 74, 75, 76, 81, 82, 146, 149, 154, 155, 157, 159, 161
CNS central nervous system. 30, 62, 72, 123
CPP cerebral perfusion pressure. 28, 32, 34, 37
CSD cortical spreading depolarization. 20, 26, 39, 41, 43, 44, 48, 49, 50, 51, 53, 59, 68, 69, 70, 72, 76, 123, 138, 140, 141, 142, 143, 144, 146, 149, 151, 154, 155, 156, 157, 159, 161, 162, 163, 164, 165, 166
CSF cerebro-spinal fluid. 32, 36
CT computerized axial tomography scan. 13, 32, 34
CTE chronic traumatic encephalopathy. 16
CTH capillary transit time heterogeneity. 19

DC direct current. 41, 43, 44
DTI diffusion tensor imaging. 13

EEG electroencephalography. 30, 41, 43
EVD external ventricular drainage. 32, 44

FAD flavin adenine dinucleotide. 73

GA3P glyceraldehyde-3-phosphate. 26
GCS Glasgow coma scale. 11, 12, 13, 15, 16, 34

GFAP glial fibrillary acidic protein. 62, 64, 122
GLUT glucose transporters. 21, 23, 76, 78
GOS Glasgow outcome scale. 13, 16, 36

H_2O_2 hydrogen peroxide. 74, 128, 129, 163, 164

ICP intra-cranial pressure. 18, 28, 30, 32, 33, 34, 36, 37, 38, 41, 59
ICU intensive care unit. 13, 14, 15, 18, 21, 30, 34, 35, 36, 37, 38, 39, 41, 49, 72

K_{Ca} large-conductance Ca^{2+}-sensitive potassium channels. 20

L/P lactate pyruvate ratio. 39, 157, 159
LDF laser Doppler flowmetry. 53, 70, 71, 74, 75, 76, 138, 141, 142, 144, 146
LFPI lateral fluid percussion injury. 2, 53, 58, 59, 60, 59, 60, 61, 62, 69, 71, 76, 121, 122, 123, 134, 137, 138, 140, 141, 142, 143, 144, 146, 149, 151, 154, 155, 157, 161, 163, 164, 165
LFPot local field potential. 68, 138, 142, 146, 149, 151, 154, 155, 164, 165
LOI lactate-oxygen index. 36

MAP mean arterial pressure. 18, 28, 34
MCT monocarboxylate transporters. 20, 23, 166
MR metabolic ratio. 36, 37
MRI magnetic resonance imaging. 13, 21, 35, 56, 62, 70, 72, 76, 78, 79, 155

NAD+ nicotinamide adenine dinucleotide oxidized. 26
NADH nicotinamide adenine dinucleotide reduced. 21, 26, 157
NMDAR N-methyl-D-aspartate receptors. 28, 51, 53, 163, 165
NO nitric oxide. 20, 44, 163, 164

OGI oxygen-glucose index. 36

PB phosphate buffer. 121
PBS phosphate buffer saline. 121, 127, 128, 129, 143
PBST PBS, 3% triton-X-100. 121
$PbtO_2$ brain tissue oxygen partial pressure. 3, 4, 38, 39, 49, 53, 68, 71, 74, 75, 76, 134, 137, 138, 140, 141, 142, 143, 144, 146, 149, 154, 155, 157, 159, 161, 165
PEGDE poly(ethylene-glycol) diglycidyl ether. 127
PET positron emission tomography. 21, 35, 39, 70, 72, 75, 79
PFA para-formaldehyde. 121
PGE2 prostaglandins-E2. 20
PGTs prostaglandin transporters. 20
PO_2 oxygen partial pressure. 71, 132, 133
PPD poly-m-phenylenediamine. 74, 127, 143
PRx pressure reactivity index. 28, 34
PTS post traumatic seizure. 15

ROI region of interest. 38, 122
ROS reactive oxygen species. 30, 161, 162, 163, 166

SMCs smooth muscle cells. 19, 20, 164
SOD superoxide dismutase. 163
$SvjO_2$ venous jugular oxygen saturation. 36

TBI traumatic brain injury. 10, 11, 12, 13, 14, 15, 16, 18, 21, 23, 28, 30, 32, 33, 34, 35, 36, 37, 39, 41, 43, 44, 48, 49, 53, 56, 58, 59, 60, 62, 66, 68, 69, 121, 140, 141, 144, 146, 154, 155, 157, 161, 163, 166
TCD trans-cranial Doppler. 34

Part I

Introduction

M.C. Escher, ***Dag en nacht - 1938, Woodcut in black and grey.***

The term, “traumatic brain injury (TBI)” encompasses a heterogeneous group of pathological disorders, each with its own clinical presentation, pathophysiology, natural history, treatment, and prognosis. Anticipation of clinical course and prognostic determination are landmark feature that underpin the need for intervention or treatment. These questions daily challenge physicians, and therefore are the basis of every classification, as well as clinical or pre-clinical trials.
The fact that brain damage not only results from the initial physical insult (primary injury), but also continues to occur in the ensuing hours to days because of secondary brain aggressions, is a major concept that became the basis of current TBI care. Several new techniques have been developed over the past decades to evaluate these brain aggressions and make bounds with clinical course and outcome.

The introduction part of my thesis will be organized around these concepts of secondary brain aggressions in the context of TBI:
In the first instance, I will give a description of TBI main characteristics and classifications.
The second chapter will be dedicated to the description of secondary brain aggressions with a close focus on brain metabolism physiology.
Subsequently, different techniques available for brain monitoring will be presented with their advantages and drawbacks.
Finally the last chapter will discuss the relevance of “cortical spreading depolarizations” as part of brain aggressions.

This part will broach several concepts underlying my work about the neuro-chemical analysis of cortical spreading depolarizations after severe traumatic brain injury.

Chapter 1

Traumatic brain injury: repercussion and evaluation

1.1 Epidemiology

TBI Incidence shows a substantial variation between countries with an estimates for hospitalizations ranging from 100 to 400 new cases per 100 000 population per year, which makes it the second neurological disorder in etiology [1, 2]. With 3.7 million patients in Europe and 3.3 million in the US (1.1% of total population), TBI's direct cost was estimated over $7 billions with an additional indirect cost almost twice as high (i.e. €33 billions, in Europe year 2010) [3, 4]. However the TBI incidence has been calculated according to hospitalized patients, therefore mild or moderate TBI might be miss-evaluated. Even though, the incidence of TBI is decreasing, mainly thanks to prevention measure among the youth and road safety improvement [5]. Some countries (e.g. New Zealand, Denmark or Canada) did not display significant decrease of TBI during the past decade [6, 7, 8].
Locally using the Rhône (France) car accident register, Orriols et al. found that the incidence of severe traumatized patients younger than 10 years old was dropping [9]. Worldwide TBI epidemiology is operating a switch during the past decade. Injuries begin to result now predominantly from falls rather than traffic accident with larger proportion of older patients with more co-morbidity compromising their outcome [10, 7, 8].
A large proportion of TBI victims are still children and young adults, and TBI remains the leading cause of disability in people under 40 years of age. For that matter TBI is a major public health issue, so that large clinical trials are ongoing and received huge European funding. The TBIProject started in 2011 and aims to provide an objective and evidence-based solution for management of TBI by improving diagnostics and treatment decisions for an individual patient. As part of the TBIProject the "International Mission for Prognosis and Analysis of Clinical Trials in TBI" (IMPACT) lead in 2010 to recommendation for improving clinical trials design [11] with a large database that allow investigators to develop a prognosis score in 2008 available on-line (http://www.tbi-impact.org/?p=impact/calc) [12]. More recently, the CENTER-TBI project started in October 2013 and aims namely at refining and improving outcome assessment and develop health utility indices for TBI, using multidimensional approaches. It will collect multiple data (genetic, MRI, electro-physiology, bio-markers...) from many centers across Europe.

Score	Motor response	Verbal response	Eye opening
1	None	None	None
2	Decerebrate	Incomprehensible	To pain
3	Decorticate	Inappropriate	To Speech
4	Withdrawal	Confused	Spontaneous
5	Localizing	Oriented	
6	Obeying		

Table 1: **Glasgow coma score** as it is use nowadays, adapted from Teasdale publication [13]. *The motor response* to oral command or painful stimulus range from 1 to 6, *the verbal response* from 1 to 5 and *the eye opening* from 1 to 4. Overall the GCS range from 3 to 15.

1.2 Classification and scores

1.2.1 Early evaluation

To classify injury severity in patients undergoing accidental trauma (with or without head injury), the "Advancement of Automotive Medicine Association" described the abbreviated injury scale (AIS) with the first version of in the 70s and the latest revision being the AIS© Update 2008. This anatomical scoring takes into account lesions sites and severity, ranking from 1 (minor) to 6 (fatal), and is the basis for the Injury Severity Score (ISS) calculation of patient with multiple injuries.
Among these injuries, direct or indirect head impact lead to a wide range of different lesions. TBI may be categorized by mechanism of injury, clinical severity, radiological appearance, pathology or distribution (focal *vs.* diffuse). Homogeneous edema and axonal lesions are the landmark of diffuse injury, for example during deceleration, blast or sport accident. Conversely heterogeneous injury encompass bone fracture, penetrating lesions, hematoma or edema, with or without visible external injury.
TBI severity ranges from minor (minimal complaints, no visible structural damage) to virtually fatal. Therefore, a clinical score has been described by Graham Teasdale in 1974, which measures independently three behavioral aspects (i.e. motor responsiveness, verbal response and eye opening) [13] (table 1). This Glasgow coma scale (GCS) is easy to asses and remains a gold standard for daily consciousness assessment of comatose patients, and is use for TBI acute severity classification and help predicting patient's outcome [12]:

- **Mild**: GCS ≥ 13.
- **Moderate**: GCS $9 \mapsto 13$
- **Severe**: GCS ≤ 8

It should be noted that the GCS can be difficult to determine in some situation when any behavioral aspect cannot be assessed (e.g. verbal response in artificially ventilated patients or the motor response if paresis is present).
Although TBI is considered to be self-explanatory, in practice this terminology continues to be plagued by ambiguity, especially at the mild end of the severity spectrum. Indeed, mild TBI definition lack information about loss of consciousness, amnesia, confusion ... Therefore, the American Academy of neurology refined its classification in 3 subgroups allowing for a more detailed clinical analysis:

- **Grade 1**: Transient confusion lasting less than 15 minutes, without loss of consciousness.

Category	Definition
Diffuse injury I	No visible intra-cranial pathology seen on CT scan
Diffuse injury II	Cisterns are present with midline shift 0–5 mm and/or lesions densities present; no high or mixed density lesion $\geq$ 25 cc may include bone fragments and foreign bodies.
Diffuse injury III	Cisterns compressed or absent, with midline shift of 0–5 mm, no high or mixed density lesions of $\geq$ 25 mL
Diffuse injury IV	Midline shift of $>$ 5 mm, no high or mixed density lesion of $\geq$ 25 mL
Evacuated mass lesion (V)	Any lesion surgically evacuated
Nonevacuated mass lesion (VI)	High or mixed density lesion of $\geq$ 25 mL, not surgically evacuated

Table 2: **Marshall computerized tomography classification**

- **Grade 2**: Transient confusion lasting greater than 15 minutes, without loss of consciousness.
- **Grade 3**: Any loss of consciousness.

During the early period of patients care, TBI severity will be determine according to clinical examination using GCS. If any loss of consciousness was present, brain computerized axial tomography scan (CT) is an essential exam to map precisely any intra-cranial lesion. With data from the "Traumatic Coma Data Bank" Marhsall et al. build a classification for severe TBI [14, 15] (Table 2. This scale provide an average evaluation of the prognosis 6 month after the injury (ROC AUC = 0.74), with good inter-rater and intra-rater reliability [16].
More recently, data from the IMPACT database indicate that Marshall CT classification was strongly related to outcome. The worse outcomes were found in patients with CT class III or IV, prognosis in patients with mass lesions was better for epidural hematoma and poorer for an acute sub-dural hematoma. Moreover, multi-variable analysis indicated that individual CT characteristics added substantial information to the prognostic value of the CT classification alone, meaning that physician have to read into CT more than just the Marshall classification [17].
Even though CT is unavoidable and easily accessible in every hospital, magnetic resonance imaging (MRI) overstep its ability especially when clinical examination is very little affected.

1.2.2 Post-acute and follow-up evaluation

The ultimate goal and also the more challenging is long term outcome evaluation. Glasgow outcome scale (GOS) is commonly used for long term outcome scoring after brain injury. Ranging from 1 to 5, this scale is alike the modified Rankin scale ($1 \mapsto 6$) used to evaluate patients after cerebral ischemic stroke. It class patients between dead, comatose, or presenting severe to low disability (Table 3). The extended GOS add an upper and lower scale to the $3 \mapsto 5$ categories, allowing for a more precise distinction of better outcomes [18]. These categorizations are easy to asses during clinical trials, however they still rough for neurological functions follow up during post-acute and rehabilitation period. Therefore additional evaluation scales have been developed.
The coma recovery scale revised (CRS-R©) explore different neurological functions (i.e. auditory, visual, motor, verbal, communication, arousal and brain-stem reflexes) and can be used to follow their progress during post-acute care and rehabilitation. Further evaluation use during

rehabilitation encompass *daily life ability* (e.g. functional independence measure (FIM), frontal assessment battery at bedside (FAB) and Neurobehavioral Rating Scale(NRS)) and *quality of life* features (e.g. quality of life after brain injury (QOLBI) questionnaire).
Early clinical examination together with anatomical data from brain CT fails to give a reliable long term prognosis evaluation. Therefore more accurate imaging techniques have been used to address the relation between anatomical lesions and neurological deficits.
Since MRI spatial resolution is over 10 times that of conventional CT, it became a preferred technique for anatomical injury mapping. Conventional morphological MRI include T1, T2, T2* and FLAIR (axial fluid attenuated inversion recovery) weighted images. T2 and FLAIR sequences are better for edema, contusion, hematoma and sub-arachnoid hemorrhage visualisation. Whereas T2* highlight diffuse axonal lesions as multiple white matter micro hemorrhage. However even T2* underestimates white matter injury, which are more precisely measured with diffusion tensor imaging (DTI) sequence [19]. It should be noted that MRI lesions are dynamic after TBI, and while some might disappear over time (edema or hematoma), other can come out as a consequence of secondary brain aggressions or natural primary lesion evolution.
Even thought, brain imaging is not recommended after mild TBI without loss of consciousness or amnesia, white matter lesions have been shown in US military personnel who had a mild TBI [20]. Moreover it has been shown that these DTI modifications are associated with cognitive dysfunction such as memory and learning [21, 22].
In the intensive care unit (ICU), acute management of severe TBI might no allow an extended MRI with DTI sequence. Thereby MRI is usually perform in the sub-acute period ($\geq$ 10 days), trying to predict consciousness recovery and long term disability. The team in the "Pitié-salpêtrière hospital" lead by Pr Louis Puybasset (Paris, France) shown in 2009 that DTI imaging was a reliable bio-marker. In fact fractional anisotropy in the inferior longitudinal fasciculus, in cerebral peduncle, in posterior limb of the internal capsule, and in posterior corpus callosum was specifically decreased in unfavorable outcome group compare to the favorable one [23]. In 2012 they even build a DTI score that has a 64% sensitivity and a 95% specificity for the prediction of unfavorable outcome (i.e. extended GOS of 1, 2 or 3-) [24].
In the end, what matters to many intensivists is whether patient will have favorable or unfavorable outcome. Indeed this rough dichotomy is used in many clinical trials analysis, as describe above with DTI evaluation. If (1) dead or comatose patient are commonly accepted as "bad" outcome and (2) low to moderate disability as "good" outcome, the GOS 3 (i.e. moderate disability with the need for assistance in everyday-life) is matter of struggling debate. Indeed decreasing mortality in favor of severe handicap should be a matter of society. Therefore available techniques interpretation for prognosis or clinical course evaluation should be taken with great precaution as it can end up with discussion about intensity of care limitation.

1.3 Traumatic brain injury sequels

1.3.1 Mortality

Severe TBI reaching the ICU have between 30% and 70% mortality rate [25, 26, 27]. Although it should be noted that 54% of severe traffic accident (at least one AIS $\geq$ 4 lesion) with an associated head trauma will die, 80-90% of the fatalities occurring on the scene of the accident [9, 28]. In Pennsylvania the overall mortality rate was 7.8% with a decreasing trend from 1998 to 2007 [29]. Between 2006 and 2010 in Canada, there was a 15% mortality increase, likely related to increased patient's age and comorbidity. The in-hospital mortality rate was mainly related to TBI severity, age, and comorbidity index [8].
Moreover, TBI survivors keep a vulnerability compared to general population, decreasing their

Score	outcome	description	eGOS
1	Dead or no consciousness		
2	Persistent vegetative state	Severe damage with prolonged state of unresponsiveness and a lack of higher mental functions	
3	Severe disability	Severe injury with permanent need for help with daily living	U/L
4	Moderate disability	No need for assistance in everyday life, employment is possible but may require special equipment	U/L
5	Low disability	No or light damage with minor neurological and psychological deficits	U/L

Table 3: **Glasgow outcome scale** and extended GOS adding upper and lower categories to GOS 3 to 5

life expectancy. In fact, a follow-up Scottish study shown a 7 fold higher mortality rate 13 years after TBI compared to general population, even in the elderly [30]. 75% of deaths occurred during the first year after TBI, and this early mortality rate was twice that of traumatized patients without head injury and close to 10 times that of general population (age, sex, social status ... matched) [30].

1.3.2 Post traumatic seizure

Post traumatic seizure (PTS) is often the first episode of seizure secondary to TBI, with epilepsy (i.e. recurrent seizure) appearing over time. According to TBI severity and latency, its incidence ranges between 2 and 66% [31, 32, 33, 34]. PTS onset can be either immediate, early (i.e. within 7 days) or late [35]. In the ICU, around 22% of moderate or severe TBI patients undergo non-convulsive seizure, 25% of whom will develop a non-convulsive status epilepticus [36].
The main risks factor for developing PTS are an early seizure, an acute intra-cranial hematoma or concussion, GCS ≤ 9 and scalp fracture [35, 37]. More recently, a prospective multi-center study in China identified 3 main factors using multivariate analysis: Frontal or temporal lobar contusion (OR= 2), linear fracture (OR= 2.9) and the initial GCS (9-12: OR= 2, 3-8: OR= 4.1) [34].
Even though PTS are associated with TBI severity and intra-cranial lesions, prophylactic treatment is not recommended [32]. In fact prophylactic phenitoine or valproate administration did not prevent late PTS, even though it decreased early PTS rate [38, 39]. However, recommendations for PTS management rely on very few studies [32] and new anti-epileptic drugs still have to prove their beneficial effects.

1.3.3 Sensory and motor disability

Sensory and motor disability prevalence depends on TBI severity, the existence of intra-cranial hematoma and surgical procedure. It can be absent after mild TBI and rise to 100% in severe TBI survivors.
Theses disabilities are very heterogeneous depending on brain lesion's localization, and include:

- motor dysfunction such as paresis, axial hypotonia, dyskinesia and extrapyramidal syndrome

- sensory deficit including anesthesia, hypoesthesia, allodynia, spatial neglect, visual deficit, vertigo
- cranial nerve palsy
- algodystrophy, chronic pain, that are more related to trauma severity than to TBI [40], like peripheral neuropathy
- urinary tract and digestive dysfunction
- sleep disorders

Even if 85% of severe TBI survivors regain consciousness, 25 to 45% keeps a severe disability and only 10 to 15% have a good recovery [41]. Therefore, rehabilitation is a crucial period that can take several months or years before consolidation, and should be started as soon possible to improve patient outcome [42].

1.3.4 Cognitive dysfunction

Severe TBI cause initial major consciousness disorder and depending on injury location can lead to persistent vegetative state (no evidence of awareness without interaction with other people) or minimally conscious state (fragment of meaningful interaction with the environment are preserved such as eye contact, grasping to command or answer with a word). Up to 50% of mild and moderate TBI, and 76% of severe TBI suffer from memory loss or mood disorder one year after the accident [43]. After severe TBI, 10% of the survivors will develop agitation [44], over 30% irritability [45], and up to 35% aggressive behavior [46].
Mood disorder such as anxiety seems to correlate with major depression [47] and addictive behavior after TBI [48]. Depression usually occurs late after the injury in 25 to 50% of severe TBI. Suicide is also 4 times more frequent after severe TBI than in general population (matched for social, economic en geographic features) [49].

1.3.5 Chronic traumatic encephalopathy

Chronic traumatic encephalopathy (CTE) was originally reported in 1928 by Harrison Martland, a New Jersey pathologist, who described the clinical aspects of a progressive neurological deterioration ("punch drunk") that occurred after repetitive brain trauma in boxers [50]. CTE is clinically associated with symptoms of irritability, impulsivity, aggression, depression, short-term memory loss and heightened suicidal that usually begin 8–10 years after experiencing repetitive mild traumatic brain injury. With advancing disease, more severe neurological changes develop that include dementia, gait and speech abnormalities and Parkinsonism. In late stages, CTE may be clinically mistaken for Alzheimer's disease or frontotemporal dementia.
CTE is a progressive tauopathy that occurs as a consequence of repetitive mild TBI [51]. The spectrum of pathological hyperphosphorylated tau locations ranged in severity from focal to disseminated brain regions, including the medial temporal lobe. The degree of lesion's extension is correlated with clinical symptoms [51].
Nevertheless single moderate to severe TBI can lead to widespread and extensive tau and Aβ pathology many years after injury. This could represent a substrate for the long-term development of neurodegenerative disease, such as Alzheimer's disease, known to be at increased incidence in long-term TBI survivors [52].

1.3.6 Social rehabilitation

Among a 1000 patient cohort who underwent mild TBI after traffic accident, although 75% felt well before the accident, 70% felt accident related difficulties afterwards. 30% reported bad health condition whereas almost all felt healthy prior the accident [53]. Among traumatized people, 80% underwent work interruption whatever the trauma location. Likewise, up to 72% young victims interrupted their study after traffic accident [40].
GCS, amnesia duration, hospital length of stay, cognitive dysfunction, and GOS were all correlated to social rehabilitation (i.e. work return, hobbies, family and social relationships ...) [54, 49].

Brain injury that underpin impaired neurological functions and outcome results from the initial physical insult (primary injury), but also from secondary brain aggressions appearing within the first minutes after the injury and lasting days to months or even years following the TBI. Multiple and intricate mechanisms take place during TBI clinical course. The Next chapter will describe known processes acting on brain tissue, with a special focus on brain metabolism physiology.

Chapter 2

Secondary brain aggressions patho-physiology

The concept of secondary brain aggression after TBI date from the mid-60s based on post-mortem histological analysis showing necrotic lesions in the *corpus callosum*, the *hippocampus*, the white matter, the *external capsula*, and the brain-stem that were not direct consequences of head injury [55]. Therefore emerges the distinction between **primary injury** that is a direct consequences of head injury, and **secondary brain aggressions** that can induce new injuries within the first minutes to hours or days after the accident [56].
Physicians can-not act on primary lesions apart from preventing traffic, sports and everyday life, accidents. Conversely secondary brain aggressions are a central component of TBI care management.
The next sections will describe on one hand what is called "systemic insults to the brain", and then more recent discovery about local aggressions including: brain vascularization, inflammation, excito-toxicity, electrophysiological events and metabolic modifications.

2.1 Systemic insults to the brain

The first studies conducted in dogs about systemic insult to the brain such as hypoxia or hypotension showed similar histological lesions of the white matter and the *centrum semiovale* [57]. After severe TBI either hypercapnia ($PaCO_2 > 45mmHg$) or hypotension (mean arterial pressure (MAP)$< 90mmHg$) has been observed and linked to increased intra-cranial pressure (ICP) [58]. Likewise, hypertension and hypoxia are known since the 70s to be more frequent in TBI patients with worse outcome [59].
Nowadays "systemic insults to the brain" (Table 4) have been integrated in head injured patients prognosis score such as the one from the IMPCAT trial [12]. Apart from hypoxia and hypotension, anemia is also one of the systemic insults that can occur after a trauma with hemorrhage. It will decrease the arterial content of oxygen and therefore brain energy supply. In fact it has been shown that red blood cell transfusion can increase brain oxygen concentration after sever brain injury [60].
Patients with severe head injury also have increased serum glucose which level is associated with in adverse patient outcome [61]. Recently studies have investigated glycemic control in the neurocritical care population. Research in severe brain injury documents deleterious effects of tight glucose control, and cerebral micro-dialysis (cMD) studies demonstrate lower brain glucose and increased episodes of hypoglycemia with tight glucose control (80-100 mg/dL) [62, 63]. Therefore present recommendations target a blood glucose concentration between 144 and 180 mg/dL (8-10mmol/L) [64]. These "moderate" insulin protocols are common in ICUs and appear to avoid hyperglycemia and low glucose variability [64]. Finally electrolyte disorders such

Insult category	Grade 1	Grade 2	Grade 3
Raised ICP	mean $\geq 20mmHg$	mean $\geq 30mmHg$	mean $\geq 40mmHg$
Hypotension	mean $\leq 70mmHg$ or systolic $\leq 90mmHg$	mean $\leq 55mmHg$ or systolic $\leq 70mmHg$	mean $\leq 40mmHg$ or systolic $\leq 50mmHg$
Hypertension	mean $\geq 110mmHg$ or systolic $\geq 160mmHg$	mean $\geq 130mmHg$ or systolic $\geq 190mmHg$	mean $\geq 150mmHg$ or systolic $\geq 220mmHg$
Low CPP	mean $\leq 60mmHg$	mean $\leq 50mmHg$	mean $\leq 50mmHg$
Hypoxia	$SaO_2 \leq 90\%$	$SaO_2 \leq 85\%$	$SaO_2 \leq 80\%$
Pyrexia	Temp $\geq 38^oC$	Temp $\geq 39^oC$	Temp $\geq 40^oC$
Tachycardia	HRT $\geq 120bpm$	HRT $\geq 135bpm$	HRT $\geq 150bpm$
Bradycardia	HRT $\leq 50bpm$	$HRT \leq 40bpm$	$HRT \leq 30bpm$

Table 4: **Systemic insult to the brain defined by the Edinburgh University secondary insult grades (EUSIG)**. Definition of secondary insult grades: Each derangement must be sustained for at least 5 minutes to be deemed a secondary insult, with the exception of pyrexia, which must last at least 60 minutes. Adapted from signorini et al. 1999 [66].

as metabolic acidosis or dys-natraemia are also related to worse outcome [65].

2.2 Brain metabolism

2.2.1 General physiology

About 20% of the oxygen and 25% of the glucose consumed by the human body are dedicated to cerebral functions and homoeostasis (oxygen cerebral metabolic rate ($CMRO_2$) $\approx 5ml \cdot min^{-1} \cdot 100g^{-1}$ and glucose cerebral metabolic rate ($CMR_{glucose}$) $\approx 31\mu mol \cdot min^{-1} \cdot 100g^{-1}$). Therefore 20% of cardiac output is delivered to the brain which represents only 2% of the total body mass. Maintenance and restoration of ion gradients dissipated by signaling processes as well as uptake and recycling of neurotransmitters, are the main processes contributing to the high brain energy needs under physiological conditions. However brain aggression induces inflammation, oxidative stress, cell destruction or edema, thereby enhancing energy demand. Nevertheless a little is known about how the brain is able to adapt to such a challenge.

2.2.2 Neuronal activity, metabolism and vascular coupling

2.2.2.1 Neuro-vascular coupling

The vascular cortical organization includes deep capillary beds fed by perpendicularly oriented penetrating arterioles that branch from superficial pial arteries [67] (Fig 1A). The topology and morphology of this microvasculature are characterized by a large degree of heterogeneity that can change over time. As a consequence, erythrocyte fluxes and velocities in capillaries is also miscellaneous [68]. Interestingly this heterogeneity appears to be reduced during brain activation with functional hyperemia [68]. Based on these observation, a model emerges whereby capillary transit time heterogeneity (CTH) reduction during functional hyperemia (i.e. capillaries diameter homogenization) counteract inherent reduction in oxygen extraction fraction as cerebral blood flow (CBF) increase [68, 69]. Indeed, according to this model, oxygen availability depends on blood flow and dynamic changes in oxygen conductance: as capillary transit times becomes short, an increasing proportion of blood is shunted through the capillary bed, and its oxygen unavailable to brain tissue. Thereby under fixed CTH any increase in the CBF would

decrease oxygenation [70].
The vasomotricity of Arterioles and veinules depends on circumferential smooth muscle cells (SMCs) placed around arterioles and with a more fenestrated patch-work phenotype around veinules. Smaller vessels $3 - 10\mu m$ (branches of penetrating arterioles) are covered with NG2 expressing cells including SMCs and pericytes [71, 72]. During physiological *in vivo* brain activation, increases in CBF almost always accompany evoked neuronal activity. This vasodilation occurs first in capillary regions covered by NG2-cells [73]. Based on NG2-cells morphology, Hill et al recently suggested that small vessels diameter ($< 10\mu m$) depend on SMCs intracellular calcium modification but not on pericytes which does not express smooth muscle actin [71].
Indeed, functional hyperemia occurs first in the deeper vessels and is characterized by an early peak and a late plateau. The early vasodilation displays a retrograde propagation to the pial artery spreading threw endothelial cells gap-junctions (over 2mm/s) [74, 75, 76]. This endothelial propagation leads to the shortest route to larger arteries, selecting the optimal arteriolar branches to generate a localized increase in CBF. Then a more localized and sustained parenchymal hyperemia occurs, that is dependent to the stimulus duration [74]. Hence, Chen et al. hypothesized that this pattern may be representative of a threshold effect, whereby endothelial hyperpolarization occurs only at the onset of stimulation, whereas slower NO and prostanoid-dependent dilation is repeatedly triggered by continuing stimulation [74]. What drives vasodilation onset remains controversial, and may imply both astrocytes and vasoactive neurons.
All vessels below the pial surface are surrounded by astrocytes, especially capillaries covered by astrocyte processes [77]. Astrocytes occupy non-overlapping territories wrapping a large proportion of dendrites [78]. Thereby, their ability to sense neuronal activity through these "synaptic islands" together with their strong relationship with capillaries make them good candidates for local neuro-vascular coupling. In fact increased extracellular glutamate during neuronal activity will induce an increase in astrocytic intracellular calcium that can potentially activate two pathways (Fig 1A):

- Cytoplasmic phospholipase A2 generating arachidonic acid, which is converted to prostaglandins and epoxy-eicosatrienoic acid, both able to relax SMCs [74]. It has also been suggested that arachidonic acid diffuses to vascular smooth-muscle cells and is metabolized to 20-hydroxyeicosatetraenoic acid (20-HETE), a vasoconstrictor that can inhibit smooth muscle's large-conductance Ca^{2+}-sensitive potassium channels (K_{Ca}) [79, 80]. This vasoconstriction is blocked during neuronal activation by nitric oxide (NO) release [73]. However, both NO and 20-HETE synthesis are supposed to be limited under *in vivo* oxygen concentration [81]. During pathological process such as cortical spreading depolarization (CSD) 20-HETE release has been shown to engage in the sustain hypo-perfusion that follow the depolarization [82]. Therefore acting on either NO or 20-HETE can be a way to improve CSD subsequent vascular pattern [82, 83].

- K_{Ca} opening in the plasma membrane of astrocytic end-feet. Increases in extracellular potassium concentration can subsequently hyperpolarize SMCs through inward rectifier potassium channels, leading to a vasodilation. Conversely, at extracellular levels ≥ 20 mM, K^+ depolarizes SMCs, activating voltage-dependent calcium channels and inducing vasoconstriction [80].

Beside astrocyte's action on vascular diameter, general brain condition such as oxygen concentration and cell metabolism can modulate vascular tone. For example, *in vivo* oxygen concentration leads to an increase in extracellular adenosine concentration that can promote vasodilation either through endothelial cells [74, 76] or through A2A adenosine receptor on SMCs [84]. Finally, the action of prostaglandins-E2 (PGE2) is terminated when astrocyte's or neuron's prostaglandin transporters (PGTs) take up PGE2 by an exchange of intracellular

lactate. Thereby, extracellular lactate increase through monocarboxylate transporters (MCT) during neuronal activation (see section below, "modelling brain metabolism") hinders passive PGE2 clearance by PGTs and increases extracellular PGE2, which further dilates arterioles [84].

2.2.2.2 Neuronal activity and brain metabolism

One striking brain feature is the tight coupling that exists between neuronal activity and blood supply for oxygen and carbohydrate. Indeed neuronal activity increases with CBF and also with $CMR_{glucose}$, demonstrating a neuro-metabolic coupling. Positron emission tomography (PET) and other functional brain imaging are based on this correlation between brain activity and CBF, $CMRO_2$ or $CMR_{glucose}$ [85, 86, 87]. As neurons are the most energy consuming cells during brain activation, $CMR_{glucose}$ measured by PET with ^{18}F-Fluoro-2-deoxyglucose was supposed to be a surrogate to neuronal glucose expenditure [86]. Further investigation by ox and Raichle in the 80s found that even if CBF and $CMRO_2$ were correlated at resting state, they were not coupled during neuronal activation [88]. Indeed, physiological neuronal activity increases glucose uptake and cerebral blood flow much more than $CMRO_2$. Glucose uptake is usually in excess of that consumed by oxidative metabolism [89].
As a result, local temporary mismatch between oxygen supply and consumption leads to less desaturated hemoglobin in an activated area. Thereby, the increased oxy/deoxy hemoglobin ratio yields a different signal detected by MRI, paving the way to functional MRI measuring the blood oxygenation level-dependent (BOLD) contrast [87].
These observations rise fundamental questions about the contribution of neurons and astrocytes to brain glycolysis and oxidative metabolism. The next section will discuss what is known about the cooperation between these two cell types.

2.2.2.3 Glucose metabolism

Glucose is supposed to be the major energetic fuel of the mammalian brain. Glucose is passively transmit from blood through glucose transporters (GLUT) and either diffuses in the extracellular space or transfers to astrocytic end-feet (Fig 2). Subsequently interstitial glucose is passively transferred to neurons and glial cells by a family of membrane-spanning carrier proteins: the GLUTs [90] (Fig 2). Several GLUT isoforms are present in the brain: GLUT1 is present in all brain cells including the endothelial capillary cells and is consider the main carrier at the blood–brain barrier (BBB), while GLUT3 is almost restricted to neurons [90]. GLUTs are differentially express between cell types but may also vary during acute brain injury thereby influencing energetic substrate capture [91, 92, 93]: A reduction in endothelial GLUT1 expression has been reported in epileptic human brain [93]; In a diffuse TBI rat model neuronal GLUT3 was found to increase by at least 300% whereas GLUT1 expression did not change [91]. A better understanding of how brain take and consume energetic substrate under pathological condition is fundamental to further investigate the way we manage carbohydrate supply in the ICU.
Cellular glucose is either directly exported into the interstitial medium or metabolized to glucose-6-Phosphate. Glucose-6P can be processed into three main metabolic pathways: glycolysis, pentose phosphate or glycogen synthesis (Fig 3). Glycolysis theoretical approach encompass two different chain reaction whether oxygen is involve or not:

- **Anaerobic glycolysis**: Glucose-6P is converted during multiple reaction to pyruvate and subsequently to lactate by lactate dehydrogenase. This chain reaction produces nicotinamide adenine dinucleotide reduced (NADH) and only 2 ATP molecules.

A. **B.**

Figure 1: **Neuro-vascular coupling mechanisms**: **A. Astrocyte** hypothesized to sense glutamate through mGluR increasing intracellular calcium and generating AA from PLA2 which is converted by COX1 (or 3) to PG and by P450 epoxygenase to EETs. Both PGs and EETs can relax SMCs. Increasing intracellular calcium can also open K_{Ca} and subsequently modify SMCs tone threw sarcolemma K_{ir} [80]. **Endothelial cells** can increase their intracellular calcium in response to receptor (R) binding causing IP3-mediated release of calcium from the endothelial ER. PLC (or PLA2) can also produce EETs and AA derivatives both of which can drive SMC relaxation. Intracellular calcium increases can also lead to endothelial hyperpolarization through opening of KCa. Endothelial hyperpolarization can spread rapidly to adjacent endothelial cells through gap junctions and is coupled to encircling SMCs either through MEGJs or some other EDHF. SMC hyperpolarization causes relaxation through closure of Cav. Adapted from Chen et al 2014 [74] **B.** vascular organization of the cerebral cortex, with deeper capillary beds (3) fed by perpendicularly oriented penetrating arterioles (2) that branch from superficial pial arteries (1). Confocal laser scanning microscopy, from fixed human brain. Scale-bar = $500\mu m$. adapted from Alfonso Rodriguez Baeza et al 1998 [67].
Abbreviation : *mGluR*, Metabotropic glutamate receptor; PLA_2, Phospholipase A_2; *AA*, Arachidonic acid ; *PG*, Prostaglandins; *EETs*, Epoxy-eicosatrienoic acid; *20 HETE*, 20-hydroxyeicosatetraenoic acid; *SMCs*, Smooth muscle cells; *R*, Receptor; *ACh*, Acetylcholine; *BK*, Bradykinin; *ATP*, Adenosine triphosphate; *ADP*, Adenosine diphosphate; *UTP*, Uridine triphosphate; IP_3, Inositol triphosphate; *ER*, Endoplasmic reticulum; *PLC*, Phospholipase C; *DAG*, Diacyl-glycerol; *NO*, Nitric oxide; PGI_2, Prostacyclin; K_{Ca}, Calcium-dependent potassium channels; *MEGJs*, Myoendothelial gap junctions; *EDHF*, Endothelium-derived hyperpolarizing factor; Ca_v, Voltage-dependent calcium channels; K_{ir}, Strong inward rectifier potassium channels; *(?)*, Potential signaling pathways.

A. B.

Figure 2: **Brain Nutriment transport A.** Diagrammatic representation of potential routes of glucose diffusion from blood ROUTE 1: Glucose traverse the basal lamina whence it is transported into the astrocytic endfoot. ROUTE 2: Diffusion of glucose throughout the basal lamina, into the interstitium. **B.** A schematic representation of the cellular localization of glucose transporter (GLUTs) and monocarboxylate transporters (MCTs) in mammalian brain. Adapted from Simpson et al 2007 [90]

- **Aerobic complete glycolysis**: Complete oxidation of glucose whereby pyruvate is converted in acetyl-CoA instead of lactate, and enters mitochondrial tricarboxylic acid cycle (oxidative pathway). The respiratory chain subsequently produces 30-34 ATP molecules using NADH molecules.

Glucose can also serve neurotransmitter synthesis such as glutamate, acetyl-choline and γ-aminobutyric acid. Neurons and astrocytes metabolic specificity and interactions are still debated (see section below: "Modelling brain metabolism").

2.2.2.4 Other substrates

Apart from glucose, the brain has the capacity to use other blood-derived energy substrates, e.g. ketone bodies during development and starvation or lactate during periods of intense physical activity [94, 85]. Long considered as an end product of anaerobic glycolysis, lactate is known to act as a "Cell-Cell" shuttle in many organs (e.g. muscle, liver, kidney, heart and brain) and even as an energetic shuttle between remote organs during exercise. For instance, during sustained exercise lactate consumption equals or exceeds that of glucose in heart and muscle [95]. Facilitated transport of lactate across membranes is accomplished by a family of MCT that account also for pyruvate, acetoacetate, and β-hydroxybutyrate (ketone bodies) transport. MCTs are differentially expressed in cells and tissues (e.g. Fig 2 in brain cells) and their cerebral expression can increase during physiological process (development [96] or exercise [95]) or during pathological situation such as TBI [97].

Figure 3: **glucose metabolic pathway**: Glucose enters cells through glucose transporters (GLUTs) and is phosphorylated by HK to produce glucose-6-phosphate (glucose-6P). Glucose-6P can be processed into three main metabolic pathways. **Glycolysis** giving rise to pyruvate. Pyruvate can then enter mitochondria, where it is metabolized through the tricarboxylic acid (TCA) cycle (oxidative pathway), or be reduced to lactate by lactate dehy-drogenase (LDH). Alternatively, glucose-6P can be processed through the **pentose phosphate pathway**, leading to the production of reducing equivalent in the form of NADPH. Finally, glucose-6P can also be used to store glucosyl units as **glycogen**. Adapted from Bélanger et al 2011 [85]

Abbreviations : *GPI*, glucose-6-phosphate isomerase; *PFK*, phosphofructokinase-1; *Fructose-1,6-P2*, fructose-1,6-bisphosphate; *DHAP*, dihydroxyacetone phosphate; *TPI*, triose phosphate isomerase;*GA3P*, glyceraldehyde 3P; *G6PDH*, glucose-6-phosphate dehydrogenase; *6-PGL*, 6-phosphoglucono-d-lactone; *6-PG*, 6-phosphogluconate; *6 PGDH*, 6-phosphogluconate dehydrogenase; *ribulose-5P*, ribulose-5-phosphate; *ribose-5P*, ribose-5-phosphate; *xylulose-5P*, xylulose-5-phosphate; *TK*, transketolase; *sedoheptulose-7P*, sedoheptulose-7-phosphate; *TA*, transaldolase; and *erythrose-4P*, erythrose-4-phosphate.

A. B.

Figure 4: **Brain metabolism hypothesis**: **A.** The astrocyte-to-neuron lactate shuttle. **B.** The redox switch/redox coupling. Adapted from Cerdán et al 2006 [102]
Abbreviations : *Asp*, aspartate; *Glc*, glucose; *Gln*, glutamine; *Glu*, glutamate; *GLUT1 and GLUT3*, glucose transporters 1 and 3; *a-KG*, α-ketoglutarate; *Lac*, lactate; *LDH1 and LDH5*, lactate dehydrogenase 1 and 5; *Mal*, malate; *Pp*, derived from extracellular monocarboxylates; *Pg*, derived from glycolysis.

2.2.3 Modelling brain metabolism

2.2.3.1 Astrocyte-to-neuron shuttle

Understanding metabolic coupling between neurons and astrocytes remains a struggling question. In 1994 Pellerin and Magistretti proposed the so called **"Astrocyte-to-Neuron lactate shuttle"** [98]. Using primary culture of cerebral astrocytes together with a radioactive glucose tracer (2-Deoxy-D-[1,2-^{3}H]glucose) they shown that L-Glutamate stimulates glucose uptake and phosphorylation by astrocytes in a concentration dependent manner (EC_{50}=80μM), with a release of lactate and pyruvate in the medium. This effect was abolished by the glutamate transporter inhibitor DL-*threo*-β-hydroxyaspartate. Together with observations of astrocyte's end-feet en-warping brain capillaries, the authors suggested the existence of a cooperative mechanism whereby glutamate uptake triggers glycolysis in astrocytes (glucose utilization and lactate production). Lactate once release can be taken-up by neurons and serve as an energy substrate (Fig 4 A.).
From then on, many *in vitro* studies support this hypothesis where astrocytes are specialized in glycolysis and glycogen storage, whereas neurons are more prone to oxidative pathway [85]. For instance, cultured astrocytes were found to metabolize glucose mainly to lactate and release it into the external medium, but have limited capacity to oxidise glucose or lactate. In contrast, neurons released less lactate into the medium and oxidized both glucose and lactate to CO_2 far more rapidly than astrocytes [99]. Furthermore, proteomic analysis shows that although phosphofructokinase mRNA is present in both neurons and astrocytes, the protein is absent in neurons through post-transcriptional degradation. In these experiments the rate of glucose consumption through the pentose phosphate pathway double the one through glycolysis in neurons whereas astrocytes depict a substantial glycolysis [100]. Finally by inactivating an astrocyte-specific glutamate transporter (GLAST) *in vivo*, Cholet et al. evidenced a significant reduction in cerebral glucose uptake triggered by a sensory stimulation [101]. However considering the 7.4 fold higher affinity of neuronal GLUT3 compare to astroglial GLUT1, the "astrocyte-to-neuron" shuttle model fails to predict data from carbohydrate flux on slice or during visual stimulation [90, 103, 104]. Therefore Simpson et al. published a "neuron-to-astrocyte" shuttle, lactate being released more by neurons that astrocytes, with good prediction of lactate dy-

namics during hippocampal stimulation [90, 104]. Moreover *in vivo* experiments using labelled glucose found glucose uptake to be even or higher in neuron than in astrocytes [105, 106]. The high hexokinase level found in neuron's soma compared to astrocytes by Lungaarg et al. also support neuronal glycolysis capacity [107].

2.2.3.2 Redox switch/redox coupling

In 2004 Kasischke et al. pave the way to a redox coupling view of astrocytes-neurons interaction, with a sub-cellular compartmentalization. After hippocampal stimulation, they described a biphasic NADH response very similar to extracellular lactate modifications measured with enzyme-based biosensor [90, 104] (Fig 5). It turns out that this biphasic modification include two anti-localized component [108]:

- An initial neuronal dip in NADH fluorescence, that mostly reflect oxidative metabolism (mitochondrial NADH consumption for ATP production).
- A late astrocytic over-shoot of NADH fluorescence, that reflect anaerobic glycolysis with NADH production.

These results suggest very local coupling between neurons with a high mitochondrial density and astrocyte's processes, depending on their NADH/nicotinamide adenine dinucleotide oxidized (NAD+) ratio.

Using U-$^{13}C_6$ glucose and 3-^{13}C pyruvate with primary cultured neurons, it is possible to discriminate lactate coming from glucose (2,3-$^{13}C_2$) and extracellular pyruvate (3-^{13}C). This technique allow Cruz et al. in 2001 to evidence two different pools of intracellular pyruvate derive either from extracellular glucose (Pg) or monocarboxylates (Pp) [109]. Together with Kasischke's results Cerdán et al. suggest a subcellular compartmentalization of pyruvate and glutamate in neurons and astrocytes [102], with a **"redox switch/redox coupling"**: The subcellular compartmentalization of pyruvate allows neurons and astrocytes to select between glucose and lactate as alternative substrates, depending on their relative extracellular concentration and the operation of a redox switch. This mechanism is based on the inhibition of glycolysis at the level of glyceraldehyde-3-phosphate (GA3P) dehydrogenase (GA3P $\leftrightarrow$ Pyruvate, Fig 3) by NAD+ limitation, under sufficiently reduced cytosolic NAD+/NADH redox conditions. Lactate and pyruvate recycling through the plasma membrane allows the return to the extracellular medium of cytosolic monocarboxylates enabling their trans-cellular, reversible, exchange between neurons and astrocytes. Together, intracellular pyruvate compartmentalization and monocarboxylate recycling result in an effective trans-cellular coupling between the cytosolic NAD+/NADH redox states of both neurons and glial cells (Fig 4 B.). This coupling could therefore operate differently in remote cell compartments (e.g. neuron's dendrite, axons and soma).

These two models of metabolic cellular cooperation are not mutually exclusive. In fact during physiological brain activation, the "redox switch/redox coupling" prediction fit the "astrocyte-to-neuron" lactate shuttle. However, during pathological process with great metabolic challenge, the redox cooperation might be different.

Most of our knowledge about brain metabolism is based on experiments conducted either *in vitro* (i.e. cell culture and brain slices) or *in vivo* in healthy animals. Yet, these models validity during pathological processes such as acute brain injury where heterogeneous parameter's modifications will take place is poorly understood. Low oxygen and/or glucose concentration in brain slice's medium allow for *in vitro* brain aggression modeling. Either of this condition will induce neuronal depolarization (also called anoxic depolarization) that can be recorded *in vivo* in human or animal during cardiac arrest. It turns out that neither lactate nor pyruvate, in the

Figure 5: **NADH-NAD+ and lactate coupling**: **A.** Online extracellular lactate concentration recordings with an enzymatic biosensor after hippocampal stimulation *in vivo*. Note the initial dip prior to the overshoot. The black arrow display the stimulation's onset. Adapted from Hu et al. [104]. **B.** NADH dynamic and **C.** location during Schaffer pathway stimulation: intrinsic tissue fluorescence imaging on hippocampal slice. The initial NADH dip (green) concomitant with the lactate decrease (A.) is located in the neuropil whereas the following overshoot (red) is localized in astrocytes. The black curve in (B.) represent total NADH fluorescence. Adapted from Kasischke et al 2006 [108]. **Abbreviations**: *NADH*, nicotinamide adenine dinucleotide reduced. White scale bar in C. 50μm.

presence of oxygen, were able to prevent neuronal depolarization when blocking glycolysis at the GA3P dehydrogenase level. However glucose infusion seems sufficient to sustain energetic expenditure in the absence of oxygen [110].
During pathological conditions brain tissue can also be challenged by spreading depolarizations: CSDs. Upon such depolarization the local redox state does not depend on cell types but rather on their distance to the vasculature: tissues located closer than 8–10 mm from a capillary vessel wall showed NADH dips, whereas those located further away showed NADH overshoots [111].

2.3 Cerebral perfusion and blood flow alterations

The Scottish anatomist Alexander Monro first described the ICP in 1783 [112]. In 1926, Harvey Cushing, an American neurosurgeon, formulated the doctrine as we know it today, namely that with an intact skull, the volume of the brain, blood, and CSF is constant. An increase in one component will cause a decrease in one or both of the other components [113].
Brain blood flow can be modelled with Ohm's law which states that flow is proportional to the difference in inflow and outflow pressure (ΔP) divided by the resistance to flow (R): flow $= \Delta P/R$. In the brain, ΔP is cerebral perfusion pressure (CPP): arterial pressure - pressure in veins. Systemic venous pressure is normally low (2–5 mmHg) so that brain venous flow is influenced directly by ICP. Therefore, CPP is calculated as the difference between MAP and ICP.
Under physiological situations CBF range between 46 and $62ml\cdot 100g^{-1}\cdot min^{-1}$ in humans [114, 115]. After TBI global CBF is lower [115], and displays heterogeneous distribution because of edema, contusions and other lesions [116]. Ischemic thresholds that have been determined after carotid surgery or ischemic stroke (18-20 $ml\cdot 100g^{-1}\cdot min^{-1}$) [117], lead to the concept of "penumbra area" between the ischemic core and well perfused remote brain tissue. In traumatic brain injury there is increasing evidence for the existence of a "traumatic penumbra" most at risk of secondary ischemic neuronal injury [116]. However the threshold bellow which irreversible tissue damages occur, is lower ($15ml\cdot 100g^{-1}\cdot min^{-1}$ [116]) with an intermediate oligemic threshold of 33-35$ml\cdot 100g^{-1}\cdot min^{-1}$ [118, 119].
Blood flow also depends on Poiseuielle's law that states that flow is directly related to ΔP, blood viscosity, and the length of the vessel (assumed to be constant) and inversely related to vessel's radius to the fourth power: flow $= (8 \times \eta \times L)/r^4$. Radius appears to be the most powerful determinant of blood flow and even small changes in lumen diameter have significant effects on CBF [120].
At a macroscopic level, auto-regulation of CBF is the ability of the brain to maintain relatively constant blood flow despite changes in CPP, in the range of ≈60-160 mmHg, mainly by vessels radius changes. Above and below these limits, auto-regulation is lost and cerebral blood flow becomes dependent on mean arterial pressure in a linear fashion. Lowering MAP within limits of auto-regulation may increase vessel's diameters and thereby cerebral blood volume. If the brain pressure-volume curve is steep (e.g. during brain edema or intra-cranial mass expansion), any increase in cerebral blood volume will result in a raise in ICP [121].
During brain aggressions like severe TBI, brain vessels can lost their auto-regulation properties. In such situation, CBF and subsequently cerebral blood volume, will follow MAP in a linear relationship. Therefore, correlation between MAP and ICP fluctuation has been used, in the pressure reactivity index (PRx) calculation, as a surrogate to cerebral autoregulation ability [122]. PRx is calculated online as the moving Pearson's correlation coefficients (i.e. $\in [-1;1]$) between 40 past consecutive 5 second averages of ICP and MAP (i.e. a 5 seconds moving window). When cerebro-vascular reactivity/autoregulation is intact, PRx has negative or zero values, otherwise PRx is positive [123, 121].

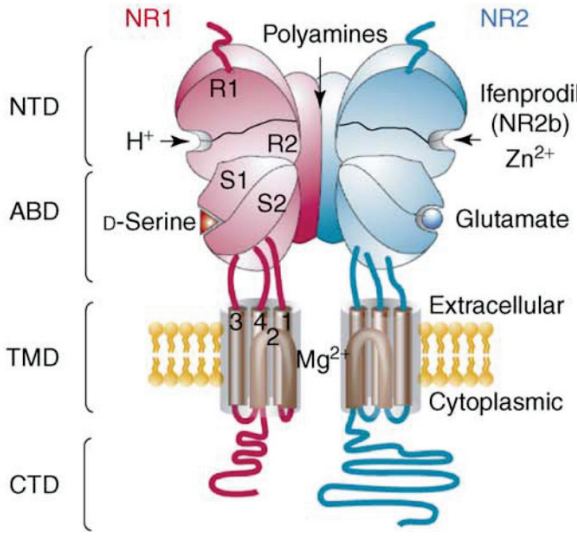

Figure 6: **NMDA receptor binding sites**: Glutamate will bind the NR2 subunit so as Zn^{2+}, whereas the glycine binding site is located on the NR1 subunit and binds either D-serine or glycine. Abbreviations: *CTD*: C terminal domain, *TMD*: trans-membrane domain, *ABD*: Amino-acid binding domain, *NTD*: N terminal domain.

2.4 Excitotoxicity

Glutamate is the main excitatory amino-acid in the central nervous system. It is released in the extracellular space mainly by neurons, and recaptures through NA^+ dependent transporters on neurons (EEAC-1) or astroglial cells (GLAST, GLT-1) [124]. Aside from its neurotransmitter action, glutamate is also known to play important roles during both brain development and pathology.

Glutamate can activate either ionotropic or metabotropic receptors. N-methyl-D-aspartate receptors (NMDAR) are ionotropic glutamate receptors, permeable to divalent (e.g. Ca^{++}) and monovalent ions (e.g. Na^+). It is a heterodimer composed of two subunits (NR1 and NR2). The NR1 subunit is ubiquitous whereas the NR2 has different subtypes (NR2A, B, C or D) that are differentially expressed between brain regions and during development. NMDAR can be located in the synapse or outside the synaptic cleft. The NR2A-containing NMDAR heterodimer subtype is preferentially located at the synapse whereas NR2B-containing NMDAR is predominant outside the synaptic cleft in the adult cortex [125]. The cell membrane needs to depolarize and glutamate with a co-agonist (D-serine or glycine) to bind, in order to activate NMDAR. Glutamate binding site is located on the NR2 subunit, whereas its co-agonist glycine or D-serine will reach the glycine binding site on the NR1 subunit (Fig 6). As a matter of fact, inward current through this receptor can be gated by co-agonist extracellular concentrations. Additional divalent ions binding sites on the NR2 subunit (for Zn^{2+}) or the trans-membrane domain (for Mg^{2+}, Fig 6) can change NMDAR sensitivity to glutamate.

NMDAR lead to paradoxical actions. On one hand, it plays an important role in neuron survival since elimination of NMDAR activity *in vivo* causes widespread apoptosis [126]. On the other hand, over-activation of NMDAR, by sustained NMDA or glutamate exposure, can promote neuronal death. This over activation of NMDAR is called excitotoxicity [127, 125]. It has been proposed that NMDAR location is the main factor that determines their pro-apoptotic or pro-survival effects. Synaptic NMDAR are admitted to be neuroprotective, whereas extrasynaptic receptors over activation will promote cell death [127]. However, the question is still under debate since recent study shows that blocking extra-synaptic NR2B-containing NMDAR do not reduce excitotoxicity. Conversely cell death was prevented by reducing D-serine extracellular concentrations (that preferentially binds synaptic NR2A-containing NMDAR) but not glycine (that preferentially binds extra-synaptic NR2B-containing NMDAR). The authors suggested that synaptic NR2A-containing NMDAR was more prone to induce excitotoxicity [125]. However D-serine is present both inside and outside synaptic cleft, with a $3.1 \pm 0.4 \mu M$ extra-

cellular concentration measured *in vivo* with biosensor [128]. These concentrations are much lower that the one used by Papouin et al. *in vitro* (0.1-0.5mM) [125], but still way above NMDAR glycine binding site ED_{50} for D-serine or glycine ($< 1\mu M$) [129]. Therefore under such extracellular concentrations the glycine binding site would be saturated.
Evidence about excitotoxic glutamate effect through NMDAR have been demonstrated upon high concentrations of glutamate or NMDA cell exposure. However the exact threshold of glutamate concentrations or NMDAR inward currents, promoting excitotoxicity are unknown. Even extracellular *in vivo* concentrations are still debated. Indeed, glutamate concentrations have been measured with cMD $< 2\mu M$ [130, 124] and around $1.2\mu M$ with biosensor *in vivo* [131]. Based on NMDAR inward current recorded in brain slices, some authors even suggested that lower extracellular concentrations near 25nM are needed to prevent NMDAR opening [132].
Mechanisms as well as glutamate and D-serine concentrations that mediate excitotoxicity through NMDAR remain to be clarified.

2.5 Inflammation

Neuroinflammation in brain injury can been viewed as a double-edged sword mediating both short-term beneficial effects for injured parenchyma and neuronal survival but also adverse influences that contribute to secondary brain damage and neuronal loss. Early after brain injury, chemokines release as well as expression of adhesion molecules (I-CAM and V-CAM) by endothelial cells will drive leukocytes extravasation across the BBB [133, 134, 135, 136]. Monocytes and microglial cells during these pathological conditions encompass different phenotypes. In fact if microglial cells will be involved in injury repair, they can also release toxic agent such as reactive oxygen species (ROS) [137, 133]. It is well established that microglial form and function are inextricably linked. In recent years, the traditional view of microglial form ranging between "ramified resting" and "activated amoeboid" has been emphasized through imaging techniques that point to highly dynamic microglial forms. Moreover, microglia adopt intermediate forms, with considerable crossover in function and morphologies as they cycle, migrate, phagocytose, and extend and retract fine and gross processes [138, 139]. Images from brain slice of moderate to severe TBI survivors suggest that persistent inflammation with microglial activation in white matter promotes degeneration and chronic encephalopathy [140].
Microglia can be looked at from different perspectives: their form but also their chemokines expression. As peripheral tissue macrophages, microglial cells seems to have the capacity for multiple activation states according to their environment. Their activation spectrum spans several stages with different functions, between an "M1 pro-inflammatory" (with ROS and TNFα release) to an "M2 anti-inflammatory" type (with IL10 and TGFβ production) [141, 142].
Next generation therapeutic acting on neuro-inflammation will probably try to promote one microglial phenotype over the others instead of blocking leukocytes extravasation or use large anti-inflammatory molecules.
Finally the role of infiltrating T cells has not received a great interest. Recently Walsh et al. published evidences that CD4 T-cells mediate neuroprotection after central nervous system (CNS) injury that is independent of the major histocompatibility complex and the T-cell receptor (MHCII/TCR). Conversely, CD4 T-cells produced IL-4 which attenuate damage via IL-4 receptors on neurons [143].

2.6 Abnormal brain activity

Neuronal activity is usually altered during acute brain injury. Either because of brain aggression or sedative drugs administered in the ICU. Spontaneous electroencephalography (EEG)

can for example display transient electrocerebral silence or decrease in alpha rhythm power (8-12Hz). However these patterns are only surrogates of altered brain condition and might not be deleterious *per se*.
Conversely epileptic activity results from excessive and abnormal cortical nerve cell activity, and is consider a huge energy expenditure [144]. Convulsive seizures can occurs in 11% to 55% of patients undergoing severe TBI [145] and non-convulsive seizure in 22% of moderate or severe TBI, 25% of whom will develop a non-convulsive status epilepticus [36]. Such adverse events are considered part of secondary brain aggressions as they can lead to sustain increase in ICP or altered brain metabolism (e.g. metabolic crisis with a sustain increase in lactate/pyruvate ratio) [145, 146]. Moreover epileptic activity has been found to rise brain glutamate concentration and thereby are considered to generate excitotoxic injury [145, 146].
More recently large waves of depolarizations have been recorded in the human injured brain with sub-dural electrodes recordings called "Cortical spreading depolarizations". Those are waves of electrical silence caused by massive neuronal depolarizations that spread across the brain, causing a local loss of function. The brain's electrical activity will eventually recover. However, with each brain depolarization considered as "tsunami" waves, damage to cells may worsen. Further insight about their contribution to secondary brain aggressions will be discuss later in a dedicated chapter 4.

Over the past decades, major achievements have been made in neurological ICU, mainly regarding monitoring techniques design to address these secondary brain aggressions. So far these techniques were mostly evaluated to assess prognosis evaluations. The next neurological ICU revolution will probably define a conjunction of surrogate markers based on multi-modal monitoring information (e.g. CBF indexes, MRI, biomarkers and electro-physiological signals) in order to develop custom therapeutic interventions to act on local secondary brain aggressions. The next chapter will describe advantages and drawback of different monitoring device available in the ICU.

Chapter 3

Monitoring techniques and their implication in clinical course evaluation

3.1 Usual monitoring techniques

3.1.1 Intra-cranial pressure

ICP devices can be implanted during different pathological states such as severe TBI, subarachnoid hemorrhage, intra-cranial hematoma, hydrocephalus, central nervous system infection, malignant stroke. Several different invasive methods for measuring ICP exist. Depending on the technique, ICP measurement can be undertaken in different intracranial anatomical locations: intraventricular, intraparenchymal, epidural, subdural, and subarachnoid.

External ventricular drainage (EVD) is considered the gold standard, and can also be used for cerebro-spinal fluid (CSF) drainage and administering of medicine intrathecally. In a meta-analysis Binz et al. found the overall hemorrhage risk associated with ventriculostomy placement to be 5.7%, but raise to 10% if systematic CT were performed (Clinically significant hemorrhage $< 1\%$) [147]. The infection or colonization rate is hard to asses depending on its definition (catheter culture or repeated CSF sample) and range between 2 and 20% [148]. Gram-positive cocci (consistent with skin flora) such as *Staphylococcus epidermidis* and *Staphylococcus aureus* are the most common pathogens involved. The main risk factors are: non adherence to rigid insertion and maintenance protocols, leakage of CSF, catheter irrigation and the frequency of EVD manipulation [148].

Microtransducer ICP monitoring devices include fiber-optic devices, strain gauge devices, and pneumatic sensors. Their infection rate is very low (0-8%) like the hemorrhage one ($< 2\%$) [149]. Fiber optic devices, such as the Camino ICP Monitor, transmit light via a fiber-optic cable towards a displaceable mirror. Changes in ICP will move the mirror, and the differences in intensity of the reflected light are translated to an ICP value. The Codman MicroSensor, the Raumedic Neurovent-P ICP sensor, and the Pressio sensor belong to the group of piezoelectric strain gauge devices. When the transducer is bent because of the ICP, its resistance changes, and an ICP can be calculated. Pneumatic sensors (Spiegelberg) use a small balloon in the distal end of the catheter to register changes in pressure, and additionally allows quantitative measurement of intracranial compliance.

The most widely used ICP microtransducers, are those measuring ICP intraparenchymally, usually placed in the right frontal region at a depth of approximately 2 cm. However, depending on known or suspected pressure gradients across intracranial compartments, the placement can be modified.

It is important to realize that even with a ventricular catheter, uniformly distributed ICP will only be observed when CSF circulates freely between all its natural pools. An intraparenchymal

Figure 7: **Visualization of correlation between GOS and average number of ICP insults per GOS category**: **Left** adult cohort. **Right** pediatric cohort. Each color-coded point in the graph refers to a number of episodes of ICP, defined by a certain ICP intensity threshold (X-axis), and a certain duration threshold (Y-axis). The univariate correlation of each type of ICP insult with outcome is color-coded: Dark red episodes mean that such ICP insults are associated with worse outcome; dark blue episodes mean that such ICP insults are associated with better outcome. The contour of zero correlation is highlighted in black. Adapted from Güizan et al. 2015 [154]

probe measures local pressure that can be compartmentalized and is not necessarily identical with intraventricular pressure. Significant pressure gradients may exist in patients with intracranial hypertension. For example supratentorial measurements do not necessarily reflect infratentorial pressure and bilateral ICP monitoring has demonstrated large ICP gradients in patients with expanding mass lesions, subdural hematomas, or even in absence of space occupying lesions [150, 151].
Normal ICP varies with age and body posture but is generally considered to be 5-15 mmHg in healthy supine adults, 3-7 mmHg in children and 1,5-6 mmHg in infants [152, 149]. Average ICP $>$ 20mmHg in the first 48 h of monitoring is an independent predictor of mortality and functional 6-month outcome in moderate or severe TBI patients [153, 154]. Recently data from the "European Union Brain-IT project" showed that the cumulative intracranial pressure-time burden is independently associated with mortality. In fact ICP above 20 mmHg lasting longer than 37min in adults, and longer than 8 min in children, are associated with worse outcomes [154]. But long lasting ICP between 15 and 20 mmHg can also lead to bad outcome [154] (Fig 7). This highlights that not only ICP threshold is important but other features such as the time spend above a threshold and the CPP (i.e. mean arterial pressure - ICP) are important.
Different patterns of ICP changes are typically observed after TBI:

- Low ($<$ 20 mm Hg) and stable ICP: This pattern is seen after uncomplicated head injury or during the early hours after severe TBI, before brain swelling evolves.
- High ($>$ 20 mm Hg) and stable ICP: This is the most common pattern seen after severe TBI.
- ICP waves: These reflect reduced intracranial compliance and are discussed in detail

below.

- ICP changes related to changes in arterial blood pressure: These occur in the presence of abolished cerebral auto regulatory responses when ICP changes directly with arterial blood pressure. See details about the PRx below.

- Refractory intracranial hypertension: In the absence of aggressive treatment strategies this may progress to herniation and death.

In 1965, Lundberg et al. characterized ICP slow waves. "A" waves or "plateau" waves are steep increases in ICP from baseline to peaks of 50-80 mm Hg that persist for 5-20 min. These waves are always pathological and may be associated with early signs of brain herniation, such as bradycardia and hypertension. They occur in patients with intact autoregulation and reduced intracranial compliance and represent reflex, phasic vasodilation in response to reduced cerebral perfusion. The development of plateau waves leads to a vicious cycle, with reductions in CPP predisposing to the development of more plateau waves, further reductions in CPP and irreversible cerebral ischemia. "B" waves are rhythmic oscillations occurring at 0.5-2 waves/min with peak ICP increasing to around 20-30 mm Hg above baseline. They are related to changes in vascular tone, probably due to vasomotor instability when CPP is at the lower limit of pressure autoregulation. "C" waves are oscillations occurring with a frequency of 4-8/min and are of much smaller amplitude than B waves, peaking at 20 mm Hg. They occur synchronously with ABP, reflect changes in systemic vasomotor tone, and are of no pathologic significance [155, 152].
As describe in the previous chapter 2, PRx represent a surrogate to cerebral autoregulation. It is computed online as the correlation between ICP and MAP in a 5 sec moving window [122]. When cerebro-vascular reactivity is intact, PRx has negative or zero values, otherwise PRx is positive [123]. PRx has been related to patient's mortality and outcome, and have different thresholds for survival (0.25) and for favorable outcome (0.05) [156]. CPP is also associated with survival, but the optimal CPP might be different between each patients. Therefore, finding the ideal CPP that provide sufficient energy supply while avoiding edema and increases in ICP is a key element of severe TBI management in the ICU. Optimal CPP can be defined when the lowest PRx (i.e. the best autoregulation index) is reached. Patients with a mean CPP close to their optimal CPP are more likely to have a favorable outcome. Hence, minimal achievable PRx, have been proposed to guide CPP in head injured patients [157].

3.1.2 Trans-cranial Doppler

Trans-cranial Doppler (TCD) uses ultrasounds applied at each temporal windows of the skull. It is a bedside non-invasive technique used in the ICU or the emergency room, as well as out-of-hospital [158]. The first mode commonly used is "B-mode" imaging, which displays a 2-dimensional image as seen by the ultrasound probe. The "B-mode" gives anatomical information about brain parenchyma and ventricles. Some authors used it for hydrocephalus (third ventricle size) [159, 160, 161], cerebral hernia (mid-line shift) [162], or intra-cranial hematoma identification [163].
The second mode use color Doppler images to find desired blood vessel. Subsequently blood flow velocities may be measured with a pulsed Doppler effect, which graphs velocities over time in a small anatomical window. Most commonly insonated in clinical practice is the middle cerebral artery which is easily accessible [164]. The difference between systolic and diastolic flow velocity, divided by the mean flow velocity, is called the pulsatility index (PI, equation (1)).

$$PI = \frac{Vs - Vd}{Vm} \tag{1}$$

Where *Vs* is systolic velocity, *Vd* the diastolic velocity and *Vm* the mean velocity. Measurements of flow velocity are only estimators of CBF, and changes in flow velocity correlate with the changes in CBF only if the angle of insonation and the diameter of the insonated vessel remain constant. Indeed, CBF is related to flow velocity as follows: $CBF = HR \times TVI \times blood\ vessel\ cross-sectional\ area$, where HR is heart rate and TVI is the time velocity integral (i.e. area under the spectral curve). Blood flow in the basal cerebral arteries, as in the arteries of other vital organs (liver, kidney, and heart), has a prominent diastolic component. Vd reflects the degree of downstream vascular resistance, whereas Vs depends on upstream determinants, that is, cardiac output, ipsilateral carotid blood flow, and arterial blood pressure. Vm is the weighted flow velocity that takes into account the different velocities of the formed elements in the blood vessel insonated, and decreases with low CBF. In TBI patients, a low Vd, a peaked waveform, and higher pulsatility index values can be observed during high vascular bed resistance induced by elevated intracranial pressure ICP or hypocapnia [165, 166, 164].
After mild to moderate TBI (i.e. GCS 9-15), one of the key management issue in these patients is to recognize early those at high risk for neurological deterioration despite their initial reassuring presentation. TCD has been found be a reliable tool to identify such patients when Vd$< 25cm/s$ and IP> 1.25 [167]. Therefore, TCD on admission may complete CT for accurate patient evaluation.
After severe TBI TCD has been use to identify and treat brain hypoperfusion (i.e. Vm $<$ 30cm/s, Vd $<$ 20cm/s or PI $>$ 1.4) [168, 158], that is related to bad outcome [169]. In such high-risk patients, early TCD goal-directed therapy can restore normal cerebral perfusion and might then potentially help in reducing the extent of secondary brain injury [168].

3.1.3 Pupil reactivity

The main brain-stem reflex that is always assessed by physicians, even during out-of-hospital management, is pupil reactivity. The photosensitive retinal ganglion cells convey light information to the optic nerve. The optic nerve connects to the pretectal nucleus of the upper midbrain, bypassing the lateral geniculate nucleus and the primary visual cortex. From the pretectal nucleus, axons connect to neurons in the Edinger-Westphal nucleus, whose axons run along both the left and right oculomotor nerves. Parasympathetic neurons from the oculomotor nerve synapse on ciliary ganglion neurons. Finally short ciliary nerves leave the ciliary ganglion to innervate the iris sphincter muscle of the iris. Under normal conditions, the pupils of both eyes respond identically to a light stimulus, regardless of which eye is being stimulated. Light entering one eye produces a constriction of the pupil of that eye, the direct response, as well as a constriction of the pupil of the unstimulated eye, the consensual response. Lack of the pupillary reflex or an abnormal pupillary reflex can be caused by optic nerve damage, oculomotor nerve damage, brain stem death and depressant drugs, such as barbiturates. Comparing these two responses in both eyes is helpful in locating a lesion.
Traditionally, pupil measurements have been performed with a pen flashlight to evaluate reactivity and pupil size. Pupil can be either “reactive”, “slightly reactive” or “non-reactive”. Anisocoric or bilateral non-reactive pupil has been evaluated in the IMPACT and CRASH TBI databases with an adjusted OR close to 2 for unfavorable outcome [12].
However these are subjective terms with a significant level of inter-examiner variability when slight reactivity is present. Hence, automated infra-red pupillometer are used daily in the ICU for brain injury follow-up. Moreover, quantitative pupil reactivity is able to predict cardiac arrest outcome with comparable sensitivity and specificity than EEG and evoked potentials [170].

3.2 Brain metabolism assessment methods

PET is broadly use to investigate brain metabolism and perfusion. For instance ^{18}F-2-deoxyglucose tracer allow for global and local $CMR_{glucose}$ with a spatial resolution in the order of millimeters. Likewise spectroscopic MRI gives precise information about global and local brain molecules concentration such as glucose or lactate [171]. Unfortunately, even if those imaging techniques are of great interest, their application remain limited to research protocols.
Instead global and/or local techniques allow for cerebral metabolism follow-up at the bedside in the ICU.

3.2.1 Global assessment

3.2.1.1 Oxygen

Venous jugular oxygen saturation ($SvjO_2$) can be used in the ICU to follow the ration between brain oxygen consumption and supply. $SvjO_2$ needs a retrograde internal jugular catheterization placed in the jugular bulb to avoid extra-cranial blood contamination. Placement of the catheter have to be confirmed by lateral skull x-ray [172, 173, 115]. $SvjO_2$ can be measured continuously with an optic fiber (calibration needed each 12-24h, more prone to thrombosis) [174, 115], or by repeated blood sample (results are dependent on aspiration procedure) [175].
According to the Fick principle, the arterio-venous difference in oxygen content ($avDO_2$), which is a surrogate to brain oxygen extraction, is proportional to $CMRO_2$ and CBF :

$$avDO_2 = \frac{CMRO_2}{CBF} = (SaO_2 - SvjO_2) \times Hb \times 1.34 + (PaO_2 - PvO_2) \times 0.03 \qquad (2)$$

Where SaO_2 the arterial oxygen saturation, PaO_2, arterial oxygen partial pressure, PvO_2 jugular venous oxygen partial pressure and Hb blood haemoglobin. The last part can be neglect leading to:

$$SvjO_2 = SaO_2 - \frac{CMRO_2}{CBF \times Hb \times 1.34} \qquad (3)$$

$SvjO_2$ average in a normal awake subject, is 62% with a range of 55% to 71%. [176, 177]. According to equation (3), decreased values can come from (1) any numerator increase (e.g. CMRO2 increase during seizure, consciousness, or fever) or (2) any denominator element decrease: insufficient CBF (e.g. during hypotension or increased ICP) or anemia.
Although values $\leq 50\%$ are associated with low GOS in patients with severe TBI [178], the last "guidelines for the management of severe TBI" from 2007 (build by the brain trauma foundation and the American Association of Neurological Surgeons (AANS) and the Congress of Neurological Surgeons (CNS)) hold only a level III to $SvjO_2$ monitoring [179].

3.2.1.2 Glucose and lactate

Not only retrograde jugular line is used for $SvjO_2$ measures, but also for global carbohydrate metabolism evaluation with glucose and lactate blood content. Hence, the arterio-venous difference in glucose blood content (avD_{gluc}), arterio-venous difference in lactate blood content (avDL), or $avDO_2$, gives a global brain metabolism overview.
In 2003 Glenn et al. gives an extensive description of the mean global parameters in healthy and TBI patients with retrograde jugular line [115] (Table 5). They point out that in sedated TBI patients both $CMRO_2$, $CMR_{glucose}$ were depressed. In this study, multivariate analysis shows that the mean parameters most related to the outcome were $CMRO_2$, arterial lactate levels, arterial glucose levels and a trend for CBF. They also found a CMR_{lact} increase after TBI, and that episodes of increased lactate uptake occurred most frequently in unfavorable

Parameter	TBI patients	healthy volunteers	p
CBF ($ml.100g^{-1}.min^{-1}$)	40.17 ± 13.2	46.2 ± 10.5	0.01
$CMRO_2$ ($ml.100g^{-1}.min^{-1}$)	1.4 ± 0.43	3.10 ± 0.56	0.0001
CMR_{glc} ($mg.100g^{-1}.min^{-1}$)	3.43 ± 2.32	4.46 ± 1.16	0.0002
CMR_{lac} ($mg.100g^{-1}.min^{-1}$)	0.0355 ± 0.41	-0.18 ± 0.21	0.0001
$avDO_2$ ($ml.dl^{-1}$)	3.76 ± 1.37	6.89 ± 1.35	0.0001
avD_{glc} ($mg.dl^{-1}$)	8.94 ± 6.57	9.89 ± 2.92	0.002
avD_{lac} ($mg.dl^{-1}$)	0.0464 ± 0.94	-0.40 ± 0.48	0.0002
Art glucose ($mg.dl^{-1}$)	122.7 ± 33.8	82.2 ± 8.3	0.0001
Art lactate ($mg.dl^{-1}$)	14.05 ± 8.2	6.7 ± 2.1	0.0001
Metabolic Ratio	4.11 ± 2.11	5.83 ± 1.41	0.0001
Jugo2Sat (%)	72.9 ± 8.6	61.7 ± 5.9	0.0001
Arto2Sat (%)	98.5 ± 1.5	97.5 ± 1.2	0.0001

Table 5: **Carbohydrate metabolic rate**. Adapted from Glenn et al. 2003 [115]

outcome patients (i.e. GOS 1-3) [115].
During hypoxia or ischemia, brain metabolism is altered and increased brain lactate can be observed using cMD or in the CSF [115, 180] and will lead to an increased avDL. Thereby, the first index that can be extracted from these values is the lactate-oxygen index (LOI) ($avDL/avDO_2$). It is an estimation of the anaerobic brain metabolism. Hence, increased LOI > 0.08 reflect a mismatch between oxygen supply and brain metabolism, and is associated with a bad outcome [181].
The second parameter is the oxygen-glucose index (OGI) defined by equation (4). The metabolic ratio (MR) often use as a surrogate is the ration between $avDO_2$ and avD_{gluc}, but omit that 6 oxygen molecules are needed to oxidize one of glucose. This index represents the oxidative glucose metabolism within the brain.

$$OGI = \frac{avDO_2}{6 \times avD_{gluc}} \tag{4}$$

Absolute hyperglycolysis is defined as a $CMR_{glucose}$ greater than the 97.5th percentile of normal for an awake human (i.e. $CMR_{glucose} > 6.69 mg.100g^{-1}.min^{-1}$, normal $= 4.46 \pm 1.16$, Table 5). On the other hand relative hyper-glycolysis (i.e. when glucose uptake exceed oxygen consumption) is defined as a MR below the 2.5th percentile of normal values (i.e. $MR < 3.44$, normal $= 5.83 \pm 1.41$, Table 5) [115, 182]. However even if relative hyperglycolysis appeared to be more frequent in patients who died, neither episodes of absolute nor relative hyper-glycolysis were strongly associated with 6 month GOS [115].
At the bedside, following global brain metabolism with retrograde jugular line requires repeated combine arterial and jugular sample. Aspiration have to be gentle, and samples must be put immediately in ice. These parameters were the first available to measure brain metabolism in the ICU and have been related to the outcome [181, 115], or ischemic lesions during carotid surgery in awake patient [183].
However some discrepancy restricted their daily use. For instance, it can be caught off guard during anemia and has been shown not to be always correlated with brain lactate concentration [184]. Finally this monitoring fails during unilateral ischemia, with discrepancies between both sides leading the authors to conclude that unilateral jugular venous monitoring reliability monitoring was suspicious [185].
Although it might be useful for diffuse TBI monitoring to manage CPP, there is no level I or II recommendation for its daily use in the ICU.

3.2.2 Local measures

To overcome jugular measures limitation, such as extra-cranial blood blending or transient event missing, local techniques have been developed to measure similar parameters (i.e. oxygen and carbohydrate concentrations) directly within brain tissue. It seems that after diffuse head injury, local monitoring values (i.e. oxygen, CBF or cMD) are correlated to the overall white matter CBF (R^2=0.49) [119]. In the same study, Bouzat et al. found multi-modal monitoring to better predict CBF than ICP alone, and should be therefore be use to detect oligemic events [119]. However, this might not be the case when focal lesions take place with huge metabolic discrepancies over the brain.

3.2.2.1 Brain oxygen partial pressure

In 1997 Charbel et al in were among the first to measure $PbtO_2$ continuously in the human brain with the Paratrend 7^{TM}system. This device gives concomitant $PbtO_2$, CO_2, pH and brain bicarbonate concentrations. They found normal $PbtO_2$ to be 33 ± 11mmHg [186], but during neurosurgery it can range between 12 and 50mmHg in the grey matter [187].
$PbtO_2$ can be measured with different techniques: electrochemical (*Clark* type micro-electrode), optical with luminescent material, electron paramagnetic resonance, or mass spectroscopy. At the bedside $PbtO_2$ is measure using either electrochemical (Licox®, Integra neuroscience) or optical technology (OxyLab pO_2®, Oxford optronics, using ruthenium luminescent molecules). There is a greater body of literature that describes the Licox® system. The electrochemical measurements of oxygen with *Clark* type micro-electrode is based on oxygen reduction at a polarized cathode surface, producing an electrical current. In the 1950s, Clark enhanced the performance and consistency of electrodes for use in biologic fluids and tissues by electrically insulating the anode and cathode with a gas-permeable, but not liquid-permeable, membrane [188].
Factory probes calibration gives a linear relationship between electrical current and oxygen concentration. Like all chemical reaction, the reduction of oxygen rate depend on temperature, so that the relation between $PbtO_2$ and the oxidative current have to be adjusted to brain/body temperature.

Brain tissue oxygen
$PbtO_2$ is heterogeneous and the $PbtO_2$ at any given point will be a product of highly variable local factors: the distance from vessels, the PO_2 in those vessels, the local diffusion coefficient and the local rate of O_2 consumption. Hence, there is no "characteristic oxygen tension", rather there is an oxygen tension field in brain tissue that range between 6 and 25mmHg [189, 190].

Brain vascular oxygen content
PO_2 values in the pial vessels range from approximately 60-110mmHg in arterioles and approximately 35-60mmHg in venules. Using two-photon imaging, Sakadzić et al. measured PO_2 in penetrating arterioles and venules in the cortex, reporting that PO_2 in descending arterioles at the pial surface was approximately 60-70 mmHg, and that of ascending venules was around 40 mmHg. They noted that the vascular PO_2 decreased in line with increasing branching order and depth ($\approx 10 mmHg$ between 0-240μm below the pial surface) [189]. Finally PO_2 in capillaries was found around 30mmHg whatever the depth [189, 191, 192]. It is very important to note that vascular O_2 content is still debated since these measures are highly dependent on hematocrite, CBF and region of interest (ROI) location *vs* red blood cells [192, 189, 191].

$PbtO_2$ in the ICU
Given the large probe size (i.e. 600-800μm) with a sampling area around 14mm^2 and the high density of the capillary bed (Fig 1), $PbtO_2$ measures in the ICU are a mix of capillaries, intra and extracellular oxygen concentrations. $PbtO_2$ probes are usually implanted in white matter

parameter	Normal values [200, 201]		Critical values [202, 203]	
	Schultz	Reinstrup	High	Low
lactate (mmol/L)	3.06 ± 0.32	2.9 ± 0.9	> 4	> 2.5
Glucose (mmol/L)	2.12 ± 0.15	1.7 ± 0.9	< 0.2	< 1
Pyruvate (μmol/L)	151 ± 11.5	166 ± 47	< 25*	
Lactate/Pyruvate (%)	20 ± 2	23 ± 4	> 40	> 25
Glutamate (μmol/L)	14.4 ± 3.3	16 ± 16	> 5*	
Glycerol (μmol/L)	81.6 ± 12.4	82 ± 44	> 50*	

Table 6: **Cerebral Microdialysis parameters**: Normal values in anaesthetized patients during neurosurgery in two studies [200, 201], and critical thresholds defined by Paul Vespa (hight) [202] or Juan Sahuquillo (low) using the 95 percentile of normal values for lactate and 25% as L/P thresholds [203, 180]; *, were used by Judith Marcoux et al. in 2008 [204].

where normal values range between 25 and 35mmHg [186, 193].
$PbtO_2$ is linked to CBF, arterial oxygen content, oxygen extraction fraction, and $CMRO_2$ [194]. Thereby, a $PbtO_2$ decrease reflects either a decrease in CBF, an increase in $CMRO_2$, or a decrease in oxygen arterial content.
$PbtO_2$ values $<$ 15mmHg have been related to an unfavorable outcome or death, however like for ICP, the longer a patient experiences a $PbtO_2 <$ 15mmHg, the greater the chance of death [195]. There is also a critical threshold of 5mmHg below which most patients will die [195].

3.2.2.2 Carbohydrate brain concentrations

cMD aims at sampling interstitial fluid threw a dialysis membrane in any tissue. It has been used since the 70s for research purpose in animals brain [196]. The first sterile catheter was designed for human implantation in the 90s (CMA Microdialysis) [197]. After initial use during epilepsy, it is now used during neurosurgery or in the ICU as part of acute brain injured patient multi-modal monitoring.
cMD tip is made of a semi-permeable polyamide membrane (10-30mm long, outer diameter 200-600μm). Driven by the gradient between interstitial fluid and the microdialysate, molecule will diffuse through the membrane. Usually the probe cut-off is around 20kDa allowing to study small molecules such as glucose, lactate pyruvate or glutamate. The equilibrium of such molecules is incomplete. The probes yield depend mainly on the membrane cut-off and microdialysate perfusion rate. The CMA-70 probes yield (10mm length, 20kDa cut-off) range between 70% (at $0.3\mu l.min^{-1}$) and 30% (at $1\mu l.min^{-1}$) [198, 199]. Usually, cMD are use with a $0.3\mu l.min^{-1}$ perfusion rate, providing a 60min sampling rate [199].
Normal brain concentrations of glucose, lactate, pyruvate as well as the "anaerobic" thresholds, are still quite arbitrary. They are extrapolated from animal studies made in different organs, or from patients who underwent neurosurgical operations for posterior fossa lesions or epilepsy [200, 201, 203] (Table 6).
Low extracellular brain glucose has been associated with bad outcome during acute brain injury [115, 202]. In 2011 Timofeev et al. found that increased lactate ($> 4mmol$/L), L/P ($> 25\%$) and low glucose ($<$ 1mmol/L) were also more frequently observed in patients with unfavorable outcome after severe TBI [205]. Several interpretations of carbohydrate brain concentrations were hypothesized based on glucose metabolism pathways: Anaerobic or anaerobic glycolysis (Fig 3).
Recently Sahuquillo et al. showed that no relationship exist between L/P and lactate concentration [203]. Because lactate results from glycolysis, brain lactate concentrations correlates with

Brain metabolism	description	glucose	lactate	pyruvate	L/P	$PbtO_2$
Compensated	normal	N	N/low	N/low	low	N
	aerobic hyper-glycolysis	low	high	N/low	low	N
Altered: MC	type 1 or anaerobic hyper-glycolysis (with ischemia)	low	high	low	high	low
	type 2 or low pyruvate state (without ischemia)	low	N/low	low	high	N

Table 7: **Summary of different brain metabolic states** as describe by several authors using cMD, $PbtO_2$ and PET to define ischemic threshold [203, 202, 206, 207].
Abbreviations: L/P, lactate/pyruvate ratio; N, normal; MC, metabolic crisis.

$CMR_{glucose}$ [202], whereas extracellular pyruvate concentrations dependent on both glycolysis rate and oxygen consumption (mitochondrial tricarboxylic cycle). Given this, several authors tried to delineate different metabolic patterns depending on brain glucose, lactate, pyruvate, oxygen and CBF (measured with PET). These different definitions are summarize in the table 7.
A linear relationship exists between $CMR_{glucose}$ and the cMD levels of lactate and pyruvate but not with the L/P [203]. In fact L/P displays a negative correlation with $CMRO_2$ [202], suggesting that it is more a surrogate of the cellular redox state. It has been postulated that glycolysis up-regulation in an injured brain indicates a hyper-metabolic state directed toward restoring perturbed ionic homeostasis or the uptake of high extracellular levels of glutamate. Increase in $CMR_{glucose}$ in these patients is often indicative of hyperglycolysis and not of a shift towards anaerobic metabolism. The main difference between aerobic hyperglycolysis and an anaerobic profile is that the L/P is significantly increased in the latter.
Among anaerobic patterns, the type 1 is the classical ischemic metabolic state where the NAD+/NADH ratio is shifted toward NADH as a result of mitochondrial oxidative pathway dysfunction. Then, lactate dehydrogenase reaction is oriented toward lactate formation, with a subsequent high L/P. However anaerobic hyperglycolytic pattern do not necessarily mean ischemia but rather that oxygen supply does not fit energetic needs, as described in the type 2 pattern, also called “low pyruvate”. During such situations the $PbtO_2$ and CBF remained in the rage of normal values [202, 207, 206].
Hypermetabolism following TBI occurs because oxidative phosphorylation normally runs at near maximal capacity, consequently an increased energy demand should be supplied by an increase in glycolysis [208, 203]. In fact this adapted reaction of aerobic hyperglycolytic pattern to an aggression is more frequent in patients with good neurological recovery than anaerobic pattern [208, 209].
Apparently, increments of microdialysis L/P ratio unrelated to ischemia are quite common in TBI patients [206, 207]. The corresponding “low pyruvate” pattern reported by several authors [203, 206, 204], can be consider as an indicator of type 2 anaerobic metabolism. A few mechanisms have been proposed to explain this metabolic behavior including a switch from glycolysis to pentose phosphate pathway or mitochondrial dysfunction. However, additional studies are needed to conclude, and the impact of “low pyruvate” phenomenon on the outcome of TBI patients remains to be determined [207].

Although these profiles have been related to patient’s outcome, these metabolic patterns are

the consequence of several secondary brain aggressions that have to be clarify. For instance, epileptic seizure or reduced CBF are known to impair brain metabolism [146, 210]. But other pathological events such as CSD are under estimate and could play an important role when brain homoeostasis is altered.

3.3 Electro-physiology

Head trauma is associated with both "primary" and "secondary" dysfunction, which will give rise to a complex mixture of focal and diffuse lesions. Since secondary brain aggression might progress over time, the earlier the evaluation, the higher the rate of false, especially over-optimistic, predictions. EEG examination looks for baseline ongoing activity, epileptic seizure, electric reactivity to sensory stimulus, or evoked potentials. In 2009, a consensus on the use of neurophysiological tests in the intensive care unit (ICU) was published in clinical neurophysiology including TBI associated patterns [211] (table 8).
Spontaneous EEG can have non-specific altered patterns, such as focal or global decrease in alpha rhythm power (8-12Hz) with increased theta and delta activity. This pattern has been described for example on continuous EEG during delayed cerebral ischemia following subarachnoid hemorrhage, or decreased CBF [212, 145].
Epileptic events can be recorded in brain injured patients and are called "post traumatic seizure" after TBI. In the ICU, around 11% to 55% of moderate to severe TBI patients undergo non-convulsive seizure, 25% of whom will develop a non-convulsive status epilepticus [36, 145]. These episodes of non-convulsive seizure are considered to be part of secondary brain aggression as they can lead to sustain increase in ICP, metabolic crisis and can raise brain glutamate concentration [145, 146].
However these markers are not sufficient to predict patient's outcome. Usually more advanced electro-physiological examination are performed to evaluate functional consequences of anatomical lesions. Early and middle latency evoked-potentials gives information about either somatosensory or auditory pathways integrity. On the other hand late evoked potentials are more determined by pre-attentional and attentional processes. The N100 is the negative potential generated in the supra-temporal cortex, in response to an auditory "click". After an infrequent change in a repetitive sequence of sounds, the N100 amplitude negativity is increased. This phenomenon is called the "mismatch negativity" (MMN). When present, MMN and the N100 differ from those found in normal subjects in terms of latencies and amplitudes. As a predictor of return of consciousness MMN had high specificity and low sensitivity, whereas the N100 had high sensitivity and low specificity [213]. P300 is a later response reflecting patient's attentional focus toward an odd stimulus. In the auditory modality, the P300 can be enhanced using the subjects own name among others. This late component seems to engage distributed cortical regions as well as the hippocampus, and reflect complex auditory and linguistic processes [214]. The use of P300 elicited by subject's own name increases the prognostic value of MMN alone and improves the assessment of comatose patients by demonstrating the activation of higher-level cognitive functions [215].

However many standard EEG amplifiers are built with a high pass filter (0.5-1Hz cut-off), in order to avoid non-specific large direct current (DC) shifts. Indeed such large baseline modifications can be of high amplitude and eventually lead to signal saturation. If no baseline correction is performed, the signal can be lost for long periods of time.
Since the mid-90s, diagnosing CSD have been done in the human brain with specific amplifier settings. Indeed these large DC modifications ($\approx 5-10$ fold that of a *status epilepticus*) requires amplifiers without any high pass filter (i.e. low cut-of of 0-0.02Hz). Unfortunately, CSD can-not be specifically identify on the scalp EEG.

Prognostic	Description	Remarks
Death	EEG: electrocerebral silence in the absence of sedative drugs, EP: pattern of brain death	Just confirmatory test
Ominous	BAEP: level 2, SEP level 3, (P14 present) EEG: malignant patterns	Pontine involvement in transtentorial herniation Usually reflect secondary complications (ischemia, epilepsy, intracranial hypertension)
Uncertain patterns	BAEP level 0, SEP level 2 ("midbrain pattern") EEG: uncertain pattern without reactivity	Midbrain dysfunction: uncertain despite poor clinical examination (GCS 4/15), requires MRI
Good prognosis	EEG: uncertain pattern (Synek) with variability and/or reactivity and/or spindles Normal BAEP and normal SEP or level 1 abnormalities	
Best prognosis, more than 95% of patients wake up	Preservation of ERP (MMN, P3)	Justifies maximal resuscitation

Table 8: **Prognostic value of EEG and EP patterns in post-traumatic coma**. Adapted from Guerit et al. 2009 [211, 216, 217, 218]. **Abbreviations**: *EEG*: electroencephalography, *EP*: evoked potentials, *BAEP*: brainstem auditory EP, *SEP*: somatosensory EP, *ERP*: event-related potentials, *MMN*: mismatch negativity. *EP modifications*: Level 0: normal, level 1: inter-peak latency increase, level 2: Distortion without disappearance, level 3: Disappearance.

The next chapter will discuss patho-physiological issues about CSDs during acute brain injury.

Chapter 4

Cortical spreading depolarization

4.1 From bench to bedside

In 1944 Aristides A. Leão was studying, for his doctorate in Harvard University, the propagation of epileptic activity in the cerebral cortex. He approached the problem by applying electrical stimulation to the frontal convexity cortex of anesthetised rabbits, and recording from an array of corticography electrodes posterior to this. Instead of seeing propagating epileptic activity, he observed a period of electrical silence, which was first seen adjacent to the stimulating electrodes, and did propagate from the site of stimulation backwards along the cerebral hemisphere at a rate of around 3 mm/minute. The phenomenon resolved spontaneously after 5-15 minutes, with apparently full resumption of cortical electrical activity. He reported his findings in a landmark paper entitled "Spreading depression of activity in the cerebral cortex" [219]. A few years later he described the large depolarization associated with these depressions of cortical activity and found that they looked like the slow DC shifts he observed after prolonged cerebral ischemia (during carotid artery occlusion) [220]. Triggering CSD in different conditions, he already suggested that their development and characteristics were not determined by the stimuli, but depended on the local characteristics and conditions of the affected regions [220].
The slow potential change of spreading depolarization seems to be invisible in scalp EEG recordings, whereas the tenfold smaller discharges of epileptic seizures are easily identified. This paradox results from the potent capacitive resistance of the dura and skull, which filters slow voltage changes but allows high-frequency epileptic activity to pass through. For decades, this simple physical problem has led to the false conclusion that CSD does not occur in human brain [221].
In 1977 CSD have been elicited in the human brain (caudate nucleus and hippocampus) seeking to treat focal epilepsy [222]. Fortunately this has not been replicated and only electrocorticography with subdural or depth electrodes has now provided unequivocal evidence that spreading depolarizations occur in abundance in people with structural brain damage. In 1966, Mayevsky et al. were the first to record CSD correlates in human cortex after TBI (one over 14 patients) using a multiparametric device with depth electrodes [223]. In 2002 Strong et al. set up a linear subdural strip, made of 6 platinum electrodes, placed on the cortex after a craniotomy in order to record both the depolarization and its spread [224]. This subdural strip of electrodes had become the standard recording technique in the human brain. From now on an international group of investigators build the "**C**ooperative **S**tudies on **B**rain **I**njury **D**epolarization" (COSBID, http://www.cosbid.org/) to discuss ways to advance these findings and further investigate their implications.
Different CSD patterns have been described based on their electric signature (Fig 8):

- *Cortical spreading depolarization*: the generic term for the whole spectrum of waves in the central nervous system.

- *Terminal depolarization* also called *anoxic depolarization*: spreading depolarization without neuronal repolarization; occurs in the presence of severely noxious conditions such as anoxia, aglycemia or severe focal or global ischemia. The depression of brain activity might occur before the depolarization (Fig 8C.).

- *Intermediate depolarization* also called *peri-infact depolarization* or sometimes *iso-electric depolarization*: Prolonged spreading depolarization with a character between terminal depolarization and short-lasting spreading depolarization. Intermediate spreading depolarizations can occur, for example, under hypoxia, hypoglycemia or in the ischemic penumbra where they are often referred to as peri-infarct depolarizations. They usually occur in a cluster of recurrent events, and are associated with persistent depression of activity between the events (Fig 8B.).

- *Spreading depression*: As it was the first element to be described by Leão in 1944 it is often use to name CSD. However depression of ongoing electric brain activity during spreading depolarization is not always present, and CSD has to be refer as spreading depolarization but not depression. Therefore CSD can be associated with a spreading depression (Fig 8A.) or not when cortical electric activity is already low (also refers as *isoelectric depolarization*, Fig 8B.).

4.2 CSD in brain pathology

To date CSD recording technique needs electrodes to be placed either on the surface or into the cortex. Therefore the only way to be sure of CSD occurrence in humans is by surgical craniotomy. CSDs have only been recorded in severely brain injured patients after neurosurgery procedure for intracranial hematoma evacuation, aneurysm clipping or decompressive craniectomy [224]. More recently the same 5mm diameter strip of electrodes have been placed through an extended burr-hole for EVD [226].
CSDs can be detected among 56% of patients undergoing severe TBI. Moreover, CSD occurrence appears to be associated with patient's unfavorable outcome after controlling for conventional prognostic variables [225]. Among depolarizations events, iso-electric depolarizations were the one more related to unfavorable outcome (OR=7.58 (2.64–21.8)), whereas CSD without iso-electric ones had no significant effect on outcome (OR=1.56 (0.72–3.37)) [225]. Likewise, CSDs occur in over 70% of patients with high grade sub-arachnoid hemorrhage (Fischer 3-4). The CSD pattern again reflects the impact it will have on brain tissue. Indeed patients who developed prolonged depression periods lasting more than 10 min had worse outcome. Moreover, delayed cerebral deficit ± ischemia was time-locked to new clusters of spreading depolarizations [227].
Finally, CSDs can be recorded in gyrencephalitic brain after an ischemic stroke. In such condition, peri-infarct depolarization occurrence will expand the hypo-perfused area [228, 229, 230]. In fact, the higher the rate of recurrence of peri-infarct depolarizations, the earlier did the cortical DC potential convert into terminal depolarization, as an indicator of functional deterioration and infarct growth [231].
To conclude, isolated CSD does not seem to be very harmful, and some authors even suggest that it can have preconditioning properties [232]. Then when CSD turns into intermediate or terminal depolarization, they lead to ischemic lesion progression and unfavorable outcome.

Figure 8: **Cortical spreading depolarization patterns**: **A.** Cortical depolarization spreading from electrode 1 to 2 with an associated depression [225]. **B.** Cluster of iso-electric depolarization spreading from electrode 1 to 2. Note the absence of ongoing brain activity [225]. **C.** One cortical depolarization followed by a terminal depolarization [221].

4.3 Mechanisms of spreading depolarization

Although brain represents ≈2% of body mass, its energy expenditure reaches ≈20% of total body consumption. Maintenance of neuronal membrane potential at resting state and during signaling by the Na^+/K^+ ATP_{ase} pump represents over 50% of grey matter ATP consumption [233]. Nevertheless, the amount of energy being consumed at any moment in time for the signaling and maintenance of the resting potential and ion gradients is small in relation to the total electrochemical energy that is already stored up in the system in the form of physiological ion gradients. This implies that much more energy is required to reboot the system after a breakdown than to maintain the system [144].
From an energetic point of view, life and subsequently brain homoeostasis is a non-equilibrium steady state, whereas death incurs no cost by itself. Two pathological states can challenge this steady state: ictal epileptic activity and spreading depolarization. They are essentially characterized by an abrupt, partial loss of the ion gradients across the membrane that is much larger after CSD [144].
Neurons and their proximal dendrites are the main active players of spreading depolarization. The near complete breakdown of ions gradients that takes place [234] lead to an initial explosive opening of conductance along pyramidal neuron with trans-membrane potential reaching almost zero, and followed by a wave-like centripetal closure towards the apical dendrites [235] (Fig 9A and B).
Potassium release with sodium, chlorine and calcium inward current overcome the pumps capacity and lead to a near complete loss of electrochemical energy with a passive ion distribution across the membrane. Intracellular hyperosmolality due to charged proteins will lead to cellular swelling and distortion of dendritic spine (Fig 9C). However, in healthy well perfused cortex sodium ATP_{ase} pumps induce a rapid recovery of this ionic breakdown, and restore cell morphology within minutes. Conversely, clusters of peri-infarct depolarizations induce sustain dendritic beading, suggesting that energy needs for recovery exceeded energy supply of compromised blood flow [236].
Interestingly, it seems that not only neurons are affected and required to recover from a CSD. In fact, reducing intracellular ATP concentration in astrocytes by blocking their mitochondrial oxidative cycle with fluorocitrate lead CSD to exceed energy supply and subsequently to neuronal damage [237].

Spreading depolarization typically spread at a rate of 2-6 mm min [221]. Mechanisms of spreading have not been clearly elucidated. As potassium and glutamate have been found to be released in the extracellular space during CSD [238, 239, 240], it has been hypothesized such neuro-active substances will first excite and then depress neurons while forcing them to release more excitatory transmitters acting on surrounding cells [221]. The separate idea that K^+ might diffuse slightly further in the extracellular space and cause depolarization in non-contiguous neurons was explored in detail by Gardner-Medwin et al., who determined a rate for cortical extracellular diffusion of K^+ slower than that of CSD propagation [241]. A further argument against extracellular diffusion of K^+ as the basis of propagation is that in CSD, no increase in K^+ can be recorded in the cortex prior to the DC depolarization [234, 242].
Another mechanism that has been suggested is a trans-cellular pathway for the reaction/diffusion via neuronal and/or glial gap junctions that accounts for prodromal synchronization ahead of the advancing DC and potassium front [243, 244]. In the case of astrocytes, it is now abundantly clear that in cultures of astrocytes studied with intracellular calcium-sensitive dyes, waves of transient increase in intracellular calcium ion can be initiated by glutamate, NO or mechanical stimulation, and will then propagate across the culture at a rate very similar to that of CSD in the intact cortex [245, 244].
Last but not least remains the question about mechanisms that initiate CSD. So far, only hy-

Figure 9: **Cortical spreading depolarization mechanism**: **A.Top**, in the healthy brain impermanent negatively charged proteins inside the neuron cause small cations such as sodium and calcium to enter from the extracellular space, producing a small dendrite inward current (I_{in}, pink arrow). Compensation for this constant inward current by dendrite outward current (I_{out}, green arrow) of the sodium pump. **A.Bottom**, the core process of spreading depolarization is failure of sodium and calcium pumps to provide sufficient dendritic outward currents to balance the persistent inward currents through pink and purple channels. If net dendritic current turns inward (persistent influx of sodium and calcium is more than the out-flux of potassium) a near-complete loss of electrochemical energy occurs with almost passive ion distribution across the membrane, intracellular hyperosmolality with cellular swelling and distortion of dendritic spines. Adapted from Dreier 2011 [221]. **B** Extracellular ion concentrations changes during a spreading depolarization represented in grey as its extracellular voltage DC shift. Recording were made in a healthy cerebellar cortex. Adapted from Kraig et al. 1978 [234]. **C** Dendrites in the penumbra of an ischemic stroke undergo a rapid cycle of beading and recovery coinciding with the passage of CSD. Two photon images of dendrites (green) as well as blood vessels (red; labelled with Texas Red dextran) from layer I of somatosensory cortex, before and immediately after a peri-infarct depolarization. Adapted from Risher et al. 2010 [236].

pothesis have been made about how primary affected regions might have cell destructions with membrane rupture and massive ion spillage and glutamate release. Indeed, extracellular K^+ has been found to increase when CBF drop below $10ml \cdot 100g^{-1} \cdot min^1$ [246] or during hypoglycemia [247]. Subsequently passive ion diffusion across the extracellular space may establish sustained potential differences. Lack of oxygen and/or glucose should also be considered as trigger factors, but none is essential, as those potentials also develop in normoxic/normoglycemic tissues [221].
Recently Daniel von Bornstaädt et al. in 2015 showed that CSD can be initiated in the penumbra area of an ischemic stroke by worsening the supply-demand mismatch. In fact tactile stimulation while activating the ischemic hemisphere increases the oxygen extraction and worsen the supply-demand mismatch. Subsequently the somatosensory stimulation will give rise to a peri-infarct depolarization originating from its cortical somatotopic representation [248].

4.4 Brain homoeostasis modifications during CSD

4.4.1 Micro-vascularization changes during CSD

As describe above, restoration of the ionic gradients after CSD is extremely energetically demanding, and in the normal brain, the rise in metabolism is matched by a huge increase in CBF. In 1944 Leão already described a very conspicuous dilatation of the pial arteries that occurred as the electrical activity become progressively more and more depressed. This hyperemic response was occasionally followed by, a long period of a relatively much slighter reduction of vessel's calibre. The hyperemic vasomotor spread was strictly analogous to that of the depression of the electrical activity [249]. From now on this pattern has been extensively reproduced and is now consider as a specific feature, so that some authors use it as a surrogate to electro-physiologic recordings for CSD detection [250].
However CSD consequences on micro-vascularization looks more complex in human brain pathology. Indeed, laser Doppler flowmetry recording's modification range from a classic hyperemic response to a flat one or even and ischemic response [226]. Experimentally it has been shown that systemic hypoxia and/or hypo-tension can modify the hyperemic pattern. Both systemic aggression will induce a triphasic vascular response with: (1) an initial dip in CBF which duration was correlated to the length of the depolarization and which amplitude was correlated to blood pressure or PO_2; (2) the subsequent local CBF increase was three times lower than in normo-tensiv normoxic animals, similarly correlated to systemic blood pressure and PO_2; (3) The following slight hypo-perfusion was not significantly impacted by systemic aggression [251].
Local brain conditions can also play a role on CSD micro-vascular responses. For instance after middle cerebral artery occlusion in rats, different CBF supplies take place depending on the distance from the ischemic core. If a CSD occurs it will have different vasomotor consequences as the depolarization spread across differentially perfused cortical area [252, 229, 228]. A classic hyperemic patterns can be recorded in normally perfused cortex (remote from the stroke), whereas in the ischemic core an inverse ischemic response occurs like in terminal depolarization [252, 228]. In between (the so called penumbra are), a range of multiphasic patterns can be observed. Again an initial dip (also called spreading oligemia) occurs, which duration is related to the depolarization length. This dip is usually followed by a reduced hyperemic response [252, 228]. In this model, the slope of the hyperemic response was found to correlate with pre-CSD CBF level [252]. Using laser speckle imaging in a rat model of middle cerebral artery occlusion, Bere et al. described an extensive overview of vascular response based on pre-CSD blood supply and CSD feature [253]. Fig 10 describe the vascular responses within the first minutes following CSD depending on CBF supply.

Figure 10: **Overview of various conceptual cerebral blood flow (CBF) responses to spreading depolarization (SD)** in intact cerebral cortex **A**, and during ischemia **B to F**. Solid, black lines depict theoretical CBF responses based on our present and previous observations. Dotted lines in **B to F** indicate the physiologic CBF response to SD, for comparison with those under ischemia. Gray lines and shaded areas stand for ideal SD: short transient in **A to D**, intermediate in **E**, and terminal in **F**. Baseline CBF (100%) is given as a horizontal line. Adapted from Bere et al. 2014 [253]

Likewise CSD that occurs after severe TBI can also display such inverse neuro-vascular coupling. In 2014 Hinzman et al. showed that if regional vascular reactivity was preserved, CSD had a "normal" hyperaemic response. Conversely in case of impaired vascular reactivity, CSD can have an oligemic inverse response [254].
Finally, in well perfused cortex, CSD can lead to a sustain oligemic or ischemic response when neuro-vascular coupling needed compound concentrations are modify. For example scavenging NO with Hb, or decreasing its release with NO synthase inhibitors, under high potassium concentrations will lead to a prolonged terminal depolarization with a subsequent ischemic vascular response [83, 255]. Together with the fact that CSD set up during neurological worsening after subarachnoid hemorrhage, these observation drives to the conclusion that such process underpin delayed cerebral ischemia [227, 221].

4.4.2 Oxygen concentration changes during CSDs

When O_2 consumption was first evaluated, Leão and Morrison in 1945 found a decreased O_2 concentration in blood samples taken from the sagital sinus during CSD [256]. Since the 50s various techniques has been used to describe local O_2 concentration modification. However, as describe in the section 3.2.2.1, brain oxygenation is much more complex to asses, and one might observe different $PbtO_2$ values depending on where and how the recordings are set up.
In fact the early studies (using large electrodes that might record melt signal from penetrating vessels as well as brain parenchyma) found complex $PbtO_2$ patterns with a fickle initial dip followed by a subsequent increase, like the multiphasic vascular response described above [257]. More recently thin PO_2 electrodes (3-10μm tip) have been developed, allowing more precise cortical measures, away from large vessels. With such electrodes different teams described, under ketamine or α-chloralose anesthesia, an initial decrease in $PbtO_2$ down to a few mmHg. The dip duration was increase if there was a pre-existent hypoxemia [111, 258, 82]. The $PbtO_2$ dynamics during CSDs seem to be related to arterial PO_2: It will return to the pre-CSD value when animals breath air or can develop a biphasic pattern (returning to baseline or even increasing, followed by a sustain decrease) when animals breathe a gas mixture with increased

Figure 11: **CSD induce PtO_2 modification**: **A.** tissue oxygen pressure ($PbtO_2$) in a mouse ventilated with 100% O_2, room air or 15% O_2. Adapted from Takano et al. 2007 [111]. **B.** Three different types of $PbtO_2$ responses are found in the cortex of subarachnoid hemorrhage patients: Biphasic $PbtO_2$ response with an initial decrease and a secondary increase, monophasic pbtO2 decrease, and monophasic $PbtO_2$ increase. Arrows indicate the onset of CSD in the electrocorticography channel next to the pbtO2 probe. Adapted from Bosche et at. 2010 [259]

O_2 partial pressure [111, 258, 82] (Fig 11A.).

In human brain pathology, $PbtO_2$ can be recorded in the ICU with larger probes (see section 3.2.2.1). With such electrodes, CSD-induced $PbtO_2$ modifications appeared to be somehow different. In fact both in patients with sub-arachnoid hemorrhage or TBI, it looks like $PbtO_2$ patterns displayed a continuum from a monophasic increase, to a monophasic decrease with biphasic pattern in between (Fig 11B.) [259, 254]. It is likely that these changes reflect both probes technical differences and distance from vessels, as well as cortex pathological state. A clear $PbtO_2$ modification pattern remains to be clarify.

4.4.3 Glucose and lactate changes during CSDs

As discussed in the chapter 2.2 "brain metabolism", glucose is the major energetic fuel of the mammalian brain. During neuronal activation a transient increase in glycolysis with a subsequent extracellular lactate release occurs. Therefore the very large cation shifts that takes place in CSD make it likely that similar changes in glycolysis would occur.

Recording of such fast dynamic change in glucose and lactate with sufficient temporal resolution is challenging. There are two main strategies for the measurement of neurochemicals *in vivo*: implanted biosensors and cMD. Advantage and drawback of each technique will be discussed in the "Method" part, section 3.4. In 2003 the *Biomedical Monitoring Group* (Department of Chemistry) in the King's college of London, set-up technique combining cerebral cMD with biosensors (not implanted in the brain though), providing a faster time resolution but loosing the real concentration information (relative values) [260]. From that time, they were the only one to publish glucose and lactate dynamics during CSD in both animals and human.

It had become clear that CSD in a normal cortex is followed by a decrease glucose with a release of lactate in the extracellular space [239, 261]. However the amplitude and duration remains unclear: sometimes it still transient (5-10 min) with full recovery [239, 260], and sometimes glucose and lactate remains altered during the whole recording period [261].

In human brain pathology or animals after middle cerebral artery occlusion, the metabolic patterns are more complex since glucose and lactate can have trends independent from CSD [262, 263]. On the hole per-infarct/contusion depolarization lead to a decrease in glucose with a

release in lactate [264, 263]. Nevertheless, both in animal model and human patients, some will recover whereas persistent modifications can occur. Moreover, some patients did not display any modifications after CSDs.
This suggests that cortical metabolic responses to an energetic challenge induced by CSDs might be different between cortical areas in pathological conditions. The exact patterns of metabolic modifications remains to be clarified in an injured cortex but also in a well fed cortex.

4.4.4 Excitotoxicity and CSDs

The postulate that glutamate is involved in CSD has been initially supported by the observation that glutamate (≈15mM) applied topically to the rabbit's cortex can elicits CSD [238]. The first evidence of glutamate release in the extracellular space after CSD were made by Van Harreveld and Fifková in 1970, eliciting depolarizations on retina in a super-fused chamber with ^{14}C-glutamate [265]. A transient increase in extracellular glutamate concentration was confirmed later with rapid sampling cMD *in vivo* in rats [266]. However hypothesis about glutamate implications during CSDs have been mainly based on indirect observations, using NMDAR blockers to stop glutamate transmission. In fact, NMDAR blockers, such as MK-801 or ketamine, are known to decrease CSD occurrence with some kind of tolerance after repeated injections [267, 268]. This effect was not reproduced with non-NMDAR blocker [268]. An observational study in acute brain injured patients reported that ketamine was able to decrease CSD occurrence unlike other general anesthetic drugs [269].
More recently a few studies described glutamate dynamics with a high temporal resolution during CSD in healthy animals or after middle cerebral artery occlusion. Using fluorescent probes expressed *in vivo* on the extracellular surface of either neurons or astrocytes, Enger et al. in 2015 were able to describe a glutamate wave travelling at $51.7 \pm 0.3 \mu m/s$ (not significantly different from the speed of the Ca^{2+} waves in neurons and glia). This extracellular transient glutamate increase occurred after the passage of the neuronal Ca^{2+} wave-front, but before the arrival of the astrocytic Ca^{2+} wave [242]. Likewise, a similar glutamate transient release ($11.6 \pm 1.3 \mu M$) was describe by Hinzman et al. in 2015 with enzyme based biosensors, in healthy rats that was able to triggered neuronal lesions if glutamate uptake was inhibited [240]. They also report a glutamate release during anoxic or peri-infarct depolarization which duration was related to the depolarization length [240]. Based on these observations, the authors suggesting that CSD can mediate excitotoxicity after brain aggression.

Part II

Aims and hypothesis

Over the past decades it has become clear that CSD are fundamental events occurring in the early period of acute brain injury. Monitoring their occurrence and features can improve the way clinicians assess patient's prognosis since CSD are related to unfavorable outcome in all major severe brain aggression (i.e. TBI, sub-arachnoid hemorrhage or ischemic stroke). Moreover repeated CSD within clusters seems to have the worse consequences on brain condition and consequently on patient outcome.
CSD vascular consequences have been well explored both in human and animal models. To date the vascular response is considered as a continuum between a "normal" hyperemic reaction and an inverse ischemic response with intermediate oligemic biphasic pattern in between. How vascular response will be located in this spectrum is partly attributable to cortical blood supply: the less blood supply, the worse the response. This has been clearly demonstrated after middle cerebral artery occlusion where homogeneous vascular modifications takes place (*vs* the distance from the ischemic core), but a little is known in more heterogeneous pathology such as TBI that namely lead to edema and hemorrhage rather than ischemia.
On the other hand, the cortical metabolic reaction to CSD remains unclear. Even if there is an emerging pattern resembling hyper-glycolysis (decrease in glucose with subsequent increase in extracellular lactate), the quantification of such modifications as well as the influence of pre-CSD cortical conditions are unknown. Likewise, miscellaneous $PbtO_2$ observations have been made in animal models and human injured cortex. Therefore, a clear spectrum of brain oxygen modifications has also to be defined based on brain energetic supply.
Finally CSDs are supposed to mediate excitotoxicity through extra synaptic glutamate release. However recent studies indicates rather transient glutamate increase, and it is unclear whether it will lead to NMDAR over-activation with excitotoxic consequences.

Based on these observations we made the hypothesis that CSDs have different neuro-chemical consequences in healthy tissue compared to a "traumatic penumbra" where neuronal death is expected to occur. Our second hypothesis was that clusters of CSDs will have worse consequences after TBI that isolated CSDs.

Our main goal was to describe the changes in micro-vasculature, metabolism and glutamate concentrations elicited by CSD that occurred after a severe experimental TBI. We chose to use an animal model of TBI (1) to improve injury reproducibility and (2) to have access to continuous highly sensitive techniques such as biosensors for neuro-chemical recordings that are not available in humans.
Our objectives were to:

- Describe the metabolic (glucose, lactate, $PbtO_2$) and micro-vascular patterns observed during and after CSDs in a healthy cortical tissue.
- Report how these patterns are altered during spontaneous isolated CSDs after severe TBI.
- Determine if cluster of CSDs will have worse consequences.

However, these goals requires preliminary studies:

- Due to TBI heterogeneity, and considering CSD as a promoter of neuronal death, our main goal requires the delineation of brain regions where neuronal death occurs in order to record CSD in this area.
- We had also to check for the biosensor reliability in brain parenchyma, as *in vivo* conditions could be far away from the standard *in vitro* procedures for biosensor's calibration.

The first part of my experimental plan was devoted to mapping neuronal and glial injury in the LFPI model of severe TBI (part IV). Then, we were able to define the affected areas within which we would implant different monitoring probes (i.e. $PbtO_2$, biosensors, laser Doppler flowmetry (LDF)) for CSD neuro-chemical recordings.
The second part was devoted to the characterization of oxidase-based electrochemical biosensor recordings, especially the validation of electrochemical monitoring during changes in $PbtO_2$ and temperature (part V).
Finally, I will describe our results on neuro-chemical consequences of CSDs in healthy and injured cortex in part VI entitled "Metabolic and micro-vascular consequences of cortical spreading depolarizations, in a normal or injured brain".

Part III

Methods

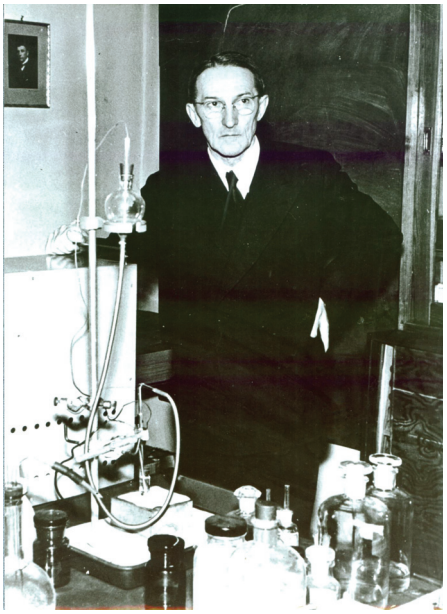

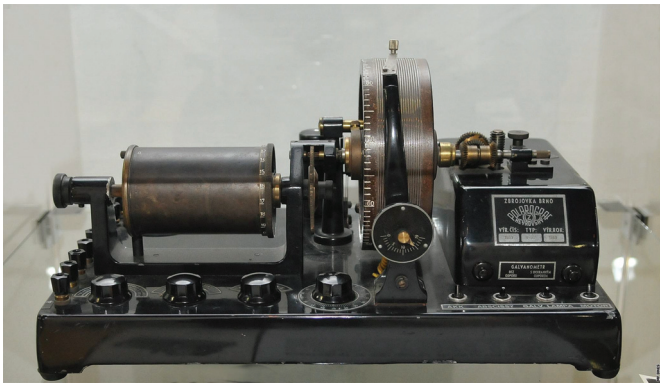

J. Heyrovsky, ***1959 Nobel Prize in Chemistry for the discovery and development of polarographic methods of analysis.***

Chapter 1

Modeling traumatic brain injury: Choosing the right model

1.1 Different animal models

Pre-clinical studies are usually needed prior phase one clinical trial. In view of the heterogeneous nature of the clinical situation in TBI, numerous animal models of such injury have been developed. Although larger animals are closer in size and physiology to humans, rodents have become the main species in biomedical research over the past decades, owing to a modest cost, a good reproducibility and standardized techniques available to study their physiology and behavior. Likewise head injury models have been mainly developed in rats, sometimes in mice, and only very few studies in larger animals such as pigs or cats.
Addressing TBI outcome being the main purpose of a clinical or pre-clinical studies, behavioral surrogates have been developed in rodents. Whereas mortality is easy to asses and is mainly due to respiratory arrest [270, 271], long term cognitive dysfunction is more subtle. Sensory and motor deficits can be assessed by a *composite neurological score* (involving clinical examination of how the animal moves and behaves), the *adhesive removal test* (that measures the duration an animal takes to remove adhesive tape on his paw), or the *foot fault test* (which counts how many rung are missed by a rat walking on an horizontal ladder). Memorization and learning ability can be assessed by the *Morris water maze test* in which animals have to memorize a platform location in a circular swimming pool, and anxiety can be assessed by the *WET* where animals have to explore a pool without escape [272].
Although functional deficits due to TBI exposure are the principal health problem in modern warfare, rats do display only light deficits from mild or moderate head injury so that many studies focus on tissue destruction rather than functional deficits. For that matter, the present study will address anatomical modifications at the cellular levels of both neurons and glial cells.
TBI models include two different approaches, either **closed head injury** or open skull injury after surgery.

1.1.1 Closed head injury models

A so-called "Diffuse Brain Injury" model was developed in 1994 by Marmarou et al. to produce diffuse lesions like those observed after falls or car accident trauma [270]: the controlled head injury (CHI). Head injury device consists of a sectioned brass weight set that falls freely from a designated height through a tube. In anesthetized rats with skull exposure made by a mid-line incision, a stainless steel disc is mounted with glue to the skull mid-line between lambda and bregma to prevent skull fracture, but some author used a lateral percussion [273] (Fig 12E). The more the height, the more the lesions and the mortality [270]. To generate axonal lesions

Figure 12: **Experimental set-ups for the animal models of TBI**: **A-LFPI** : The lateral fluid percussion injury device uses rapid injection of a fluid pulse into the epidural space; **B-CCI**: The controlled cortical impact injury model uses an air or electromagnetic driven piston to penetrate the brain at a known distance and velocity; **C-PBBI**: The penetrating ballistic-like brain injury involves the transmission of projectiles with high energy (transmission of a metal rod or expansion of the probe's elastic balloon); **D-Weight-drop**: weight-drop model, a free weight is released directly onto the exposed dura; **E-CHI**: Closed head injury uses a metal disk is placed over the skull to prevent bone fracture; **F-Blast**: Blast brain injury can be caused by the primary injury related to the blast and other mechanisms. Adapted from Xiong et al 2013 [271]

the weight must be at least 450g and dropped from a height of 1.5-2 meter. This model yields a 40-70% mortality rate, reduced to 10-25% with artificial ventilation [270].
CHI is characterized by widespread and bilateral damage of neurons, axons, dendrites and microvasculature as well as extensive diffuse white matter injury, particularly in the corpus callosum, internal capsule, optic tracts, cerebral and cerebellar peduncules, and the long tracts in the brainstem [271, 274]. At a cellular level, these macroscopic lesions are associated with activated microglia and astrocytes as well as degenerating neurons [275]. Diffuse brain edema seen with MRI is associated with microcirculatory collapse due to astrocyte swelling [276]. The subsequent functional deficit include sensory-motor and cognitive deficits such as difficulties with beam walking and memory [270, 275, 271].
A blast-induced TBI rat model that mimics real blast-induced mild TBI seen in recent military conflicts has been developed (Fig 12F). This recent model is in the way of its full description of behavior, MRI and neurochemical consequences. Non-impact blast injury is characterized by diffuse cerebral brain edema, extreme hyperemia and a delayed vasospasm. Diffuse axonal injury was the most prominent feature during the initial 2 weeks [277, 271].

1.1.2 Open skull experimental models

1.1.2.1 Lateral fluid percussion injury

LFPI models have been designed in the Virginia University by Thompson and McIntosh to replicate human TBI without skull fracture [278, 279]. The insult is inflicted by a pendulum striking the piston of a reservoir of fluid to generate a fluid pressure pulse to the intact dura through a craniotomy. The craniotomy can be made either centrally around the mid-line between bregma and lambda, or laterally over the parietal bone between bregma and lambda [278, 271] (Fig 12A, see methods, chapter 1 for further details).
The site of craniotomy is crucial in determining the extent and location of tissue injury produced. The mid-line percussion model was initially developed for use in cats and rabbits, subsequently adapted for use in rats and then modified to produce the lateral percussion model in rodents.
The location and severity of the neurological lesions that can be generated by LFPI has not received a great deal of systematic study [280, 281]. LFPI appears to produce a complex pattern of widespread lesions throughout the injured hemisphere, which encompass intra-cranial hemorrhage, brain swelling and gray matter damage. These grey matter damage have been described in cortical, hippocampal, and thalamic brain regions [282, 281]. Interestingly, the sites of the most intense neuronal loss are often remote from the site of impact. For example, maximal damage is usually observed in the temporal cortex or deep in the thalamus [280, 283].
LFPI produces neurobehavioural and cognitive deficits that are commonly seen in patients with TBI: difficulties with movement and vestibular function as well as memory and cognitive deficit as measured by the Morris water maze test [284]. Cognitive dysfunction and neurological impairments persist for more than a year following severe LFPI [285].
LFPI models have high mortality compared with other models, which is probably due to the brainstem-compromised prolonged apnea. LFPI severity can be assessed by measuring the duration of initial respiratory arrest and the latency of the righting reflex recovery [286]. In our experiments 3 ATA was considered as moderate with an apnea $< 30sec$, a lack of response to tail pinch for at least 2 min and a suppression of righting reflex lasting between 25 and 35 min. A 3.8 ATA LFPI induced prolonged apnea necessitating artificial ventilation for at least 30-45 min and was considered a severe TBI.

1.1.2.2 Control cortical impact

The controlled cortical impact (CCI) model uses a pneumatic or electromagnetic impact device to drive a rigid impactor onto the exposed, intact dura. The controlled impact is delivered to the intact dura through a unilateral craniotomy lying most often between bregma and lambda, which causes deformation of the underlying cortex [271] (Fig 12B). The advantage of this injury model over other TBI models is the ease with which mechanical factors, such as time, velocity and depth of impact, can be controlled.
The histopathological lesions mimics cortical tissue loss, acute subdural hematoma, axonal injury, concussion and BBB dysfunction. The subsequent functional deficits observed in CCI encompass cognitive impairments (which have been detected in the Morris water maze test), sensory-motor deficit or emotional and anxiety behavior (as quantified in the WET test), and even coma [287, 288, 271].
The functional deficits observed are highly related to both the depth of deformation and the velocity of the impact. After deep deformation there almost always exists a penetrating lesion [289, 290], making this model closer to a penetrating wound TBI.

1.1.2.3 Weight drop injury

In weight-drop models, the skull is exposed to a free falling, guided weight. Injury severity in these models can be altered, like in the CHI model, by adjusting the mass of the weight and the height from which it falls which was often the tenth of those used in the CHI model [271] (Fig 12C).
Morphologically, these injuries progress from hemorrhages in white matter directly under the contused cortex during the first few hours after injury to the development of a necrotic cavity by 24 hours. The cavitation appears to expand over the subsequent 2 weeks [291, 271].

1.1.2.4 Penetrating ballistic-like brain injury

Penetrating ballistic-like brain injury is caused by transmission of projectiles with high energy and a leading shock-wave, which produces a temporary cavity in the brain that is many times the size of the projectile itself [292] (Fig 12C). The outcome in this model is directly related to the anatomical path of the projectile and the degree of energy transfer. Several pathophysiological characteristics are similar to those reported in other models, including the presence of hemispheric swelling, increased ICP, remote white matter injury and neuro-inflammation. However, it causes extensive intra-cerebral hemorrhage throughout the primary lesion [271].

1.2 Which model suits best our needs?

TBI models include two different approaches, either closed head injury or open skull injury, as described above. LFPI is one of the most widely used TBI animal model, even if there is a recent resurgence of interest in mid-line fluid percussion and CHI because of the increased interest in diffuse brain injury associated with sport and blasts [278, 271].
Our main interest was to compare CSD neurochemical consequences in a healthy cortical matter to an injured “traumatic penumbra” area like a peri-contusional cortex. For that matter we needed a TBI model giving rise to both diffuse and focal lesions like open skull animal models. We chose the LFPI model over the others because: (1) it is the most extensively described model in the literature and (2) it will produce a complex pattern of lesions with neuronal loss in the temporal cortex [280, 293, 282, 283]. Nevertheless precisely mapping the lesions produced by LFPI appears a prerequisite to choose the cortical area of interest for CSD neuro-chemical study. Therefore the first part of our study will focus on mapping LFPI induces injury (Part

"anatomical modification").

Although CSDs have been recorded in patients undergoing a severe TBI, only few studies reported CSD occurrence after experimentally induced TBI in the literature. One explanation would be the low rate of CSD events after moderate LFPI (i.e. < 2 in 5 hours post trauma) [294]. Similar results have been reported using either CCI [295] or ballistic models [296], so that some authors triggered additional CSD with potassium cortical apposition [295, 232]. Nevertheless, increasing LFPI intensity up to 5 ATA will lead to further increase in ICP and in CSD frequency, up to 4/hours [294].
Therefore, we chose to perform a severe LFPI and kept the animals for 5 hours post injury under light anesthesia for spontaneous CSDs recordings. In another set of experiments clusters of CSDs have been triggered with cortical potassium apposition. This model, as described below, requires a surgical window on the parietal bone to expose the dura, which makes easier sensors implantation for brain metabolism follow-up.

1.3 LFPI experimental setup

Animals were anesthetized with isoflurane and placed in a stereotaxic frame (Stoelting, Dublin, Ireland) with their body temperature maintained around 37 ^{o}C with a homeothermic blanket (Harvard apparatus®). A subcutaneous infiltration of 0.5 mL of 3 mg/ml ropivacaine (Naropeine® $7.5mg\cdot ml^{-1}$ in saline) was performed prior to scalp opening. A circular craniotomy (5 mm diameter) located 3.8 mm caudal to Bregma and 3.0 mm lateral from the mid-line was then performed under aseptic conditions. A hollow plastic cap, the "injury cap", was first attached to the skull using cyanoacrylate, then secured with dental acrylic. A 1 mm diameter stainless steel screw, inserted into the skull, served as an anchor for the dental acrylic and the injury cap was filled with sterile saline. The animal was then removed from the stereotaxic frame and brought to the lateral fluid percussion device (Custom Design and Fabrication, Virginia Commonwealth University Richmond, Virginia, USA, Fig 13). Rats received a single 20 ms fluid percussion pulse of 3.0 or 3.8 ATA under light anesthesia, in which the animal was removed from the anesthesia mask and the LFPI impact was administered at the first signs of a hind limb response to a gentle toe pinch. The cap was then removed, anesthesia was resumed, and the scalp was sutured.
To avoid respiratory arrest after severe TBI, mechanical ventilation (Harvard apparatus®, Ispra MA1 55-7058, Vt = $6ml\cdot kg^{-1}$, breath rate = $60\cdot min^{-1}$, Peep = 5cm H_20) was performed through a 16 gauge tracheal catheter placed prior to TBI (induction with 5% isoflurane in O_2).

Figure 13: **Lateral fluid percussion device**, Custom Design and Fabrication, Virginia Commonwealth University Richmond. A freely moving hammer is drop on a water filled cylinder transmitting the pressure wave to the dura on the other side. Adapted from Thomson et al. 2005 [278]

Animals were then kept under light anesthesia (0.8-1.5% isoflurane with 30% O_2 in air)

for brain metabolism study, or ventilated until they recovered spontaneous breathing for histological analysis. In that case animals were single-housed for 7 days, with assisted drinking and feeding if necessary. Buprenorphine 0.05 mg/kg was administered twice at 12h interval after surgery. Exclusion of animals was decided if mechanical ventilation could not be resumed within the first 45 min post-TBI or if animals lost more than 25% of their initial body weight.

Chapter 2

Mapping brain cells injury

2.1 How to assess cells injury after TBI?

As in human brain pathology, experimental TBI induces heterogeneous macroscopic and microscopic lesions that can be assessed by different techniques. Morphological MRI (T1, T2, T2*, flair sequences) makes it easy to map brain injury over the whole brain and gives macroscopic information on hematoma, cerebral hernia, intra/extra cranial hemorrhage, or edema. Moreover advanced sequence such as DTI MRI gives additional information about white matter injury, and arterial spin labeling about CBF. However even if the spatial resolution is <1mm, these imaging techniques does not reach that of cell visualization.
Unlike in patients, animal models allow reproducible histological analyses that are required for closer microscopic evaluation. Different approaches are needed to address either global overview or perform precise analysis on specific regions. Whole brain histological imaging can be challenging and time consuming, even without stereologic reconstruction. For that matter, automated slice scanning methods are now available to process large numbers of histological slices.
Several cell types compose the brain tissue and can be damaged following LFPI. Since neurons are considered the primary signaling cells in a living brain, we first focused our analysis on neuronal injury. Injured neurons can be identified by staining brain sections with several methods. A first approach consist in neurons counting using different dye: (1) Nissl staining typically marks the endoplasmic reticulum due to ribosomal RNA as well as the nucleus and other accumulations of nucleic acid [280]; (2) hematoxylin and eosin is one of the principal stains in histology. Hematoxylin colors cell's nuclei in blue, whereas the eosin counter-staining colors eosinophilic structures in various shades of red, pink and orange [297, 298]. Degenerating neurons can also be detected based on cell shrinkage and hyperchromatism (pyknosis), as well as by vacuolation of the cytoplasm. However, these methods can easily produce false positives or fail to detect degenerating neurons [299].
Other approaches used several dye targeting specifically dying neurons. Indeed, neurons with terminal damages displays a cytoplasm with a selective affinity for acid dyes such as acid fuchsin, which persist until lysis of the cell [280, 300]. Likewise, Fluoro-Jade stains are highly acidic anionic derivatives of fluorescein. Among them Fluoro-Jade C exhibits the greatest signal to background ratio, as well as the highest resolution and has been used to assess neuronal damage after brain injury [283, 282]. These methods stains all degenerating neurons regardless of specific insult or mechanism of cell death. However, the mechanism by which they labels degenerating neurons is unknown thus creating some controversy to the actual physiological condition of the labeled cells.
Finally TUNEL (Terminal Deoxynucleotidyl Transferase dUTP Nick End) detect fragmented DNA resulting from apoptotic mechanisms by staining nucleic acid end chain [301]. However

TBI involves both necrotic and apoptotic mechanisms. Fluoro jade-C is currently regarded to be a superior method for detecting degenerating neurons, although the mechanism by which this reagent labels injured cells is unknown, and there is a debate regarding whether all Fluoro-Jade positive neurons ultimately die, or if some may recover [299, 302]. Moreover, only a few dying neurons are usually detected in each section at a given time, and the significance of such small numbers of labeled neurons in a given brain structure is difficult to interpret.
Thus, quantifying the overall neuronal density several days after injury appears to be the best strategy, as it directly estimates the extent of cumulated neuronal death. Neuronal density is typically assessed by manual cell counts in a delineated brain sections [303, 304, 305, 306], sometimes followed by stereological reconstruction of the brain structure [293, 307, 308]. However, these techniques are slow and time-consuming. We recently developed an automated method based on the open source ImageJ software. This macro quantifies neuronal density in brain sections based on immunoreactivity to the nuclear neuronal marker NeuN and stained with the fluorescence DNA dye 4',6'-diamidino-2-phenylindole (DAPI) [309]. Our first step analysis was to determine neuronal density modification using this automated analysis on confocal images, after selecting region of interest base on whole slide NeuN images. NeuN immuno-reactivity stains the nuclei of most neuronal cell types in both the central and peripheral nervous systems, with some exceptions, but has not been observed in glial cells. It was not until 17 years after its discovery that NeuN was identified as the RNA splicing regulator Rbfox3 [310]. To date it has been shown that NeuN immuno-reactivity (trough Rbfox3 expression) can vary both during physiological neuronal activity and subsequently to pathological process [311]. Therefore, neuronal loss cannot be address by measuring staining intensity modifications but require manual or automated counts.

Based on our observations about the pattern of neuronal loss, we then addressed the question of how glial cells are affected by LFPI. Likewise, we labeled glial cells using astrocytes or microglia specific antigens, to approach their number and morphology.
Expression of glial fibrillary acidic protein (GFAP) has become a prototypical marker for immunohistochemical identification of astrocytes. Nevertheless, it is important to recognize the appropriate uses and limitations of GFAP as an astrocyte marker. GFAP was first isolated as a protein highly concentrated in old demyelinated plaques from multiple sclerosis patients and was then found to be associated immunohistochemically with reactive astrocytes in such plaques and in other pathological contexts. In line with this original mode of identification, GFAP expression can be regarded as a sensitive and reliable marker that labels most, if not all, reactive astrocytes that are responding to CNS injuries. However, GFAP is not an absolute marker of all non-reactive astrocytes and is often not immunohistochemically detectable in astrocytes in healthy CNS tissue or remote from CNS lesions [312].
Microglia can be visualized in human and animal brain tissue sections and in cultures by a variety of cell surface-associated or intracellular/cytosolic molecules. Usually the molecules targeted by staining have an established function as receptors, adhesion molecules, or enzymes in macrophages. For example the CD11b/CD18 integrin, which we used in our study, binds complement C3b. Like with astrocyte, the expression level of many of these molecules, such as for example CD11b, mostly increases with microglial activation [138]. Finally, while microglial cells can be easily distinguished from other brain cells, this is not always possible with respect to non-CNS monocytes that also exhibit the same antigens [138].

2.2 Immuno-fluorescence

Staining a molecule at the surface or within cells or tissue with a primary antibody is called immuno-chemistry. Immuno-fluorescence techniques use a second antibody, from another species,

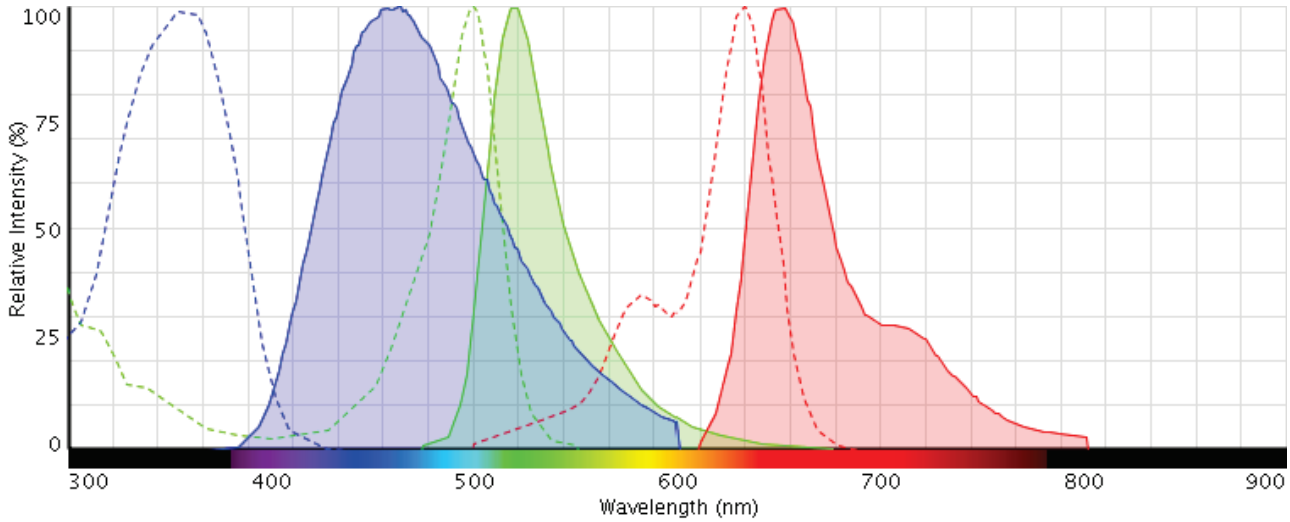

Figure 14: **fluorescent dye excitation and emission spectrum**: dashed lines represent excitation and solid lines emission spectrum of DAPI (blue), Alexa Fluor 488 (green) and Alexa Fluor 633 (red).

targeting the primary antibody's heavy and/or light chain. Several secondary antibodies can bind the primary one, thus magnifying the signal. This secondary antibody is coupled with a fluorescent molecules characterized by a wavelength of excitation and emission (Fig14). The emitted light has a longer wavelength, and therefore lower energy, than the absorbed radiation (excitation wavelength).
Several characteristics are noteworthy:

- *Fluorescence excitation spectrum*: Optimum instrument setup should deliver excitation light as close as possible to the peak of the excitation spectrum of the fluorophore.
- *Fluorescence emission spectrum* describe light density emitted after excitation by a radiation within the fluorescence excitation spectrum.
- *Stoke shift*: the difference (in wavelength or frequency units) between positions of the band maxima of the absorption and emission spectra. The more the stroke shift, the easier the discrimination between excitation and emission wavelength.
- *Fluorescence lifetime*: the average time the molecule stays in its excited state before emitting a photon. Usually in nanoseconds it has to be the shortest for repeated excitations.
- *Quantum yield*: It gives the efficiency of the fluorescence process, and is defined as the ratio of the number of photons emitted to the number of photons absorbed. The maximum fluorescence quantum yield is 1.0 (100%); each photon absorbed results in a photon emitted. Compounds with quantum yields of 0.10 are still considered quite fluorescent.

In our experiments we performed multiple labeling on rat brain slices (20-30μm thick). It was important to choose fluorescent molecules with fluorescent spectra as different as possible to distinguish between the different markers that we stained (e.g. NeuN, GFAP or CD11b). Therefore cell nuclei were stained with the intercalating agent DAPI, and neurons with a mice primary antibody targeting NeuN protein. NeuN is a protein localized in neuron nucleus and perikarion. In another set of experiments, our primary antibodies targeted against the GFAP or CD11-b, with secondary antibody conjugated respectively with Alexa FLuor 488 or Alexa Fluor 633 (Fig 14). Sequential acquisitions were performed for each fluorescent molecule in order to

avoid possible interferences. DAPI fluorescence was assessed at an excitation wavelength of 405 nm and emission wavelengths of 418-473 nm, while the signal for Alexa Fluor 488 was assessed at an excitation wavelength of 488 nm and emission wavelengths of 510-613 nm, and Alexa FLuor 633 was assessed at an excitation wavelength of 621 nm and emission wavelengths of 650-750 nm.

2.3 Imaging brain slices

2.3.1 Whole slide imaging

In order to have slide overview, one have usually to manually image small parts of the slide and merge them afterwards. This is time consuming and can lead to homogeneous images due to contrast and or brightness differences at the edge of small images even if optic parameters remains constant.
The "Centre d'Imagerie Quantitative de Lyon Est" (CIQLE, http://ciqle.univ-lyon1.fr) has recently acquired a slide scanner: Axio Scan.Z1 (Zeiss). The Axio Scan provide automatic slide imaging with a coarse focus matrix, followed by a fine focus one. Sequential fluorescence images are then performed for each fluorochrome excitation wavelength, illuminated with LED light. Images are automatically merged resulting in on global image of the slide. The optic magnification goes up to 40X.
One of the main problems of conventional light and fluorescence microscopy, is out-of-focus blur degrading the image by obscuring important structures of interest. In fact not only is the plane of focus illuminated, but much of the specimen above and below this point is also illuminated resulting in out-of-focus blur from these areas. This raises several issues: (1) the background noise is magnified by fluorescent light coming from different z-planes, and (2) the focus still merge the slide thickness limiting the image resolution. These technical issues can be a problem for molecule co-localization.

2.3.2 Confocal microscopy

To improve the z-plane resolution, optical sectioning can discard unwanted out-of-focus fluorescence. The light from above focal-plane is focused before the pinhole and is blocked away by the pinhole. Only the light from focal plane is focused at the pinhole thus can reach the image detector (Fig 15A).
In addition, the use of lasers in confocal microscopy provides light at discrete wavelengths and has very high intensity which is advantageous for fluorescence excitation. A point-like light source is achieved by using a laser light passing through an illumination pinhole. The point-like illumination is then scanned over the specimen by the help of a scanner. The reflected emission light passes through the detecting pinhole and forms a point-like image on detector PMT (photon multiply tube) that converts detected photon into electron (Fig 15). PMT has a high dynamic range, and a high refresh rate (nanosecond level).
Thereby confocal microscopy combines several technical improvements over conventional microscopy:

- A point light source for illumination
- A point light focus within the specimen
- A pinhole at the image detecting plane

These three points are optically conjugated together and aligned accurately to each other in the light path of image formation, justifying the term "confocal". Confocal effects result in

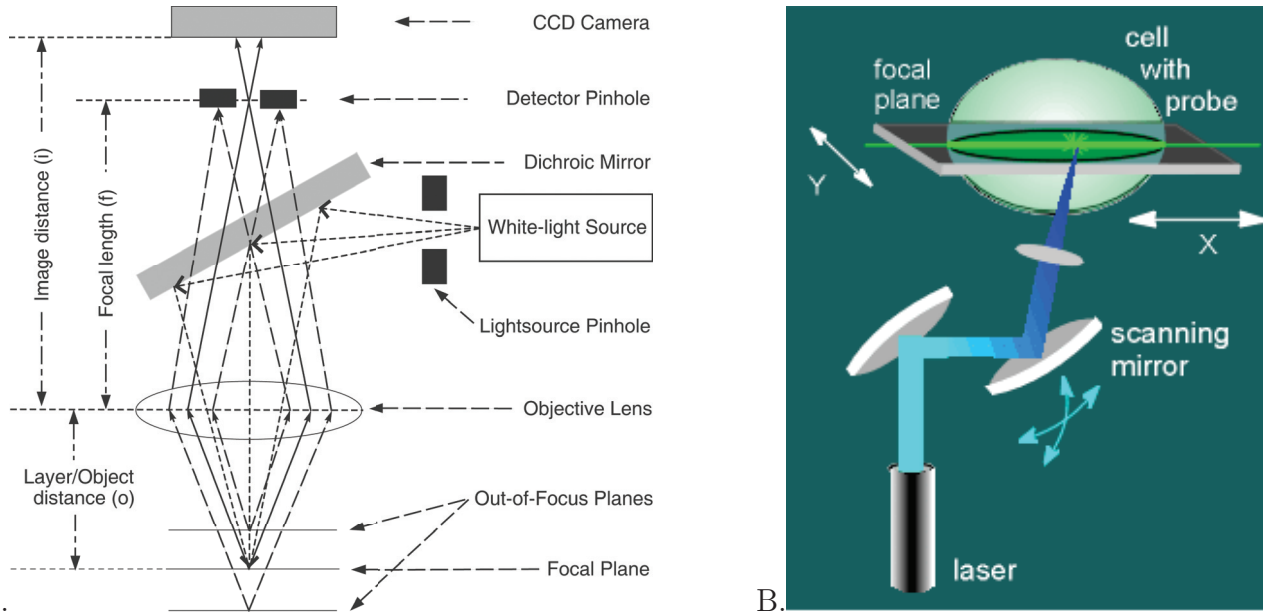

Figure 15: **Confocal microscopy principle**: **A** schematic representation of confocal optical sectioning. **B** Schematic representation of scanning mirrors providing x-y direction scan.

suppression of out-of-focal-focus light and stray light in the final image. True, three-dimensional data sets can be recorded. Scanning the object in x/y-direction as well as in z-direction (along the optical axis) allows viewing the object from all sides. Finally due to the small dimension of the illuminating light spot in the focal plane, stray light and photo bleaching are minimized.

2.4 Cell counts

Neuronal counts can be performed manually or semi-automatically using specialized image analysis software but are always time consuming. For example, neuronal density has been analyzed stereologically in the hippocampus of animals after a status epilepticus or TBI, but has seldom been analyzed in other brain regions. Moreover, neuronal counts based on NeuN immuno-labeling has important drawbacks, especially because the expression or antigenicity of NeuN protein can vary after brain injury [313]. Therefore Woeffler et al. in our laboratory developed in 2014 an automated procedure for detecting and counting neuronal nuclei, based on the analysis of confocal images of brain sections stained with DAPI and antibody to NeuN [309]. Cell density was defined as the total number of DAPI-stained nuclei per mm^2 of tissue in different regions that were defined based on slide scan overview (i.e. parietal cortex, temporal cortex, CA1, CA3, hilus, dentate gyrus, and thalamus). Neurons were identified using confocal images, as DAPI-stained nuclei present in a NeuN-positive region of the optical section. This identification was performed on the central optical section within the z-stack of each imaged region (defined as the optical section with the most intense NeuN staining). Each neuronal nucleus was then confirmed in at least 2 contiguous sections out of the four optical sections that surrounded the central one (1 μm interval [309], Fig 16).

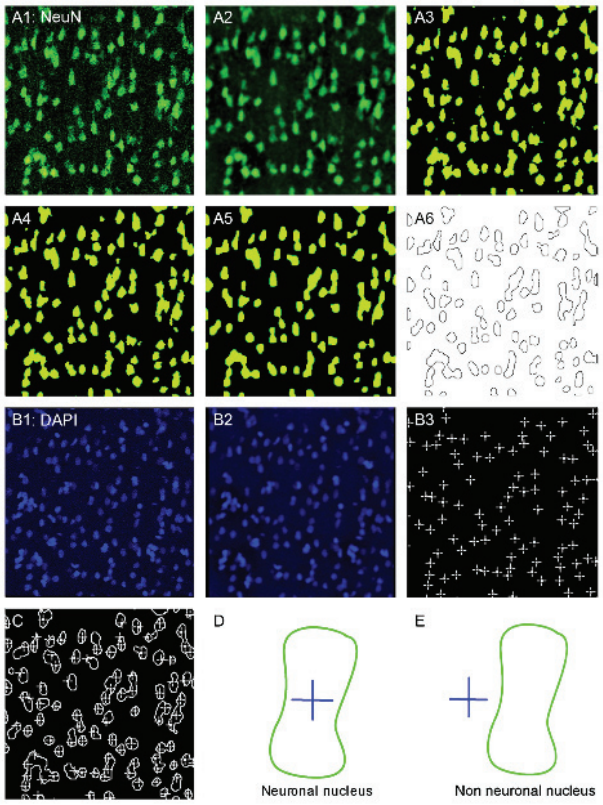

Figure 16: **Schematic representation of neuronal density quantification on a single optical section**.
A Processing of NeuN-positive regions. (A1) Original image of a brain section (cortex) in the 510–613 nm channel (NeuN-Alexa 488 staining). (A2) Digital filtering using band pass filter in the Fourier domain. (A3) Image dichotomization using an autothreshold. (A4) Removal of particles smaller than 50 square pixels. (A5) Object closure using morphomath. (A6) NeuN-positive objects are merged into a single selection. **B** Processing of DAPI-positive regions. (B1) Original image in the 418–473 nm channel (DAPI staining). (B2) Digital filtering using a band pass filter in the Fourier domain. (B3) The center of each nucleus is represented by a cross at the maximum fluorescence intensity. **C** Each cross present in the green positive region represents a neuronal nucleus. **D** Schematic representation of the NeuN/DAPI configuration leading to the recognition of a neuronal nucleus. **E** Example of an object treated as a non-neuronal nucleus. Adapted from Woeffler-Maucler 2014 [309].

Chapter 3

Brain metabolism recordings during CSDs

Our main goal was to describe the changes in micro-vasculature, metabolism and glutamate concentrations elicited by CSDs that occurred after a severe experimental TBI. To address this question we were able to measure CBF, $PbtO_2$, as well as glucose lactate and glutamate extracellular concentrations. We used several methods that are discussed in the next sections.

Cerebral metabolic rate (CMR) of oxygen and glucose are also commonly used to compare brain metabolism in normal and pathological conditions. Usually the differences between arterial and venous blood contents are used to compute these CMR at steady state (see Introduction section 3.2). However we did not have access to such parameters, and therefore we had to deduce these CMR from our extracellular measurements. Assumptions and models that underpin these calculations will be discuss in a following section 3.5.

3.1 Cortical spreading depolarization

3.1.1 Recording techniques

The historical method used by Leão in the 40s consisted in a silver-chloride Ringer-agar electrodes applied on the surface of the pial matter [220]. As silver is considered toxic these electrodes could not be transposed to clinical practice. Therefore an alternative device was developed by Strong et al. in 2002. It was made of 6 subdural platinum-iridium electrodes placed on the cortex, thereby bypassing the signal-distorting skull and intermediate tissue [224]. To date, this device became the gold standard method for CSD recordings in the human brain.
In animals small intra-cortical metal, glass or silicon electrodes are used to record neuronal activity from the extracellular space. It was first described in 1875 by Richard Caton who studied electrical brain activity with a galvanometer electrode [314]. This kind of electrode gives different information: On one hand the signal >500 Hz is related to neurons action potentials spikes, close to the electrode tip. On the other hand, signal fluctuation <300Hz, called local field potential (LFPot), represent ionic modifications around the probe and are related to spatiotemporal neuronal activity synchronization [315]. Finally, membrane potential changes in non-neuronal cells, such as glia, may also give rise to extracellular potentials. Recent studies on neuron-glia interactions have indicated that the glial syncytium may contribute to slow and infraslow (<0.1Hz) field patterns [315, 316].
Therefore LFPots are indicative of the response of a large population of neurons to a stimulus or represent their ongoing oscillations. Unlike intracellular recordings LFPot are not a standardized method but will change depending on experimental preparation.

Low impedance electrodes (i.e. 1-3MΩ) are required to record CSD with a good DC signal. In our experiments, LFPot electrodes were made with an Ag/AgCl wire inserted into a pulled 3-5 μm tip glass capillary (Harvard Apparatus, Edenbridge, U.K.), filled with a mix 2M NaCl, 1M Na citrate solution (1:1 ratio). A subcutaneous silver chloride reference was placed in the neck of the animal. These electrodes were inserted close to biosensors between 500 and 1000μm deep inside the cortex. The signal acquisition was made by a near-DC octal bioAmp amplifier (ADInstrument, Oxford, United Kingdom) with an analogue build-in 0.02 Hz high-pass filter and a 100Hz low-pass filters. Analogue-digital conversion was made by a 16 bit PowerLab 16/35 with Labchart 7 (ADInstrument).
This set-up allows us to detect CSDs but not to determine their essential features such as amplitude or duration, because we do not have real DC recording. In fact such analogue high-pass filters cut the depolarization "ultra-slow" component and modifies its onset, as well as its amplitude (Fig 17, A and B).
The biosensors used for neuro-chemical recordings during CSDs are also electrodes made of platinum. The signals of these biosensors result from: (1) the currents due to the enzymatic oxidation of a metabolite or a neurotransmitter on the surface of the electrode (see below section 3.4), and (2) currents produced by local field potentials by induction . In our laboratory, the high frequency component of the signal (typically >2Hz) can be converted into local field potentials using a resistor-capacitor circuit-based model [317]. However, unlike Ag/AgCl electrodes in which current can freely pass through by a reversible redox reaction ($AgCl+e^- \rightleftharpoons AgCl+Cl^-$), platinum electrodes are considered "polarizable". Indeed, platinum does not react with electrolytes in the medium but instead the medium will "shield" the charged/polarized metal with layers of ions that act like a capacitor. The amount of charge that can be stored in these ion layers will increase when a potential is applied to the electrode, like during our recordings. As a consequence, DC potential modifications will be filtered out by these ion layers so that the biosensor does not record the depolarization of a CSD (Fig17, C). Nevertheless, the decrease in local field potentials amplitude (i.e. the depression) can be recorded (Fig17, C grey curve). The low frequency component (typically <1Hz) recorded from these biosensor can therefore be related to extracellular concentration of molecule of interest in the interstitial medium. To completely identify the DC component of the biosensor signal, control or null biosensors coated with albumin (no enzymatic activity) can identify non specific interference from (1) a low frequency component of local field potentials that has not been completely filtered out by the electrodes, (2) the oxidation of other endogenous molecules like ascorbic acid or uric acid, and (3) local pH changes. If a signal is present of the control biosensor, it must be subtracted from that recorded by the enzymatic biosensor in order to obtain the specific oxidation current of the molecule of interest.

3.1.2 How to trigger CSDs?

CSDs can be triggered experimentally by many cortical stimuli. Leão carried out his experiment with "tetanizing" shocks delivered for a period of 3 to 5 seconds through a fine silver wire electrode [249]. Glutamate and potassium that are released in the extracellular space during CSDs, are also known to trigger such depolarization when injected in the cortex [234]. In recent studies CSDs are triggered either by potassium apposition or by a pin prick (sometimes with needle filled with a potassium chloride solution), on a site remote from the recorded area.
In our experiments we triggered CSDs with a transient increase in potassium concentration of the saline solution that was infused at the cortical surface, by stirring a drop of 1M K^+. Therefore we were able to control that only one depolarization was triggered, with a continuous flow of saline solution. However K^+ infusion induced a global depolarization of the parenchyma facing the entire cranial window, which was slightly different from a propagating CSD (for

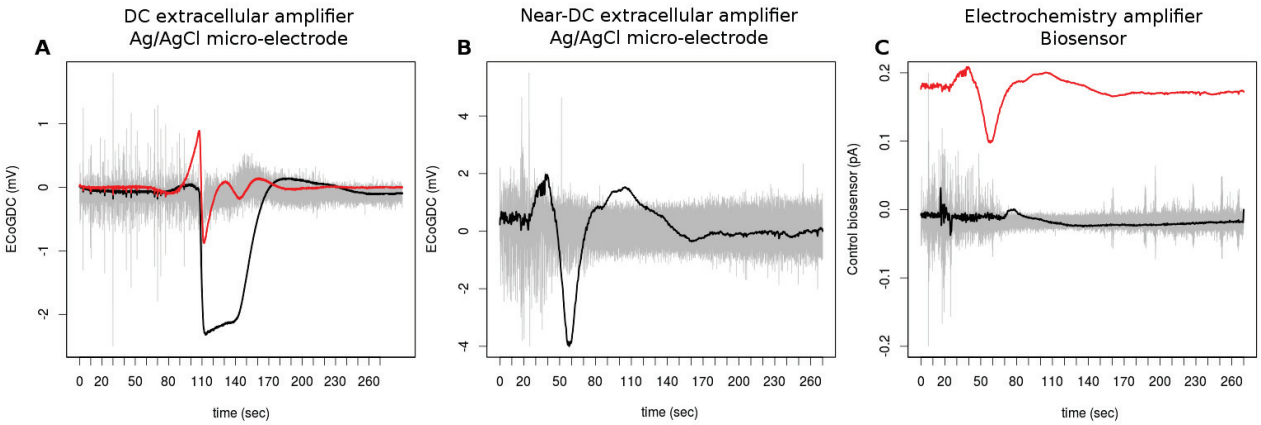

Figure 17: **Local field potential recording during a single CSD** with an LFPot glass micro-pipette connected to either a DC amplifier (A) or an near-DC amplifier (B).
(**A**) An LFPot glass micro-pipette is connected to an extracellular amplifier (EXT 10-2F, NPI Electronics). The grey curve represent the AC signal component (i.e. 0.5-30 Hz), black curve the DC signal (i.e. 0-30 Hz). The red curve represent the DC signal with an additional 0.02 Hz high pass digital filter (butterworth, second order); (*B*) The same kind of glass micro-pipette is connected to a bioAmp (ADInstrument) with a 0.02 Hz analogue build-in high filter. Black and grey curve represent also the DC and AC components.
(**C**) A control biosensor (without the enzymatic layer) is connected to a VA-10 amplifier, and polarized at +500mV. Black and grey curve represent also the DC and AC components. The red curve represent the simultaneous signal recorded from the glass micro-pipette (as in (B)).

example by a pin prick at distance) that is usually considered to better mimic the CSDs observed in brain injured patients. CSDs were defined by a large slow depolarization, with a subsequent vascular response. A depression of ongoing cortical activity was currently observed in healthy animals. In our model of severe TBI with LFPI, CSDs were observed spontaneously during the recorded period (i.e. 20min to 5hours post injury), and also characterized by a large slow depolarization with a subsequent vascular response. A depression of the ongoing activity can also be observed if not already depressed by the injury.

3.2 Cerebral blood flow

CBF can be measured using different techniques computing either absolute or relative values. Absolute values of CBF are usually obtained at steady state using a lipophilic tracer injected IV (e.g. ^{133}Xenon) crossing the BBB, therefore we have to wait for the tracer to be cleared from brain before another measurement can be performed. Radiation can be measured using single photon emission computed tomography or scalp detectors, and related to local CBF [115]. $H_2^{15}O$ tracer has been used with PET imaging to measure CBF in different experimental conditions during functional imaging studies. Finally, MRI "continuous arterial spin labeling" sequence can also extract CBF local information [318]. However these measures of absolute CBF are static, requiring long lasting acquisition time, and not adapted for CSD induced dynamic modifications.
Conversely, optical techniques using backscattered light from illuminated cortical surface gives real time information. Laser speckle contrast imaging gives a 2D blood flow representation of the illuminated cortical surface through a microscope. Hence, it becomes difficult to implant multiple electrode inside the cortex with the lens focusing on the same brain area.

Therefore, in our experiments, blood cell perfusion in the microvasculature of brain tissues was measured with a pencil Probe connected to blood Flow meter (1mm tip, MNP100XP, ADInstrument, Oxford, United Kingdom). Analog signals were acquired a 16 bit PowerLab 16/35 with Labchart 7 (ADInstrument).
The Blood FlowMeter determines the blood flow perfusion by illuminating the surface of the cortex with laser light (830 nm wavelength, visible red light) and measuring the backscattered light. The returned signal is a combination of the original light and backscattered light which results in a signal with a varying frequency content. When the tissue is illuminated by a coherent, low powered laser, light is scattered by both moving and static structures within the microcirculatory beds. Photons, scattered by moving blood cells are spectrally broadened according to the Doppler Effect. Maximum Doppler shifts occur when blood cells are moving in a direction parallel to the incident light beam. The detected light (scattered light) from the cells is detected in a direction opposite to its origin. This varying signal content is the signal of interest as it represents the Doppler shift as a result of light being backscattered off moving blood cells.
LDF produces an output signal in blood perfusion unit (BPU) that is proportional to the blood cell perfusion (or flux). This represents the transport of blood cells through microvasculature and is defined as:

$$Microvascular\ perfusion = Number\ of\ blood\ cells \times Mean\ velocity \tag{5}$$

Microvascular perfusion, therefore, is the product of the mean cell velocity and mean blood cell concentration present in the small volume of tissue under illumination from the laser beam (5). The LDF has been factory calibrated with a constant known motility standard so that, for a given perfusion situation, all probes will read the same value of BPU. However BPU is not an intrinsic physiological definition of blood perfusion, even though it can be traced to a physical standard, the measurements expressed in BPU must be considered as strictly relative.
Thus median BPU measured during the first 5min of each experiment was considered as 100% and after animals were euthanized as 0%.

3.3 Tissue oxygen concentration

Brain oxygen concentration can be measured with a wide range of techniques and the values they give are highly dependent on experimental conditions such as anesthesia or the brain region of interest monitored [192]. Two Photon microscopy has been used to describe O_2 concentration in both brain vessels and tissue, however it is hard to have simultaneous electrophysiological and biosensor recordings under a microscope due to spatial organization. What's more, our model of LFPI induces a subdural hemorrhage that might interfere with the photon tissue penetration.
Hence, we chose to measure $PbtO_2$ using an electrochemical (Clark-type) micro-sensor connected to an amplifier with a constant potential of -0.8V (OX-10, Unisense, Aarhus, Denmark). This technique is minimally invasive ($10\mu m$ tip) with a high temporal resolution. The cathode is polarized against the internal Ag/Cl reference. Driven by external partial pressure, oxygen diffuses from the environment through a silicone membrane and is reduced at the gold cathode surface. The OX-10 offers the association of a very small tip (10 μm) with a short reaction time ($\leq$ 0.1sec). Sensor oxygen consumption is also very low ($2.5 - 25.0 \times 10^{-7}\ \mu g \cdot min^{-1}$) compared to brain oxygen consumption (i.e. $2.19 \pm 0.14\ \mu mol \cdot g^{-1} \cdot min^{-1} \leftrightarrow 70.08 \times \mu g \cdot g^{-1} \cdot min^{-1}$ under α-chloralose anesthesia and normocapnia in rats [319], Table 9).
The oxygen micro-sensor has an internal guard cathode that removes oxygen in the electrolyte, thus minimizing zero-current and pre-polarization time. Oxygen sensors respond linearly in the

range of 0 to 100% (i.e. oxygen % in the bubbled gas) allowing to convert linearly the signal to oxygen partial pressure (PO_2). Like all chemical reactions, the rate of oxygen reduction depends on temperature, so that the relationship between $PbtO_2$ and the oxidative current has to be adjusted to brain/body temperature. Hence, calibration was conducted in a 37^{o}C saline (0.9%) solution, to match animals *in vivo* body temperature. atmospheric and anoxic conditions were obtained by bubbling $0.5L \cdot min^{-1}$ of either air or N_2 in a home-made chamber.

3.4 Glucose, lactate and glutamate concentrations

3.4.1 Imaging

PET is broadly used to investigate brain metabolism and perfusion. For instance ^{18}F-2-deoxyglucose tracer allow for global and local $CMR_{glucose}$ with a millimeter of spatial resolution. Likewise spectroscopic MRI gives precise information about global and local concentrations of brain metabolites such as glucose or lactate [171]. However these imaging techniques gives static images, that cannot be reproduce over time with a temporal resolution needed for the study of dynamic process such as CSD. Moreover these measurements average the vascular, intracellular and extracellular concentrations. Thereby interpreting experimental modifications of glucose or lactate detected by PET can be challenging because of their multiple possible origins.

3.4.2 Tissue measurements

3.4.2.1 Microdialysis

Although chemical signaling has a key role in every brain function, relatively few techniques allow the direct measurement of transmitters and metabolite's extracellular concentrations and the monitoring of their dynamic changes over time. Among them, cMD has been broadly used both in animal models since the 70s [196] and in the ICU since the 90s for the monitoring of acutely brain injured patients [197].
Molecules present in the interstitial fluid diffuse across a polyamide dialysis membrane into the perfusion fluid inside the catheter. The low membrane cut-off (e.g. 6-35kDa, MAB probes, Microbiotech, Sweden) permits small molecules, such as glucose, lactate or amino-acids, detection. If the membrane is long enough, the size and polarity of the molecule small enough, and the dialysate flow slow enough, the concentration in the dialysate will approach the concentration in the interstitial fluid. The usual perfusion rate ranges between 0.3 and 1 $\mu l \cdot min^{-1}$ with a 30-60 min sampling rate. With CMA-70 probes (10mm length, 20kDa cut-off) micro-dyalisate concentrations are around 70% their true value in the interstitial fluid. Overall, the temporal resolution is insufficient to detect the dynamic changes that challenge the tissue during CSD.
Recently the team led by MG Boutelle developed a rapid sampling MD technique [320]. Briefly the assay comprised a custom built valve that allows rapid flow injection of small volumes of dialysate into two separate enzyme beds (either glucose or lactate sensitive biosensors) systems at a 30 sec intervals (Fig 18). With a 2 $\mu l \cdot min^{-1}$ continuous flow rate the authors could not compute the *in vivo* recovery and were unable to quantify the glucose and lactate extracellular concentrations (i.e. *in vivo* recovery of the probe/flow-rate). Thus values of glucose and lactate levels are reported in terms of their concentrations in the dialysate.

Despite its impressive analytical power, cMD is limited on the one hand by the large size of the probes (i.e. 200-600 μm) used to collect brain samples. In particular, implantation of cMD probes into the CNS often causes lesions that impair the physiological processes taking place around the probe [321, 322]. Moreover, cMD probes are too large to be inserted into brain

Figure 18: **Schematic of rapid-sampling microdialysis system**
Dialysate stream from the patient's MD probe (CMA, Microdialysis, Sweden) flows continuously into the custom built valve. The computer switches the valve between the 2 positions to inject a 200 nL samples alternately into the glucose and lactate assays. Adapted from Parkin et al 2005 [262]

slices or small structures of rat or mouse CNS.
On the other hand, the slow diffusion of molecules through the dialysis membrane leads to a 30-60 min sampling rate to approximate the real extracellular concentrations. When trying to reach continuous measurements real cerebral concentrations cannot be quantified and are reported in terms of the dialysate concentrations. Because extracellular concentrations of neurotransmitters and metabolites can vary with fast kinetics, especially during CSD, it is essential that detection take place with a faster temporal resolution in the order of seconds.

3.4.2.2 Microelectrode biosensors

To overcome these technical limitations, a more recent avenue of research has developed microelectrode biosensors that are sensitive to a specific molecule through electrochemical detection. In 1959 J. Heyrovsky received the Nobel Prize in Chemistry for the discovery and development of polarographic methods of analysis. A dropping mercury electrode, which consists of mercury flowing through a capillary and emerging from the orifice as a continual series of mercury drops, is polarized at a fixed potential. Such electrodes have been used in analytical chemistry for the detection of electro-active species (i.e. can be made to oxidize or reduce). The potential of the electrode is controlled so that the chemical species are oxidized or reduced. The potential can be thought of as "electron pressure" which either forces a species in solution to gain an electron (reduction) or lose an electron (oxidation). As the potential of the electrode becomes more negative, it becomes more strongly reducing. Conversely, as the potential becomes more positive, it becomes more strongly oxidizing. Therefore, the redox reaction taking place on the electrode can be controlled by controlling the electrode potential. The polarographic analyzer controls the potential of the electrode against a silver chloride reference, and measures the current at the electrode that is proportional to the electro-active molecule concentration around the electrode.

This principle has been used to design microelectrodes for brain analysis, in which the dropping mercury electrode can be made of carbon, graphite, gold or platinum. These materials have been used to design microelectrode biosensors that can work within a tissue, whereas dropping mercury electrodes can only work in liquid solutions.
The first molecules to be detected in the central nervous system with carbon fiber microelectrodes were directly oxidizable (dopamine, nor-epinephrine, serotonin, or their metabolites) [323]. Other non-electro-active molecules can be detected by microelectrode biosensor based on their recognition by an enzyme belonging to the class of oxidoreductases that is directly immobilized on the surface of the microelectrode. Most oxidases utilized for biosensors have flavin adenine dinucleotide (FAD) as their co-factor and use O_2 as an electron acceptor to catalyze oxidation reaction of the type:

$$Substrate + Enzyme - FAD \mapsto OxidizedProduct + Enzyme - FADH_2 \tag{6}$$

Followed by:

$$Enzyme - FADH_2 + O_2 \mapsto Enzyme - FAD + H_2O_2 \tag{7}$$

The main interest of this type of enzymes is the production of hydrogen peroxide (H_2O_2), because it can be subsequently oxidized on the electrode surface. Enzymatic activity depends on oxygen as a co-substrate that is supposed to be available in non-limiting concentration in the brain. It is also sensitive to temperature and pH, so that these parameters can limit detection capabilities. Oxygen and temperature issues will be discussed in the part V "Electrochemical measurement validation". Depending on micro-electrode electrochemical scheme (e.g. polymer use for enzyme immobilization) and on the applied working potential used for detection, unwanted oxidation of endogenous electroactive molecules like ascorbic acid, catecholamines, uric acid or serotonin has to be considered. To prevent such interference, screening layers such as poly-m-phenylenediamine (PPD) and/or nafion can be added (Fig 19).
Different electrochemical methods can be used with biosensors:

- *Cyclic voltammetry*: The working electrode potential is ramped linearly versus time. After the set potential is reached the potential is ramped in the opposite direction to return to the initial one. These cycles of ramps in potential may be repeated at a high frequency (up to 10Hz) and the current at the working electrode is plotted versus the applied voltage to give the cyclic voltammogram trace.

- *Constant-Potential Amperometry* (used in our experiments): A fixed potential is applied between the working electrode and the reference. The measured current changes as the electroactive-analyte is oxidized (e.g. H_2O_2). The applied potential can be adjusted to maximize the response for the analyte of interest while minimizing the response for interfering analytes. Unlike voltametric techniques, constant-potential amperometry gives a **continuous** signal related to the concentration of a molecule around the tip of the electrode. For oxidase based biosensors, the sampling rate is thus dependent on (1) enzymatic reaction kinetics and (2) oxidation kinetics on the electrode surface. The oxidases we used for biosensors manufacturing (i.e. glucose oxidase, lactate oxidase or glutamate oxidase) are coated on a platinum wire polarize at +500mV for optimal H_2O_2 oxidation against a silver-chloride reference [323]. This set up offers a 1-2 sec temporal resolution (Fig 19).

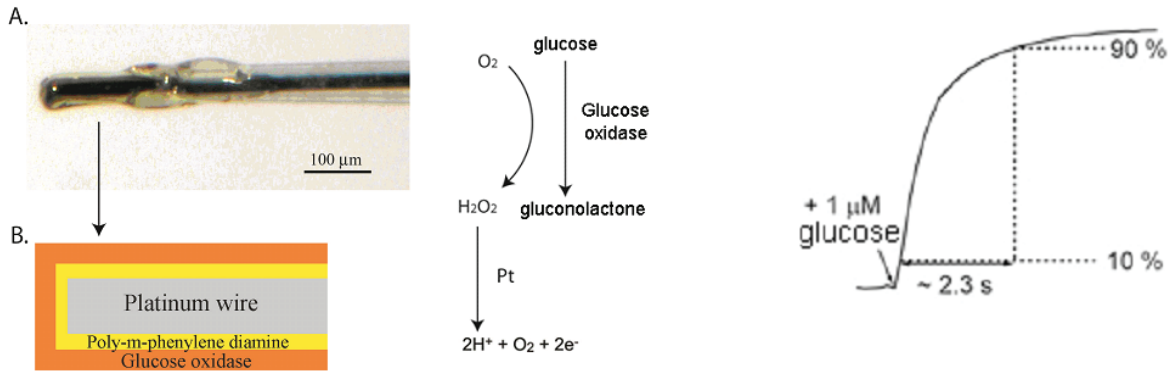

Figure 19: **Glucose sensitive biosensor principle.**
A. biosensor micro-image and **B.** schematic representation of the different layers of the biosensor. In the center; Enzymatic reaction allowing for glucose detection by its oxidation with H_2O_2 production. On the right: time-response to a 1μM glucose concentration increase.

3.5 Cerebral metabolic rate calculations

3.5.1 $CMRO_2$ calculation

$CMRO_2$ is traditionally computed from CBF and $avDO_2$ (see equation (2) in introduction, section 3.2). However such measures made at steady-state and are not appropriate for fast dynamic modification monitoring. In our experiments we measured $PbtO_2$ and CBF modifications and seek to determine also $CMRO_2$ from these values. However, using LDF and $PbtO_2$ probes imposed several assumptions:

- Since LDF only gives relative perfusion data, the absolute CBF (in $ml \cdot g^{-1} \cdot min^{-1}$) rely on data from the literature. Thereby, only relative modifications of $CMRO_2$ can be interpreted.
- Since our probe is located in the extracellular space, we have to assume that extra-cellular oxygen concentration equal intracellular and mitochondrial concentrations.
- We have also to consider the arterial oxygen content to be constant.

Using PET imaging with a ^{15}O-oxygen inhaled tracer to measure $CMRO_2$ and an $H_2^{15}O$ injected tracer to measure CBF, Gjedde et al. published in 1997 a model of the relationship between CBF and oxygen delivery during neuronal excitation [324]. According to this model, the tension of oxygen in mitochondria being negligible compared to the average capillary tension, the mean oxygen tension in the capillary drives the oxygen delivery and consumption in the tissue.
This model has been tested using the same PET approach during both visual stimulation [324] and CBF decrease with indometacine infusion [114]. Oxygen being a small molecule, it is supposed to diffuse within the tissue independently from its architecture. Therefore the authors assumed that oxygen diffusion coefficient remains constant.
Based on this model, Henning Piilgaard and Martin Lauritzen in 2009 proposed a similar algorithm to compute $CMRO_2$ based on CBF measured by an LDF probe and $PbtO_2$ measured using implanted electrochemical probes [258]. They used Gjedde's relation assuming that $PbtO_2$ equals mitochondrial oxygen concentration [114]:

$$PbtO_2 = P_{50} \cdot \sqrt[h]{\frac{2 \cdot C_a \cdot CBF}{CMRO_2} - 1} - \frac{CMRO_2}{2 \cdot L} \tag{8}$$

Where P_{50} is the half-saturation tension of the oxygen-hemoglobin dissociation curve, h the Hill's coefficient of the same dissociation curve, C_a the arterial oxygen concentration, and L the effective diffusion coefficient of oxygen in brain tissue.
To calculate the effective diffusion coefficient of oxygen in brain tissue (L) standard values of P_{50} (34 mmHg [325]) and h (2.7), were combined to C_a from our experiments (7.2 $mmol \cdot mL^{-1}$, calculated with equation (9)), CBF and $CMRO_2$ from the literature.

$$CaO_2 = (Hb \times 13.4 \times \frac{Sat\ O_2}{100}) + (PaO_2 \times 0.031) \quad (9)$$

As reported in table 9, CBF and $CMRO_2$ are highly dependent on species and anesthesia. In rats under isoflurane, that is very similar to our experimental conditions, Baughman et al. reported a CBF of 1.35 $ml \cdot g^{-1} \cdot min^{-1}$ and a $CMRO_2$ of 3.57 $\mu mol \cdot g^{-1} \cdot min^{-1}$ [326]. Using equation (8) with these parameters we computed an L value of 5.1 $\mu mol \cdot g^{-1} \cdot min^{-1} \cdot mmHg^{-1}$.
We calculate "off-line" $CMRO_2$ from simultaneously recordings of $PbtO_2$ and CBF using an L value of 5.1 $\mu mol \cdot g^{-1} \cdot min^{-1} \cdot mmHg^{-1}$, and C_a of 7.2 $mmol \cdot mL^{-1}$.
In our experiment, baseline values of $PbtO_2$ and CBF were taken as the median of a 5 min period starting the experiments, after stabilization. Baseline BPU recorded by the LDF probe was considered as 100% of initial absolute CBF, and the BPU value after the animal was euthanized as 0%.
In healthy animals, initial absolute CBF value (i.e. 100% BPU) was taken from Baughman et al. (1990) as for the L calculation: 1.35 $ml \cdot g^{-1} \cdot min^{-1}$ [326]. After LFPI Hayward et al., using ALS MRI sequence, reported a 54% decrease in CBF in the temporal cortex near the area where we have implanted our electrodes [318]. Therefore in animals undergoing severe LFPI we used $54\% \times 1.35 = 0.729\ ml \cdot g^{-1} \cdot min^{-1}$ as initial absolute CBF value.
Equation (8) was then encrypted in "R " (see chapter 4 "Statistical analysis and signal processing") with CBF as a relative value (percentage from baseline level of BPU measured with the LDF probe) as follow:

```
CMRO2.func <- function (CMR, CBF, TPO2, P50, h, Ca, L, cbfbase)
{
  cbf <- cbfbase * CBF/100
  P50 * ((2*Ca*cbf/CMR)-1)^(1/h) - (CMR/(2*L)) - TPO2
}
```

Subsequently $CMRO_2$ calculations were conducted using the uniroot() function (package stats) to determine the $CMRO_2$ value that gives the root of equation 8. CBF and $PbtO_2$ recordings were divided into 1 sec epochs, to compute second by second variations of $CMRO_2$ after CSDs:

```
for (i in 1:nrow(data)) {
  CMRO2[i] <- uniroot(CMRO2.func, c(0, maxindex),data$LDF[i],data$TPO2[i
      ],P50,h,Ca,L,cbfbase)$root
  # c(0, maxindex) define the CMRO2.func equation interval of validity.
      $
    }
```

3.5.2 $CMR_{glucose}$ calculation

Like for $CMRO_2$, $CMR_{glucose}$ is usually calculated from avD_{gluc} and CBF. For the same reasons we had to compute $CMR_{glucose}$ from extracellular glucose concentrations, measured with

Table 9: **Values of CBF and $CMRO_2$ for different anesthesia and species from the literature** [327, 328, 329, 326, 330, 331, 319, 114, 115]. Calculated from their data with 1 ml O_2 = 44.64 mmol, and an average brain density of 0.99 g/cm3 [332]

Reference	spieces	Condition	CBF $(ml \cdot g^{-1} \cdot min^{-1})$	$CMRO_2$ $(\mu mol \cdot g^{-1} \cdot min^{-1})$
Nilsson and Siesjo (1975)	rat	conscious	1.4	5.00
		50 mg/g phenobarbital	1.11	4.05
		150 mg/kg phenobarbital	0.79	2.95
		250 mg/kg phenobarbital	0.6	2.6
Harp et al. (1976)	rat	70% N_2O, 1.2% halotane	0.8	3.36
Berntman et al. (1979)	rat	70% N_2O	1.11	4.00
Baughman et al. (1990)	rat	isoflurane 1.5%	1.35	3.57
		isoflurane 2.8%	1.08	1.9
Poulsen (1997)	pig	midazolam, ketamine	0.37	1.69
Hyder et al. (2000)	rat	morphine 50 mg/kg, 70% N_2O	0.75	3.15
		α-chloralose 80mg/kg, 70% N_2O	0.4	1.51
Zhu et al. (2002)	rat	α-chloralose 15mg/h	0.53	2.19
Gjedde et al. (2005)	healthy volunteers	conscious	0.62	1.47
Glenn et al. (2003)	healthy volunteers	conscious	0.46	1.38
	TBI patients	sedation and ventilation	0.4	0.62

biosensors. However unlike oxygen, glucose is a much larger molecule that does not diffuse uniformly in brain tissue. Conversely its diffusion depends on both extracellular space tortuosity and transporters kinetics. Glucose transport across membranes is mediated by a family of membrane-spanning passive carrier proteins, the GLUTs. The repartition of several isoforms among brain cells is discussed in the introduction section 2.2.
Since GLUT1 are similarly distributed at the luminal and abluminal membranes of the endothelium, BBB can be modeled as a single membrane system in terms of glucose transport [333]. Therefore brain glucose concentration reflects the relative transport capacity at the BBB and $CMR_{glucose}$ (Fig 20B).
However, using extracellular glucose concentration to compute $CMR_{glucose}$ imposed several assumptions:

- We have to assume that the arterial blood glucose concentration remains constant.
- Since our biosensors are located in the extracellular space, we have to assume that extracellular equal intracellular concentrations. Indeed, considering the high concentrations of GLUT 3 and 1 on neurons and astrocytes, the diffusion of glucose across their membrane is not limiting and allows fast equilibrium. Accordingly, unlike other metabolite (N-acetylaspartate, choline, creatine, myo-inositol, and taurine), intra and extra-cellular glucose concentrations are very close [334]. The largest glucose gradient being at the BBB.
- Likewise, the high concentrations of GLUT 3 and 1 on cell's membranes lead to the hypothesis that glucose repartition in brain tissue is homogeneous and independent of extracellular tortuosity.
- The transport kinetics of the BBB have also to be constant. However transport kinetics as measured *in vivo* by MRI spectroscopy has been mostly determined under steady-state conditions, compatible with sufficient measurement time required for glucose equilibrium [333, 335, 336]. This might not be the case during fast glucose modifications on one side of the BBB.
- Last but not least, modeling glucose transport across BBB and $CMR_{glucose}$, for example with a reversible Michaelis-Menten equation, does not include CBF values.

Under Steady-state conditions, a near linear relationship between brain and plasma glucose has been experimentally determined and described by a reversible Michaelis-Menten model of enzyme kinetics [333]. However, a reversible model is unable to account for GLUT transport kinetics adaptation to asymmetric glucose concentrations across BBB [337]: Transacceleration and iso-inhibition describes respectively how glucose transport rate from blood (G_{blood}) to brain tissue (G_{brain}) can be increase by G_{blood} or decrease by G_{brain} [336, 337]. Therefore a "four-state" model has been developed to account for the different GLUT1 conformations at the BBB (Fig 20A). The best description of experimental observations by this "four-state" model included symmetric rather than asymmetric glucose carriers across BBB (i.e. $K_t^{G_{brain}} = K_t^{G_{plasma}}$, Fig 20) [336, 337]. Therefore, the relationship between glucose concentrations in brain (G_{brain}) and plasma (G_{plasma}) at steady-state can then be described by equation (10):

$$G_{brain} = V_d \frac{\left(\frac{T_{max}}{CMR_{gluc}} - 1\right) \times G_{plasma} - K_t}{\frac{T_{max}}{CMR_{gluc}} + 1 + \frac{G_{plasma}}{K_{ii}}} \tag{10}$$

reference	method, species, anaesthesia	K_t (mM)	T_{max} ($\mu mol \cdot g^{-1} \cdot min^{-1}$)	CMR_{gluc} ($\mu mol \cdot g^{-1} \cdot min^{-1}$)
Gruetter 1998	MRS, human, awake	0.6 ± 2	0.69 ± 0.09	0.3*
De graaf 2001	MRS, human, awake	1.2 ± 0.62	0.57 ± 0.15	0.27 ± 0.07
	grey matter	1.1 ± 0.66	0.65 ± 0.13	0.36 ± 0.07
	white matter	1.7 ± 0.88	0.24 ± 0.13	0.11 ± 0.06
Choi 2001	MRS, rat, αchloralose	3.3 ± 0.1	$T_{max}/CMR_{gluc}=2.7 \pm 0.13$	
Choi 2002	MRS, rat, pentobarbital	3.3 ± 0.1	$T_{max}/CMR_{gluc}=5.0 \pm 0.24$	
Morgenthaler 2006	brain extraction, rat, isoflurane or αchloralose	1.4 ± 0.7	$T_{max}/CMR_{gluc}=2.3 \pm 0.1$	

Table 10: **Glucose kinetic parameters** according to a reversible Michaelis-Menten model (equation (11)) [333, 338, 339, 340, 341]. Abbreviations: *MRS* Magnetic resonance spectroscopy; * $CMR_{glucose}$ was assume to remain constant.

Where V_d is the the physical distribution space volume of glucose in the brain ($0.77mL \cdot g^{-1}$), T_{max} denotes the apparent maximal transport rate across the BBB ($\mu mol \cdot g^{-1} \cdot min^{-1}$), K_t and K_{ii} denote the apparent Michaelis and inhibition constants (in mM). Adding a fourth endothelial compartment did not improve the model when confronted to different datasets [336].

It was noteworthy that K_t was on the order of a few mM, as previously determined from the reversible model. Moreover, since K_{ii} largely exceeds G_{plasma}, iso-inhibition (i.e. transport inhibition by G_{brain}) is unlikely to be of substantial importance for plasma glucose below 25 mM. As a consequence, the reversible Michaelis-Menten model (equation (11)) can account for most experimental observations under normo-glycemia and moderate cases of hypo and hyperglycemia [336, 333]:

$$G_{brain} = V_d \frac{\left(\frac{T_{max}}{CMR_{gluc}} - 1\right) \times G_{plasma} - K_t}{\frac{T_{max}}{CMR_{gluc}} + 1} \tag{11}$$

Therefore, brain glucose concentration at steady-state appears to be well defined by the ratio of T_{max} to $CMR_{glucose}$, assuming that other parameters remain constant. Several authors calculated Michaelis-Menten constants for glucose transport from a reversible model using either spectroscopy MRI or PET (Table 10). However, it is noteworthy that the spatial resolution of these imaging techniques is not enough to depict the difference between capillaries, extracellular space and intracellular compartment. Therefore, brain glucose concentrations measured by magnetic resonance spectroscopy are higher than those obtained with micro-electrode biosensors (2.2-4.1 [342] *vs* $0.59 \pm 0.3mM$ [343]).

Another caveat is that all these kinetic parameters have been determined assuming a constant $CMR_{glucose}$. Some authors even evaluate the ratio between T_{max} and $CMR_{glucose}$ as a surrogate to T_{max}, with huge variations depending on anesthesia or plasma glucose concentrations [339, 344]. To our knowledge, there is no evidence about how these parameters behave

Figure 20: **Glucose transport models**: **A**. Schematics representation of the alternating conformation kinetics of the glucose carrier. In the absence of glucose (G_{out} or G_{in}), the carrier can exist in two inter-converting isomers that are ready to bind glucose either outside (C_{out}) or inside (C_{in}) the membrane. When loaded, the carrier can also assume two isomeric forms favoring glucose release to the outer ($C_{out}G$) or inner ($C_{in}G$) side of the membrane. The rate constants k_1 and k_{-3} define glucose binding while k_{-1} and k_3 define its dissociation from the carrier. The rate constants k_2 and k_{-2} or k_4 and k_{-4} reflect the isomerisation of the loaded or unloaded carrier. **B**. Shows the simplest model of bidirectional glucose transport (T^f and T^r) which represents the forward and reverse fluxes of glucose diffusion through the BBB that was considered as a single membrane. **C**. The compartment composed by the endothelial cells was included and thus four unidirectional fluxes (T) are required to describe glucose flow through the BBB. The glucose consumption rate CMR_{glc} was considered as a metabolic compartment in the system. Adapted from Duarte et al. 2009 [336]

The four-state exchange model parameters can be describe as follow:

$$G_{brain} = V_d \frac{\left(\frac{T_{max}}{CMR_{gluc}} - 1\right) \times G_{plasma} - K_t^{G_{plasma}}}{\frac{T_{max}}{CMR_{gluc}} + \frac{K_t^{G_{plasma}}}{K_t^{G_{brain}}} + \frac{G_{plasma}}{K_{ii}^{G_{brain}}}}$$

$$T_{max} = G \frac{k_2 k_3 k_4}{(k_4 k_2 + k_4 k_{-2} + k_3 k_4 + k_2 k_3)}$$

$$K_t^{G_{brain}} = \frac{(k_4 - k_{-4})(k_{-1} k_{-2} + k_2 k_3 + k_3 k_{-1}}{k_{-3}(k_{-1} k_{-2} + k_{-2} k_{-4} + k_2 k_{-4} + k_{-1} k_{-4})}$$

$$K_t^{G_{plasma}} = \frac{(k_4 - k_{-4})(k_{-1} k_{-2} + k_2 k_3 + k_3 k_{-1}}{k_{-1}(k_2 k_4 + k_{-2} k_4 + k_3 k_4 + k_2 k_3)}$$

$$K_{ii}^{G_{brain}} = \frac{k_1(k_4 k_2 + k_4 k_{-2} + k_3 k_4 + k_2 k_3)}{k_{-3}(k_2 k_{-2} + k_1 k_2)}$$

during dynamic process such as brain activation or injury, therefore we had to consider them as constant.

In 2006, Morgenthaler et al. shown that the relationship between brain and blood glucose was not influenced by the anesthetic agent: isoflurane or αchloralose [341].
Moreover, a reversible Michaelis-Menten model gave a good description of their data. In our experiment we calculated $CMR_{glucose}$ using a reversible Michaelis-Menten equation, with Morgenthaler parameters of K_t and $T_{max}/CMR_{glucose}$. To extrapolate T_{max} from the ratio $T_{max}/CMR_{glucose}$, we used $CMR_{glucose}$ from the literature, corresponding to our experimental condition: anesthetized rats under low doses of Isoflurane (0.8-1.5%). Indeed $CMR_{glucose}$ is influence by the depth of anesthesia, ranging from $0.44 \mu mol \cdot g^{-1} \cdot min^{-1}$ under 2% Isoflurane and nitrous oxide [345] to 0.55 $\mu mol \cdot g^{-1} \cdot min^{-1}$ under 1.5% Isoflurane alone [346]. A $CMR_{glucose}$ of 0.55 $\mu mol \cdot g^{-1} \cdot min^{-1}$ lead to a T_{max} of $2.3 \times 0.55 = 1.27$ $\mu mol \cdot g^{-1} \cdot min^{-1}$.
Therefore, the equation (11), was encrypted in "R", using a Kt=1.4, a T_{max}=1.27 and a Vd=0.77:

```
CMRGluc <- function (CMRG, Gbrain, Vd=0.77, Kt=1.4, Tmax=1.27, Gplasma
    =7.3)
{
  (Vd*((((Tmax/CMRG)-1)*Gplamsa - Kt )/((Tmax/CMRG) + 1))) - Gbrain
}
```

Like $CMRO_2$, $CMR_{glucose}$ was calculated using the uniroot() function (package stats) to determine the value that gives the root of equation 11, assuming that other parameters remains constant during the experiment.

```
for (i in 1:nrow(data)) {
      CMR[i] <- uniroot(CMRGluc, c(0.0001, maxindex),Gbrain[i],Vd,Kt,
          Tmax,Gplamsa)$root # c(0.0001, maxindex) define the CMRGluc
          func equation interval of validity.$
    }
```

Chapter 4

Statistical analysis and signal processing

Many software are available to perform statistical analysis and/or signal processing. Among them "R" is a powerful and widely used open-source (GNU General Public License) programming language and software environment for statistical computing, graphics and data analysis. It is currently developed by the "R development core team" (http://www.R-project.org/; R Foundation for Statistical Computing, Vienna, Austria). We performed our analysis in RStudio (version 0.98.1103 – ©2009-2014), also a free and open source integrated development environment (IDE) with "R" (version 3.2.0, 2015-04-16).
The capabilities of "R" are extended through user-created packages, which allows specialized statistical techniques, graphical devices, import/export capabilities, reporting tools ... In our analysis we used the following additional packages:

- graphics: *graphics* (Paul Murrel, Aukland university), *ggplot2* (Hadley Wickham and Winston Chang, Rice university) and *gridExtra* (Baptiste Auguie, Wellington university)
- signal processing: *signal* (actual maintainer: Uwe Ligges, Dortmund university)
- data processing: *dplyr* (actual maintainer: Hadley Wickham, RStudio)
- model and statistical analysis: *stats* (R Core Team and contributors worldwide) and *nlstools* (actual maintainer: Florent Baty, COPSAC, Gentofte university).

Likewise, I wrote a package dedicated to biosensor and brain metabolism analysis that is available on GitHub for download (https://github.com/balanca/BrainMetabolism.git, the documentation is in appendix VIII). It includes functions for biosensor calibration and signal conversion to corresponding substrate concentration, $CMRO_2$ and $CMR_{glucose}$ calculations, and a few signal processing function. This package has been used in our analysis in order to save time, and the scripts that are included will be described along my thesis.
As we usually had a few samples in each group, a normal data distribution could not be assumed. Therefore our data will be presented as median and interquartile range [25^{th} percentile;75^{th} percentile].
Group comparisons were performed by a Wilcoxon rank sum test. When there were more than two groups to compare (histological analysis), a Kruskal-Wallis test was performed. A Wilcoxon rank sum test (with bonferroni p value adjustment) was used for post-hoc comparisons when the Kruskal-Wallis showed a significant effect.
A p value < 0.05 was considered as significant.

Part IV

Anatomical modifications following severe Lateral fluid percussion injury

Chapter 1

Neuronal loss - Accepted article

Neuronal loss as evidenced by automated quantification of neuronal density following moderate and severe traumatic brain injury in rats

Journal:	*Journal of Neuroscience Research*
Manuscript ID:	jnr-2015-Jun-6345.R1
Wiley - Manuscript type:	Research Article
Date Submitted by the Author:	10-Aug-2015
Complete List of Authors:	Balança, Baptiste; Inserm U1028, CNRS UMR5292, CRNL team waking; Hospices Civils de Lyon, Anesthesiology and intensive care dept, P. Wertheimer Neurological Hospital; University Claude Bernard Lyon I, Bapteste, Lionel; Hospices Civils de Lyon, Anesthesiology and intensive care dept, P. Wertheimer Neurological Hospital; University Claude Bernard Lyon I, Lieutaud, Thomas; University Claude Bernard Lyon I, ; Inserm U1028, CNRS UMR5292, CRNL team TIGER Ressnikoff, Denis; University Claude Bernard Lyon I, ; University Claude Bernard Lyon I, Centre d'imagerie quantitative Lyon-Est Guy, Rainui; University Claude Bernard Lyon I, ; Inserm U1028, CNRS UMR5292, CRNL team waking Bezin, Laurent; Inserm U1028, CNRS UMR5292, CRNL team TIGER; University Claude Bernard Lyon I, Marinesco, Stephane; Inserm, CRNL team Waking; Inserm U1028, CNRS UMR5292, CRNL, AniRA-Neurochem technological platform; University Claude Bernard Lyon I,
Keywords:	Injury, Hippocampus, Cell death, Cerebral cortex, Thalamic neurons

Neuronal loss as evidenced by automated quantification of neuronal density following moderate and severe traumatic brain injury in rats

Baptiste Balança[1,2,4§], Lionel Bapteste[2,4§], Thomas Lieutaud[3,4], Denis Ressnikoff[4,5], Rainui Guy[1,4], Laurent Bezin[3,4] and Stéphane Marinesco[1,4,6,*]

[1]Inserm U1028; CNRS UMR5292; Lyon Neuroscience Research Center, Team WAKING, Lyon F-69000, France.

[2]Anesthesiology and Intensive Care Department, P. Wertheimer Neurological Hospital, Hospices Civils de Lyon, Lyon, France.

[3]Inserm U1028, CNRS UMR5292, Lyon Neuroscience Research Center, Team TIGER, Lyon F-69000, France.

[4]University Claude Bernard Lyon 1, F-69000 Lyon, France.

[5]Centre d'imagerie quantitative Lyon Est (CIQLE), Lyon, France.

[6]Inserm U1028, CNRS UMR5292, Lyon Neuroscience Research Center, AniRA-Neurochem Technological Platform, F-69000 Lyon, France.

[§]these authors contributed equally to this work.

*Corresponding author: Stéphane Marinesco PhD, Lyon Neuroscience Research Center, Team WAKING, 8 Avenue Rockefeller, 69373 Lyon, Cedex 08.

Email: stephane.marinesco@univ-lyon1.fr

Running title: quantifying neuronal loss following TBI in rats

Keywords: immunohistochemistry, NeuN, lateral fluid percussion, hippocampus, cortex, AB_11210778, AB_141367

Abstract

Traumatic brain injury causes widespread neurological lesions that can be reproduced in animals using the lateral fluid percussion (LFP) model. The characterization of the pattern of neuronal death generated in this model remains unclear involving both cortical and subcortical brain regions. Here, seven days following moderate (3 atmospheres absolute, ATA) or severe (3.8 ATA) LFP, we estimated neuronal loss using immunohistochemistry together with an computer assisted automated method for quantifying neuronal density in brain sections. Neuronal counts were performed ipsilateral to the impact, in the parietal cortex ventral to the site of percussion, the temporal cortex, the dorsal thalamus, and the hippocampus. These results were compared to the counts observed at similar areas in sham animals. We found that neuronal density was severely decreased in the temporal cortex (-60%), in the dorsal thalamus (-63%), and in area CA3 of the hippocampus (-36%) of injured animals compared to controls, but was not significantly modified in the cortices located immediately ventral to the impact. Total cellular density increased in brain structures displaying neuronal death, suggesting the presence of gliosis. The increase in the severity of LFP did not change the pattern of neuronal injury. This automated method simplified the study of neuronal loss following traumatic brain injury, and allowed the identification of a pattern of neuronal loss that spreads from the dorsal thalamus to the temporal cortex, with the most severe lesions being in brain structures remote from the site of impact.

Significance statement

Traumatic brain injury (TBI) is one of the main causes of disability leading to major economic and social burdens. A better understanding of the mechanisms underlying neurological dysfunction following TBI, is therefore of importance. Lateral fluid percussion (LFP) is one of the most widely used TBI animal models, however the characterization of the pattern of neuronal

death generated in this model remains incomplete. In the present study we describe a pattern of neuronal loss seven days after LFP that spreads from the dorsal thalamus to the temporal cortex. This description paves the way for more thorough evaluations of future therapeutic interventions.

Introduction

Traumatic brain injury (TBI) is a leading cause of disability among young people, leads to major economic and social burdens and are considered to increase worldwide. A better understanding of the mechanisms underlying neurological dysfunction following TBI, as well as how to improve patient outcomes, are therefore of major importance. TBI often causes widespread neuronal injury to the central nervous system, including hemorrhage, neuronal loss, and white matter lesions with axonal injury (Mathé et al., 2005; Levine et al., 2008). This heterogeneity complicates the development of neuroprotective strategies aimed at improving patient outcome (Kabadi et al., 2014a).

Animal models of TBI allow researchers to generate damage in a reproducible manner, and are critical to an improved understanding of the mechanisms underlying the development of neurological lesions. Lateral fluid percussion (LFP) is one of the most widely used models that allows inducing moderate to severe injury by modulating the intensity of the shockwave (Li et al., 2004). The location and severity of the neurological lesions that can be generated by LFP has not received a great deal of systematic study (Hicks et al., 1996; Kabadi et al., 2014b). Therefore, precisely mapping the lesions produced by LFP appears a prerequisite for both understanding the mechanisms underlying brain injury in this model, and developing neuroprotective treatments potentially applicable to human patients.

Several studies have sought to define the characteristics of neuronal loss following LFP in rats. This TBI model appears to produce a complex pattern of widespread lesions throughout the injured hemisphere, which encompass cortical, hippocampal, and thalamic brain regions (Hicks et al., 1996; Grady et al., 2003; Sato et al., 2001). Interestingly, the sites of the most intense neuronal loss are often remote from the site of impact; for example, maximal damage has been observed in the temporal cortex or deep in the thalamus following percussive impact to the

ipsilateral surface of the brain (Hicks et al 1996; Kabadi et al., 2014b). Two major strategies have been used to determine the pattern of these brain lesions. The first one consists of assessing the number of injured neurons stained by injury markers such as Fluoro-Jade C (Raghupathi et al., 2002; Bentzer et al., 2001) or terminal deoxynucleotidyl transferase dUTP nick end labeling (TUNEL, Raghupathi et al., 2002), or by the number of visually identified hyperchromatic or shrunken neurons (Hicks et al., 1996; Bentzer et al 2001). However, these methods can potentially generate high numbers of false positives or false negatives (Schmued et al., 1997; Schmued et al., 2005). Alternatively, brain lesions can be defined by the density of neurons that remain several days following the TBI. Such studies are typically performed using visual analysis and manual cell counts, and are therefore highly labor-intensive. For this reason, the comprehensive quantification of neuronal density has, to date, been limited to few brain structures (McIntosh et al., 1989; Kabadi et al., 2014b). Given the complex and widespread nature of neural lesions following LFP injury, there is a pressing need for simpler and rapid methods for quantifying neuronal and cellular densities in brain sections.

We recently developed an automated method, based on ImageJ software, that quantifies neuronal density in brain sections immunoreactive for the nuclear neuronal marker NeuN and stained with the fluorescence DNA dye 4',6'-diamidino-2-phenylindole (DAPI) (Grady et al., 2003). Here, we applied this technique to the brains of Wistar rats subjected to moderate (3 ATA) or severe (3.8 ATA) LFP to quantify neuronal density in seven brain regions, including the parietal cortex immediately ventral to the site of percussion (impacted cortex), the temporal cortex (primary somatosensory cortex and secondary auditory cortex), the dorsal thalamus, and the hippocampus (areas CA1 and CA3, dentate gyrus, and hilus).

Materials and methods

Animals

Male Wistar rats weighing 250 - 400 g were obtained from Elevage Janvier (Le Genest Saint Isle, France). All experimental protocols were approved by the local committee on animals in research at the University Claude Bernard Lyon I (approval number: BH 2013-07), and were performed in accordance with European directive 2010/63/EU. There was no significant difference in body weight between control animals and those subjected to moderate or severe LFP (Controls 372 ± 35 g ,moderate LFP 400 ± 42 g, severe LFP 382 ± 86 g, p=0.69).

Lateral fluid percussion injury (LFP) model

Animals were anesthetized with isoflurane and placed in a stereotaxic frame (Stoelting, Dublin, Ireland) with their body temperature maintained around 37 °C with a homeothermic blanket (LSI Letica, Barcelona, Spain). A subcutaneous infiltration of 0.5 mL of 3 mg/ml ropivacaine (Naropeine® 7.5mg/ml in saline) was performed prior to scalp opening. A circular craniotomy (5 mm diameter) located 3.8 mm caudal to Bregma and 3.0 mm lateral from the midline was then performed under aseptic conditions. A hollow plastic cap was first attached to the skull using cyanoacrylate, then secured with dental acrylic. A 1 mm diameter stainless steel screw, inserted into the skull, served as an anchor for the dental acrylic and the plastic cap was filled with sterile saline. The animal was then removed from the stereotaxic frame and brought to the lateral fluid percussion device (Custom Design and Fabrication, Virginia Commonwealth University Richmond, Virginia, USA). Rats received a single 20 ms fluid percussion pulse of 3.0 or 3.8 ATA under light anesthesia: i.e. the animal was removed from the anesthesia mask and the LFP impact was administered at the first signs of a hind limb response to a gentle toe pinch. The

cap was then removed, anesthesia was resumed, and the scalp was sutured. The animals were single-housed for 7 days, with assisted drinking and feeding if necessary. Buprenorphine 0.05 mg/kg was administered twice at 12h interval after surgery.

To avoid respiratory arrest following severe LFP, mechanical ventilation (Harvard Apparatus, Ispra MA1 55-7058, Vt = 6 ml/kg, breath rate = 60/min, Peep = 5 cm H_2O) was performed following 3.8 ATA LFP until animals recovered spontaneous breathing. To accomplish this, animals were intubated with a 16-gauge catheter following the induction of anesthesia and before LFP. Animals whose mechanical ventilation could not be resumed within the first 30 min post-LFP, as well as animals that lost more than 25% of their initial body weight in the post-procedure period were excluded of the study. Control animals did not receive surgery.

Brain fixation and removal

Seven days following the LFP-mediated induction of TBI, animals were deeply anesthetized with an intraperitoneal injection of sodium pentobarbital (150 mg/kg, Ceva, Libourne, France) and intracardially perfused, first with 150 mL of a Ringer solution with 0.1% heparin at room temperature, then with 500 mL of an ice-cold fixative solution containing 4% freshly depolymerized paraformaldehyde in 0.1 M phosphate buffer (PB, pH = 7.4). The brains were removed, placed in a 30% sucrose solution (PB, 0.1 M, pH = 7.4) for 48 h, and frozen in a solution of isopentane at -50 °C before storage at -80 °C for further analysis.

Fluorescent double-labeling immunohistochemistry

NeuN immunolabelling was performed according to the method described by Woeffler-Maucler et al. (2014). Frozen rat brains were cut into 20 µm thick sections using a HM 500 OM microtome (Microm, Francheville, France), and brain sections were placed in a solution of 10

mM phosphate buffered saline (PBS, pH = 7.4, Sigma-Aldrich, St Quentin Fallavier, France). For immunohistochemistry, tissue sections were first permeabilized with a solution of PBS, 0.3% Triton-X-100, and 1% goat serum (Sigma-Aldrich, St Quentin Fallavier, France) for 30 min, washed for 10 min with PBS, and then three more times for 10 min with PBS and 0.5% Tween 20 (PBST, Sigma). The sections analyzed in this study were located between 3.2 and 4.3 mm caudal from Bregma (Paxinos and Watson 2005). Brain sections were incubated overnight at 4 °C with a mouse monoclonal antibody directed against the NeuN protein (1:4000; MAB-377, Millipore, Molsheim, France, RRID: AB_11210778) in PBST with 2% goat serum (Tab. 1). After three 10 min washes with PBST, the sections were incubated for 1 h with goat anti-mouse IgG antibody coupled to Alexa Fluor 488 (1:1000; Invitrogen, Saint Aubin, France, RRID: AB_141367) and DAPI (1:1000; Sigma-Aldrich, Saint-Quentin Fallavier, France) in PBST containing 2% goat serum (Tab. 1). The sections were then washed for 10 min in PBST followed by a 10 min wash in PBS. The sections were then mounted onto pre-cleaned microscope slides (Ground Edges 90°, Menzel-glaser®, Braunschweig, Germany) using Millipore water and coverslipped using Fluoromount mounting medium (Sigma-Aldrich, Saint-Quentin Fallavier, France), and stored at 4 °C in the dark.

Antibody characterization

Monoclonal antibodies raised against NeuN originate from the single A60 clone and have been shown to specifically recognize the so-called NeuN epitope on the splicing factor Rbfox3 (Maxeiner et al., 2014). Secondary antibodies were purified using their affinity for mouse immunoglobulins. They specifically targeted mouse gamma immunoglobulins heavy and light chains with limited cross reactivity against bovine IgG, goat IgG, rabbit IgG, rat IgG, human IgG

and human serum (https://www.lifetechnologies.com/order/genome-database/antibody/Mouse-IgG-H-L-Secondary-Antibody-Polyclonal/A-11029).

Confocal microscopy

Slides were imaged at the CIQLE Imaging Facility (Université Claude Bernard Lyon 1, Lyon, France) using a Leica SP5 confocal laser-scanning microscope (CLSM) with a 20× objective (NA: 0.7). The images were acquired by a two-step process: positivity for DAPI was assessed at an excitation wavelength of 405 nm and emission wavelengths of 418–473 nm, while the signal for Alexa 488 (NeuN immunoreactivity) was assessed at an excitation wavelength of 488 nm and emission wavelengths of 510–613 nm. A z-series consisting of 15–20 optical sections, with a 1 μm interval, were imaged within each region of interest. Individual images were averaged three times for NeuN immunoreactivity (Alexa 488) and twice for DAPI. Image analysis was performed using ImageJ software (version 1.49p, http://imagej.nih.gov, java version 1.6.0_14 (32bit), including the following plugins: RGB Grey merge, LOCI plugin, Gran filter, k-mean clustering, maximum entropy threshold, mixture modeling) and an automated custom-made macro developed at the Centre Commun de Quantimétrie (University Claude Bernard Lyon1, Lyon, France, Woeffler-Maucler et al., 2014). Overall cellular density was defined as the total number of DAPI-stained nuclei per mm^2 of tissue. Neurons were identified as DAPI-stained nuclei present in a NeuN-positive region of the optical section. This identification was performed on five consecutive optical sections spaced by 1 μm, with the central one being the optical section with the highest fluorescence intensity (usually located the 8^{th} and the 14^{th} optical section of the slice). Each neuronal nucleus had to be identified within a NeuN positive region in the optical section of highest intensity and in at least one of the four optical sections that surrounded

it. The macro required an autothreshold step to dichotomize the images in NeuN positive and NeuN negative regions. Brain regions characterized by sparse neuronal cell bodies (neocortex, hilus, thalamus) were processed using the Moments autothreshold method, whereas other areas displaying densely packed neurons (CA1, CA3 and dentate gyrus) were dichotomized using the Li autothreshold method (see Woeffler-Maucler et al., 2014, for a complete description of the method). Neuronal counts were therefore performed without human intervention.

Imaging of whole brain sections was performed using a Zeiss AXIO Scan.Z1 slide scanner with a 20× objective (NA: 0.8) and an Orca Flash 4.0 camera. Excitation and emission wavelengths were 365 nm and 420-470 nm for DAPI, and 470 nm and 500-550 nM for Alexa fluor 488 respectively.

Statistical analyses

Results are presented as median and interquartile range. Neuronal and cellular densities were expressed as the number of neurons and nuclei per mm² in 18 different animals (6 controls, 6 in 3 ATA LFP group, and 6 in 3.8 ATA LFP group). Densities in a given region of interest were assessed in 2 different brain slices and averaged for each animal. Data were then compared between the three groups by a Kruskal-Wallis rank sum test within seven brain regions, using the R software 3.2.0 (R Development Core Team, http://www.R-project.org/; R Foundation for Statistical Computing, Vienna, Austria). Pairwise comparisons using Wilcoxon rank sum test with Bonferroni p value adjustment was used to compare groups when the Kruskall-Wallis showed a significant effect. Graphics were made using the ggplot2 library. A p value < 0.05 was considered as significant.

Results

Acute behavioral effects of LFP injury

Following a moderate LFP (3 ATA; n = 7), animals exhibited a loss of consciousness characterized by a lack of response to tail pinch for at least 2 min. Short apnea lasting less than 30 s was evident, and the righting reflex was recovered between 25 and 35 min post-injury. One rat (14% of sample) died of acute cardiorespiratory failure. Overall, these acute behavioral effects following moderate LFP were consistent with definition of moderate TBI in this model (Aoyama et al., 2008; Bao et al., 2012; Shultz et al., 2013).

We subjected eight animals to severe LFP (3.8 ATA). At this intensity, the resultant apnea necessitated artificial ventilation for at least 30-45 min. After 45 min, 2 animals (25%) did not recover spontaneous breathing and died. Therefore, in our hands, LFP at 3.8 ATA produced symptoms consistent with severe TBI (Aoyama et al., 2008; Bao et al., 2012; Shultz et al., 2013).

Definition of the regions of interest

Coronal slices of brains from moderate or severe LFP injured rats were first observed using a slide scanner to obtain a preliminary estimate of the regions of most intense neuronal loss (Fig 1A). Severe neuronal loss was evident in the temporal cortex (i.e. primary somatosensory cortex and secondary auditory cortex) and in the dorsal thalamus, because NeuN immunoreactivity had dramatically decreased, leaving an apparent DAPI staining on the images (Fig. 1A).

Based on this preliminary analysis, we defined seven brain regions for confocal imaging and for the determination of neuronal densities (Fig. 1B). These were: the impacted cortex (i.e. parietal association cortex immediately underneath the site of the fluid impact, 0.555 ± 0.284 mm², Fig.1B area 1), temporal cortex (total area imaged = 0.563 ± 0.035 mm², Fig.1B area 2),

dorsal thalamus (0.575 ± 0.002 mm², Fig.1B area 3), CA1 (0.120 ± 0.019 mm², Fig. 1B area 4), CA3 (0.063 ± 0.002 mm², Fig.1B area 5), dentate gyrus (0.042 ± 0.006 mm², Fig.1B area 6), hilus (0.051 ± 0.015 mm², Fig.1B area 7). There was no significant difference between the areas of the regions of interest in control rats and in those subjected to moderate or severe LFP (df=2, Kruskal-Wallis test for impacted cortex X^2=0.09, p=0.96; temporal cortex X^2=1.65, p=0.44; CA1 X^2= 1.55, p=0.46; CA3 X^2=0.42, p=0.81; dentate gyrus X^2= 0.43, p=0.81; hilus X^2=0.88, p=0.64; thalamus X^2=5.7, p=0.06).

Effects of moderate (3 ATA) LFP on neuron densities

Surprisingly, no change in neuronal density could be evidenced in the cortex that was impacted by LFP: 919 [804-1051] neurons per mm^2 in controls vs 901 [883-918] neurons per mm^2 after LFP-3ATA (Tab.2, Fig.2A, X^2 = 2.4, df = 2, p = 0.31, n=6). However, neuronal density showed a 60% decrease in the temporal cortex, located lateral to the impact: 929 [828-1032] neurons per mm^2 in controls vs 369 [329-399] neurons per mm^2 after LFP-3ATA (Tab.2, Fig.2B, X^2 = 12.3, df = 2, p = 0.002, n=6). In the dorsal thalamus, neuronal density was decreased by 62%: 349 [328-391] neurons per mm^2 in controls vs 131 [56-209] neurons per mm² after LFP-3ATA (Tab.1, Fig.2C, X^2 = 9.6, df = 2, p = 0.008, n=6).

The hippocampus was less impacted by LFP. Only area CA3 showed a significant 36% decrease in neuronal density: 934 [908-1021] neurons per mm^2 in controls vs 592 [587-695] after LFP-3ATA (Tab.2, Fig.3B, X^2 = 6.2, df = 2, p = 0.044, n=6). There were no significant differences in neuronal density in other hippocampal regions: CA1 1453 [1371-3240] vs 1397 [1101-2667] neurons per mm^2 (Tab.2, Fig.3A, X^2 = 1.4, df = 2, p = 0.47, n=6), dentate gyrus 4012 [3861-4284] vs 3810 [3627-4661] neurons per mm^2 (Tab.2, Fig.4A, X^2 = 0.2, df = 2, p =

0.894, n=6) or hilus 502 [441-624] vs 446 [383-465] neurons per mm^2 (Tab.2, Fig.4B, $X^2 = 0.2$, df = 2, p = 0.894, n=6).

Effects of moderate (3 ATA) LFP on total cell densities

In contrast to the decrease in neuron-specific densities, we observed an increase in total nuclei density in the temporal cortex: + 39 %, 1905 [1766-2302] nuclei per mm2 in control animals vs 3107 [2692-4156] nuclei per mm² after LFP-3ATA (Tab.2, Fig.2B, $X^2 = 6.6$, df = 2, p = 0.036, n=6). Total cellular density was also increased in the thalamus: +31%, 1617 [1545-1724] nuclei per mm2 in control animals vs 2338 [2017-2461] nuclei per mm² after LFP-3ATA (Tab.2, Fig.2C, $X^2 = 6.7$, df = 2, p = 0.035,). A similar effect was evident in area CA3 of the hippocampus: +29%, 3075 [2873-3215] nuclei per mm^2 in control animals vs 4304 [3892-4760] nuclei per mm² after LFP (Tab.2, Fig.3B, $X^2 = 11.8$, df = 2, p = 0.003); and in the Hilus: +26%, 2759 [2647-3266] nuclei per mm^2 in control animals vs 3713 [3430-3957] nuclei per mm² after LFP (Tab.1, Fig.4B, $X^2= 6.3$, df = 2, p = 0.042). Statistical significance of the Wilcoxon rank sum test used for post hoc analysis was impacted by an important data dispersion, and did not reach significance in the temporal cortex (p=0.06), the thalamus (p=0.14), and the hilus (p=0.27). No significant difference in total cellular density was observed in other hippocampal areas: CA1 2746 [2404-4605] vs 2718 [2672-4453] nuclei per mm^2, (Tab.2, Fig. 3A), dentate gyrus 5544 [5237-6001] vs 6291 [5622-6826] nuclei per mm^2 (Tab.2, Fig. 4A) or in impacted cortex 2218 [2078-2380] vs 2293 [2225-2395] nuclei per mm^2 (Tab.2, Fig2A).

Effects of severe (3.8 ATA) LFP

We did not find any significant differences between moderate LFP (3 ATA)and severe LFP (3.8 ATA) neither in neuronal density: Temporal cortex (369 [329-399] moderate LFP vs 283 [221-316] neurons per mm^2 severe LFP, p=0.83), thalamus (131 [56-209] moderate LFP vs 62 [54-124] neurons per mm^2 severe LFP, p=0.89) ; nor in total nuclei density : Temporal cortex (3107 [2692-4156] moderate LFP vs 2772 [2440-4052] nuclei per mm^2 severe LFP, p=1), thalamus (2338 [2017-2461] moderate LFP vs 2753 [2216-3099] severe LFP, p=0.69), CA3 (4304 [3892-4760] moderate LFP vs 4843 [4585-5106] severe LFP, p=1) and hilus (3713 [3430-3957] moderate LFP vs 4668 [3629-5213] severe LFP, p=0.894). Therefore, the pattern of neuronal loss was similar after moderate or severe LFP although a non-significant trend for reduced neuronal densities was apparent after severe LFP.

Measurements of cortical and hippocampal surface

Neuronal loss in a given brain structure is not only dependent on neuronal density but also on its volume. This is especially important in the hippocampus and in the impacted cortex in which neuronal density was not significantly affected. We therefore measured the surface of these brain structures on our slices using the images of whole brain sections provided by the slide scanner. For the parietal cortex, the surface was defined by the cortical thickness measured between pia mater and corpus callosum, multiplied by 4.7mm (i.e. the width of the cortex impacted by LFP). For the hippocampus, we measured the total surface of the whole hippocampal formation encompassing areas CA1 to CA3 and dentate gyrus.

We found no significant changes in the impacted cortex (controls: 5.6 mm^2 [5.35 – 7.06]; 3 ATA: 6.49 mm^2 [5.93 – 6.70]; 3.8 ATA: 4.91 mm^2 [4.65 – 5.13]; Kruskal-Wallis chi-squared = 3.1696, df = 2, p-value = 0.20) or in the hippocampus (controls: 4.38 mm^2 [3.90 – 4.79]; 3 ATA: 4.94 mm^2 [443 - 534]; 3.8 ATA: 4.16 mm^2 [3.79 – 4.65]; Kruskal-Wallis chi-squared = 2.6784, df = 2,

p-value = 0.2621). Therefore, in the impacted cortex, area CA1 of the hippocampus, dentate gyrus and hilus, in which neuronal density was not significantly affected, the surface of the tissue was not significantly affected either, suggesting that neuronal loss was not present in these structures.

Discussion

In this study, we observed a significant reduction in neuronal density following moderate or severe LFP injury in the temporal cortex located lateral to the impact, in the ipsilateral dorsal thalamus, and in area CA3 of the ipsilateral hippocampus. Surprisingly, the impacted cortex, area CA1 of the hippocampus, dentate gyrus and hilus were not affected by LFP, neither in neuronal density, nor in the overall surface of the structure. Overall, the spatial organization of the brain lesions detected after moderate or severe LFP can be represented as a line extending from the dorsal thalamus to the temporal cortex (primary somatosensory cortex and secondary auditory cortex) and encompassing area CA3 of the hippocampus (Fig. 5). The pattern of these lesions, and the observed decreases in neuronal density, were not different between the moderate and the severe LFP. The relative simplicity of our automated procedure allowed us to sample seven brain regions, which represented approximately two square millimeters of grey matter in the rat brain, providing one of the most extensive quantification of neuronal death following experimental traumatic brain injury.

We have chosen the anatomical plane of interest based upon the knowledge of the location of the maximum of neuronal lesions following LFP injury (Hicks et al., 1996). Surprisingly, while differences between sham and LFP animals were evidenced, no decrease of neuronal density was observed in the severe in comparison to moderate LFP injury animals. The LFP threshold intensity at which such lesions appear is therefore below 3 ATA and it would interesting to investigate whether mild TBI could also induce significant decreases in neuronal densities. It should be noted, however, that severe LFP might have induced greater neuronal loss in adjacent and remote anatomical planes. In addition, our study was limited to the quantification of neuronal densities, which appeared to be affected only on the side of the brain ipsilateral to LFP. It is

possible that more diffuse lesions such as edema, axonal injuries or white matter lesions could also be present on the contralateral side of the brain. These issues warrant clarifications in further studies.

Several other studies have estimated the extent of neuronal loss in the brain of rats subjected to LFP. These efforts have primarily utilized two strategies that either assess the number of injured neurons or quantify the density of remaining neurons in different brain regions at a given time following injury. Injured neurons can be identified by staining brain sections with Nissl stains (Hicks et al., 1996), hematoxylin and eosin (Bentzer et al 2001; Zhang et al., 1998), acid fuchsin (Hicks et al 1996), Fluoro-Jade C (Kabadi et al., 2014b; Sato et al., 2001), or by performing TUNEL labeling (Raghupathi et al., 2002). Hematoxylin and eosin (H&E), as well as Nissl stains label all cells, and degenerating neurons can be detected based on cell shrinkage and hyperchromatism (pyknosis), as well as by vacuolation of the cytoplasm. However, these methods can easily produce false positives or fail to detect degenerating neurons (Schmued et al., 1997). Fluoro jade-C is currently regarded to be a superior method for detecting degenerating neurons, although the mechanism by which this reagent labels injured cells is unknown, and there is a debate regarding whether all Fluoro-Jade positive neurons ultimately die, or if some may recover (Schmued et al., 1997; 2005). Moreover, only a few dying neurons are usually detected in each section at a given time, and the significance of such small numbers of labeled neurons in a given brain structure is difficult to interpret. Thus, quantifying the overall neuronal density, using various staining methods, several days after injury appears to be the best strategy, as it directly estimates the extent of accumulated neuronal death. Neuronal density is typically assessed by manual cell counts in brain sections (Sanderson et al 1999; Cheney et al., 2000; Enomoto et al., 2005; Witgen et al., 2005), sometimes followed by stereological reconstruction of

the brain structure (Grady et al., 2003; Selwyn et al., 2013; Luo et al., 2013), However, these techniques are slow and time-consuming.

Neuronal loss following experimental TBI has been investigated using both of these strategies, i.e., the labeling of dying neurons (Hicks et al., 1996; Kabadi et al., 2014b; Sato et al., 2001) or the manual counting of remaining neurons (Grady et al., 2003; Zhang et al., 1998; Selwyn et al., 2013; Luo et al., 2013). Overall, loss of neurons following TBI induction by LFP has consistently been observed in the temporal cortex (Hicks et al.,1996; Kabadi et al., 2014b; Sato et al., 2001; Raghupathi et al., 2002; Bentzer et al 2001; Bao et al., 2012; Zhang et al., 1998), thalamus (Hicks et al.,1996; Kabadi et al., 2014b; Sato et al., 2001; Luo et al., 2013) , and area CA3 of the hippocampus (Hicks et al., 1996; Kabadi et al 2014b; Grady et al., 2003; Sato et al., 2001; Zhang et al., 1998; Sanderson et al., 1999; Luo et al., 2013). However, several differences should be noted between our findings and those of earlier studies. For example, neuronal loss in the hippocampus sometimes encompasses area CA1 (Sato et al., 2001), CA2 (Grady et al., 2003; Luo et al., 2013), dentate gyrus (Kabadi et al., 2014b; Luo et al., 2013), and/or hilus (Hicks et al., 1996; Grady et al., 2003), which were not affected in our study. We should note that neuronal loss in these hippocampal areas was observed in Sprague-Dawley rats, whereas the present work was performed in Wistar rats. It is possible that variation in the susceptibility of different rat strains can account for these discrepancies (Scheff and Sullivan 1999; Fujimoto et al., 2004). For example, different strains of mice can display different levels of excitotoxic cell death following kainic acid infusion or different inflammatory responses to ischemia (Steward et al., 1999). Such strain discrepancies could potentially have important implications for the reproducibility of neurodegeneration following TBI. Another matter of debate is the existence of neuronal loss in the impacted cortex, which comes into contact with the water column that transmits the percussion wave. While most studies, including ours, report no

overt neuronal injury at this site (Hicks et al., 1996; Sato et al., 2001; Gradi et al., 2003; Sato et al., 2001; Raghupathi et al., 2002; Bentzer et al., 2001; Sanderson et al., 1999), others indicate significant neuronal loss (Kabadi et al., 2014b; Shultz et al., 2013; Luo et al., 2013). The LFP protocol has the potential to induce direct damage at the percussion site, which could include subarachnoid hemorrhage or tearing of the dura that could produce neuronal injury immediately underneath the water column in a non-reproducible manner. In our hands, however, LFP did not produce cortical cavitation that would suggest *dura mater* lesion and water intrusion into the cortex, and neuronal loss was not detectable in the impacted region.

Some hallmarks of neuronal lesions following experimental TBI using LFP are their widespread nature, and the fact that the most severe neuronal loss appears in brain regions that are remote from the site of impact (Hicks et al 1996). This pattern of damage likely reflects the complexity of the forces that are transmitted through the brain parenchyma following percussion. It is possible, for example, that the impacted cortex is subjected mostly to a compression-decompression wave at the time of the impact of the fluid column, while remote sites such as the temporal cortex or the thalamus suffer from shear stress that could be more destructive for neuronal cells. The temporal cortex may also impact the skull bone in response to the percussion wave. The exact nature of the forces that are transmitted within the brain parenchyma remains poorly understood. However, it seems likely that the brain regions in which maximal neuronal loss is detected seven days following LFP are also those with maximal primary injury immediately after the percussion. Additionally, subsequent inflammation could develop at the site of primary injury and aggravate neuronal loss over time (secondary injury) (Kumar and Loane 2012).

In support of an important role for inflammation in post-LFP neuronal loss, we detected a significant increase in the total number of nuclei, which was correlated with decreased NeuN-

positive cellular density, in the temporal cortex and in area CA3 of the hippocampus following both moderate and severe LFP. This increase in non-neuronal cellular density likely reflects gliosis and inflammation in these brain regions. In fact, Selwyn et al (2013) found that microglial invasion was associated with astrocyte activation in these regions following LFP injury . The precise function of inflammation in the context of traumatic brain injury is still a topic of much debate and interest, but a number of studies agree that reducing the release of pro-inflammatory molecules like interleukin 1β (IL1β), or blocking proteins pertaining to inflammatory cascades, such as extracellular-regulated kinase 1/2 (ERK 1/2) or cyclin-dependent kinases (CDKs), can be beneficial to brain recovery (Kabadi et al., 2014b; Schultz et al., 2013; Sanderson et al., 1999; Tsai et al., 2014).

We conclude that our automated method for rapid quantifications of neuronal density in brain sections is a powerful tool for determining the extent of neuronal loss following experimental TBI in a rodent model. This is especially valuable given the widespread nature and the complex spatial pattern of these lesions. This work extends our understanding of the neuronal lesions produced by moderate to severe LFP injury by identifying a pattern of neuronal loss extending from the dorsal thalamus to the temporal cortex and indicating maximal injury deep in the cerebral parenchyma rather than in superficial structures directly impacted by the shockwave. These data pave the way for more efficient and rapid preclinical testing of neuroprotective treatments in the context of TBI in model animals.

Acknowledgements: We are grateful to Caroline Woeffler-Maucler and Estelle Enriquez for helpful technical assistance. Anne Beghin and the Centre d'Imagerie Quantitative Lyon-Est (CIQLE) were instrumental in developing the macro for the automatic quantification of neuronal density. We are also indebted to the Animalerie Rockefeller for animal care. This study was

supported by the Lyon Neuroscience Research Center, Inserm U1028, and CNRS UMR 5292, as well as by financial support from Fondation Les Gueules Cassées (contract FGC-11-2013). BB was supported by Ecole de l'Inserm Liliane Bettencour and HCL. Lionel Bapteste was a recipient of a fellowship from HCL (année recherche). The Lyon Neuroscience Research Center is part of the Structure Fédérative de Recherche Lyon-Est (SFR Lyon-Est, Inserm US7, CNRS UMS 3453).

Author Disclosure Statement: No competing financial interests exist.

Authors' contributions: All authors had full access to the data in the study and take responsibility for the integrity and the accuracy of the data analysis. Study concept and design: Thomas Lieutaud, Stéphane Marinesco. Acquisition, analysis and interpretation of data: Baptiste Balança , Lionel Bapteste, Rainui Guy, Denis Ressnikoff. Statistical analysis: Baptiste Balança. Drafting of the manuscript: Baptiste Balança, Thomas Lieutaud and Stéphane Marinesco. Critical revision of the manuscript for important intellectual content: Lionel Bapteste, Laurent Bezin and Denis Ressnikoff. Obtained funding: Baptiste Balança, Thomas Lieutaud and Stéphane Marinesco. Study supervision: Thomas Lieutaud and Stéphane Marinesco

References

Aoyama, N., Lee, S.M., Moro, N., Hovda, D.A., and Sutton, R.L. 2008. Duration of ATP reduction affects extent of CA1 cell death in rat models of fluid percussion injury combined with secondary ischemia. Brain Res. 1230: 310–319.

Bao, F., Shultz, S.R., Hepburn, J.D., Omana, V., Weaver, L.C., Cain, D.P., and Brown, A. 2012. A CD11d monoclonal antibody treatment reduces tissue injury and improves neurological outcome after fluid percussion brain injury in rats. J. Neurotrauma 29: 2375–2392.

Bentzer, P., Mattiasson, G., McIntosh, T.K., Wieloch, T., and Grande, P.O. 2001. Infusion of prostacyclin following experimental brain injury in the rat reduces cortical lesion volume. J. Neurotrauma 18: 275–285.

Cheney, J.A., Brown, A.L., Bareyre, F.M., Russ, A.B., Weisser, J.D., Ensinger, H.A., Leusch, A., Raghupathi, R., and Saatman, K.E. 2000. The novel compound LOE 908 attenuates acute neuromotor dysfunction but not cognitive impairment or cortical tissue loss following traumatic brain injury in rats. J. Neurotrauma 17: 83–91.

Enomoto, T., Osugi, T., Satoh, H., McIntosh, T.K., and Nabeshima, T. 2005. Pre-Injury magnesium treatment prevents traumatic brain injury-induced hippocampal ERK activation, neuronal loss, and cognitive dysfunction in the radial-arm maze test. J. Neurotrauma 22: 783–792.

Fujimoto, S.T., Longhi, L., Saatman, K.E., Conte, V., Stocchetti, N., and McIntosh, T.K. 2004. Motor and cognitive function evaluation following experimental traumatic brain injury. Neurosci. Biobehav. Rev. 28: 365–378.

Grady, M.S., Charleston, J.S., Maris, D., Witgen, B.M., and Lifshitz, J. 2003. Neuronal and glial cell number in the hippocampus after experimental traumatic brain injury: analysis by stereological estimation. J. Neurotrauma 20: 929–941.

Hicks, R., Soares, H., Smith, D., and McIntosh, T. 1996. Temporal and spatial characterization of neuronal injury following lateral fluid-percussion brain injury in the rat. Acta Neuropathol. (Berl.) 91: 236–246.

Kabadi, S.V., Stoica, B.A., Loane, D.J., Luo, T., and Faden, A.I. 2014a. CR8, a novel inhibitor of CDK, limits microglial activation, astrocytosis, neuronal loss, and neurologic dysfunction after experimental traumatic brain injury. J. Cereb. Blood Flow Metab. 34: 502–513

Kabadi, S.V., and Faden, A.I. 2014b. Neuroprotective strategies for traumatic brain injury: improving clinical translation. Int. J. Mol. Sci. 15: 1216–1236.

Kumar, A., and Loane, D.J. 2012. Neuroinflammation after traumatic brain injury: opportunities for therapeutic intervention. Brain. Behav. Immun. 26: 1191–1201.

Levine, B., Kovacevic, N., Nica, E.I., Cheung, G., Gao, F., Schwartz, M.L., and Black, S.E. 2008. The Toronto traumatic brain injury study: Injury severity and quantified MRI SYMBOL. Neurol. March 4 2008 70: 771–778.

Li, H.H., Lee, S.M., Cai, Y., Sutton, R.L., and Hovda, D.A. 2004. Differential gene expression in hippocampus following experimental brain trauma reveals distinct features of moderate and severe injuries. J. Neurotrauma 21: 1141–1153.

Luo, T., Wu, J., Kabadi, S.V., Sabirzhanov, B., Guanciale, K., Hanscom, M., Faden, J., Cardiff, K., Bengson, C.J., and Faden, A.I. 2013. Propofol Limits Microglial Activation after Experimental Brain Trauma through Inhibition of Nicotinamide Adenine Dinucleotide Phosphate Oxidase: Anesthesiology 119: 1370–1388.

Mathé, J.-F., Richard, I., and Rome, J. 2005. Santé publique et traumatismes crâniens graves. Aspects épidémiologiques et financiers, structures et filières de soins. Ann. Fr. Anesth. Réanimation 24: 688–694.

Maxeiner S, Glassmann A, Kao HT, Schilling K. 2014. The molecular basis of the specificity and cross-reactivity of the NeuN epitope of the neuron-specific splicing regulator, Rbfox3. Histochemistry and cell biology 141(1):43-55.

McIntosh, T.K., Vink, R., Noble, L., Yamakami, I., Fernyak, S., Soares, H., and Faden, A.L. 1989. Traumatic brain injury in the rat: characterization of a lateral fluid-percussion model. Neuroscience 28: 233–244.

Paxinos, G., and Watson, C. 2005) The rat brain in stereotaxic coordinates, 5th ed. Elsevier Academic Press.

Raghupathi, R., Conti, A.C., Graham, D.I., Krajewski, S., Reed, J.C., Grady, M.S., Trojanowski, J.Q., and McIntosh, T.K. 2002. Mild traumatic brain injury induces apoptotic cell death in the cortex that is preceded by decreases in cellular Bcl-2 immunoreactivity. Neuroscience 110: 605–616.

Sanderson, K.L., Raghupathi, R., Saatman, K.E., Martin, D., Miller, G., and McIntosh, T.K. 1999. Interleukin-1 Receptor Antagonist Attenuates Regional Neuronal Cell Death and Cognitive Dysfunction After Experimental Brain Injury. J. Cereb. Blood Flow Metab. 19: 1118–1125.

Sato, M., Chang, E., Igarashi, T., and Noble, L.J. 2001. Neuronal injury and loss after traumatic brain injury: time course and regional variability. Brain Res. 917: 45–54.

Selwyn, R., Hockenbury, N., Jaiswal, S., Mathur, S., Armstrong, R.C., and Byrnes, K.R. 2013. Mild Traumatic Brain Injury Results in Depressed Cerebral Glucose Uptake: An 18FDG PET Study. J. Neurotrauma 30: 1943–1953.

Shultz, S.R., Bao, F., Weaver, L.C., Cain, D.P., and Brown, A. 2013. Treatment with an anti-CD11d integrin antibody reduces neuroinflammation and improves outcome in a rat model of repeated concussion. J. Neuroinflammation 10(26).

Scheff, S.W., and Sullivan, P.G. 1999. Cyclosporin A significantly ameliorates cortical damage following experimental traumatic brain injury in rodents. J. Neurotrauma 16: 783–792.

Schmued, L.C., Albertson, C., and Slikker Jr., W. 1997. Fluoro-Jade: a novel fluorochrome for the sensitive and reliable histochemical localization of neuronal degeneration. Brain Res. 751: 37–46.

Steward, O., Schauwecker, P.E., Guth, L., Zhang, Z., Fujiki, M., Inman, D., Wrathall, J., Kempermann, G., Gage, F.H., Saatman, K.E., Raghupathi, R., and McIntosh, T. 1999. Genetic approaches to neurotrauma research: opportunities and potential pitfalls of murine models. Exp. Neurol. 157: 19–42.

Schmued, L.C., Stowers, C.C., Scallet, A.C., and Xu, L. 2005. Fluoro-Jade C results in ultra high resolution and contrast labeling of degenerating neurons. Brain Res. 1035: 24–31.

Tsai, Y.-T., Wang, C.-C., Leung, P.-O., Lin, K.-C., Chio, C.-C., Hu, C.-Y., and Kuo, J.-R. 2014. Extracellular signal-regulated kinase 1/2 is involved in a tamoxifen neuroprotective effect in a lateral fluid percussion injury rat model. J. Surg. Res. 189: 106–116.

Witgen, B.M., Lifshitz, J., Smith, M.L., Schwarzbach, E., Liang, S.-L., Grady, M.S., and Cohen, A.S. 2005. Regional hippocampal alteration associated with cognitive deficit following experimental brain injury: a systems, network and cellular evaluation. Neuroscience 133: 1–15.

Woeffler-Maucler, C., Beghin, A., Ressnikoff, D., Bezin, L., and Marinesco, S. 2014. Automated immunohistochemical method to quantify neuronal density in brain sections: Application to neuronal loss after status epilepticus. J. Neurosci. Methods 225: 32–41.

Xiong, Y., Mahmood, A., and Chopp, M. 2013. Animal models of traumatic brain injury. Nat. Rev. Neurosci. 14: 128–142.

Zhang, C., Raghupathi, R., Saatman, K.E., Smith, D.H., Stutzmann, J.-M., Wahl, F., and Mcintosh, T.K. 1998. Riluzole attenuates cortical lesion size, but not hippocampal neuronal loss, following traumatic brain injury in the rat. J. Neurosci. Res. 52: 342–349.

Figure legends

Figure 1. Imaging of a whole brain slice after LFP and locations of regions of interest (ROI) for neuron and total cell quantification. A. Fluorescence image of a whole brain slice after LFP, obtained with a slide scanner. NeuN appears in green and DAPI in blue. B. ROIs are displayed on a schematic brain section. The LFP impact site is represented as black arrows above the parietal associative cortex. (1) Impacted cortex (i.e. parietal associative cortex), (2) temporal cortex (i.e. somatosensory and auditory cortex), (3) dorsal thalamus, (4) CA1, (5) CA3, (6) dentate gyrus, and (7) hilus. Modified from Paxinos and Watson (2005).

Figure 2. Quantification of neuronal density in the impacted cortex and dorsal thalamus. (A) Impacted cortex: (A1) Control NeuN immunoreactivity, (A2) control DAPI staining, (A3) control merge, (A4) LFP NeuN immunoreactivity, (A5) LFP DAPI immunoreactivity, (A6) LFP merge, (A7) scatter-plots with bar-plots showing the results of neuronal (green) and total cellular density (blue) in control (n = 6), moderate (n=6) and severe (n=6) LFP animals. (B) Temporal cortex: B1-B7 are same condition as A1-A7, (C) Dorsal thalamus: C1-C7 same condition as A1-A7. Images are 760 μm × 760 μm. * represents a significant difference between control and LFP evidenced by pairwise comparisons using Wilcoxon rank sum test with bonferroni p value adjustment (when the Kruskal-Wallis ANOVA showed a significant effect)

Figure 3. Quantification of neuronal density in areas CA1 and CA3 of the hippocampus. (A) CA1: (A1) Control NeuN immunoreactivity, (A2) control DAPI staining, (A3) control merge, (A4) LFP NeuN immunoreactivity, (A5) LFP DAPI staining (A6) LFP merge, (A7) scatter-plots with bar-plots showing the results of neuronal (green) and total cellular density (blue) in control

(n = 6), moderate (n = 6) and severe (n=6) LFP animals. (B) CA3: B1-B7 same conditions as A1-A7. * represents a significant difference between control and LFP (see Fig.2).

Figure 4. Quantification of neuronal density in the dentate gyrus and the hilus. (A) Dentate gyrus: (A1) Control NeuN immunoreactivity, (A2) control DAPI staining, (A3) control merge, (A4) LFP NeuN immunoreactivity, (A5) LFP injury, DAPI staining (A6) LFP merge, (A7) scatter-plots with bar-plots showing the results of neuronal (green) and total cellular density (blue) in control (n = 6), moderate (n = 6) and severe (n=6) LFP animals. (B) Hilus: B1-B7 same conditions as A1-A7. * represents a significant difference between control and LFP (see Fig.2).

Figure 5. Anatomical extension of neuronal loss following LFP injury. The LFP impact site is represented as black arrows above the parietal associative cortex. The overall spatial organization of the brain lesions is demarcated as an area (light grey) spreading from the dorsal thalamus (62% neuron density decrease, left dark grey ROI) to the temporal cortex (60% neuron density decrease, right dark grey ROI) and which encompasses area CA3 of the hippocampus (36% neuron density decrease, middle dark grey ROI). Modified from Paxinos and Watson (2005)

Table 1: List of antibodies

Table2: Neuronal and total nuclei density, per mm², in control, moderate, and severe LFP-treated animals. Results are expressed as median and interquartile range (grey square denotes a significant effect of TBI versus control animals).

Table 1: list of antibodies

Antibody Name	Antigen	Description of Immunogen	Source, Host Species, Cat. #, Clone or Lot#, RRID	Dilution Used
Anti-NeuN, clone A60 antibody	NeuN	Purified cell nuclei from mouse brain	Merk Chemicon, mouse monoclonal IgG, Cat# MAB377, clone A60, RRID: AB_11210778	1:4000
Goat Anti-Mouse IgG (H+L) Antibody, Alexa Fluor 488 Conjugated	Mouse IgG (H+L)	Gamma Immunoglobins Heavy and Light chains	Molecular Probes (Invitrogen), goat polyclonal IgG, Cat# A-11001, lot#, RRID: AB_141367	1:1000

Table 2: Neuronal and total nuclei density, per mm², in control, moderate, and severe LFP-treated animals. Results are expressed as median and interquartile range (grey square denotes a significant effect of TBI versus control animals).

		Impacted Cortex	**Temporal cortex**	**Dorsal thalamus**	**CA3**	CA1	**Hilus**	Dentate gyrus
neurons (/mm²)	Control (n=6)	919 [804-1051]	929 [828-1032]	349 [328-391]	934 [908-1021]	1453 [1371-3240]	502 [441-624]	4012 [3861-4284]
	3 ATA (n=6)	901 [883-918]	369 [329-399]	131 [56-209]	592 [587-695]	1397 [1101-2667]	446 [383-465]	3810 [3627-4661]
	3,8 ATA (n=6)	1114 [943-1182]	283 [221-316]	62 [54-124]	901 [767-945]	1749 [1474-2768]	328 [220-444]	3803 [3627-4451]
total nuclei (/mm²)	Control (n=6)	2218 [2078-2380]	1905 [1766-2302]	1617 [1545-1724]	3075 [2873-3215]	2746 [2404-4605]	2759 [2647-3266]	5544 [5237-6001]
	3 ATA (n=6)	2293 [2225-2395]	3107 [2692-4156]	2338 [2017-2461]	4304 [3892-4760]	2718 [2672-4453]	3713 [3430-3957]	6291 [5622-6826]
	3,8 ATA (n=6)	2828 [2481-3225]	2772 [2440-4052]	2753 [2216-3099]	4843 [4585-5106]	3826 [2996-4366]	4668 [3629-5213]	5835 [5407-7460]

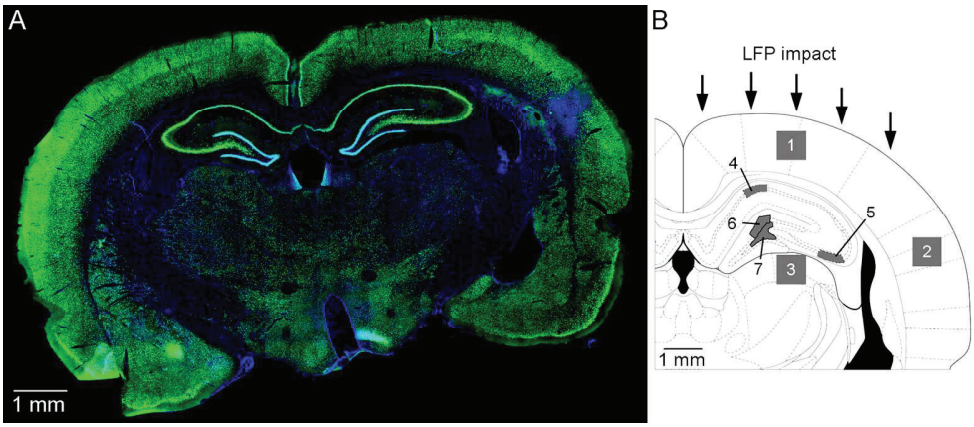

Figure 1. Imaging of a whole brain slice after LFP and locations of regions of interest (ROI) for neuron and total cell quantification. A. Fluorescence image of a whole brain slice after LFP, obtained with a slide scanner. NeuN appears in green and DAPI in blue. B. ROIs are displayed on a schematic brain section. The LFP impact site is represented as black arrows above the parietal associative cortex. (1) Impacted cortex (i.e. parietal associative cortex), (2) temporal cortex (i.e. somatosensory and auditory cortex), (3) dorsal thalamus, (4) CA1, (5) CA3, (6) dentate gyrus, and (7) hilus. Modified from Paxinos and Watson (2005).
179x76mm (270 x 270 DPI)

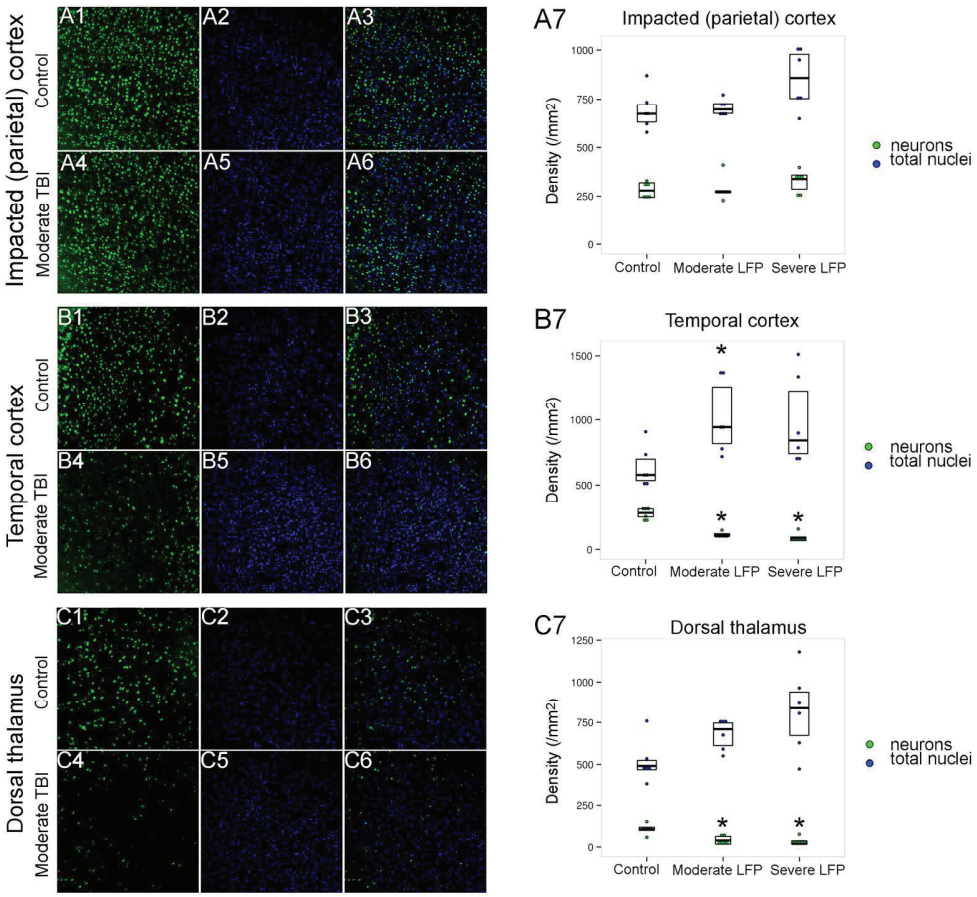

Figure 2. Quantification of neuronal density in the impacted cortex and dorsal thalamus. (A) Impacted cortex: (A1) Control NeuN immunoreactivity, (A2) control DAPI staining, (A3) control merge, (A4) LFP NeuN immunoreactivity, (A5) LFP DAPI immunoreactivity, (A6) LFP merge, (A7) scatter-plots with bar-plots showing the results of neuronal (green) and total cellular density (blue) in control (n = 6), moderate (n=6) and severe (n=6) LFP animals. (B) Temporal cortex: B1-B7 are same condition as A1-A7, (C) Dorsal thalamus: C1-C7 same condition as A1-A7. Images are 760 µm × 760 µm. * represents a significant difference between control and LFP evidenced by pairwise comparisons using Wilcoxon rank sum test with bonferroni p value adjustment (when the Kruskal-Wallis ANOVA showed a significant effect) 178x163mm (300 x 300 DPI)

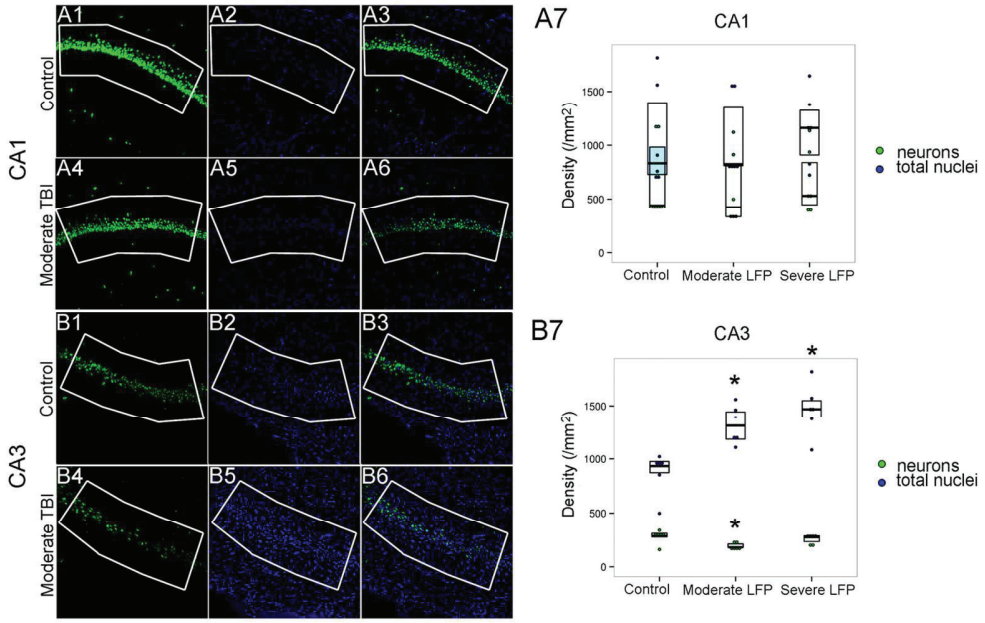

Figure 3. Quantification of neuronal density in areas CA1 and CA3 of the hippocampus. (A) CA1: (A1) Control NeuN immunoreactivity, (A2) control DAPI staining, (A3) control merge, (A4) LFP NeuN immunoreactivity, (A5) LFP DAPI staining (A6) LFP merge, (A7) scatter-plots with bar-plots showing the results of neuronal (green) and total cellular density (blue) in control (n = 6), moderate (n = 6) and severe (n=6) LFP animals. (B) CA3: B1-B7 same conditions as A1-A7. * represents a significant difference between control and LFP (see Fig.2).
125x80mm (300 x 300 DPI)

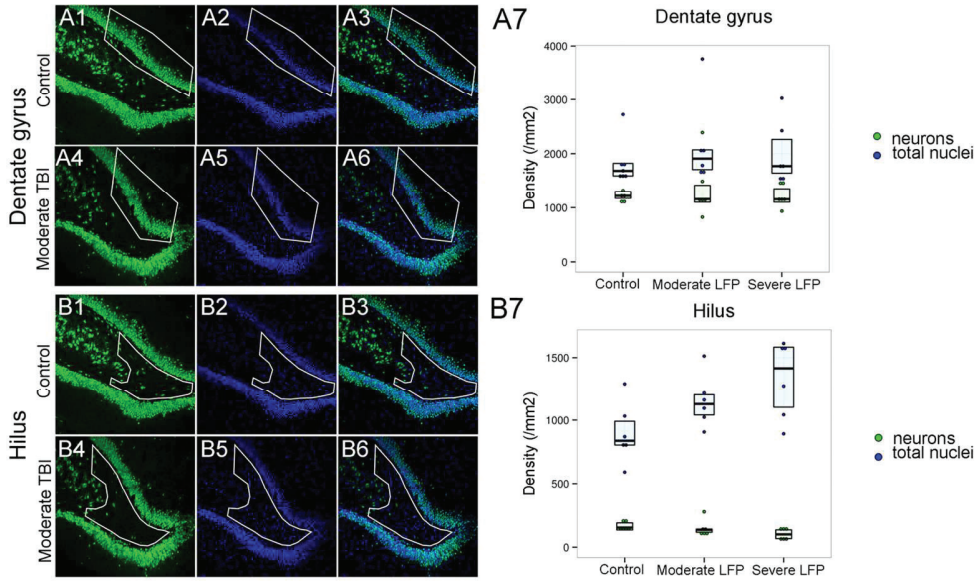

Figure 4. Quantification of neuronal density in the dentate gyrus and the hilus. (A) Dentate gyrus: (A1) Control NeuN immunoreactivity, (A2) control DAPI staining, (A3) control merge, (A4) LFP NeuN immunoreactivity, (A5) LFP injury, DAPI staining (A6) LFP merge, (A7) scatter-plots with bar-plots showing the results of neuronal (green) and total cellular density (blue) in control (n = 6), moderate (n = 6) and severe (n=6) LFP animals. (B) Hilus: B1-B7 same conditions as A1-A7. * represents a significant difference between control and LFP (see Fig.2).
122x74mm (300 x 300 DPI)

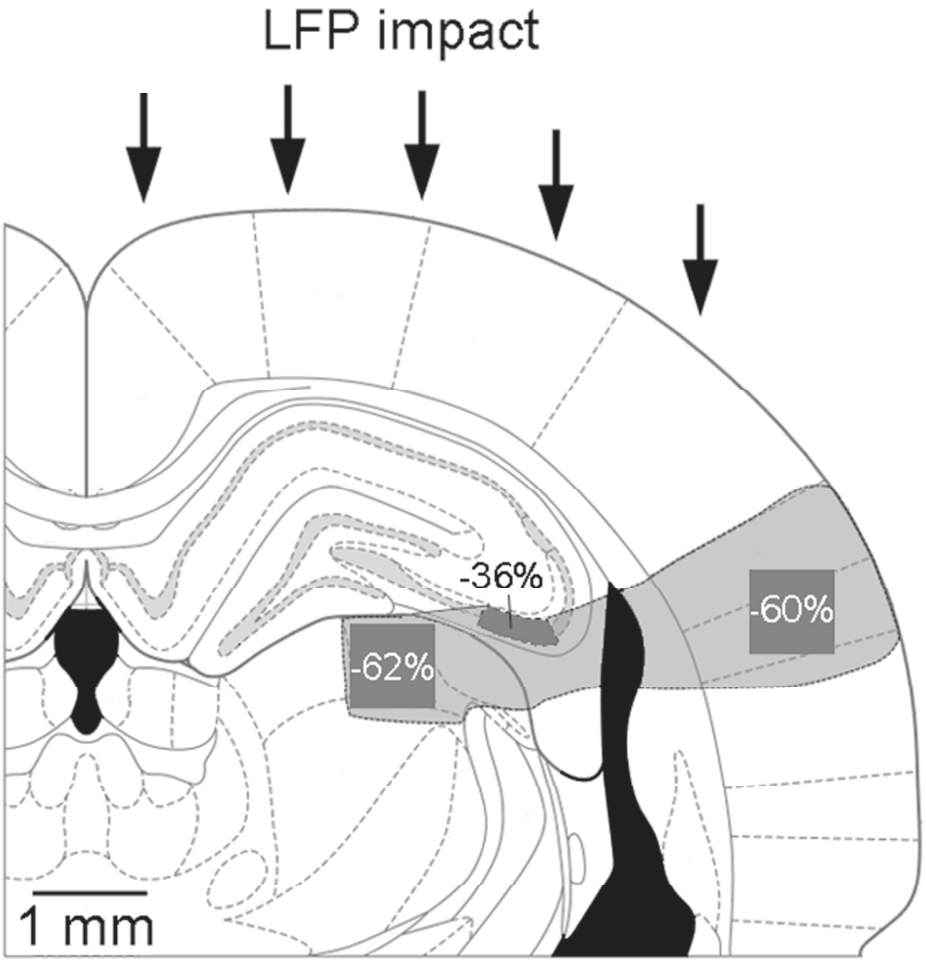

Figure 5. Anatomical extension of neuronal loss following LFP injury. The LFP impact site is represented as black arrows above the parietal associative cortex. The overall spatial organization of the brain lesions is demarcated as an area (light grey) spreading from the dorsal thalamus (62% neuron density decrease, left dark grey ROI) to the temporal cortex (60% neuron density decrease, right dark grey ROI) and which encompasses area CA3 of the hippocampus (36% neuron density decrease, middle dark grey ROI). Modified from Paxinos and Watson (2005)
55x56mm (300 x 300 DPI)

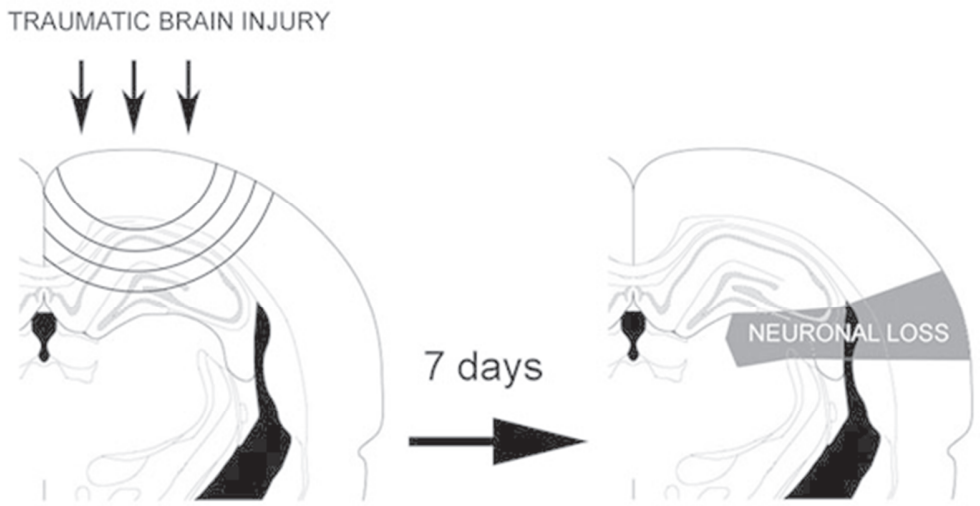

Moderate and severe traumatic brain injury administered by the lateral fluid percussion method result in a pattern of neuronal loss represented as a line extending from the dorsal thalamus to the temporal cortex (primary somatosensory cortex and secondary auditory cortex) and encompassing area CA3 of the hippocampus
200x149mm (72 x 72 DPI)

Moderate and severe traumatic brain injury administered by the lateral fluid percussion method result in a pattern of neuronal loss represented as a line extending from the dorsal thalamus to the temporal cortex (primary somatosensory cortex and secondary auditory cortex) and encompassing area CA3 of the hippocampus

Chapter 2

Glial modification

2.1 Methods

2.1.1 Animals

As a matter of conformity to the majority of TBI studies, and to prior results on glial modifications within our laboratory, these experiments have be conducted in Sprague Dawley instead of Wistar rats (250-400g) obtained from Elevage Harlan (Gannat, France). All experimental protocols were approved by the local committee on animals in research at the University Claude Bernard Lyon I (approval number: DR2014-31-V2 MESRverif), and were performed in accordance with European directive 2010/63/EU. There was no significant difference in body weight between control animals and those subjected severe LFPI.
During this experiment, we compare brain slices from control animals (without any surgery), to animals subjected to a severe LFPI (3.8ATA). As during the other experiments, animals were intubated prior to LFPI and ventilated until they recover sufficient spontaneous ventilation.
LFPI was performed as described in the methods part section 1.3, and animals received Buprenorphine 0.05 mg/kg twice at 12h interval after surgery.

2.1.2 Brain fixation and removal

Seven days after TBI, animals were deeply anesthetized with an intraperitoneal injection of sodium pentobarbital ($150 mg \cdot kg^{-1}$, Ceva®, Libourne, France) and intracardiacally perfused, first with 150 mL of a Ringer solution with 0.1% heparin at room temperature, then with 500 mL of an ice-cold fixative solution containing 4% freshly depolymerized para-formaldehyde (PFA) in 0.1 M phosphate buffer (PB) (pH = 7.4). The brains were removed, post-fixed for 2 hours in 4% PFA and placed in a 30% sucrose solution (PB, 0.1 M, pH = 7.4) for 48-72 h. Brains were then frozen in a solution of isopentane at -50^{o}C before storage at -80^{o}C for further analysis.

2.1.3 Glial cells labelling

Rat brains were cut frozen into 30 μm thick sections using a HM 500 OM microtome (Microm, Francheville, France), brain sections were placed in a solution of 10 mM phosphate buffer saline (PBS), then stored at -20^{o}C in an antifreeze buffer (buffer F in a mix of glycerol, ethylene glycol). Tissue was first rinsed in PBS for at least 5 hours, then permeabilized and saturated with a solution of PBS, 3% triton-X-100 (PBST) and 3% goat and donkey serum (Sigma-Aldrich, St Quentin Fallavier, France) for 2 hours. Brain sections were incubated overnight at 4^{o}C with a rabbit monoclonal antibody directed against the GFAP protein (diluted at 1:500, AB5804,

Millipore, Molsheim, France), and a mouse monoclonal antibody directed against the CD11b protein (diluted at 1:500, CBL1512Z, Millipore, Molsheim, France), in a solution of PBST and 3% goat and donkey serum.
After 3 washes with PBST for 10 min each, the sections were incubated overnight at 4^{o}C with a donkey anti rabbit IgG antibody coupled to Alexa fluor® 488 (diluted at 1:1500, A21206, Molecular Probes), and a goat anti mouse IgG antibody coupled to Alexa fluor® 633 (diluted at 1:1500, A21052, Molecular Probes), in a solution of PBST and 3% goat and donkey serum. Sections were washed for 10 min in PBST, and for 10 min in PBS. Then immobilized on pre-cleaned microscope slides (Ground Edges 90^{o}C, Menzel-glaser ®, Braunschweig, Germany) using tap water. Finally slides were mounted using Fluoroshield ™ with DAPI (Sigma-Aldrich, Saint-Quentin Fallavier, France) and stored at 4^{o}C C in the dark until confocal analysis.

2.1.4 Whole slide images

Imaging of whole brain sections was performed at the Cecil Imaging Facility (Université Claude Bernard Lyon 1, Lyon, France) using AXIO Scan.Z1 (Zeiss). We used a slide scanner with a 20× objective (NA: 0.8) and an Orca Flash 4.0 camera. Excitation and emission wavelengths were 353 nm and 465 nm for DAPI, 495 nm and 519 nm for Alexa fluor 488 and 650 nm and 673 nm for alexa fluor 633 respectively.

2.1.5 Confocal microscopy

Three brain regions with significant neuronal loss (i.e. temporal cortex, thalamus and CA3) were imaged with confocal microscopy to address glial morphology and density. Slides were imaged at the Cecil Imaging Facility using a Leica SP5 confocal laser-scanning microscope (CLSM) with a 40× objective (NA: 0.7). The images were acquired by a three-step process: positivity for DAPI was assessed at an excitation wavelength of 405 nm and emission wavelengths of 418-473 nm, while the signal for Alexa 488 (GFAP immunoreactivity) was assessed at an excitation wavelength of 488 nm and emission wavelengths of 510-613 nm, and Alexa 633 (CD11b immunoreactivity) at an excitation wavelength of 650 nm and emission wavelength of 650-750 nm. A z-series consisting of 10-15 optical sections, with a 1 μm interval, were imaged within each region of interest. Individual images were averaged two times for each fluorescent molecule.

2.2 Results

Using whole slide images we were able to describe a large overview of glial modification that occurs 7 days after LFPI. Subsequent confocal images give us sharper information about cells morphology, spatial organization and cell density. The present results are still qualitative and further analysis regarding glial cells counts and quantitative morphology assessment are ongoing. Nevertheless glial cells have clearly a different phenotype within the area where we observed neuronal loss, spreading from the thalamus to the temporal cortex (Fig 21).

2.2.1 Astrocyte modification

As NeuN fluorescence decreased (publication in chapter 1), GFAP over-expression spread also from the thalamus to the temporal cortex. However maximal over-expression took place at boundary layer mainly in the hemisphere under the shock (ipsilateral to the trauma). Indeed as white matter is mainly located between different structures, maximal GFAP expression occurs in the *corpus callosum* ipsilateral to the trauma, around the lateral ventricle. GFAP also

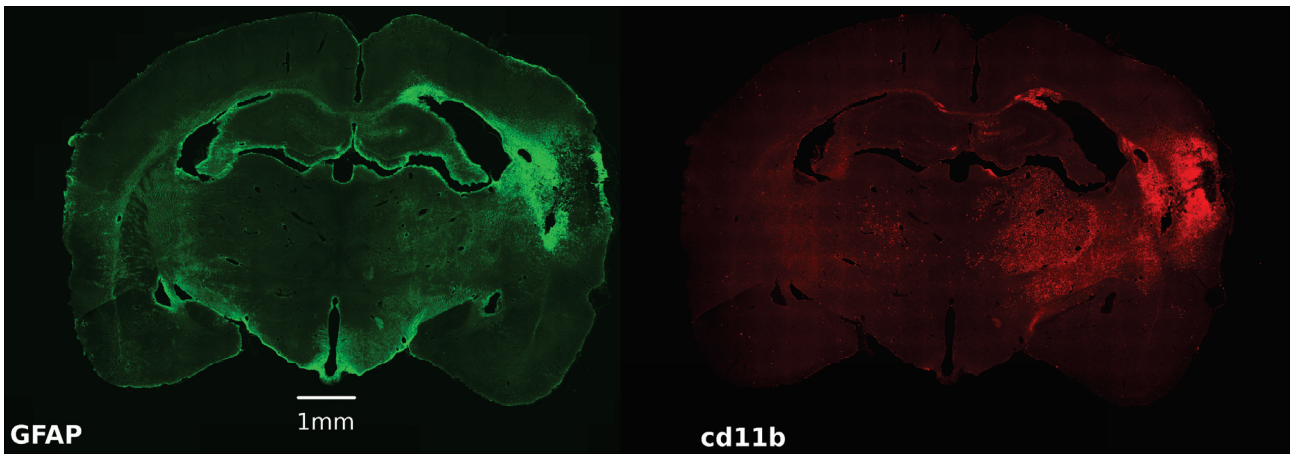

Figure 21: **Whole tissue section images of LFPI induce glial modifications**: Astrocyte are labelled in green using the GFAP, and microglia in red using the cd11b antigen

increased in the molecular layer of the CA1 area in the hippocampus, and the cortical grey matter surrounding the area of maximal neuronal loss. Noteworthy, no GFAP staining was displayed in the ROI where the neuronal loss was the worst. Conversely, within the temporal cortex astrocytes are also missing (Fig 22). The normal radial spatial organization that was observed in the cortex of control animals was completely loss in this area after LFPI (Fig 22). The closer to the core of the lesion, the more the architecture is altered with astrocyte loss. However we still need to quantify this astrocyte loss and address more precisely their morphology.
The contra-lateral hemisphere also displays smaller GFAP increases in the same areas (i.e. Temporal cortex, and white matter boundary layers, Fig 21 left image).

2.2.2 Microglia modification

It is well established that microglial form and function are inextricably linked. In recent years, the traditional view that microglial form ranges between "ramified resting" and "activated amoeboid" has been emphasized through advancing imaging techniques that point to microglial form being highly dynamic. Moreover, microglia adopt meaningful intermediate forms between categories, with considerable crossover in function and varying morphologies as they cycle, migrate, wave, phagocytose, and extend and retract fine and gross processes [138, 139].
Using confocal imaging we were able to evidence different morphological categories of microglia. In control animals the large majority was "resting" microglia with ramified fine processes and little peri-nuclear cytoplasm (Fig 22 left panel). Conversely, after a severe LFPI, the thalamus and CA3 had "bushy" and hypertrophied microglial cells, some of them unramified with an amoeboid shape. The temporal cortex that encompass maximal injury, presented a cluster of confluent unramified microglia. Such formation of rod-cells with possible cell fusion can be observed within necrotic foci of CNS parenchyma [347].
Like for astrocytes, microglial cells that over-express CD11b are not restricted to the area of neuronal loss. Maximal CD11b staining was present in the temporal cortex, the *corpus callosum* around lateral ventricle and in the thalamus ispilateral to the trauma (Fig 21, right image). Area CA3 also present activated microglia, as well as the medial part of CA1, hilus and the dentate gyrus.
A fewer amount of cells can be seen in the cotra-lateral hemisphere, namely in the thalamus and the *corpus callosum* (Fig 21, right image).

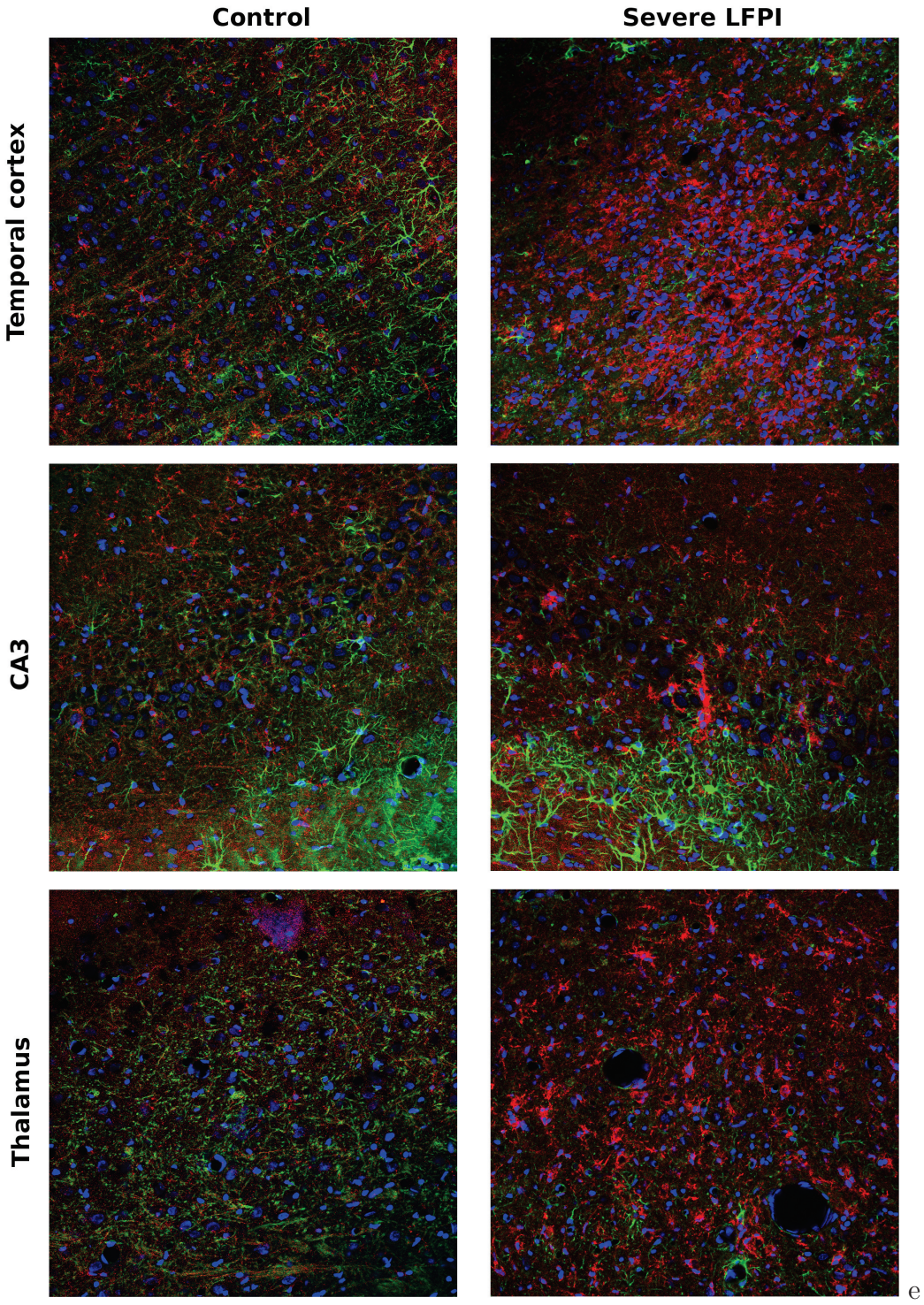

Figure 22: **whole tissue section images of LFPI induce glial modifications**: Merge images of astrocytes (green) using GFAP, microglia (red) using the cd11b antigen, and nuclei stained with DAPI (blue). Confocal microscopy images $375 \times 375 \mu m$, $40\times$ magnification, 1 μm optical section.

2.3 Conclusion

We described an extensive overview of neuronal loss and glial cell reactions after severe LFPI in adult rats. The most impacted area seven days after a severe LFPI, regarding neuronal loss, spread from the thalamus (-62% neurons) to the temporal cortex (-60% neurons) including the CA3 area of the hippocampus (-36% neurons). White matter seems also to be altered as describe by activated microglia and astrocytes locations in the *corpus callosum*. However we do have to quantify specifically this kind of injury in an ongoing study. Even if hippocampus did not present significant neuronal loss, it was infiltrated with activated microglia. This highlights that a probable aggression has occurred also in this structure.
The pressure wave generated by a severe LFPI did also reach the contra-lateral cortex. If neuronal density seems not to be affected, glial cells were activated in different part of the contra-lateral hemisphere. Further analysis are ongoing to precisely quantify astrocytic and microglial cell densities, and to depict microglial forms in the different cortical and sub-cortical area.

We have identified the area most impacted by severe LFPI and where the main neuronal loss occurs 7 days after the injury. However, as shown by Conti et al (1998), neuronal loss is a dynamic process that start at the temporal cortex within the 24 first hours post LFPI and last more than 2 weeks in other part of the brain [348].
We decided to study CSDs in this area which we consider to mimic the “traumatic penumbra”, compared to a normal cortex in health animals.
However, we had to characterize biosensors recordings validity in different ambient conditions, especially with regard to oxygen and temperature. This is an essential step to precisely use *in vitro* calibration for *in vivo* measurements interpretation.

Part V

Electrochemical measurement validation

Chapter 1

Micro-electrode biosensors

1.1 Biosensor manufacturing

Biosensors were made using a 25 mm diameter 90% Pt/10% Ir wire (Goodfellow, Huntington, U.K.) glued to a copper wire using conductive silver paint (Radiospares, Beauvais, France). The sensor wire was inserted into a pulled glass capillary (Harvard Apparatus, Edenbridge, U.K.), and the tip of the pipette was cut so the Pt wire extended from the glass approximately 100μm. The junction between the Pt and the pipette tip was sealed by locally melting the glass. The junction between the copper wire and the glass was sealed with epoxy resin (Araldite, Bostik, Paris, France). The electrodes were washed for 30 min in ethanol. A PPD screening layer was deposited by electropolymerization for 20 min in 100 mM PPD (Sigma-Aldrich) solution in 0.01 M PBS at pH 7.4 under a constant potential of +700 mV versus a Ag/AgCl reference electrode. The enzyme layer was deposited by dipping the Pt tip of the electrode in the enzyme solution (Fig 19).

Glucose oxidase (EC 1.4.3.11) from *Aspergillus niger* was purchased in powder form from Sigma-Aldrich (100-250 U/mg, Saint Quentin Fallavier, France). The final enzyme solution used for biosensor preparation contained 60 mg/mL glucose oxidase, 30 mg/mL bovine serum albumin (BSA) (Sigma), 10 $mg{\cdot}\,mL^{-1}$ poly(ethylene-glycol) diglycidyl ether (PEGDE) (Sigma-Aldrich), and 1% glycerol in PBS (0.01 M, pH 7.4). Immobilization methods involving PEGDE, was found to preserve the substrate specifcity compared to glutaraldehyde [131].

Lactate oxidase (EC 1.13.12.4) from *Pediococcus sp.* was purchased in powder form from Sigma-Aldrich ($\geq$ 20 $units{\cdot}\,mg^{-1}$, Saint Quentin Fallavier, France). The final enzyme solution used for biosensor preparation contained 60 $mg{\cdot}\,mL^{-1}$ lactate oxidase, 60 $mg{\cdot}\,mL^{-1}$ BSA (Sigma), 20 $mg{\cdot}\,mL^{-1}$ PEGDE, and 1% glycerol in PBS.

L-Glutamate oxidase (EC 1.4.3.11) from *Streptomyces sp.* X119- 6 was purchased from Yamasa Corporation (Choshi, Chiba, Japan). The working solution contained 57 mg/mL of the protein, 81 $mg{\cdot}\,mL^{-1}$ BSA, and 1% glycerol in PBS (0.01 M, pH 7.4). PEGDE (Sigma-Aldrich) was added to the enzyme aliquot prior to biosensor preparation.

Control sensors were treated using a BSA solution consisting of 400 $mg{\cdot}\,mL^{-1}$ BSA, 10 $mg{\cdot}\,mL^{-1}$ PEGDE, and 1% glycerol in PBS.

Glucose and lactate sensors were covered with an additional polyurethane membrane to increase their dynamic range and to protect the enzyme layer from biofouling in the brain. The tip of

the electrode was dipped three times in a 5% solution of polyurethane in THF (Sigma) with 10 min intervals between dips at room temperature to dry the layer.
Finally control, glucose and lactate electrodes were placed 2 h in an oven at 55^{o}C, and glutamate sensors 1h15 at 47^{o}C. Sensors were then stored at 4^{o}C for short term storage and at -20^{o}C for long term storage (delayed use).

1.2 Recordings set-up

All recordings were obtained using a VA-10 electrochemistry amplifier (NPI Electronics, Tamm, Germany) equipped with a two-electrode potentiostat. For *in vitro* experiments, analogue to digital conversions and data acquisitions were performed using a 16 bit USB-6221 acquisition board (National Instruments, Nanterre, France) controlled by home-made software based on Igor Pro 6.4 procedures (Wavemetrics, Eugene, OR). For *in vivo* experiments analogue to digital conversions and data acquisitions were performed using a 16 bit PowerLab 16/35 with Labchart 7 (ADInstrument, Oxford, United Kingdom).
The oxidation current was recorded at 1 kHz and averaged over 1000 data points, yielding a signal sampling frequency of 1 Hz. In vitro calibrations were performed in standard PBS (0.01 M, pH 7.4, at room temperature) solutions. The reference electrode was a chloride-treated silver wire (Ag/AgCl) placed directly in the recording chamber. Recordings were obtained using constant potential amperometry at +500 mV versus the Ag/AgCl reference electrode. Holding potentials between +500 and +700 mV are optimal for H_2O_2 detection [128].

Chapter 2

Biosensor reliability in changing conditions

Since biosensors are made using an oxidase, the signal relies on an oxygen dependent enzymatic reaction, with a subsequent H_2O_2 that is oxidized on the platinum surface (Fig 19). Therefore the oxidative current is the result of (1) the enzymatic oxidation and (2) the chemical H_2O_2 oxidation. As any chemical reaction, both oxidations should be dependent on the temperature in the medium. Furthermore, the enzymatic reaction rate (by the oxidase) will also depend on its substrates concentrations: That is to say oxygen and the molecule we want to detect.
Prior to each *in vivo* experiment, biosensors were calibrated *in vitro* to compute the relationship between oxidative current and substrate's concentration (glucose, lactate or glutamate) in the medium. However, both temperature and oxygen concentrations were different in PBS (used during the calibrations) and in the animal's brain (during experimentation). Therefore, we assessed how changes in temperature or oxygen concentrations modified constant potential amperometric measurements.

Biosensors were placed with a temperature and O_2 sensitive probe (OxyLab pO2^{TM}, Oxford Optronix, UK) in an airtight glass chamber filled with the enzyme substrate in PBS (i.e. 10μM glutamate, 500μM glucose or lactate; Fig 23). After signal stabilization, in the first part of the experiment the chamber's temperature rose from 5^{o}C to 40^{o}C during 1-2 hours (Fig 24A.). In a second part, at a constant temperature of 37^{o}C, N_2 was then bubbled to remove oxygen from the solution thus dropping 0_2 from ambient partial pressure (i.e. 21% atm $\equiv$ 159.6 mmHg) down to $<$ 5 mmHg, Fig 24B.).

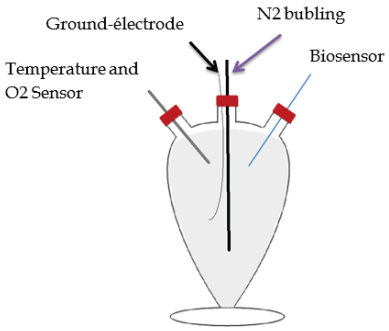

Figure 23: **Airtight glass chamber filled with the enzyme substrate in PBS.**
A temperature and O_2 sensitive probe was inserted on the left, a ground electrode and a tube for gas bubbling on the top, and a biosensor on the right. The device was immersed in a controlled temperature bath.

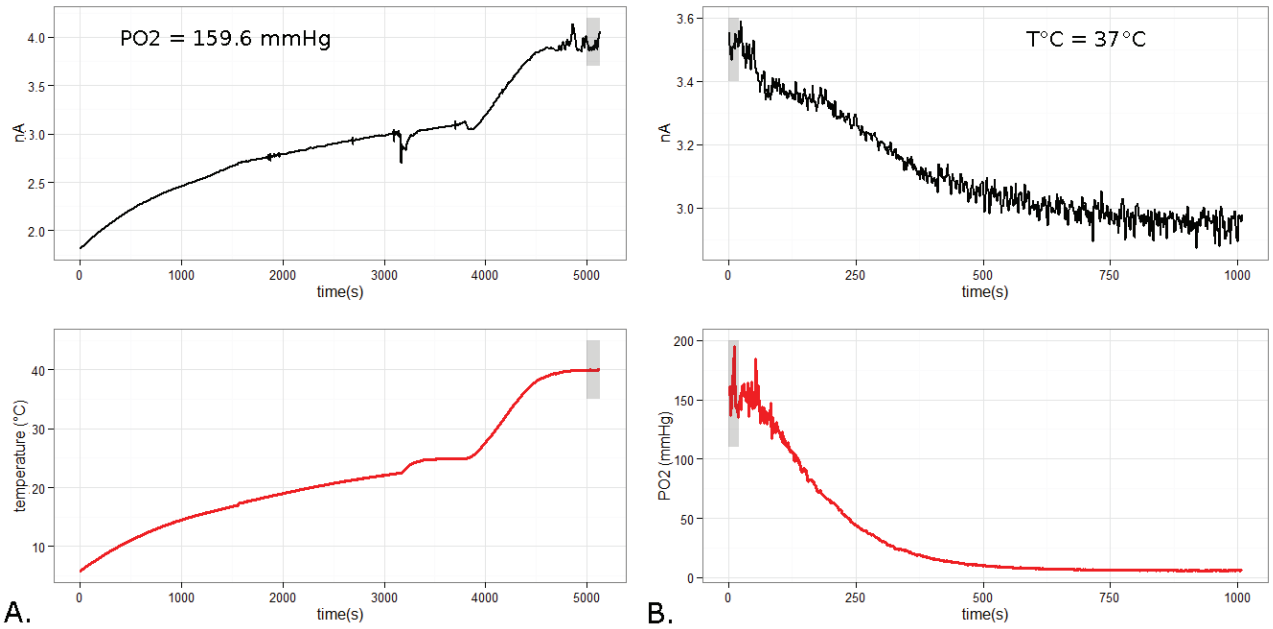

Figure 24: **raw data example of a lactate sensitive sensor during temperature and O_2 calibration.** The top black curve represent the oxidative current recorded from the biosensor. Beware of different scale between **A.** (1.5-4nA) and **B.** (2.8-3.6nA) chart. The red curve is either **A.** temperature (^oC) or **B.** oxygen partial pressure in the medium (mmHg) recorded by the Oxylab probe. Note how the oxidative current from the biosensor is increasing with temperature (indicating an increasing enzymatic reaction), and then decreasing with oxygen concentration. The gray boxes represent the values (i.e. oxidative current at $T^o = 40\ ^oC$ and $PO_2 = 159.6$ mmHg) that were used as references to compute oxygen or temperature dependency (equation (12)).

2.1 Effect of temperature variations on biosensors oxidative currents

Biosensors currents were recorded as the temperature rose slowly from $\approx 5^oC$ to 40^oC for 1-2 hours in a controlled temperature bath, at a given PO_2 (159.6 mmHg). Oxidative current was then related to the signal at 40^oC (Fig 24A, gray boxes), to compute in "R" a "normalized" percentage of variation (equation (12)).

$$\Delta\ Current(\%)_{temp/O_2} = \frac{(Current_{temp/O_2} - Current_{40^oC/159.6mmHg}) \times 100}{Current_{40^oC/159.6mmHg}} \tag{12}$$

Based on the shape of the relationship between ΔCurrent and temperature (Fig 25, left column), we first used a linear model to fit our data (i.e. $\Delta\ Current(\%)_{temp} = Slope \times Temperature + Intercept$). The lm() function (package stats) compute a linear least squares regression to estimate the best parameters of the linear model (i.e. intercept and slope). This linear model gives us good R^2 over 0.9 for glucose and glutamate sensors. Lactate sensor had a more heterogeneous reaction against temperature so that the model had worse goodness of fit (R^2=0.74). We tried to improve our models using a non-linear four parameters logistic model (equation (13)) meaning that ΔCurrent was less influenced by temperature at low and high temperature:

$$\Delta\ Current(\%)_{temp} = A + \frac{(B - A)}{1 + \exp((xmid - Temperature)/scal)} \tag{13}$$

Where A is the horizontal asymptote on the left side (low of temperature), B the horizontal asymptote on the right side (high temperature), *xmind* the temperature value at the inflection point of the curve, and *scal* a scale parameter on the temperature axis (The smaller one makes scal, the steeper the curve is at the inflection point). These parameters were estimated using the nls() function with a self-starting equation (SSfpl, package stat) that compute a non-linear least-squares regression.
The non-linear model validity was compared to the linear model by:

- An approximated R^2 as 1 minus the fraction of the residual sum of squares by the total sum of squares:

  $$R^2 = 1 - \frac{\sum residuals^2}{\sum(current\ -\ current\ mean)^2} \tag{14}$$

  However, it's not possible to calculate a valid R^2 for non-linear regressions. Unlike for linear regressions, the total sum of square is not equal to the regression sum of squares + the residual sum of square. Therefore R^2 can exceed 1 and do not always increase for better non-linear models. Thus we used 2 different methods to maximize the validity of the model: the Akaike's Information Criterion (AIC) and residuals graphical interpretation.

- AIC is a parameter that seeks a model that has a good fit to the truth (maximizing the $\log(Likelihood)$) but few parameters: $AIC = -2(\log(Likelihood)) + 2 \times K$, where K is the number of free parameters in the model. The lower the AIC the better the model fits the data [349].

- Finally, the best way to appreciate a model's goodness of fit is to visualize the residuals. We computed 2 residuals plots with the nlsResiduals() function (nlstools package): (1) the standardized residuals plot against the fitted values of ΔCurrent gives information about how the residuals behave. A random distribution that is expected will give a vertical homogeneous repartition of the residuals on both sides of the x-axis. (2) Minimizing the sum of the squared errors makes the assumption that residuals are normally distributed, which can be checked on the Q-Q plot (expected to have a linear shape).

Parameters	Glutamate oxidase	Glucose oxidase	Parameters	Lactate oxidase
A	-104.2	-92.2	Intercept	-76
B	52.6	57.5	Slope	1.9
Xmind	29.8	34.9		
scal	13	10.5		
R^2, linear model	0.93	0.91		0.74
AIC, linear model	92 525.21	190 599.2		225 335.5
R^2, logistic model	0.94	0.96		
AIC, logistic model	90 902.52	171 053.2		

Table 11: **Parameters of temperature dependency model** according to a logistic (13) or linear equation, for each enzyme. The model validity is evaluated as the R^2 (equation (14)), and the AIC: Akaike's Information Criterion.

The "R" scripts used to model ΔCurrent modifications against temperature and test models validities are as follow:

```
fit.ml<-lm(DeltaCurrent~temperature, data=DeltaCurrent.temp)
summary(fit.lm)
fit <- nls(DeltaCurrent~SSfpl(temperature, A, B, xmid, scal),data=
    DeltaCurrent.temp)
RSS <- sum(residuals(fit)^2) # Residual sum of squares
TSS <- sum((DeltaCurrent - mean(DeltaCurrent))^2) # Total sum of squares
r.squared <- 1 - (RSS/TSS)
AIC(fit, fit.lm) # Akaike's Information Criterion
Resuduals <- nlsResiduals(fit)
plot(Resuduals, which = 0) # 4 graphs of residuals
```

Glucose and glutamate biosensors had homogeneous reactions against temperature so that the R^2 were over 0.9 in both models. The four parameters logistic equation improved the model as shown by the decrease in the AIC as well as an increased R^2. Lactate oxidase covered biosensors had more heterogeneous reactions against temperature so that we were not able to evaluate a logistic equation. Residuals behave randomly with an even vertical distribution (Standardized residuals plot, Fig 25), and looks normally distributed on the Q-Q plot.
Estimated parameters values for each enzymatic layer (i.e. glucose oxidase, lactate oxidase or glutamate oxidase) are summarized in table 11, as well as the R^2 and the AIC of each model. Fig 25 displays the ΔCurrent modifications plotted against temperature (one color for each sensor, n=6), with the modeled data as a dashed black line.

2.2 Effect of oxygen concentration variations on biosensor oxidative current

The airtight chamber was then maintained at a constant temperature of 37^{o}C by the controlled temperature bath, and N_2 bubbling starts until PO_2 drop below 5 mmHg after around 20 min (Fig 24). Like for the temperature calibration, the percentage of current variation was compared to the one at 159.6 mmHg (ambient oxygen partial pressure: $1Atm \times 0.21 \equiv 760.001mmHg \times 0.21 \equiv 159.6mmHg$) using the same equation (12).

Parameters	Glutamate oxidase	Glucose oxidase	Lactate oxidase
Asym = 0			
R0	-72.2	-43.9	-21.8
Lrc	-2.9	-2.6	-3.17
R^2	0.93	0.72	0.82
AIC	47115.56	67488.09	47138.90
free Asym parameter			
Asym	-2.3	-2.7	-1.1
R0	-73.1	-46.2	-22.7
Lrc	-2.8	-2.42	-3.0
R^2	0.94	0.72	0.82
AIC	46953.77	67353.06	46956.33

Table 12: **Parameters of oxygen sensitivity model** according to the asymptotic equation (15) for each enzyme. The horizontal asymptote on the right side (Asym) was fixed to a null value

Based on the shape of the relationship between ΔCurrent and temperature (Fig 26), we chose an asymptotic equation to fit our data:

$$\Delta\ Current(\%) = Asym + (R0 - Asym) \times \exp(-\exp(lrc) \times PO_2) \tag{15}$$

Where *Asym* is the horizontal asymptote on the right side (high values of PO_2), *R0* the response when PO_2 is zero, *lrc* the natural logarithm of the rate constant. Since the value at 159.6 mmHg correspond to a ΔCurrent of 0%, *Asym* was set to 0%.
The nls() function was used to compute a non-linear least-squares regression to estimate these parameters. The starting values of R0 and lrc were respectively -50% and -3. We also tested the effect of leaving Asym as a free parameter and compared the two models with an approximated R^2, and the AIC. The "R" scripts used to model our data and test the goodness of fit were as follow:

```
fit1<-nls(DeltaCurrent ~ 0+(R0-0)*exp(-exp(lrc)*PO2), start=list(R0=-50,
    lrc=-3), data = DeltaCurrent.PO2)
fit1<-nls(DeltaCurrent ~ A+(R0-A)*exp(-exp(lrc)*PO2), start=list(R0=-50,
    lrc=-3, A=0), data = DeltaCurrent.PO2)
RSS <- sum(residuals(fit)^2) # Residual sum of squares
TSS <- sum((DeltaCurrent - mean(DeltaCurrent))^2) # Total sum of squares
r.squared <- 1 - (RSS/TSS)
AIC(fit1, fit2) # Akaike's Information Criterion
Resuduals <- nlsResiduals(fit1)
plot(Resuduals, which = 0) # 4 graphs of residuals
```

Leaving the Asym parameter free did not improve the R^2 and had a little effect on the AIC. Therefore we chose to keep the model with Asym set at 0%. Indeed an asymptote to 0% modification under high PO_2 is meaningful in order to use this model for *in vivo* currents correction.
Model's parameters were evaluated separately for each enzymatic layer (i.e. glucose oxidase, Lactate oxidase or glutamate oxidase) and are reported in table 12. The ΔCurrent modifications were plotted against PO_2 (one color for each sensor, n=6), with the modeled data (using

Asym=0) as a dashed black line (Fig 26, left column). Like for the temperature calibrations, model's validities were also evaluated using 2 residuals plots with the nlsResiduals() function (nlstools package, Fig 26 right column).
Every sensors had an asymptotic relation to PO_2, but they did not behave evenly as PO_2 goes down. Therefore glucose and lactate residuals were not as randomly distributed as those of temperature models. Conversely they were more widely distributed at low PO_2 (Fig 26 A and B).
Glutamate oxidase covered sensors had a more homogeneous reaction, so that residuals behave randomly across different PO_2 (Fig 26 C). However when we began bubbling of N_2 gas, it induced artifact that spread data at high PO_2. Consequently the residuals distribution was larger, but remains symmetric around the x-axis (Fig 26, C). These artifact were also present when we used glucose and lactate oxidase covered sensors, however their baseline signal was higher improving signal to noise ratio for the same artefact amplitude (Fig 24).

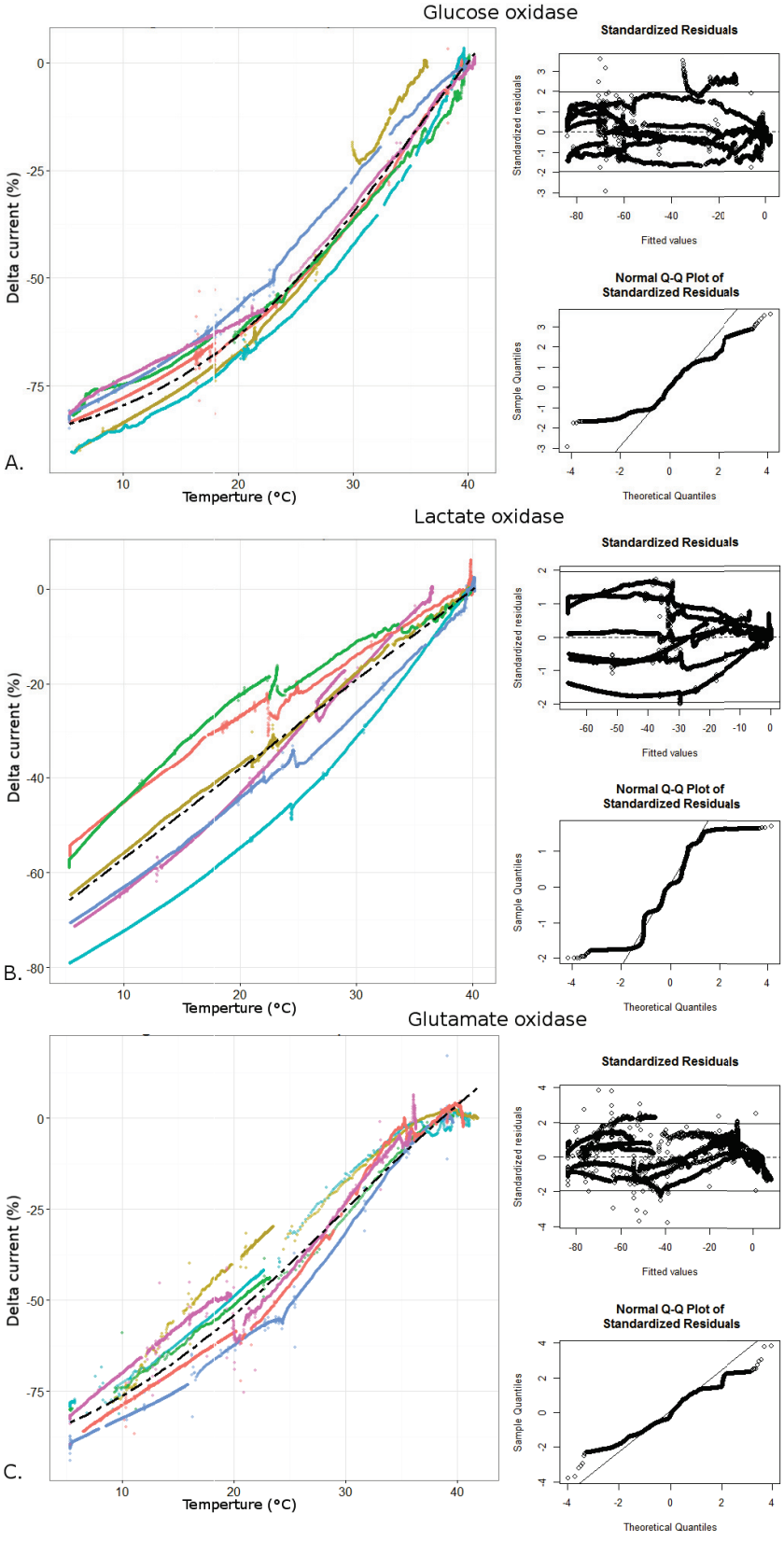

Figure 25: **Sensors temperature calibrations**: **Left column**: each panel plots the delta of currents (%, see equation (12)) against temperature, for a sensor type (A: Glucose oxidase, B: lactate oxidase and C: glutamate oxidase). 6 sensors were recorded for each sensor type and are plotted in different colors. Modeled data are represented as a dashed black line. **Right column**: 2 plots of model's residuals (i.e. standardized residuals against fitted values and normal Q-Q plot) are represented leftward from each corresponding sensor plot.

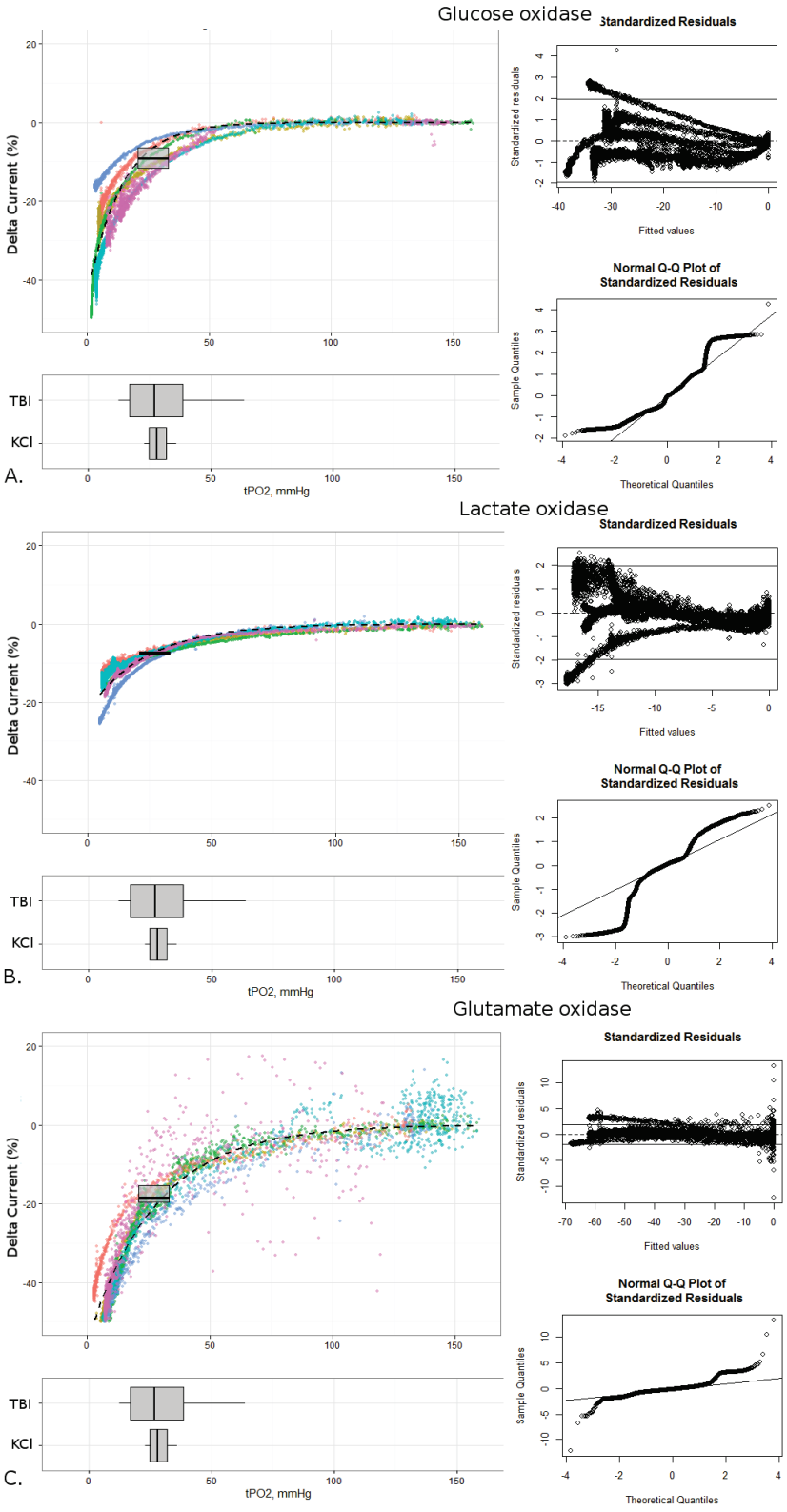

Figure 26: **Sensors PO_2 calibrations**: **Left column**: each panel plots the delta of currents (%, see equation (12)) against PO_2, for a sensor type (A: Glucose oxidase, B: lactate oxidase and C: glutamate oxidase). 6 sensors were recorded for each sensor type and are plotted in different colors. Modeled data are represented as a dashed black line. **Right column**: 2 plots of models residuals (i.e. standardized residuals against fitted values and normal Q-Q plot) are represented leftward from each corresponding sensor plot.
Box plots above each graphs represent the $PbtO_2$ recorded in anesthetized rats (KCl) or after sever LFPI (TBI). The box plot on the top of each graph represent the percentage of decrease at these $PbtO_2$.

Chapter 3

Implication for *in vivo* experiments

During *in vivo* experiments, animal's temperature was kept at 37^{o}C with a homeothermic blanket using a rectal temperature probe (Harvard apparatus®). Animals breathed a mixture of 30% oxygen in air, with 0.8-1.5% Isoflurane. The $PbtO_2$ recorded in adult anaesthetized Wistar rats was similar in animals subjected to a severe LFPI (27.5 [18.2;36.6]) and in control animals (28.1 [26;31.8], W=134 p= 0.96). The overall $PbtO_2$ in all animals was 27.08 [23;35.5]
We expected that oxygen would not limit the oxidase reaction, and that changes in PO_2 from 159.6 mmHg (*in vitro* calibration) to around 27 mmHg (physiological *in vivo* $PbtO_2$) would not interfere with our measurements. Conversely, we observed that all oxidase start to depend on oxygen at physiological ranges of *in vivo* $PbtO_2$ (i.e. 27.08 [23;35.5]). Indeed in this interval of $PbtO_2$, sensors covered with glucose oxidase displayed a -9.1% [-11.7;-6.3] decrease, those with lactate oxidase -7.3% [-7.6;-7], and those with glutamate oxidase -18.4% [-19.7;-15.2], when compared to measures made at PO_2 = 159.6 mmHg (as during *in vitro* calibration).
The measurements made with the chamber in a controlled temperature bath, revealed that at 25^{o}C (i.e. room temperature) glucose sensors lost -41.7% [-46.1;-39] compared to the oxidative current at 37^{o}C (i.e. animals central temperature), glutamate sensors lost -47.5% [-49.9;-43.5] and lactate sensors -25.9% [-31.6;-15.2].
In order to extrapolate the closest substrate concentrations from oxidative currents, we need to consider calibration data as well as experimental conditions. The "R" package written includes functions to compute biosensors calibrations and corrections for different temperature and oxygen conditions between *in vitro* and *in vivo* set-ups (see documentation in Appendix VIII).
The functions called correction.Temp() and correction.TPO2() returns a corrected signal based on calibration and experimental temperature or $PbtO_2$, using parameters and equations described above. The functions are encrypted in "R" as follow:

```
correction.Temp<-function(x,enz,temp.calib=25,temp.exp=37) {
  if (enz=="glutamate") {
    A<- -104.2 ; B<- 52.6 ; xmid<- 29.8 ; scal<- 13
    delta.exp<-A+(B-A)/(1+exp((xmid-temp.exp)/scal))
    delta.calib<-A+(B-A)/(1+exp((xmid-temp.calib)/scal))
  }
  if (enz=="glucose") {
    A<- -92.2 ; B<- 57.5 ; xmid<- 34.9 ; scal<- 10.5
    delta.exp<-A+(B-A)/(1+exp((xmid-temp.exp)/scal))
    delta.calib<-A+(B-A)/(1+exp((xmid-temp.calib)/scal))
  }
  if (enz=="lactate") {
    inter<- -76 ; slope<- 1.9
    delta.exp <- slope*temp.exp + inter
    delta.calib <- slope*temp.calib + inter
  }
  if (enz=="daao") {
    A<-1 ; B<-1 ; xmid<-1 ; scal<-1
    delta.exp<-A+(B-A)/(1+exp((xmid-temp.exp)/scal))
    delta.calib<-A+(B-A)/(1+exp((xmid-temp.calib)/scal))
  }

  return(volt.temp.cor<-x*(1+(delta.calib/100))/(1+(delta.exp/100)) )
}

correction.TPO2<-function(x,enz,TPO2=28) {
    if (enz=="glutamate") {
      Asymp<- -0 ; R0<- -74.2 ; lrc<- -2.9
    }
    if (enz=="glucose") {
      Asymp<-0 ;R0<- -43.9 ;lrc<- -2.6
    }
    if (enz=="lactate") {
      Asymp<-0 ;R0<--21.8 ;lrc<- -3.17
    }

    delta<- Asymp + (R0-Asymp) * exp(-exp(lrc)*TPO2)
    return(volt.O2.cor<-x/(1+(delta/100)) )
}
```

Furthermore it is possible that when dynamic process challenge brain tissue metabolism with large $PbtO_2$ modifications, such as during CSD or ischemic events, biosensors signals must be corrected on-line with the results obtained from a $PbtO_2$ probe implanted at the same time. Due to the lack of space in a rat brain we were not able to record $PbtO_2$, LFPot, LDF, and several biosensors simultaneously. Instead, we proceeded to an "off-line" correction of the raw data obtained from biosensor's oxidative currents. To compute this correction, we used the median $PbtO_2$ values recorded in other animals obtained in the same conditions: either after CSDs triggered by KCl apposition in healthy animals or spontaneous CSDs after LFPI.

Part VI

Metabolic and micro-vascular consequences of cortical spreading depolarizations, in a normal or injured brain.

Chapter 1

Introduction

CSDs have been observed in the human brain since the mid-90s [223, 224]. There are growing evidence to consider CSDs as an important bio-marker for prognosis evaluation in several acute brain injury (i.e. TBI, ischemic stroke or sub-arachnoid hemorrhage) [225, 227].
Their implication as local "secondary brain aggressions" have been discussed in different animal models. It appears that CSDs have different consequences depending on the state of brain tissue (e.g. healthy, injured or ischemic). Local brain micro-vascularization has been extensively studied in the normal brain and in ischemic models where CBF rated between normal and ischemic levels. To date CBF modifications following spreading depolarizations are considered to range between a hyperemic response to a terminal ischemic response with intermediate biphasic patterns. These intermediate patterns triggered by CSDs encompassed spreading oligemic and/or reduced hyperemic responses [252, 253]. Nevertheless, very few studies have presented these results after TBI where miscellaneous CBF modifications take place [254].
Carbohydrate and oxygen metabolism have not received such extensive descriptions, with heterogeneous published results. Only a few recent experimental studies has reported $PbtO_2$ modifications that seemed to encompassed either an initial dip or biphasic patterns, with subsequent decrease in $PbtO_2$ [111, 258, 82]. However further descriptions under different experimental conditions are needed to define a clear pattern for $PbtO_2$ during CSDs.
Glucose and lactate metabolisms are even harder to study because of the temporal resolution required to observe dynamic processes such as CSDs. So far, the team led by MG Boutelle in London is the only one that reached a temporal resolution in the order of the minute with rapid sampling cMD [320]. They described, in anaesthetized animals, a brain glucose decrease associated with an increase in lactate extracellular concentrations following CSDs [239, 261]. Unfortunately the rapid sampling cMD did not provide real brain concentrations, but only relative values. More-over when looking at pathological brain either in human or animals, the results are much more heterogeneous [264, 263] and require further descriptions to understand how CSDs challenge brain tissue after brain injuries.
In this study we aimed to describe micro-vascular, oxygen and carbohydrate metabolisms (i.e. glucose and lactate) variations that accompanied CSDs in the normal brain and after a severe TBI. Therefore we had several objectives that were: (1) To describe the micro-vascular and metabolic (glucose, lactate, $PbtO_2$) responses observed during and after CSDs in a healthy cortical tissue; (2) To report how these patterns are altered during spontaneous isolated CSDs after severe TBI; (3) To determine if clusters of CSDs are generating a worse reponse after LFPI, compared to isolated ones.

Chapter 2

Methods

2.1 Animals

Experiments were conducted in adult male Wistar rats of 250-400g from Elevage Janvier(Le Genest Saint Isle, France). All experimental protocols were approved by the local committee on animals in research at the University Claude Bernard Lyon I (approval number: DR2014-31-V2 MESRverif), and were performed in accordance with European directive 2010/63/EU. There was no significant difference in body weight between control animals and those subjected to severe LFPI.

2.2 Experimental design

We used a 3.8 ATA LFPI as model of severe TBI as previously described. Animals were intubated and artificially ventilated prior LFPI. After LFPI animals were placed again in the stereotaxic frame under light anesthesia (0.8-1.5 % isoflurane in 30% oxygen with air) for 5 hours and were then euthanized. Animal's temperature was kept at 37^{o}C with a homeothermic blanket using a rectal temperature probe (Harvard apparatus®). SpO_2 was monitored with foot clip connected to a MouseOxPlus system (Starr Life Sciences, Oakmont, USA), and arterial blood pressure through an arterial line with a pressure sensor connected to a Bioamp (ADInstrument). Signals acquisitions and analogue-digital conversions were made with a 16 bit PowerLab 16/35 with Labchart 7 (ADInstrument)
Between 30min and 1h after LFPI, we performed arterial blood gas in 9 animals under mechanical ventilation (Harvard apparatus®, Ispra MA1 55-7058, Vt = $6ml\cdot kg^{-1}$, breath rate = $60\cdot min^{-1}$, Peep = 5cm H_20). The samples (200-400μL) were analyzed with a GEM 300 device (Instrumentation Laboratory, Bedford, USA): pH=7.35 [7.34-7.38], PaO_2=144 mmHg [136-149], PaCO2=47 mmHg [44-51], HCO_3^-=25.5 mmol/L [24.7-26.8], Ht=38 % [34-41] and Hb=11.8 g/dl [11.2-12.7].
Non-traumatized animals remain in the stereotaxic frame, breathing spontaneously under light anesthesia (0.8-1.5 % isoflurane in 30% oxygen with air) for the duration of the experiment, with the same monitoring.

In different experiments we compared $PbtO_2$, local CBF using LDF and biosensors signals modifications during CSDs, which were triggered by different stimuli:

- **KCl** experimental condition: CSDs were triggered by a transient increase in potassium concentration of the saline solution that was infusing the cortical surface, by stirring a drop of 1M KCl. This increase in KCl concentration was rinsed with a continuous flow of

saline solution (5ml/min during 1min). Two CSDs were triggered at least 30 min apart, in each animals.

- **TBI**$_{ISOLATED}$ experimental condition: Spontaneous CSDs occurred after a severe LFPI, during the recording period (i.e. 20min-5h post trauma). Neuro-chemical recordings were made in the temporal cortex (i.e. the "traumatic penumbra", as defined in the part IV). We observed only occasional clusters of CSDs in some animals. Due to the lack of frequent spontaneous clusters, we triggered additional ones after LFPI in other experiments.

- **TBI**$_{CLUSTER}$ experimental condition: After a severe LFPI as in the TBI$_{ISOLATED}$ condition, CSDs were triggered by 1M KCl apposition on the cranial window (without rinsing), and occurred every 3-5 min. Neuro-chemical recordings were made remotely, also in the temporal cortex. KCl apposition was made 30-45 min after the LFPI and we recorded at least 10 successive CSDs during 40-50 min.

Due to the small size of a rat head we were not able to perform all recording at once because of spatial overload. LFPot electrodes and LDF probes were always implanted to detect CSDs occurrence. In different sets of experiments we recorded $PbtO_2$ (n=6 in each condition), glucose and lactate (n=6 in each condition).
In the **KCl** condition, a surgical parietal cranial window was performed on the parietal bone, and the dura was carefully removed to avoid bleeding and expose the parietal cortex. A 0.9% saline solution was infused on the cranial window (4ml/hour). The LDF probe was placed on the exposed cortex away from big vessels, without pressure on the cortical matter. Other monitoring electrodes (i.e. $PbtO_2$ or biosensors) and LFPot electrodes were inserted between 500 and 1000μm deep inside the cortex, under the LDF probe.
In the **TBI** conditions, we intended to record neuro-chemical modifications in the temporal cortex that we found to be a "traumatic penumbra" area after sever LFPI (see part IV). Therefore, the temporal bone facing the temporal cortex was drilled until we see the dura and the LDF probe was placed on this thinned bone, under microscopic vision, not to apply any pressure on the dura matter. Other electrodes (i.e. $PbtO_2$ or biosensors, and LFPot) were inserted through the cranial window made for the LFPI with a 25^o angle, 2 mm deep to the temporal cortex.

2.3 Recordings set-up

2.3.1 CSDs detection

LFPot electrodes were made with an Ag/AgCl wire inserted into a pulled 3-5 μm tip glass capillary (Harvard Apparatus, Edenbridge, U.K.), filled with a mix 2M NaCl, 1M Na citrate solution (1:1 ratio). A subcutaneous silver chloride reference was placed in the neck of the animal. The signal acquisition was made by a near-DC octal bioAmp amplifier (ADInstrument, Oxford, United Kingdom) with an analogue build-in 0.02 Hz high-pass filter and a 100Hz low-pass filter.
As discussed in the Methods part, our amplifier allowed us to detect CSDs but not to determine their essential features such as amplitude or duration, because we did not have real DC recording (see part methods, section 3.1.1).
CSDs were defined by a large slow depolarization, with a subsequent vascular response. A depression of ongoing cortical activity was currently observed in healthy animals (KCl group). In the TBI$_{ISOLATED}$ and TBI$_{CLUSTER}$ groups, CSDs were also charaterized by a large slow depolarization with a subsequent vascular response. A depression of the ongoing brain electrical activity can also be observed if not already depressed by the injury or previous depolarizations.

2.3.2 Neuro-chemical and Micro-vascular recordings

2.3.2.1 Microvascular recording

Micro-vascular response was recorded with a pencil LDF probe connected to a blood Flow meter (1mm diameter tip, MNP100XP, ADInstrument, Oxford, United Kingdom). Analogue-digital conversion and data acquisition were made by a 16 bit PowerLab 16/35 with Labchart 7 (ADInstrument). Median BPU measured during the first 5min of each experiment was considered as 100% and after animals were euthanized as 0%. The LDF probe signal will thus be expressed as a percentage of the BPU measured during the 5 min starting the experiments.

2.3.2.2 $PbtO_2$ recordings

$PbtO_2$ recordings were made with an electrochemical (Clark-type) micro-sensor connected to an amplifier with a constant potential of -800mV (OX-10, Unisense, Aarhus, Denmark). Analogue-digital conversion and data acquisition were also made with the same PowerLab 16/35 with Labchart 7 (ADInstrument)

2.3.2.3 Biosensors for glucose and lactate recordings

Extracellular glucose or lactate concentrations were made using oxidase-based biosensors, connected to a VA-10 amplifier (NPI electronics) with a constant potential of +500mV. All sensors were tested before and after each *in vivo* experiments to ensure that the sensitivity and specificity remained stable all along the experiment.
Indeed, unwanted oxidation of endogenous electroactive molecules like serotonin has to be considered to ensure biosensors specificity. To prevent such interference, a screening PPD layer was present on the surface of the platinum electrode. An additional layer was applied on the surface of each biosensor prior each *in vivo* experiment.
Biosensors calibrations encompass several steps that include selectivity assessment with serotonin (20 μM) detection. Then the relationship between the oxidative current and the enzyme substrate concentration, was tested with a range of concentrations in PBS (i.e. $200 \mapsto 15000\mu$M glucose or lactate), at room temperature and ambient oxygen concentration.
Only those electrodes sensitive enough (i.e. $\geq$ 50 pA$\cdot 100\mu M^{-1}$ of glucose or lactate) with an effective PPD screening layer (<1.2 pA$\cdot$mM^{-1} response to serotonin) were used.
Assuming high extracellular concentrations of glucose and lactate in the brain, the signal to noise ratio from glucose and lactate sensors allow us to avoid control sensor implantation thus limiting spatial set-up overload.

In the next chapters I will describe our results about neurochemical monitoring of CSDs after a severe LFPI, in comparison to those observed in a non-injured cortex. The first chapter will give an overview of LFPI effect on systemic and local brain parameters. Then I will report in different chapters vascular, $PbtO_2$, glucose and lactate modification that occurred in our different experimental conditions.

Chapter 3

Effect of severe LFPI on systemic and brain hemodynamic and metabolic parameters

3.1 Vascular modifications

All recordings (brain or systemic) begun 20 min after LFPI (time to implant our different sensors) and ended 4 hours later. During this 4 hours time window, 79% of the animals displayed CSDs. Among them, we were able to record 2 [1.75;4] isolated CSDs per animal.
CSDs did not induce changes in systemic hemodynamic parameters (blood pressure or heart rate), in both groups (KCl of TBI). Systolic arterial blood pressure remained stable at a mean of 111 mmHg [105;121]. Despite baseline LDF was impossible to compare between groups due to its relative value, we observed that cerebral perfusion, measured by the LDF, decreased over the experiment ending at 67% [44;101] (100% being the LDF signal at the beginning of the experiment). This trend was not observed in control non-injured animals (KCl). Moreover, this decreases in the LDF signal tended to be more important in TBI animals that sustained CSDs (57 % [30;101]) than in those without CSDs (99 % [68;112], W=77, p=0.076).

3.2 Metabolic modifications

3.2.1 Systemic blood concentrations

Baseline arterial blood glucose concentrations were higher (8.64 mmol/L [7.98;8.9]) in the TBI groups compared to control animals in the KCl group (7.3 mmol/L [6.4;9.3]; W=24.5, p=0.46). Beside lactate blood concentrations were not different in the TBI groups (1.7 mmol/L [1.68;1.99]) and in the KCl group (1.7 mmol/L [1.4;2.3]; W=31.4, p=0.96).
LFPI had no impact in $PbtO_2$ that were similar in the KCl (28.1 mmHg [26;31.8]) and the TBIs groups (27.5 mmHg [18.2; 36.6], W=134 p=0.96).

3.2.2 Brain concentrations

On the other hand, carbohydrate metabolism was impacted in the "traumatic penumbra" after the severe LFPI. Indeed brain glucose concentration was decreased in the TBI groups (0.42 mmol/L [0.32;0.59]) compared to the KCl group (1.55 mmol/L [1.18;1.89], W=33, p=0.015). Conversely extracellular lactate concentrations were very close in the TBI groups (0.49 mmol/L

[0.20;0.79]) compared to the KCl group (0.33 mmol/L [0.11;1.69], W=17, p=0.93).
The $PbtO_2$ recorded in animals subjected to a severe LFPI (27.5 [18.2;36.6]) was not different than those in control animals (28.1 [26;31.8], W=134 p= 0.96) before subsequent CSDs.

Chapter 4

Cortical spreading depolarizations consequences in a normal or injured brain.

4.1 Micro-vascular changes

4.1.1 LDF recordings during isolated CSDs

Since the LDF probe was present during each experiment and helped us to detect CSDs occurrence (large depolarization with an associated micro-vascular hyperemic response), 18 animals ($PbtO_2$: n=6, glucose and lactate: n=6, glutamate: n=6) were analyzed in each groups (KCl, $TBI_{ISOLATED}$ and $TBI_{CLUSTER}$).
As the CBF decreased slowly after LFPI the pre-CSD LDF level was lower in the $TBI_{ISOLATED}$ group (n=18, 68 % [54.3;81.9]) compared to the KCl group (n=18, 98.2 [92.39;118.4], W=276, p<0.001, Fig 27 A). CSDs induced a similar hyperemic response in both groups (Fig 27). However the area under the curve (AUC) of the hyperemic response was lower in the $TBI_{ISOLATED}$ group (6120 %.sec [3455;8873]) compared to the KCl group (23220 %.sec [13620;30640], W=279 p«0.001). We then separated the LDF signal after the depolarization into 2 min epochs. In this analysis the pre-CSD percentage was subtracted to the LDF value to compare relative data over time. Indeed a repeated measure ANOVA including both "time" and "groups" as factors evidenced different responses between the KCl and the $TBI_{ISOLATED}$ group (df=20, F=4.2, p«0.001, Fig 27 A). Post-hoc analysis did not reach significance because of multiple comparisons.
20 min after the CSD, CBF remained lower in the $TBI_{ISOLATED}$ group (52.1 % [33.6;66.0]) compared to the KCl group (100.8 % [86.5;116.0], W=289 p«0.001). Moreover in the $TBI_{ISOLATED}$ group, these final LDF levels were lower than the pre-CSD values (v=30 p=0.014). Conversely in the KCl group, CBF had recovered its baseline levels and final values were not different from the pre-CSD levels (V=44 p=0.07).

4.1.2 LDF recordings during clusters of CSDs

When we triggered clusters of CSDs after LFPI ($TBI_{CLUSTER}$ group) we observed repeated episodes of hyperemia after each depolarization (Fig 28), with a tendency for the pre-CSD level of CBF to increase with CSDs repetition (Fig 28 *pre-CSD LDF* panel, repeated measure ANOVA df=9 F=3.9 p«0.001). However, the amplitude of the hyperemic response (measured by the AUCs) decreased with CSDs repetition in a cluster (Fig 28 *Hyperemic LDF AUC* panel, repeated measure ANOVA df=9 F=2.9 p=0.003).

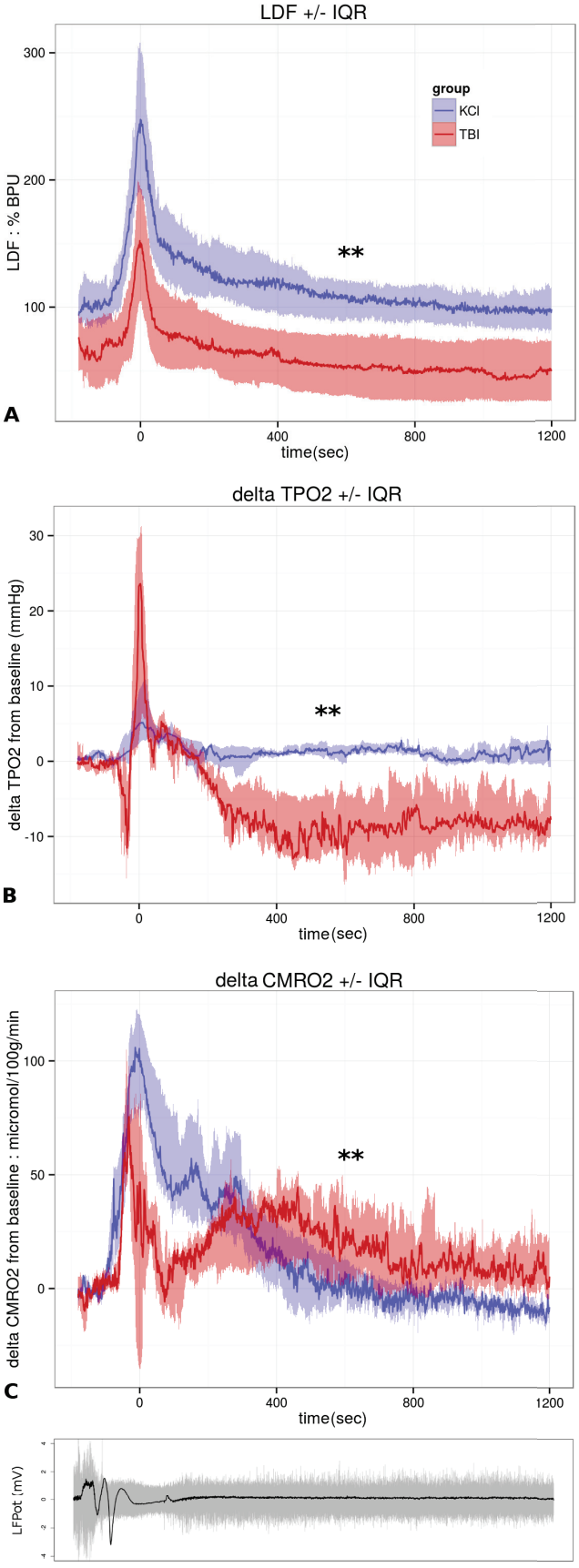

Figure 27: **Laser Doppler Flowmetry (LDF), $PbtO_2$ and $CMRO_2$ modifications during the first 20 min following a CSD**.
A LDF modifications after a CSD: 100% correspond to the signal at the beginning of the experiment and 0% after the animal was euthanized.
B: $PbtO_2$ modifications after a CSD: $PbtO_2$ values are reported in mmHg, as the differences from the pre-CSD level.
C: $CMRO_2$ modifications after a CSD: $CMRO_2$ was calculated from the LDF and $PbtO_2$ values and is expressed in $\mu mol \cdot 100g^{-1} \cdot min^{-1}$, as the difference from the pre-CSD level.
The panel under all graphics is an example of LFPot recordings during CSDs. The gray curve represents the AC signal (0.5-50Hz) and the black curve the DC signal (0.02-0.5Hz) in mV.
The red curves represent data observed after a severe LFPI ($TBI_{ISOLATED}$ group). Whereas the blue curves represent those in control animals (KCl group). For statistical analysis, data (post-CSD value - pre-CSD value) were separated into 2 min epochs and compared by a repeated measured ANOVA. ** $p<0.05$: Difference between the KCl and the $TBI_{ISOLATED}$ group.

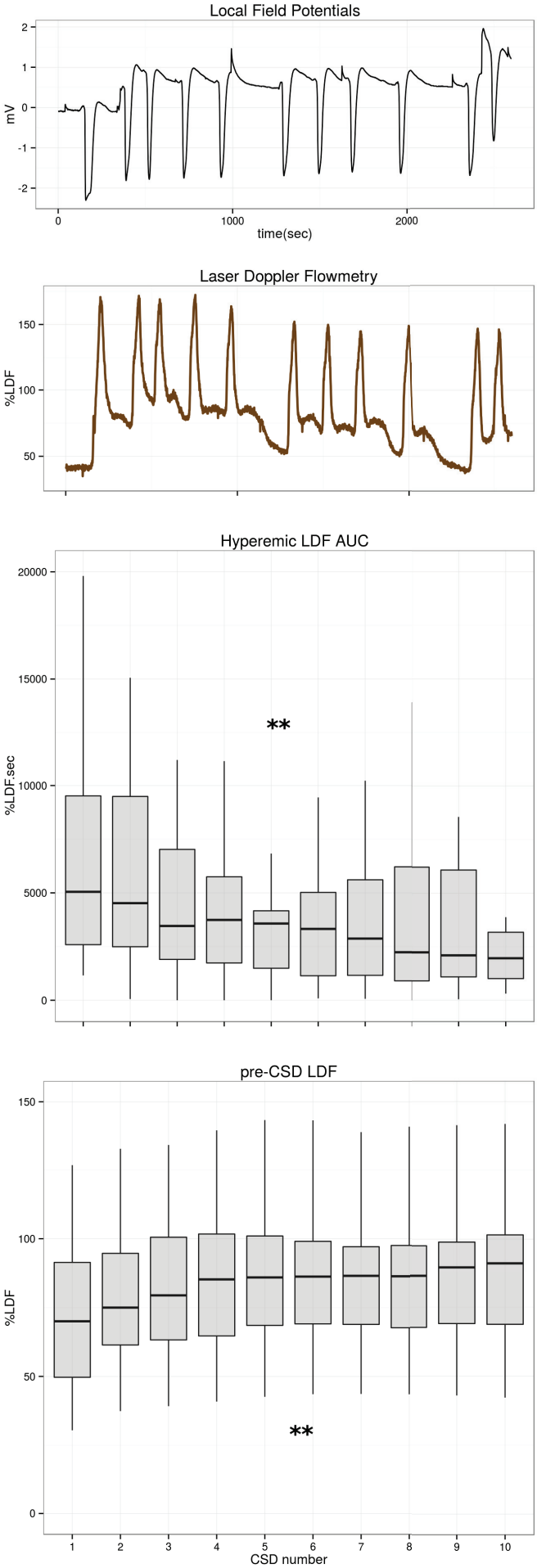

Figure 28: **Laser Doppler Flowmetry (LDF) response during a cluster of CSDs.**
Local Field Potentials: The upper black curve is an example of the LFPot recorded during a cluster of CSDs with the subsequent vascular response represented below in brow (**Laser Doppler Flowmetry**).
Hyperemic LDF AUC: the area under the curve (AUC) of the hyperemic response is plotted against the CSD index within the cluster.
pre-CSD LDF: Boxplots of the LDF values before each depolarization are plotted against the CSD index within the cluster in the lower panel.
** p«0.001 repeated measured ANOVA

4.2 Oxygen concentration ($PbtO_2$) and consumption ($CMRO_2$) modifications

4.2.1 $PbtO_2$ recordings during isolated CSDs

There was no difference on $PbtO_2$ induced by LFPI in comparison to control animals (see above section 3.2.2). In control animals (KCl), CSDs induced an hyperemic reaction that was accompanied by a 9 mmHg [5;11.7] transient increase in $PbtO_2$ (Fig 27 B), that return to pre-CSD values afterwards. Conversely, in the $TBI_{ISOLATED}$ group, $PbtO_2$ displayed a first dip of -16.4 mmHg [-21.2;-12.3] preceding the hyperemic response. This dip was significantly lower after TBI than in the KCl group in which it was usually absent (W=42, p=0.02). However the AUC of the increase in $PbtO_2$ was not different between the two groups (W=21, p=0.75). We then separated the $PbtO_2$ in 2 min epoch to compare the two groups responses over time, using a repeated measures ANOVA with "groups" and "time" as factors. Using this analysis, we were able to show that the $TBI_{ISOLATED}$ group had a different time decay compared to the KCl group (df=20, F=4.29, p«0.001). We also evidenced that the $PbtO_2$ decreased during the 20 min following the depolarization in the $TBI_{ISOLATED}$ group, unlike in healthy animals. Moreover if the $PbtO_2$ were similar before the CSD in the two groups, 20 min after the depolarization the $PbtO_2$ was significantly lower in the $TBI_{ISOLATED}$ group (19.8 mmHg [12.75]) compared to the KCl group (28.1 mmHg [26.3;32], W=43 p=0.012).
As described in the Method part (section 3.5), we computed $CMRO_2$ from the LDF and the $PbtO_2$ values. As expected during the energetic challenge represented by CSDs, the $CMRO_2$ was increased in the KCL group (111.3 $\mu mol \cdot 100g^{-1} \cdot min^{-1}$ [96.5;124.9]) like in the $TBI_{ISOLATED}$ group (139.2 $\mu mol \cdot 100g^{-1} \cdot min^{-1}$ [93.8;177], W=17 p=0.413). However the $CMRO_2$ responses were different between the two groups when we used the repeated measures ANOVA performed on 2 min epochs following CSDs (df=20 F=6.6 p«0.001). However, after 20 min post-CSD the $CMRO_2$ regain its initial value in both groups.

4.2.2 $PbtO_2$ recordings during clusters of CSDs

In the $TBI_{CLUSTER}$ group, the hyperemic responses following each CSD were accompanied by biphasic $PbtO_2$ modifications (initial dip and subsequent increase like after isolated CSDs, Fig 29). As compared with a repeated measures ANOVA, both the dip and the increase responses were not different from one depolarization to another (respectively df=9 F=1.1 p=0.405 and df=9 F=0.56 p=0.497). Likewise the pre-CSD $PbtO_2$ value remained constant over CSDs repetition in clusters (df=9 F=1.4 p=0.207).
The $CMRO_2$ displayed transient increases during each depolarization that were similar over the clusters (df=9 F=1.4 p=0.24). Nevertheless the pre-CSD $CMRO_2$ was increasing as CSD repeated in clusters (Fig 29 *pre-CSD CMRO2*, df=9 F=4 p«0.001).

4.3 Glucose, Lactate and $CMR_{glucose}$ modifications

4.3.1 Biosensors recordings during isolated CSDs

In control animals (KCl), isolated depolarizations led to a decrease in extracellular glucose from 1.55 mmol/L [1.18;1.89] to 0.63 mmol/L [0.43;1.52]. This dip in glucose lasted 16.5 min [11.7;30.7] and was followed by a overshoot peaking to 1.89 [1.61;2.95]. Finally brain extracellular glucose concentrations returned to their initial values 20-30 min after the CSD (Fig 30 A). The $CMR_{glucose}$ calculated from extracellular glucose values (see part Methods section 3.5)

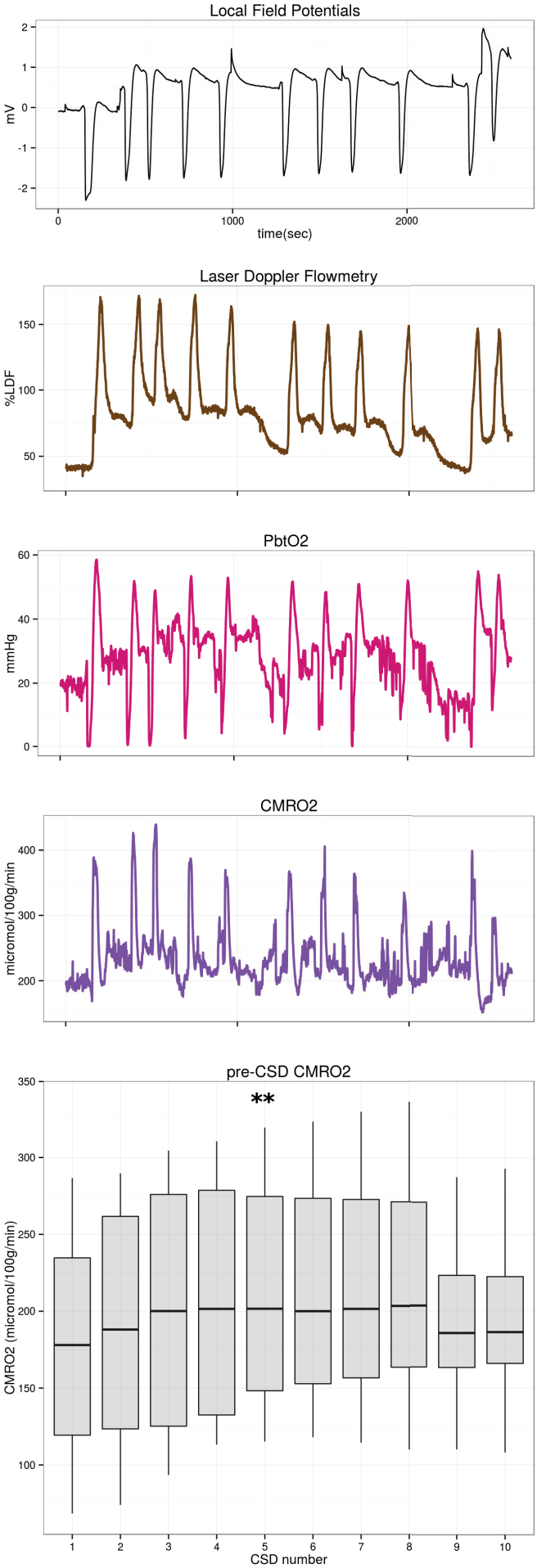

Figure 29: **Laser Doppler Flowmetry (LDF), $PbtO_2$ and $CMRO_2$ modifications during a cluster of CSDs.**
Local Field Potentials: The upper black curve is an example of the LFPot recorded during a cluster of CSDs with the subsequent examples of (1) the micro-vascular response represented below in brow (**Laser Doppler Flowmetry**), (2) the **$PbtO_2$** in pink and (3) the **$CMRO_2$** in purple.
pre-CSD $CMRO_2$: Boxplots of $CMRO_2$ values in $\mu mol \cdot 100g^{-1} \cdot min^{-1}$ before each depolarization are plotted against the CSD index within the cluster.
** p«0.001 repeated measured ANOVA

displayed a 17.8 $\mu mol \cdot 100g^{-1} \cdot min^{-1}$ [17;21.9] transient increase. 20 min after the depolarization the $CMR_{glucose}$ displayed a -5.6 $\mu mol \cdot 100g^{-1} \cdot min^{-1}$ [-11.7; -2.9] decrease compare to pre-CSD value (V=21 p=0.031, Fig 30 B).
After LFPI ($TBI_{ISOLATED}$), initial brain extracellular glucose concentrations were lower (0.41 mmol/L [0.32;0.59]) than those of control animals. These values also dropped down to 0.2 mmol/L [0.167;0.242] during 15.6 min [8.2;25.1]. 20 min after the depolarizations, brain glucose also return to concentrations close to the pre-CSDs one (0.40 mmol/L [0.32;0.55], V=7 p=0.56).
This repeated measures ANOVA with "group" and "time" as factors performed on 2 min epochs of relative glucose concentrations (post-CSD - pre-CSD), showed that the two groups had different time decay (df=20 F=2.4 p«0.001): The amplitude of the glucose decrease was lower and no overshoot was observed in the $TBI_{ISOLATED}$ group.

Lactate modifications were more heterogeneous in the KCl group but always exhibited a delayed large increase from 0.33 mmol/L [0.11;1.69] to 1.93 mmol/L [0.28;3.63], that returned to concentrations close to the initial value after 20min (0.37 mmol/L [0.13;4.18], V=19 p=0.09, Fig 30 C). In the $TBI_{ISOLATED}$ group lactate concentrations had a different pattern. However it did not reach a significant difference from the control group, because of the KCl responses heterogeneity (repeated measures ANOVA with "group" and "time" as factors on 2 min epochs of relative concentrations (post-CSD - pre-CSD), df=20 F=1.4 p=0.096). Brain lactate concentrations changes started with an initial dip from 0.49 mmol/L [0.2;0.78] to 0.13 mmol/L [0.11;0.14] that was not observed in the KCl group (W=31 p=0.041). This dip was followed by a transient increase peaking to 0.53 mmol/L [0.41;0.88] almost time locked with the vascular response: its peak occurred 31.5 sec [16.3;43] after the hyperemic acme. Unlike in the KCl group, extracellular lactate concentrations did not display such large increase. Finally, the lactate concentrations during the 20 min following CSDs in the $TBI_{ISOLATED}$ group tended to be lower than the pre-CSD levels (0.11 [0.08;0.14], W=6 p=0.06).
The lactate/glucose ratio had similar changes in the KCl and $TBI_{ISOLATED}$ groups: As glucose was decreasing the lactate/glucose ratio increased from 0.23 [0.07;0.94] to 1.96 [0.76;3.25] in the KCL group, and from 0.79 [0.58;1.21] to 2.52 [2.00;2.69] after LFPI (W=15 p=0.69). Both groups recovered initial lactate/glucose values 20 min after the depolarizations (i.e. 0.24 [0.06;0.92] in the KCl group and 0.58 [0.43;0.99] after LFPI).

4.3.2 Biosensors recordings during clusters of CSDs

When we triggered cluster of CSDs in animals with concomitant glucose and lactate recordings we observed more heterogeneous patterns. On the one hand brain glucose concentrations always decreased during the cluster, thus the median concentrations remains lower than the pre-cluster values (repeated measures ANOVA, df=10 F=3.8 p«0.001, Fig 31). Subsequently the $CMR_{glucose}$ was increasing during the cluster compared to the pre-cluster value (repeated measures ANOVA, df=10 F=4.2 p«0.001).
On the other hand lactate exhibited biphasic patterns with an initial dip and subsequent increase, like the early modifications induced by isolated CSDs ($TBI_{ISOLATED}$). Both the dip and the increase were constant over CSDs repetition in clusters (respectively df=9 F=0.7 p=0.68 and df=9 F=1.4 p=0.23). In some animals extracellular lactate tended to increase whereas no clear trend can be observed in other animals (Fig 31 Lactate modifications). Therefore no median brain lactate modifications were evidenced during clusters compared to the pre-cluster lactate levels (df=10 F=0.7 p=0.73). The lactate/glucose ratio increased to 1.87 [1.30;5.33] during the first depolarization and was not significantly impacted by CSDs repetition (df=10 F=1.28 p=0.26).

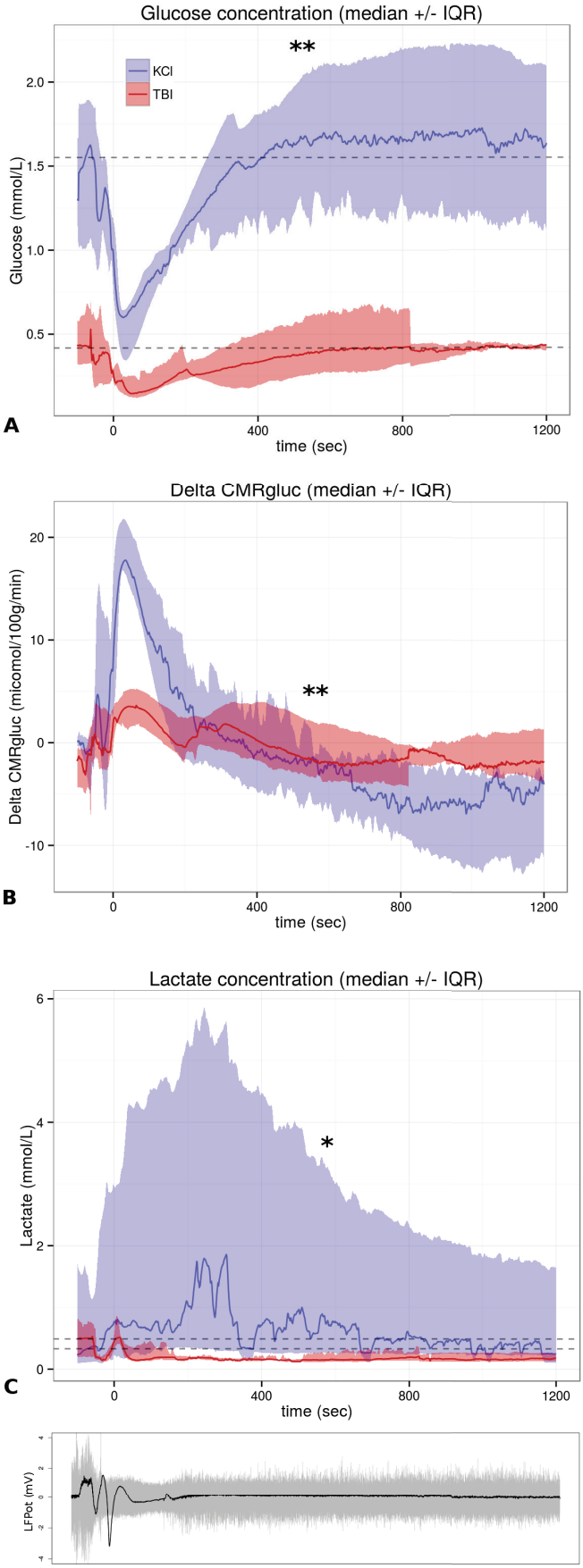

Figure 30: **Glucose, lactate and $CMR_{glucose}$ modifications during the first 20 min following a CSD**. **A** Extracellular brain glucose concentrations modifications in mmol/L. The horizontal dashed black lines point out the basal levels either in the KCl or in the $TBI_{ISOLATED}$ group.
B: Relative values of $CMR_{glucose}$ from the pre-CSD levels, in $\mu mol \cdot 100g^{-1} \cdot min^{-1}$.
C: Extracellular lactate modifications in mmol/L. The horizontal dashed black lines point out the basal levels either in the KCl or in the $TBI_{ISOLATED}$ group.
The red curves represent values observed after a severe LFPI ($TBI_{ISOLATED}$ group). Whereas the blue curves represent the signals in control animals (KCl group).
The panel under all graphics is an example of LFPot recordings during CSDs. The gray curve represents the AC signal (0.5-50Hz) and the black curve the DC signal (0.02-0.5Hz) in mV.
For statistical analysis, signals were separated into 2 min epochs versus pre-CSD levels (post-CSD signal - pre-CSD value). ** $p<0.05$, *$p<0.1$: Difference between the KCl and the $TBI_{ISOLATED}$ group using a repeated measured ANOVA.

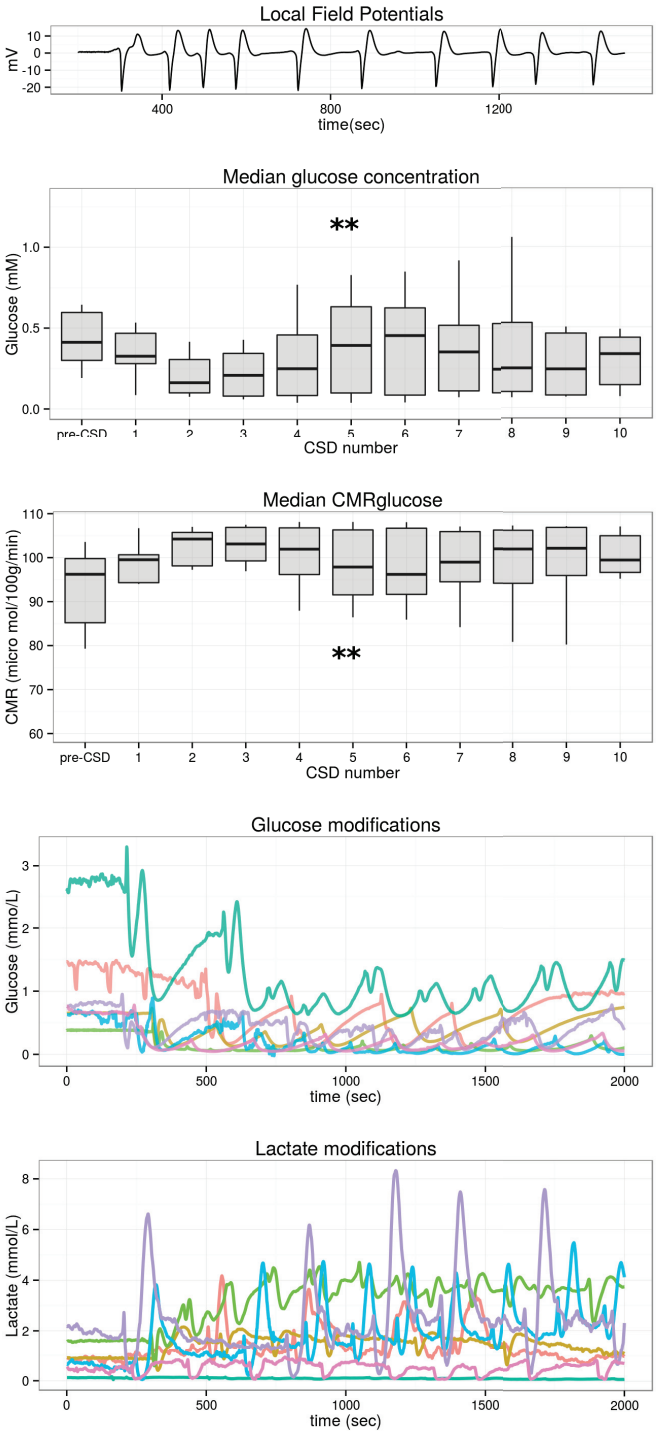

Figure 31: **Glucose and lactate modifications during a cluster of CSDs**.
Local Field Potentials: Example of the LFPot recored during a cluster of CSDs, with the subsequent:
(1) boxplots of **median glucose concentration** modification during each CSD, and (2) boxplots of **median $CMR_{glucose}$** modifications during each CSD.
The last two panels display simultaneous glucose and lactate recordings during clusters of CSDs. Each color correspond to the recording in one animal (n=6). Glucose and lactate concentrations are plotted in two separate panels with the same time and color scales.
** p«0.001 repeated measured ANOVA

Chapter 5

Discussion

In this part we have described the neuro-chemical and micro-vascular consequences of severe LFPI and the effects of CSDs occurring either in a "traumatic penumbra" cortex or in a normal brain tissue.
Our data provide a clear metabolic signature of CSDs in the healthy brain, with a decrease in brain glucose concentrations and a subsequent delayed increase in brain lactate concentrations. The $PbtO_2$ displayed a transient increase following the hyperemia and was associated with an increase in $CMRO_2$. Brain metabolism recovered pre-CSD levels after 20-30 min.
In the "traumatic penumbra" following a severe LFPI, the basal brain glucose concentrations were lower than in healthy tissue and nonetheless decreased when a CSD was passing through. Unlike in healthy brain tissue, lactate exhibited an initial biphasic pattern. No delayed increase was observed but rather a decrease in extracellular brain lactate concentrations that might sign an intracellular lactate consumption. $PbtO_2$ had a similar response than that of lactate, with an initial biphasic pattern during the depolarization and a subsequent prolonged decrease. 20-30min after the depolarization onset in the traumatized cortex, lactate concentrations and $PbtO_2$ remained lower compared to pre-CSD levels.

5.1 How severe LFPI affected brain tissue

Animals subjected to a severe LFPI with mechanical ventilation support, underwent no systemic secondary brain aggression: their systolic blood pressure was over 90 mmHg and they had a normal blood oxygenation (PaO_2>100mmHg). Nevertheless, our respiratory assistance lead to a light respiratory acidosis (pH=7.35, $PaCO_2$=47mmHg), that might influence CBF with a small vasodilation.
This experimental procedure did not produce significant other organ dysfunction as blood lactate levels remained below 2 mmol/L in both control (KCl) and traumatized (TBI) animals. Under Isoflurane anesthesia control or traumatized animals did not present any hypoglycemia. Conversely severe TBI animals had around 1 mmol/L increase in blood glucose concentrations compared to control animals, suggesting a stress response to the brain trauma. A similar increase has been described in patients after moderate or severe TBI, levels above 11 mmol/L being observed among patients with the worse outcome [61].
79% of traumatized animals displayed at least one CSD during the first 4 hours following the LFPI. In human pathology, the rate of CSD is lower (58% after severe TBI [225]), however recordings are made later in the clinical course and usually began after neuro-surgical procedures (i.e. at least 5-10 hours after the trauma). Therefore, it is possible that more CSDs occurred within the first hours, which can match the time window we studied. Similarly, other authors showed that every animal had one heterogeneous DC potential shift immediately after LFPI, with a subsequent low rate of CSDs 0.38 CSD/h like in our experiments [295].

Finally, we observed that animals with CSDs had a progressive decrease in CBF in the "traumatic penumbra" dropping to -43% 4-5 hours after the trauma. Our observations are close to the values reported by Hayward et al. (54% decrease in CBF 6 hours after the LFPI) in a similar temporal cortex, using the arterial spin labelling-MRI technique [318]. The fact that animals without CSDs tended to have a higher CBF suggest that CSD repetition during the first hours after the injury played a role in the decrease of regional CBF. Moreover, it is possible that the CBF decline observed in some animals without CSDs, was the result of early depolarizations that occurred before we implanted the LFPot electrode. Indeed vascular responses like CSDs induced hyperemia, were sometimes recorded while we were implanting LFPot electrodes.

5.2 Micro-vascular modifications

In our experiments CSDs induced hyperemic responses in both conditions (KCl or TBI), even though these responses were less important after LFPI. Unlike in ischemic stroke models, we did not evidence inverse vascular response with a terminal ischemia [252]. The "traumatic penumbra" might differ from the "ischemic penumbra" in several ways namely due to different CBF supply from pial arteries. Hayward et al. reported CBF values in the "traumatic penumbra" (-54% $\equiv 60\ ml \cdot 100g^{-1} \cdot min^{-1}$) which were well above either ischemic ($15ml \cdot 100g^{-1} \cdot min^{-1}$ [116]) or oligemic thresholds (33-35$ml \cdot 100g^{-1} \cdot min^{-1}$ [118, 119]).
In our experiments we used low doses of Isoflurane (0.8-1.5%) as anesthetic agent. Like other halogenated drugs, low doses of Isoflurane are known to increase CBF compared to other anesthetic agent [326, 331, 319]. CBF has been reported at least 2 fold higher during Isoflurane anesthesia [326] compared to either α-cholarlose [319] or Ketamine [330]. Together with a light increase in $PaCO_2$, our set-up could have led to a "luxury" perfusion compared to experiments conducted under α-cholarlose anesthesia. This is a possible reason why we did not evidenced transient or prolonged ischemia.
As evidenced by several authors, in ischemic models, the CBF levels before CSD onset will drives the following micro-vascular response features. Prolonged ischemia can be observe in the ischemic core following the depolarizations. While the CBF increases in remote areas, transient ischemia and hyperemic responses may appear in the cortex [252, 253]. In TBI models like LFPI, heterogeneous CBF modifications occurs corresponding to different vascular responses. The hyperemic response we observed in the $TBI_{ISOLATED}$ group, were not that of healthy tissue and matched more the microvascular response observed in a remote area of the ischemic core [252, 253].
During clusters of CSDs we still observed episodes of hyperemia, but their amplitude was reduced with the repetition of CSDs. Somme author described a similar decrease in the hyperemic response during repeated peri-infarct depolarization [252]. However, instead of ischemic processes, basal CBF was increasing during clusters of CSDs. Such pattern is closer to those described during vasogenic edema formation observed with MRI after severe TBI [350] or ischemic stroke [351]. In fact, repeated CSDs are known to generate both cytotoxic edema with cell swelling [236], and BBB disruption with vasogenic edema [352, 353, 354].

5.3 $PbtO_2$ modifications

In our experiments, CSDs led to an increase in $PbtO_2$ that followed the micro-vascular hyperemia, before returning to its initial values in control animals (KCl). This pattern is quite different from those described by both Piilgaard et al. in rats and Takano et al. in mice. They rather described either a monophonic decrease when animals breath air [111] or an initial biphasic pattern with a subsequent prolonged decrease when animals breath an oxygen-enriched

gas mixture [258] (Fig 11, Introduction part section 4). Nevertheless monophasic increase in $PbtO_2$ like those we reported in our experiments, has also been reported in the human brain during CSDs [259].
One explanation might be again the difference in the anesthetic agent employed (i.e. Isoflurane in 30% O_2) which generate higher baseline CBF values than those during experiments conducted under α-cholarlose anesthesia. These experimental conditions led us to record higher $PbtO_2$ (28.1 [26;31.8]) compared to those reported by Piilgaard et al. (18±1.9). This higher blood and oxygen supply could have prevented the drop in $PbtO_2$ induced by the increase in $CMRO_2$.
Surprisingly the initial biphasic pattern, described by these authors, is closer to the signals we have recorded in animals subjected to a severe TBI. This rise the question about the monitoring probes location inside the cortex.
In control animals we implanted our electrodes ($PbtO_2$, LFPot and biosensors) deeper than 500 μm, because we usually found very low values of glucose or $PbtO_2$ in upper cortical layers. We hypothesized that these superficial layers have been impacted by the surgery and the dura removal, and therefore resemble an injured cortex. Then we decided to avoid the first 500μm of the cortex for neuro-chemical brain assessment. This could explain why other authors reported patterns closer to those we recorded in traumatized animals since they implanted their probes between 300 and 600μm [258].
$CMRO_2$ calculated from $PbtO_2$ and CBF displayed a similar increase than the one described by Piilgaard et al. using the same algorithm (i.e. 100-150 $\mu mol \cdot 100g^{-1} \cdot min^{-1}$) [258]. The $CMRO_2$ has then recovered its initial values 20-30 min following the depolarization, faster in a healthy cortex than after TBI.

It seems that $PbtO_2$ variations during CSDs encompass a range of modifications depending on CBF and oxygen supplies: (1) Under high CBF and oxygen concentration, CSD triggers a transient monophasic $PbtO_2$ increase subsequently returning to baseline values. (2) When CBF decreases under high oxygen concentrations, the $PbtO_2$ will display an initial biphasic pattern (short dip followed by a transient increase), with a subsequent prolonged decrease for at least 20 min. In this situation the the $CMRO_2$ increase starts to exceed oxygen supply. (3) If oxygen supply is also missing (e.g. breathing either air or lower oxygen gas mixture) then $PbtO_2$ undergoes a monophasic decrease which duration rise as the oxygen supply goes down.

During clusters of CSDs after LFPI, $PbtO_2$ went through repeated biphasic modifications like during isolated depolarizations. The pattern was not significantly altered over the clusters. Conversely, CSD repetition induced a progressive increase in $CMRO_2$ that might be deleterious in already injured areas. . However, this can also be the signature of the cortical ability to extract O_2 from the blood compartment, in reaction to an aggression.

5.4 Glucose and lactate metabolism

As glucose is the main energetic substrate in the brain, it is expected that CSDs induce a decrease in its cortical concentration to produce ATP. Prior studies had already showed such effects with rapid sampling cMD [239, 261]. The present results are, to our knowledge, the first to provide real brain glucose and lactate concentrations with a high temporal resolution in the order of a second. In the normal brain submitted to KCl induced CSD, we recorded a decrease of brain glucose concentrations from normal values (1.55 mmol/L) to 0.63 mmol/L lasting around 16 min. This large dip was followed by a small overshoot to 1.89 mmol/L before recovering normal values 20-30 min after the depolarization.
In the “traumatic penumbra”, baseline cerebral glucose concentrations were already lower (<1mmol/L) than those in control animals. Such values below 1mmol/L have been associ-

ated with a bad outcome in patients with acute brain injury [203, 62]. Moreover, CSDs still induced a decrease in cerebral glucose reaching a critical value of 0.2mmol/L. This threshold (0.2mmol/L) was used by Vespa et al. to define metabolic crisis with cMD [202]. This deep drop in brain glucose concentrations may be associated either to a lack of blood glucose supply or to an excess in glucose fuelling by cells. As calculated by a reversible Michaelis-Menten model from brain glucose, $CMR_{glucose}$ increased in both groups (KCl and TBI). This increase in glucose consumption can be related to several metabolic states usually described in the human brain with cMD [203, 202]:

- Aerobic hyperglycolysis characterized by a Lactate increase, a low L/P ratio, and low glucose concentrations.
- Anaerobic hyperglycolysis, also called metabolic crisis, characterized by a hight L/P ratio and low glucose. This altered patterns has been divided in two different entities:
    1. A type 1 ischemic pattern with a lactate increase, a high L/P ratio, a low glucose, and low $PbtO_2$ levels.
    2. A type 2 "low pyruvate" pattern where glucose is low, $PbtO_2$ is normal, and L/P is high because of low pyruvate brain concentrations. Lactate concentrations remain normal or low.

Even if pyruvate sensitive biosensors are not yet available, brain lactate concentrations had clear different responses in the normal and injured brain. As previously described with cMD [239, 261], CSDs induced in a non-injured brain a large and delayed increase in extracellular lactate concentrations to almost 2 mmol/L, which was returning to normal values 20-30 min after the depolarization. The lactate/glucose ratio was also transiently increased but remained in the range of normal values indicating that most glucose molecules are metabolized in the oxidative pathway [355, 356]. This patterns of glucose decrease and lactate release was associated with an increase in $CMRO_2$, and resembled the "aerobic hyperglycolysis" state. This metabolic state is considered a normal reaction of brain tissue to an aggression, and has been associated with a better outcome in human pathology [208, 209].
Other authors studied lactate dynamics in the brain, for example after electrical stimulation, and described similar results with a large delayed increase in lactate during 15-20 min [357, 104, 358, 359]. The results from Hu and Wilson in 1997 are usually taken as a model of physiological brain activations. However they needed to repeat electrical stimulation (1-ms pulse width, 40 Hz at $250\mu A$) for at least 5 seconds to see any modification in brain lactate or glucose concentrations. Shorter duration caused no observable change [104]. Likewise Kuhr et al. as well as Kruger et al. used electroconvulsive shock to model brain aggression or seizure, and found similar brain lactate concentrations changes [359, 358]. Like in 1944 when Leão discovered CSDs trying to study epileptic activity with 1-5 sec "tetanizing" current [219], these stimulations probably triggered CSDs rather than seizures or normal brain signaling!
Therefore the model published in 2007 by Simpson et al. based on Hu and Wilson results could explain brain metabolism during CSDs in a normal brain tissue. Under such circumstances it seems that glucose catabolism and lactate production are supported by both neurons and astrocytes [90].
Takano et al. described, with 2-photon imaging, NADH spatial and temporal modifications during CSD in the normal brain. Unlike during physiological brain activity where a redox-coupling has been described between astrocyte and neurons [108], changes in NADH fluorescence was a function of the distance to the vasculature: (1) tissues located closer than 8–10 μm from a capillary vessel wall showed NADH dips (indicating oxidative metabolism), whereas (2) those located further away showed NADH overshoots, consistent with a shift in the NADH/NAD+ ratio toward NADH because of inadequate oxygenation to support increased aerobic

metabolism [111].
These results are in accordance with a glucose uptake by both neurons and astrocytes with different cellular cooperation.

After TBI, CSD induced a lactate initial dip from 0.49 mmol/L to 0.13mmol/L followed by a transient and small increase to 0.53mmol/L. Then lactate concentrations either remained at its initial value or even decreased. Unlike after CSDs in a non-injured brain, prolonged increase in lactate concentrations was never observed in traumatized animals. Similar modifications has been described with cMD in some animals or patients who displayed no lactate modifications after CSDs [264, 263]. One possible explanation could be that oxidative pathway already worked at its full capacity after LFPI, and therefore all glucose molecules consumed during glycolysis goes to the mitochondria in the tricarboxylic acid cycle. Indeed the lactate/glucose ratio remains in a normal range of values after LFPI (2.7 [1.5;4.9] [356]) indicating a preserved oxidative pathway [355, 356]. Then we would expect that pyruvate molecules are not converted into lactate as during type 1 anaerobic glycolysis, but rather into acetyl-Coa to enter the tricarboxylic acid cycle.
It is possible that extracellular lactate and pyruvate were transferred to the intracellular compartment resulting in a decrease in their extracellular brain concentrations that are accessible to biosensors or cMD. Even if we did not have pyruvate concentrations recordings, we hypothesized that CSDs could underpin the type 2 "low pyruvate" state described with cMD, whereby glucose, lactate and pyruvate extracellular concentrations are low.
Two patterns emerge from our data: (1) a "normal" hyperglycolylis in healthy brain tissue, whereby glucose will decrease with a subsequent increase in lactate, and recover after 20-30min. The L/P ratio is expected to remain normal. (2) An impaired response in the "traumatic penumbra", with a decrease in brain glucose and a lactate concentrations, reflecting their intracellular consumption. These modifications will eventually recover after 20-30 min. However, in some animals glucose and lactate concentrations remained at low levels after the CSD.

Finally clusters of CSDs led to a sustain decrease in glucose with a subsequent increase in $CMR_{glucose}$. Brain lactate had more heterogeneous responses with alternating release and consumption during each CSD. The overall lactate concentrations sometimes increased or remained stable in other animals. These differences might reflect a range of metabolic patterns depending on cellular capacity to use glucose in the tricarboxylic acid cycle (oxidative pathway). In animals where the brain glucose was the lowest (Fig 31, dark green and blue curves) lactate tended to increase, indicating that mitochondrial oxidative pathway was overwhelm and needed additional anaerobic glycolysis for ATP production. This would be a mechanism leading to type 1 "metabolic crisis" with low glucose, high lactate and expected high L/P ratio. On the other hand animals with higher levels of glucose (Fig 31, turquoise and red curves), lactate concentrations remained stable indicating that all glucose is consumed in the oxidative pathway as during isolated CSDs (type 2 "metabolic crisis").

Chapter 6

Conclusion

These experiments described the metabolic and micro-vascular consequences of CSDs depending on pre-CSD brain state, either a normal or a traumatized brain tissue. We also gave an overview of the modifications generated by clusters of depolarizations after brain trauma, which are supposed to be associated with the worst outcome in human pathology [225].
The view whereby micro-vascular response is influenced by pre-CSD CBF levels also applies to carbohydrate and oxygen metabolism:

- In a cortex with high energetic supply (CBF, oxygen and glucose), a single depolarization will trigger transient modifications characterized by (1) an increase in CBF, (2) an increase in $CMRO_2$ that does not exceed oxygen supply. Therefore $PbtO_2$ variations will mimic those of CBF. (3) A physiologic aerobic hyper-glycolysis with a brain glucose decrease and a delayed prolonged lactate increase. Brain tissue will then recover from this huge metabolic challenge approximately 20-30 min after the depolarization.

- When energetic supplies are inadequate, then (1) a paradoxical decreased micro-vascular response can take a variety of forms depending on CBF level. (2) $CMRO_2$ starts to exceed oxygen supply. Then $PbtO_2$ variations will range between a biphasic pattern with a subsequent decrease, to a monophasic decrease, depending on pre-CSD $PbtO_2$ levels. (3) Hyper-glycolysis still occurs, however energetic needs seems to drive every glucose molecule to the mitochondria. This pathological reaction could be related to the type 2 "low pyruvate" state observed with cMD in humans, where brain glucose, lactate and pyruvate are low and the L/P is high. To confirm this, we will need to study the conditions with pyruvate biosensors.

- Finally when energetic supplies are missing like in the ischemic core, then terminal depolarization with terminal ischemia will occur. $PbtO_2$ is also very low, and at these oxygen concentrations oxidase-based biosensors will not be reliable. Maybe cMD will provide such informations in the future.

Part VII

Conclusion and perspectives

Katsushika Hokusai, Under the Wave off Kanagawa - Thirty-six Views of Mt. Fuji.

Chapter 1

General conclusion

At the beginning of my thesis we made the hypothesis that CSDs have different neuro-chemical consequences in healthy tissue compared to a "traumatic penumbra" where neuronal death is expected to occur. Our second hypothesis was that clusters of CSDs would have worse consequences after TBI than isolated CSDs.
Then, our objectives were to:

1. Describe the metabolic (glucose, lactate, $PbtO_2$) and micro-vascular patterns observed during and after CSDs in a healthy cortical tissue.
2. Report how these patterns are altered during spontaneous isolated CSDs after severe TBI.
3. Determine if cluster of CSDs would have worse consequences.
4. Study CSDs direct toxicity through glutamate release or ROS.

So far we achieved the description on isolated and clusters of CSDs in regard to metabolic and micro-vascular changes, and the results can be summarized as follow.
A fundamental step was the analysis of severe LFPI consequences on brain parenchymal to define the "traumatic penumbra" where to study CSDs. We found the most affected areas after LFPI to be in the thalamus, the CA3 area and the temporal cortex ipsi-lateral to the injury. These regions exhibited, 7days after the trauma, 40-60% neuronal loss and an infiltration with activated microglia. We then chose to study CSDs in the temporal cortex, located lateral to the impact, which mimic a cortical "traumatic penumbra". Moreover we found that the metabolic state of this "traumatic penumbra" resemble those of patients with bad outcomefollowing brain injury with low brain glucose concentrations, and low regional CBF.

However, before *in vivo* experiments analysis, we questioned the validity of oxidase-based biosensors as experimental conditions were supposed to be different between the *in vitro* calibration and the *in vivo* implantation. It was expected that temperature, and oxygen concentration available, would impact the oxidase responses, despite it was previously admitted that *in vivo* oxygen concentrations were not limiting the enzymatic reactions. Surprisingly, we found that all oxidase-based biosensors were significantly impacted by oxygen concentrations as well as temperature. Therefore we developed algorithms to compute real brain concentrations of glucose or lactate from oxidative currents, depending on oxygen and temperature.

Once we were confident about both our TBI model and the monitoring techniques reliability, we then described CSDs neuro-chemical and micro-vascular consequences in different conditions: (1) Isolated CSDs in a normal brain, (2) isolated CSDs after a severe LFPI or (3) repeated CSDs in clusters after a severe LFPI.
Our data provide a clear metabolic signature of CSDs in the healthy brain close to an aerobic hyper-glycolysis. We observed a decrease in brain glucose concentrations and a subsequent

delayed increase in brain lactate concentrations. The $PbtO_2$ displayed a transient increase following the hyperemia and was associated with an increase in $CMRO_2$. Brain metabolism recovered pre-CSD levels after 20-30 min.
In the "traumatic penumbra" following a severe LFPI, the basal brain glucose concentrations were lower than in healthy tissue and nonetheless decreased when a CSD was passing through. Unlike in healthy brain tissue, brain lactate concentrations exhibited an initial biphasic pattern. No delayed increase was observed but rather a decrease in extracellular brain lactate concentrations that might sign an intracellular consumption. $PbtO_2$ had a similar response than that of lactate, with an initial biphasic pattern during the depolarization and a subsequent prolonged decrease. 20-30min after the depolarization onset in the traumatized cortex, lactate concentrations and $PbtO_2$ remained lower compared to pre-CSD levels. We made the hypothesis that such pattern could underpin "low pyruvate" states observed in some patients with cMD and that are currently poorly understood.
Finally clusters of CSDs after TBI led to a progressive increase in CBF, $CMRO_2$ and $CMR_{glucose}$. However brain lactate concentrations had miscellaneous variations, depending on how brain parenchyma can sustain such energetic expenditure.

Our data confirm that CSDs have different consequences on brain tissue depending on the pre-CSD state, with an altered metabolic response in the "traumatic penumbra". Clusters of CSDs led to a prolonged metabolism alteration, which can eventually turn into a pattern looking like a metabolic crisis.
These results rose several questions about CSDs toxicity and therapeutic actions to consider:

- Does CSDs lead to additional neuronal damage in an injured brain tissue?
- Are these damages due to a direct toxicity of CSDs through glutamate and/or ROS? Or is it only due to an excessive energetic expenditure?
- Is there a way to help brain tissue to recover from CSDs? Should we block CSDs occurrence?

Chapter 2

Perspectives

2.1 Does CSD lead to neuronal damage?

The question whether spontaneous CSDs occurring after brain injury would lead to additional secondary neuronal damage is hard to answer. It seems complicated to trigger specifically such interlinked phenomena triggered by primary injuries and/or spreading depolarizations. In fact therapeutic agent like NMDAR antagonists, usually used to block CSDs [267, 268, 269] may act on several mechanisms independent from the depolarization.
Therefore, instead of decreasing the CSD rate, we will try to address the consequences of increasing CSDs rate after LFPI on neuronal density and glial cells behavior.

2.2 What about glutamate and ROS during CSDs?

2.2.1 Introduction

The first evidence of glutamate release in the extracellular space after CSDs were made on the retina by Van Harreveld and Fifková in 1970 [265]. A transient increase in extracellular glutamate concentrations during CSDs was confirmed later with rapid sampling cMD *in vivo* in rats [266]. Hypothesis about glutamate implications during CSDs have been mainly based on indirect observations, using NMDAR blockers to stop glutamate transmission [267, 268, 269].
More recently a few studies described glutamate dynamics with a high temporal resolution during CSD in healthy animals or after middle cerebral artery occlusion. A glutamate transient release ($11.6 \pm 1.3 \mu M$) was described by Hinzman et al. in 2015 with enzyme based biosensors, in healthy rats that was able to triggered neuronal lesions if glutamate uptake was inhibited [240]. They also reported a glutamate release during anoxic or peri-infarct depolarization which duration was related to the depolarization length [240]. Based on these observations, the authors suggested that CSDs can mediate excitotoxicity after brain aggression.
The term ROS is a collective one that includes not only oxygen-centered radicals such as superoxide ion ($O_2^{\cdot -}$), $NO^{\cdot}$ and $OH^{\cdot}$ but also some non-radical derivatives, such as H_2O_2, singlet oxygen, and hypochlorous acid. $O_2^{\cdot -}$ can be converted to H_2O_2 spontaneously or via superoxide dismutase (SOD) [360], and may also react with $NO^{\cdot}$ to give peroxynitrite [361]. ROS, such as $O_2^{\cdot -}$, NO and H_2O_2, are involved in physiological phenomena such as apoptosis [362], cell growth [363], modulation of long term potentiation [364, 365], and signal transmission [366, 367] or neuro-vascular coupling [73]. However, the excess of ROS production has damaging effects such as membrane lipid peroxidation, protein oxidation and DNA degradation [368, 369].
Only a few studies described H_2O_2 or NO increase after CSD using fluorescent probes usually without any time resolution [255, 370].

In preliminary experiments we aimed to describe real time glutamate and ROS modifications triggered by CSDs in the normal brain or after a severe TBI.

2.2.2 Methods

During these analysis, we followed the same experimental design as described in the previous part VI. We studied brain glutamate concentration in the same 3 experimental groups:

- **KCl** experimental condition: CSDs were triggered by a transient increase in potassium concentration of the saline solution that was infusing the cortical surface, by stirring a drop of 1M KCl.
- **TBI**$_{ISOLATED}$ experimental condition: Spontaneous CSDs occurred after a severe LFPI.
- **TBI**$_{CLUSTER}$ experimental condition: Clusters of CSDs were triggered by 1M KCl apposition on the cranial window.

H_2O_2 measurements have been performed only in the KCl and the TBI$_{ISOLATED}$ groups, whereas only a few preliminary experiments of NO recordings were made in the KCl group.
Extracellular H_2O_2 measurements were made using the comparison of oxidative currents obtained by two different biosensors: (1) A control biosensors (covered only with albumin), since the oxidative current is based on ambient H_2O_2 oxidation on the platinum surface, and (2) a catalase covered biosensor, where catalase decomposed H_2O_2 in water and oxygen ($2 \cdot H_2O_2 \mapsto 2 \cdot H_2O + O_2$). These sensors are only sensitive to all other non-specific current modifications, and had a lower increase in oxidative current during CSDs (Fig 32 A, red curve). Comparing their signals gave us the current coming from extracellular H_2O_2.
NO detection was made with carbon fibre sensors (100 μm length, 7 μm diameter). The active part of the electrode undergoes various treatments, including a porphyrines-nickel layer and Methyltrimethoxysilane screening layer [371].
Extracellular brain glutamate concentrations were obtained using oxidase-based biosensors, which were tested before and after each *in vivo* experiments to ensure that the sensitivity and specificity remained stable all along the experiment. Due to the very low extracellular concentrations of glutamate in the cortex, glutamate biosensors were implanted *in vivo* close to a control biosensor (i.e. covered only with BSA). Signals from control sensors were then subtracted from those of the glutamate biosensor, to remove non-specific current modifications.

2.2.3 Reactive oxygen species release

We were able to record a 1.12 $\mu mol/L$ [0.37;2.48] H_2O_2 transient release during 22.5 sec [7.5;36] in the KCl group. In the TBI$_{ISOLATED}$ group a similar release was also recorded of 1.78 $\mu mol/L$ [0.51;2.24] (W=21, p=1), during 33 sec [16.5;43] (W=15.5 p=0.8). These values are close to those reported by Viggiano et al. in 2011 with cMD after repeated CSD (i.e. 10-20% increase from a baseline of 9.1 $\mu mol/L \equiv 0.9 - 1.8 \mu mol/L$) [370]. They also reported that this increase in H_2O_2 was associated with an increase in SOD activity and a subsequent decrease in O_2^- concentrations [370].
In a few preliminary experiments we used carbon micro-electrodes to record extracellular NO modifications during CSD after KCl cortical apposition (like in the KCl group). 30-40 min after the first depolarization we perfused the neuronal NO-synthase inhibitor (L-NNA) during 45 min and triggered a second CSD with KCl.
The first depolarization triggered a transient increase in extracellular NO (Fig 32 B, black curve) that was suppressed during the second CSD by L-NNA cortical infusion (Fig 32 B, red

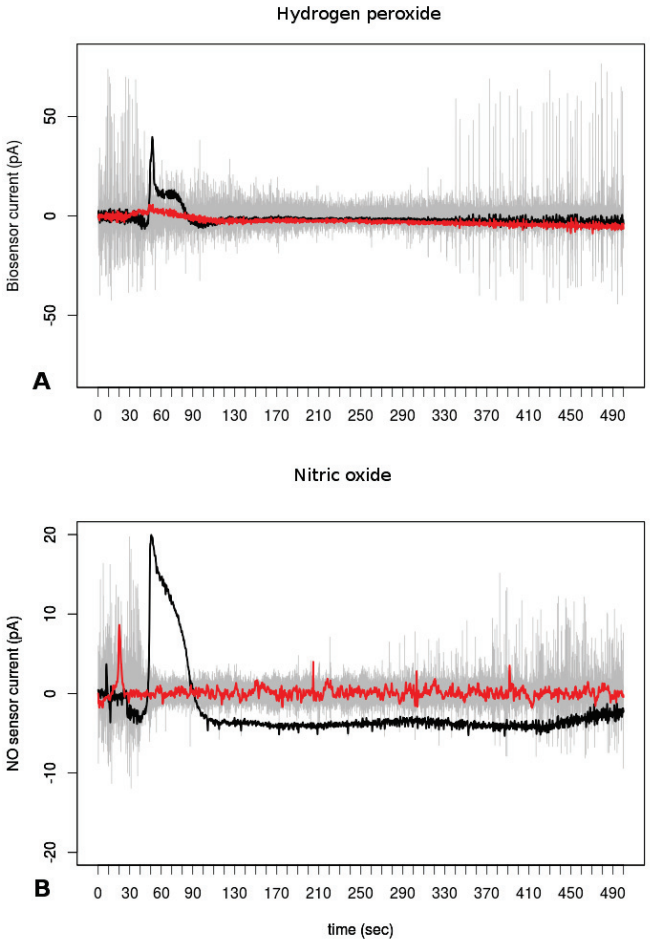

Figure 32: **Hydrogen peroxide and nitric oxide sensors signals during a CSD**. **A. Hydrogen peroxide**: The DC (0-0.5 Hz) of a micro-electrode biosensor covered only with albumin (no enzymatic layer) is represented in black. This signal represent the oxidative current generated by extracellular H_2O_2 oxidation on the platinum surface. The AC (0.5-30Hz) LFPot is also recorded by the electrode and the gray curve point out the depression part of the CSD. To control for non-specific modifications a second sensor covered with catalase (not sensitive to H_2O_2) was placed close to the other biosensor. DC signal is represented in red. **B. nitric oxide**: the AC signal (0.5-30 Hz) of the NO sensitive sensor is represented in gray whereas the DC signal (0-0.5 Hz) is in black. Note the increase in oxidative current during the depression of LFPot that represent NO release in the extracellular space. A second CSD was triggered after an NO synthase inhibitor (L-NNA) cortical infusion. The signal recorded from the same NO sensitive sensor, during the second depolarization, is represented in red. The increase in oxidative current is abolished after L-NNA infusion.

curve). These results are in agreement with an NO release produced by the neuronal NO-synthase during CSDs. NO release during CSDs has been evidenced with fluorescent [255]. If NO release is blocked by L-NNA or scavenged by hemoglobin, then the high K^+ concentration would lead to a vaso-constriction through SMCs depolarization [80, 83].

2.2.4 Glutamate release

Every isolated depolarization (KCL or TBI) triggered a transient extracellular glutamate concentration increase. Extracellular glutamate peaked to 7.7 $\mu mol/L$ [7.1;15.9] in control animals from a baseline concentration of 2.49 $\mu mol/L$ [0.8;5.6] (KCl). Baseline brain glutamate concentrations following the LFPI tended to be higher than in KCL group (5.2 $\mu mol/L$ [3.7;8.9], W=108 p=0.09). Glutamate release during spontaneous depolarization after LFPI was also larger: 32.4 $\mu mol/L$ [26.8;39.9] (W=16 p=0.046, Fig 33). Similar concentrations have recently been observed by Hinzman et al. with larger biosensors (i.e. 11.6 $\mu mol/L \pm 3$) [240]. Using a different ischemic model, these authors did not find that the amplitude of the glutamate release was enhanced during peri-infact depolarizations [240]. However they did not measure the $PbtO_2$ in the cortex where they implanted their biosensors. As presented in the previous part V, oxidase based biosensors are dependent on oxygen concentrations. Thus, as previously mentioned, the lower the oxygen the lower the oxidative current. Therefore it is possible that they had underestimated the glutamate release in the ischemic core as well as in the penumbra area where $PbtO_2$ was expected to be lower compared to normal brain tissue [372].

Overall, the glutamate released peak occurred 12 sec [2;36.5] before the hyperemic acme and 11.5 sec [2;26] after the depolarization nadir. The duration of the glutamate release was not different in the KCl (118.5 sec [54.1;218.9]) and in the $TBI_{ISOLATED}$ group (125.5 sec [87;147], W=35 p=0.765).

During repeated CSDs in clusters ($TBI_{CLUSTER}$), the glutamate release decreased from 18.3 $\mu mol/L$ [2.9;32.3] to 3.1 [1.56.7] (repeated measures ANOVA, df=9 F=5.2 p«0.001), without increase in basal glutamate concentrations. Similar processes have also been suggested during repeated peri-infact depolarization [240].
High levels of extracellular glutamate was expected to mediate neuronal death through NMDAR over activation [127, 125]. However NMDAR inward current can be modulated by several extracellular co-factors such as D-Serine, which binds the glycine binding site on the NR1 subunit (Fig 6). The lower the extracellular D-Serine concentration, the lower the NMDAR inward current [125]. Therefore further investigations on NMDAR co-agonist levels during CSDs may provide more information about their toxicity.

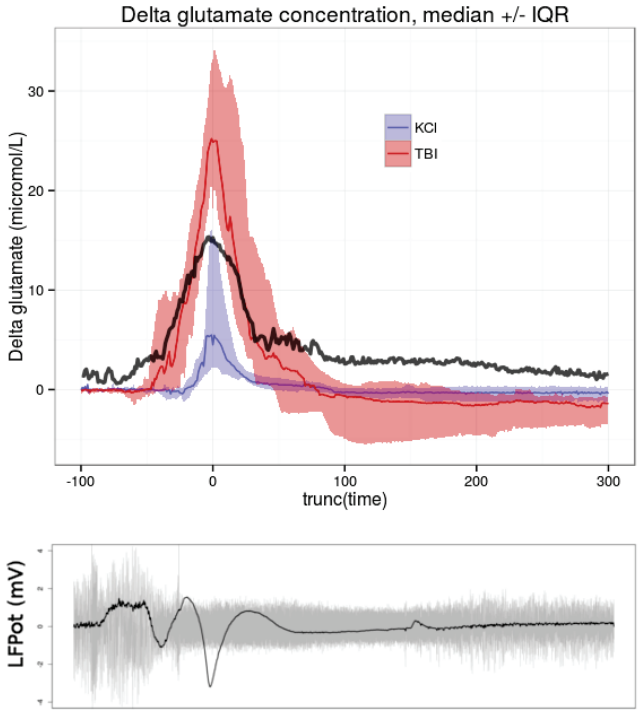

Figure 33: **Glutamate release following isolated CSDs**.
The red curves represent values observed after a severe LFPI ($TBI_{ISOLATED}$ group), whereas the blue curves represent the signals in control animals (KCl group). The black curve point out the micro-vascular response after TBI as recorded by the LDF probe. The graphic represent a 400 seconds recording surrounding the depolarization.
The lower panel is an example of LFPot recordings during CSDs. The gray curve represents the AC signal (0.5-50Hz) and the black curve the DC signal (0.02-0.5Hz) in mV.

2.3 Fuelling the injured brain?

Based on our preliminary results, it is unclear if CSDs have a direct toxicity on injured brain tissue via glutamate or ROS. However the metabolic modifications described in the part VI argue in favor of an indirect toxicity through excessive energetic expenditure. Therefore we chose to pool our efforts on a way to improve altered brain metabolism.
The objective of a first set of experiments will be to determine how different oxygen supply (15% to 100% oxygen gas mixture) impact brain carbohydrate concentrations. Indeed several oxygen conditions are interchangeably used during *in vivo* or *ex vivo* (e.g. brain slice) experiments, that could underpin some results discrepancies. Moreover the influence of hypoxia will give further insight on brain adaptations to high altitude in healthy subjects or after TBI.
Recent studies observed that during a systemic stress induced by a severe TBI, the large

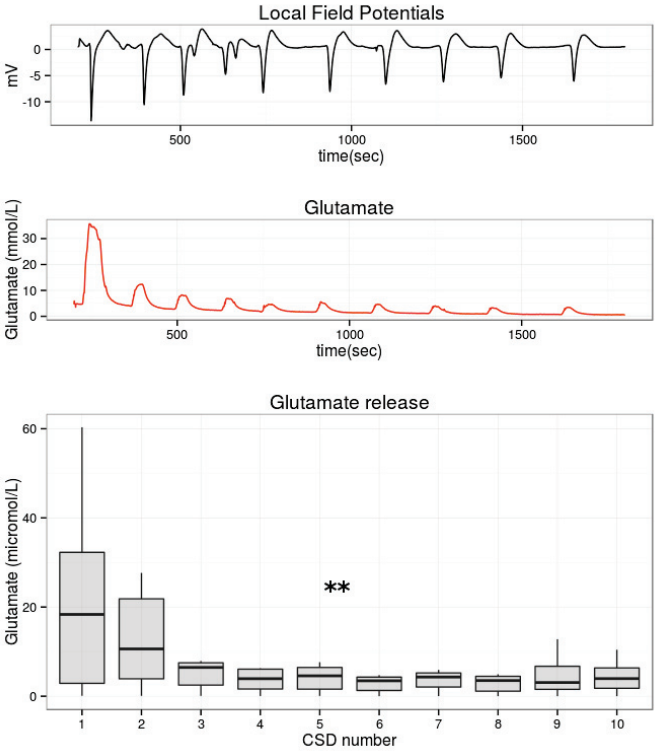

Figure 34: **Glutamate release modifications during a cluster of CSDs**.
Local Field Potentials: Example of the LFPot recorded during a cluster of 10 CSDs, with the subsequent **glutamate concentration** modifications during each CSD.
glutamate release: boxplots of maximum glutamate release during each CSD in a cluster of 10 depolarizations.
** p«0.001 repeated measures ANOVA

majority of brain carbohydrate consumption derives from systemic lactate [373, 115]. The monocarboxylate transporters are responsible for the transport of ketones, pyruvate and lactate across the BBB and cell membranes. As MCT brain expressions can increase after TBI [97], it has been suggested that lactate act as a metabolic shuttle between stressed organs (e.g. brain) and those where glycogen is stored (e.g. liver or muscles). Even if systemic lactate infusion seems to improve cMD parameters after TBI [374], the impact of such therapeutic intervention and their way of actions at the cellular and tissue levels may be clarified.
Therefore subsequent experiments will focus on the effect of different systemic carbohydrate infusion on basal brain metabolism in a normal or injured brain. Moreover, we will intend to study these therapeutic intervention on brain metabolism parameters during CSDs.

Part VIII

R package documentation

Package 'BrainMetabolism'

August 23, 2015

Type Package

Title calculate brain metabolism rates from extracellular conentrations

Version 1.0

Date 2015-03-03

Author baptiste balanca

Maintainer baptiste balanca <baptiste.balanca@gmail.com>

Depends R (>= 3.1.0), ggplot2, stats

Imports ggplot2

Description calculate CMRO2, CMRgluc, mitochondrialPO2 ... provide functions to process data from biosensors

License MIT

NeedsCompilation no

R topics documented:

BrainMetabolism-package . . . 2
auc . . . 3
calibration . . . 3
CMRGluc.calc . . . 4
CMRO2.calc . . . 5
correction.Temp . . . 6
correction.TPO2 . . . 6
IO2.calc . . . 7
L.calc . . . 8
noise.na . . . 9
OGI.calc . . . 9
polyfit . . . 10
polyval . . . 10
roll.funct . . . 11

Index **12**

`BrainMetabolism-package` *calculate brain metabolism rate from extracellular conentrations*

Description

calculate CMRO2, CMRgluc, mitochondrialPO2 ...
provide functions to process data from biosensors

Details

Package:	BrainMetabolism
Type:	Package
Version:	1.0
Date:	2015-03-03
License:	MIT

Author(s)

Baptiste Balanca
Lyon Neuroscience Research Center
Team TIGER

Maintainer: baptiste balanca <baptiste.balanca@gmail.com>

References

Piilgaard Lauritzen JCBFM (2009) 29, 1517
Gjedde et al JCBFM (2005) 25(9), 1183
Gjedde et al JCBFM (2000) 20(4), 747
Du et al JCBFM 2012 32(9)
Gruetter et al J Neurochem 1998 70(1)
balanca et al (2016) in preparation

Examples

```
MyTPO2<-23 #mmHg
MyLDF<-95 #percent
MyL<-L.calc(CMR=219, TPO2=MyTPO2, P50=36, h=2.7, Ca=8, cbf=53 )
MyCMRO2<-CMRO2.calc(LDF=MyLDF, MyTPO2, P50=36, h=2.7, Ca=8, L=MyL,cbfbase=53)

MyGlucBrain<-1 #mM
MyGlucPlasma<-6 #mM
MyCRMgluc<-CMRGluc.calc(MyGlucbrain, Vd=0.77, Kt=13.4, Tmax=1.35, Gplasma=MyGlucPlasma)
```

auc *area under the curve*

Description

take a numeric vector and return the area under the curve (AUC)

Usage

```
auc(data, pos = TRUE)
```

Arguments

data	: a numeric vector
pos	: a logical value. if TRUE (default) AUC is calculated on positive values, if FALSE on negative values.

Value

auc : area under the curve

max/min : maxiaml value (or minimal if pos=FALSE)

calibration *Sensor calibration*

Description

Fit an nth degree polynom

$$(y = C_n X^n + C_{n-1} X^{n-1} + \ldots + C_1 X + C_0)$$

to vectors x=volt and y=concentration

Usage

```
calibration(volt, mol, order = 1)
```

Arguments

volt	: a numeric vector of the biosensor voltage
mol	: a numeric vector of the molecule conentration in the medium (x and y must have the same length)
order	: a numeric value for the polynomial degree. default is one.

Value

Coef : coeficients in ascending order (i.e. C0, C1, C2, . . . , Cn)

R2 : goodness of fit

`CMRGluc.calc` *CMRGluc calculation*

Description

take extracellular glucose concentration and return brain metabolic rate of glucose, using a reversible Michaelis-Menten model equation:

Usage

```
CMRGluc.calc(Gbrain, Vd = 0.77, Kt = 1.4, Tmax = 1.27, Gplasma = 7.3)
```

Arguments

`Gbrain`	: a vector/numeric value of extracellular glucose concentration in mmol/L, time decay
`Vd`	: glucose brain space diffusion (default is 0.77 ml/g)
`Kt`	: glucose apparent maximal transport rate (default is 1.4 mmol/L)
`Tmax`	: the apparent maximal transport rate (default is 1.27 micormol/g/min)
`Gplasma`	: plasma glucose concentration (default=6mmol/L)

Details

$$G_{brain} = V_d \frac{\left(\frac{T_{max}}{CMR_{gluc}} - 1\right) \times G_{plasma} - K_t}{\frac{T_{max}}{CMR_{gluc}} + 1}$$

Value

CMRGlucose : numeric value of Cerebral metabolic rate of glucose in micromol/g/min

References

Morgenthaler et al. Neurochem Int 2006, 48

Ori et al. Anesthesiology 1986, 65(2)

Duarte et al. Front in Neuroenrgetics 2009, 1

Gruetter et al J Neurochem 1998, 70(1)

CMRO2.calc *CMRO2 calculation*

Description

take tissue oxygen pressure (tPO2) and cerebral blood flow (relative value, e.g. laser doopler lowmetry BPU)

Usage

```
CMRO2.calc(LDF, TPO2, P50 = 36, h = 2.7, Ca = 8, L = 4.03,
  cbfbase = 53)
```

Arguments

LDF	: a vector/numeric value of LDF (percentage of baseline, i.e: basal value is 100 %)
TPO2	: a vector/numeric value of brain oxygnen pressure (mmHg)
P50	: half-saturation tension of hemoglobine (default is 36 mmHg)
h	: hill's coeficient
Ca	: oxygen arterial concentration (default is 8 micromol/ml)
L	: effective diffusion coefficient of oxygen in brain tissue, default is 4.03 micomol/100g/mmHg, but one should use the L.calc function to calculate it from their data.
cbfbase	: basal expected value of CBF (default is 53 ml/100g/min wich was used to calculate L) LBF and TPO2 must be the same length

Details

$$PbtO_2 = P_{50} \cdot \sqrt[h]{\frac{2 \cdot C_a \cdot CBF}{CMRO_2} - 1} - \frac{CMRO_2}{2 \cdot L}$$

Value

CMRO2 : vector/numeric value of Cerebral Metabolic Rate of Oxygen in micromol/100g/min

References

Gjedde et al JCBFM (2005) 25(9), 1183

Piilgaard et al JCBFM (2009) 29, 1517

`correction.Temp` *Temperature correction*

Description

Biosensor enzymatic reaction, that underpin amperometric measures, has a sigmoid relation to temperature :

$$m(x, P) = \frac{P_1 + (P_2 - P_1)}{(1 + \exp((P_3 - x)/P_4))}$$

parameters are different for each enzyme and has been measured in vitro.
This function correct biosensor signal depending on temperature conditions during calibration and experimentation

Usage

```
correction.Temp(x, enz, temp.calib = 25, temp.exp = 37)
```

Arguments

`x`	: a numeric vector of the biosensor voltage
`enz`	: enzyme on the biosensor i.e. "glucose", "lactate", "glutamate, "daao"
`temp.calib`	: temperature of the medium where sensor has been calibrated the default is 25^oC (i.e. room temperature).
`temp.exp`	: temperature of the medium during experiment the default is 37^oC (i.e. animal central temperature)

Value

volt.temp.cor : a vector of corected x values for temperature

References

balanca et al 2015

`correction.TPO2` *Oxygen Tension correction*

Description

Biosensor enzymatic reaction, that underpin amperometric measures, has an asymptotic relation to oxygen tention in the medium :

$$m(PO_2, P) = P_1 + (P_2 - P_1) \times \exp(-\exp(P_3)PO_2)$$

parameters are different for each enzyme and has been measured in vitro
This function correct biosensor signal depending on PO2 conditions during calibration and experimentation

Usage

```
correction.TPO2(x, enz, TPO2 = 28)
```

Arguments

x	: a numeric vector of the biosensor voltage
enz	: enzyme on the biosensor i.e. "glucose", "lactate", "glutamate, "daao"
TPO2	: oxygene tension in the medium during the experiment. the default is 30mmHg measured in anesthetized rat brain.

Value

volt.O2.cor : a vector of corected x values for TPO2

References

balanca et al 2015

IO2.calc *Oxidative index calculation*

Description

take CMRO2 and LDF to give an oxidative index

Usage

```
IO2.calc(CMRO2, LDF, cbfbasal = 53)
```

Arguments

CMRO2	: vector/numeric value of Cerebral metabolic rate of oxygen in micromol/100g/min
LDF	: a vector/numeric value of LDF (percentage from baseline, baseline is 100 %)
cbfbasal	: basale expected value of CBF from the litterature (default is 53 ml/100g/min wich was used to calculate L)

Details

$$IO2 = CMRO2/(cbfbasal * LDF)$$

Value

IO2 : oxidative index, reflect the degree of flow metabolism coupling

References

Gjedde et al JCBFM (2000) 20(4), 747

`L.calc` *Calculate the effective diffusion coefficient of oxygen in brain tissue, L.*

Description

take CMRO2 and cerebral blood flow (CBF) to calculate the effective diffusion coefficient of oxygen in brain tissue (L)

Usage

```
L.calc(CMR = 219, TPO2, P50 = 36, h = 2.7, Ca = 8, cbf = 53)
```

Arguments

`CMR`	: Cerebral Metabolic Rate of Oxygen, default is 219 micro mol/100
`TPO2`	: numeric value of brain oxygnen pressure (mmHg)
`P50`	: half-saturation tension of hemoglobine (default is 36 mmHg)
`h`	: hill's coeficient
`Ca`	: oxygen arterial concentration (default is 8 micromol/ml)
`cbf`	: expected value of CBF (default is 53 ml/100g/min wich was used to calculate L

Details

$$PbtO_2 = P_{50} \cdot \sqrt[h]{\frac{2 \cdot C_a \cdot CBF}{CMRO_2} - 1} - \frac{CMRO_2}{2 \cdot L}$$

Value

L : numeric value of the effective diffusion coefficient of oxygen in brain tissue micomol/100g/mmHg

References

Gjedde et al JCBFM (2005) 25(9), 1183

Piilgaard et al JCBFM (2009) 29, 1517

`noise.na` *Remove artifacts from biosensor signal, based on data's standar deviation*

Description

Remove artifacts from biosensor signal, based on data's standar deviation

Usage

```
noise.na(data, z = 20, width = 30)
```

Arguments

`data`	: a numeric vector
`z`	: a numeric value. Number of SD over which values should be exculded
`width`	: size of the window used to roll SD over data (see roll.funct)

Value

a vector with NA remplacing exculded values

`OGI.calc` *Oxygene Glucose index (OGI)*

Description

take CMRO2 and CMRGlucose to give an OGI

Usage

```
OGI.calc(CMRO2, CMRGluc)
```

Arguments

`CMRO2`	: vector (numeric value) of Cerebral metabolic rate of oxygen in micromol/100g/min
`CMRGluc`	: a vector (numeric value) of CMRGlucose in micromol/100g/min

Details

$$OGI = CMRO2/CMRGlucose$$

Value

OGI

polyfit *polynomial fit*

Description

Fit a nth degree polynom

$$(y = C_n X^n + C_{n-1} X^{n-1} + \ldots + C_1 X + C_0)$$

to vectors x and y

Usage

```
polyfit(x, y, order = 1)
```

Arguments

x	: a numeric vector
y	: a numeric vector (x and y must have the same length)
order	: a numeric value for the polynomial degree. default is one.

Value

model formula

Coef: coeficients in ascending order (i.e. C0, C1, C2, ..., Cn)

R2: Rsquare

polyval *polynomial evaluation*

Description

evaluation a nth degree polynom

$$(y = C_n X^n + C_{n-1} X^{n-1} + \ldots + C_1 X + C_0)$$

at given values of x

Usage

```
polyval(x, coef)
```

Arguments

x	: a numeric vector
coef	: a n dimention vector corresponding to the polynom coefficient (ascending order, i.e. C0, C1, C2, ... , Cn)

Value

y

`roll.funct` *apply a function FUN on a rooling windows of a vector*

Description

apply a function FUN on a rooling windows of a vector

Usage

```
roll.funct(data, width, FUN, size = T, ...)
```

Arguments

`data`	: a numeric vector
`width`	: the size of the rolling window
`FUN`	: the function to apply
`size`	: a logical value indicating if the returned vector have the same length as original data. default is TRUE.
`...`	: additional argument to pass to the FUN

Value

a vector with FUN result

Index

∗Topic **package**
BrainMetabolism-package, 2

auc, 3

BrainMetabolism
(BrainMetabolism-package), 2
BrainMetabolism-package, 2

calibration, 3
CMRGluc.calc, 4
CMRO2.calc, 5
correction.Temp, 6
correction.TPO2, 6

IO2.calc, 7

L.calc, 8

noise.na, 9

OGI.calc, 9

polyfit, 10
polyval, 10

roll.funct, 11

Part IX

Communications and publication

This work has been the subject of one publication in an international journal:

- Neuronal loss as evidenced by automated quantification of neuronal density following moderate and severe traumatic brain injury in rats. Balança B, Bapteste L, Lieutaud T, Ressnikoff D, Guy R, Bezin L, Marinesco S.*J Neuroscience Research*, 2016 Jan;94(1):39-49.

And several communications in national or international congress:

- **SFAR 2013 (R207)**: Exploration électrocorticographique et microvasculaire des courants corticaux lents de dépolarisation (CSD) après un traumatisme crânien sévère chez le rat. *B. BALANCA, C. MAUCLER, A. MEILLER, T. LIEUTAUD, S. MARINESCO*

- **SFAR 2014 (R037)**: Couplage neuro-vasculaire et production d' H_2O_2 lié aux «cortical spreading depolarization» après un traumatisme crânien expérimental sévère chez le rat. *B BALANCA, S MARINESCO, A MEILLER, T LIEUTAUD*

- **SFAR 2015 (R150)**: Modifications métaboliques lié aux dépolarisations corticales envahissantes après un traumatisme crânien sévère chez le rat: une origine des crises métaboliques? *B BALANCA, S MARINESCO, A MEILLER, T LIEUTAUD*

- **FENS 2014**: Cortical spreading depolarization consequences on cerebral blood flow and metabolism. *B. BALANCA, T. LIEUTAUD, A. MEILLER, S. MARINESCO*

- **COSBID 2014**: Cortical spreading depolarization consequences on cerebral blood flow, cortical oxygenation and metabolism: comparison of healthy and traumatized brain. *B BALANCA, T LIEUTAUD, A MEILLER, S MARINESCO.*

- **COSBID 2015**: Real time glutamate dynamics during cortical spreading depolarizations. *B. BALANCA, T. LIEUTAUD, A. MEILLER, S. MARINESCO*

Bibliography

[1] B. Roozenbeek, A. I. Maas, and D. K. Menon, "Changing patterns in the epidemiology of traumatic brain injury.," *Nature reviews. Neurology*, vol. 9, no. 4, pp. 231–236, 2013.

[2] D. Hirtz, D. Thurman, G. K, M. Mohamed, A. Chaudhuri, and R. Zalutsky, "How common are the "common" neurologic disorders?," *Neurology*, vol. 68, no. 5, pp. 326–337, 2007.

[3] J. Olesen, A. Gustavsson, M. Svensson, H. U. Wittchen, B. Jönsson, C. study group, and E. B. Council, "The economic cost of brain disorders in europe.," *European journal of neurology : the official journal of the European Federation of Neurological Societies*, vol. 19, no. 1, pp. 155–162, 2012.

[4] V. Y. Ma, L. Chan, and K. J. Carruthers, "Incidence, prevalence, costs, and impact on disability of common conditions requiring rehabilitation in the united states: stroke, spinal cord injury, traumatic brain injury, multiple sclerosis, osteoarthritis, rheumatoid arthritis, limb loss, and back pain.," *Archives of physical medicine and rehabilitation*, vol. 95, no. 5, pp. 986–995.e1, 2014.

[5] D. Thurman and J. Guerrero, "Trends in hospitalization associated with traumatic brain injury.," *JAMA*, vol. 282, no. 10, pp. 954–957, 1999.

[6] J. A. Myburgh, D. Cooper, S. R. Finfer, B. Venkatesh, D. Jones, A. Higgins, N. Bishop, T. Higlett, A. T. B. I. S. A. I. for the Australian, and N. Z. I. C. S. C. T. Group, "Epidemiology and 12-month outcomes from traumatic brain injury in australia and new zealand.," *The Journal of trauma*, vol. 64, no. 4, pp. 854–862, 2008.

[7] L. Odgaard, I. Poulsen, L. P. Kammersgaard, S. P. P. Johnsen, and J. F. F. Nielsen, "Surviving severe traumatic brain injury in denmark: incidence and predictors of highly specialized rehabilitation.," *Clinical epidemiology*, vol. 7, pp. 225–234, 2015.

[8] T. S. Fu, R. Jing, S. R. McFaull, and M. D. Cusimano, "Recent trends in hospitalization and in-hospital mortality associated with traumatic brain injury in canada: A nationwide, population-based study.," *Journal of Trauma and Acute Care Surgery*, vol. Publish Ahead of Print, 2015.

[9] L. Orriols, B. Delorme, B. Gadegbeku, A. Tricotel, B. Contrand, B. Laumon, L. R. Salmi, E. Lagarde, and C. research group, "Prescription medicines and the risk of road traffic crashes: a french registry-based study.," *PLoS medicine*, vol. 7, no. 11, p. e1000366, 2010.

[10] J. P. Cuthbert, C. Harrison-Felix, J. D. Corrigan, S. Kreider, J. M. Bell, V. G. Coronado, and G. G. Whiteneck, "Epidemiology of adults receiving acute inpatient rehabilitation for a primary diagnosis of traumatic brain injury in the united states," *The Journal of Head Trauma Rehabilitation*, vol. 30, no. 2, pp. 122–135, 2015.

[11] A. I. Maas, E. W. Steyerberg, A. Marmarou, M. G. S, H. F. Lingsma, I. Butcher, J. Lu, J. Weir, B. Roozenbeek, and G. D. Murray, "IMPACT recommendations for improving the design and analysis of clinical trials in moderate to severe traumatic brain injury.," *Neurotherapeutics : the journal of the American Society for Experimental NeuroTherapeutics*, vol. 7, no. 1, pp. 127–134, 2010.

[12] E. W. Steyerberg, N. Mushkudiani, P. Perel, I. Butcher, J. Lu, M. G. S, G. D. Murray, A. Marmarou, I. Roberts, J. Habbema, and A. I. Maas, "Predicting outcome after traumatic brain injury: development and international validation of prognostic scores based on admission characteristics.," *PLoS medicine*, vol. 5, no. 8, p. e165; discussion e165, 2008.

[13] G. Teasdale and B. Jennett, "Assessment of coma and impaired consciousness. a practical scale.," *Lancet (London, England)*, vol. 2, no. 7872, pp. 81–84, 1974.

[14] L. F. Marshall, S. B. Marshall, M. R. Klauber, M. v. B. Clark, H. M. Eisenberg, J. A. Jane, T. G. Luerssen, A. Marmarou, and M. A. Foulkes, "A new classification of head injury based on computerized tomography," *Journal of neurotsurgery*, vol. 75, no. 1s, pp. S14–S20, 1991.

[15] L. Marshall, S. Marshall, M. Klauber, M. Van Berkum Clark, H. Eisenberg, J. Jane, T. Luerssen, A. Marmarou, and M. Foulkes, "The diagnosis of head injury requires a classification based on computed axial tomography.," *Journal of neurotrauma*, vol. 9 Suppl 1, pp. S287–S292, 1992.

[16] P. Vos, A. van Voskuilen, T. Beems, P. Krabbe, and O. Vogels, "Evaluation of the traumatic coma data bank computed tomography classification for severe head injury.," *Journal of neurotrauma*, vol. 18, no. 7, pp. 649–655, 2001.

[17] A. I. R. Maas, E. W. Steyerberg, I. Butcher, R. Dammers, J. Lu, A. Marmarou, N. A. Mushkudiani, G. S. McHugh, and G. D. Murray, "Prognostic value of computerized tomography scan characteristics in traumatic brain injury: Results from the IMPACT study," *Journal of Neurotrauma*, vol. 24, no. 2, pp. 303–314, 2007.

[18] G. M. TEASDALE, L. E. PETTIGREW, J. L. WILSON, G. MURRAY, and B. JENNETT, "Analyzing outcome of treatment of severe head injury: A review and update on advancing the use of the glasgow outcome scale," *Journal of Neurotrauma*, vol. 15, no. 8, pp. 587–597, 1998.

[19] K. M. Kinnunen, R. Greenwood, J. H. Powell, R. Leech, P. C. Hawkins, V. Bonnelle, M. C. Patel, S. J. Counsell, and D. J. Sharp, "White matter damage and cognitive impairment after traumatic brain injury.," *Brain : a journal of neurology*, vol. 134, no. Pt 2, pp. 449–463, 2011.

[20] C. L. Mac Donald, A. M. Johnson, D. Cooper, E. C. Nelson, N. J. Werner, J. S. Shimony, A. Z. Snyder, M. E. Raichle, J. R. Witherow, R. Fang, S. F. Flaherty, and D. L. Brody, "Detection of blast-related traumatic brain injury in U.S. military personnel.," *The New England journal of medicine*, vol. 364, no. 22, pp. 2091–2100, 2011.

[21] C. Salmond, D. Menon, D. Chatfield, G. Williams, A. Pena, B. Sahakian, and J. Pickard, "Diffusion tensor imaging in chronic head injury survivors: correlations with learning and memory indices.," *NeuroImage*, vol. 29, no. 1, pp. 117–124, 2006.

[22] F. Christidi, E. D. Bigler, S. R. McCauley, K. P. Schnelle, T. L. Merkley, M. B. Mors, X. Li, M. Macleod, Z. Chu, J. V. Hunter, H. S. Levin, G. L. Clifton, and E. A. Wilde, "Diffusion tensor imaging of the perforant pathway zone and its relation to memory function in patients with severe traumatic brain injury," *Journal of Neurotrauma*, vol. 28, no. 5, pp. 711–725, 2011.

[23] V. Perlbarg, L. Puybasset, E. Tollard, S. Lehéricy, H. Benali, and D. Galanaud, "Relation between brain lesion location and clinical outcome in patients with severe traumatic brain injury: a diffusion tensor imaging study using voxel-based approaches.," *Human brain mapping*, vol. 30, no. 12, pp. 3924–3933, 2009.

[24] D. Galanaud, V. Perlbarg, R. Gupta, R. D. Stevens, P. Sanchez, E. Tollard, N. M. de Champfleur, J. Dinkel, S. Faivre, S. Gustavo, B. Veber, V. Cottenceau, F. Masson, T. Tourdias, E. André, G. Audibert, E. Schmitt, D. Ibarrola, F. Dailler, A. Vanhaudenhuyse, L. Tshibanda, J. F. Payen, J. F. Le Bas, A. Krainik, N. Bruder, N. Girard, S. Laureys, H. Benali, L. Puybasset, N. I. for Coma Emergence, and R. Consortium, "Assessment of white matter injury and outcome in severe brain trauma: a prospective multicenter cohort.," *Anesthesiology*, vol. 117, no. 6, pp. 1300–1310, 2012.

[25] F. Masson, M. Thicoipe, T. Mokni, P. Aye, P. Erny, P. Dabadie, and A. G. for Severe Brain Injury Study, "Epidemiology of traumatic comas: a prospective population-based study.," *Brain injury*, vol. 17, no. 4, pp. 279–293, 2003.

[26] W. Mauritz, I. Janciak, I. Wilbacher, M. Rusnak, and A. S. T. S. Investigators, "Severe traumatic brain injury in austria IV: intensive care management.," *Wiener klinische Wochenschrift*, vol. 119, no. 1-2, pp. 46–55, 2007.

[27] R. Firsching and D. Woischneck, "Present status of neurosurgical trauma in germany.," *World journal of surgery*, vol. 25, no. 9, pp. 1221–1223, 2001.

[28] A. Ndiaye, M. Chambost, and M. Chiron, "The fatal injuries of car drivers.," *Forensic science international*, vol. 184, no. 1-3, pp. 21–27, 2009.

[29] J. H. Mena, A. I. Sanchez, A. M. Rubiano, A. B. Peitzman, J. L. Sperry, M. I. Gutierrez, and J. C. Puyana, "Effect of the modified glasgow coma scale score criteria for mild traumatic brain injury on mortality prediction: Comparing classic and modified glasgow coma scale score model scores of 13," *Journal of Trauma and Acute Care Surgery*, vol. 71, no. 5, pp. 11–85, 2011.

[30] M. TM, G. Teasdale, C. Weir, and E. Stewart, "Death after head injury: the 13 year outcome of a case control study.," *Journal of neurology, neurosurgery, and psychiatry*, vol. 82, no. 8, pp. 931–935, 2011.

[31] E. Beghi, "Overview of studies to prevent posttraumatic epilepsy.," *Epilepsia*, vol. 44 Suppl 10, pp. 21–26, 2003.

[32] S. L. Bratton, R. M. Chestnut, J. Ghajar, F. F. M. Hammond, O. A. Harris, R. Hartl, G. T. Manley, A. Nemecek, D. W. Newell, G. Rosenthal, J. Schouten, L. Shutter, S. D. Timmons, J. S. Ullman, W. Videtta, J. E. Wilberger, and D. W. Wright, "XIII. antiseizure prophylaxis," *Journal of Neurotrauma*, vol. 24, no. supplement 1, pp. S–83S, 2007.

[33] D. H. Lowenstein, "Epilepsy after head injury: an overview.," *Epilepsia*, vol. 50 Suppl 2, pp. 4–9, 2009.

[34] H. Wang, T. Xin, X. Sun, S. Wang, H. Guo, C. Holton-Burke, and Q. Pang, "Post-traumatic seizures—A prospective, multicenter, large case study after head injury in china," *Epilepsy Research*, vol. 107, no. 3, pp. 272–278, 2013.

[35] L. C. Frey, "Epidemiology of posttraumatic epilepsy: a critical review.," *Epilepsia*, vol. 44 Suppl 10, pp. 11–17, 2003.

[36] P. Vespa, M. Nuwer, V. Nenov, R. E, D. Hovda, M. Bergsneider, D. Kelly, N. Martin, and D. Becker, "Increased incidence and impact of nonconvulsive and convulsive seizures after traumatic brain injury as detected by continuous electroencephalographic monitoring.," *Journal of neurosurgery*, vol. 91, no. 5, pp. 750–760, 1999.

[37] N. R. Temkin, "Risk factors for posttraumatic seizures in adults.," *Epilepsia*, vol. 44 Suppl 10, pp. 18–20, 2003.

[38] N. Temkin, S. Dikmen, A. Wilensky, J. Keihm, S. Chabal, and H. Winn, "A randomized, double-blind study of phenytoin for the prevention of post-traumatic seizures.," *The New England journal of medicine*, vol. 323, no. 8, pp. 497–502, 1990.

[39] N. Temkin, S. Dikmen, G. Anderson, A. Wilensky, M. Holmes, W. Cohen, D. Newell, P. Nelson, A. Awan, and H. Winn, "Valproate therapy for prevention of posttraumatic seizures: a randomized trial.," *Journal of neurosurgery*, vol. 91, no. 4, pp. 593–600, 1999.

[40] M. Hours, M. Bernard, P. Charnay, L. Chossegros, E. Javouhey, E. Fort, D. Boisson, P. O. Sancho, and B. Laumon, "Functional outcome after road-crash injury: description of the ESPARR victims cohort and 6-month follow-up results.," *Accident; analysis and prevention*, vol. 42, no. 2, pp. 412–421, 2010.

[41] J. F. Mathé, I. Richard, and J. Rome, "Santé publique et traumatismes crâniens graves. aspects épidémiologiques et financiers, structures et filières de soins," *Annales Françaises d'Anesthésie et de Réanimation*, vol. 24, no. 6, pp. 688–694, 2005.

[42] J. Bernhardt, M. N. Thuy, J. M. Collier, and L. A. Legg, "Very early versus delayed mobilisation after stroke.," *The Cochrane database of systematic reviews*, no. 1, p. CD006187, 2009.

[43] S. Thornhill, G. Teasdale, G. Murray, M. J, C. Roy, and K. Penny, "Disability in young people and adults one year after head injury: prospective cohort study.," *BMJ (Clinical research ed.)*, vol. 320, no. 7250, pp. 1631–1635, 2000.

[44] M. Brooke, D. Patterson, K. Questad, D. Cardenas, and F. L, "The treatment of agitation during initial hospitalization after traumatic brain injury.," *Archives of physical medicine and rehabilitation*, vol. 73, no. 10, pp. 917–921, 1992.

[45] S. Kim, F. Manes, T. Kosier, S. Baruah, and R. Robinson, "Irritability following traumatic brain injury.," *The Journal of nervous and mental disease*, vol. 187, no. 6, pp. 327–335, 1999.

[46] I. J. Baguley, J. Cooper, and K. Felmingham, "Aggressive behavior following traumatic brain injury: how common is common?," *The Journal of head trauma rehabilitation*, vol. 21, no. 1, pp. 45–56, 2006.

[47] R. E. Jorge, R. G. Robinson, D. Moser, A. Tateno, C. Benedicto, and S. Arndt, "Major depression following traumatic brain injury.," *Archives of general psychiatry*, vol. 61, no. 1, pp. 42–50, 2004.

[48] R. E. Jorge, S. E. Starkstein, S. Arndt, D. Moser, C. Benedicto, and R. G. Robinson, "Alcohol misuse and mood disorders following traumatic brain injury.," *Archives of general psychiatry*, vol. 62, no. 7, pp. 742–749, 2005.

[49] A. Engberg and T. Teasdale, "Psychosocial outcome following traumatic brain injury in adults: a long-term population-based follow-up.," *Brain injury*, vol. 18, no. 6, pp. 533–545, 2004.

[50] H. S. MARTLAND, "PUNCH DRUNK," *JAMA: The Journal of the American Medical Association*, vol. 91, no. 15, pp. 1103–1107, 1928.

[51] M. A. C, R. A. Stern, C. J. Nowinski, T. D. Stein, V. E. Alvarez, D. H. Daneshvar, H. S. Lee, S. M. Wojtowicz, G. Hall, C. M. Baugh, D. O. Riley, C. A. Kubilus, K. A. Cormier, M. A. Jacobs, B. R. Martin, C. R. Abraham, T. Ikezu, R. R. Reichard, B. L. Wolozin, A. E. Budson, L. E. Goldstein, N. W. Kowall, and R. C. Cantu, "The spectrum of disease in chronic traumatic encephalopathy.," *Brain : a journal of neurology*, vol. 136, no. Pt 1, pp. 43–64, 2013.

[52] V. E. Johnson, W. Stewart, and D. H. Smith, "Widespread α and amyloid-β pathology many years after a single traumatic brain injury in humans.," *Brain pathology (Zurich, Switzerland)*, vol. 22, no. 2, pp. 142–149, 2012.

[53] S. Zhang, L. J. Carroll, J. Cassidy, and C. Paniak, "Factors influencing self-rated health in traffic-related mild traumatic brain injury.," *Journal of rehabilitation medicine*, vol. 41, no. 13, pp. 1062–1067, 2009.

[54] T. Teasdale and A. Engberg, "Subjective well-being and quality of life following traumatic brain injury in adults: a long-term population-based follow-up.," *Brain injury*, vol. 19, no. 12, pp. 1041–1048, 2005.

[55] N. Müller, "Weitere beobachtungen sekundärer traumatischer veränderungen des gehirns," *Acta Neurochirurgica*, vol. 11, no. 4, pp. 545–558, 1964.

[56] G. Peters, "Die bedeutung der primär und sekundär traumatischen hirnveränderungen für das klinische syndrom," *Acta Neurochirurgica*, vol. 23, no. 2-3, pp. 187–198, 1970.

[57] A. J. Lewis and W. Zingg, "Experimental brain damage in dogs due to systemic, induced hypotension and Head-Up tilt for short periods," *Angiology*, vol. 17, no. 11, pp. 800–818, 1966.

[58] W. B. Jennett, "Secondary ischaemic brain damage after head injury.," *Journal of clinical pathology. Supplement (Royal College of Pathologists)*, vol. 4, pp. 172–175, 1970.

[59] D. J. E. Price and A. Murray, "The influence of hypoxia and hypotension on recovery from head injury," *Injury*, vol. 3, no. 4, pp. 218–224, 1972.

[60] M. J. Smith, M. F. Stiefel, S. Magge, S. Frangos, S. Bloom, V. Gracias, and P. D. L. Roux, "Packed red blood cell transfusion increases local cerebral oxygenation*," *Critical Care Medicine*, vol. 33, no. 5, p. 1104, 2005.

[61] A. Rovlias and S. Kotsou, "The influence of hyperglycemia on neurological outcome in patients with severe head injury.," *Neurosurgery*, vol. 46, no. 2, pp. 335–42; discussion 342, 2000.

[62] M. Oddo, J. M. Schmidt, E. Carrera, N. Badjatia, E. S. Connolly, M. Presciutti, N. D. Ostapkovich, J. M. Levine, P. L. Roux, and S. A. Mayer, "Impact of tight glycemic control on cerebral glucose metabolism after severe brain injury: A microdialysis study*," *Critical Care Medicine*, vol. 36, no. 12, pp. 3233–3238, 2008.

[63] P. Vespa, M. D. L, N. Stein, S. C. Huang, W. Shao, M. Filippou, M. Etchepare, T. Glenn, and D. A. Hovda, "Tight glycemic control increases metabolic distress in traumatic brain injury: a randomized controlled within-subjects trial.," *Critical care medicine*, vol. 40, no. 6, pp. 1923–1929, 2012.

[64] M. M. M, D. A. Horowitz, and P. in the International Multidisciplinary Consensus Conference on Multimodality Monitoring, "International multidisciplinary consensus conference on multimodality monitoring: ICU processes of care.," *Neurocritical care*, vol. 21 Suppl 2, pp. S215–S228, 2014.

[65] E. Jeremitsky, L. Omert, C. Dunham, J. Protetch, and A. Rodriguez, "Harbingers of poor outcome the day after severe brain injury: hypothermia, hypoxia, and hypoperfusion.," *The Journal of trauma*, vol. 54, no. 2, pp. 312–319, 2003.

[66] D. F. Signorini, P. J. D. Andrews, P. A. Jones, J. M. Wardlaw, and J. D. Miller, "Adding insult to injury: the prognostic value of early secondary insults for survival after traumatic brain injury," *Journal of Neurology, Neurosurgery & Psychiatry*, vol. 66, no. 1, pp. 26–31, 1999.

[67] R. A, F. Reina-De La Torre, O. M, and S. J, "Perivascular structures in corrosion casts of the human central nervous system: a confocal laser and scanning electron microscope study.," *The Anatomical record*, vol. 252, no. 2, pp. 176–184, 1998.

[68] S. N. Jespersen and L. Østergaard, "The roles of cerebral blood flow, capillary transit time heterogeneity, and oxygen tension in brain oxygenation and metabolism.," *Journal of cerebral blood flow and metabolism : official journal of the International Society of Cerebral Blood Flow and Metabolism*, vol. 32, no. 2, pp. 264–277, 2012.

[69] P. M. Rasmussen, S. N. Jespersen, and L. Østergaard, "The effects of transit time heterogeneity on brain oxygenation during rest and functional activation.," *Journal of cerebral blood flow and metabolism : official journal of the International Society of Cerebral Blood Flow and Metabolism*, vol. 35, no. 3, pp. 432–442, 2015.

[70] H. Angleys, L. Østergaard, and S. N. Jespersen, "The effects of capillary transit time heterogeneity (CTH) on brain oxygenation.," *Journal of cerebral blood flow and metabolism : official journal of the International Society of Cerebral Blood Flow and Metabolism*, vol. 35, no. 5, pp. 806–817, 2015.

[71] R. A. Hill, L. Tong, P. Yuan, S. Murikinati, S. Gupta, and J. Grutzendler, "Regional blood flow in the normal and ischemic brain is controlled by arteriolar smooth muscle cell contractility and not by capillary pericytes.," *Neuron*, vol. 87, no. 1, pp. 95–9110, 2015.

[72] J. Schallek, Y. Geng, H. Nguyen, and D. R. Williams, "Morphology and topography of retinal pericytes in the living mouse retina using in vivo adaptive optics imaging and ex vivo characterization.," *Investigative ophthalmology & visual science*, vol. 54, no. 13, pp. 8237–8250, 2013.

[73] C. N. Hall, C. Reynell, B. Gesslein, N. B. Hamilton, A. Mishra, B. A. Sutherland, F. M. O'Farrell, A. M. Buchan, M. Lauritzen, and D. Attwell, "Capillary pericytes regulate cerebral blood flow in health and disease," *Nature*, pp. 55–60, 2014.

[74] B. R. Chen, M. G. Kozberg, M. B. Bouchard, M. A. Shaik, and E. M. Hillman, "A critical role for the vascular endothelium in functional neurovascular coupling in the brain.," *Journal of the American Heart Association*, vol. 3, no. 3, pp. 1–14, 2014.

[75] B. R. Chen, M. B. Bouchard, M. A. F, S. A. Burgess, and E. M. Hillman, "High-speed vascular dynamics of the hemodynamic response.," *NeuroImage*, vol. 54, no. 2, pp. 1021–1030, 2011.

[76] D. Collins, M. WT, and M. Ellsworth, "Conducted vascular responses: communication across the capillary bed.," *Microvascular research*, vol. 56, no. 1, pp. 43–53, 1998.

[77] M. A. F, B. R. Chen, A. J. Radosevich, B. Cauli, and E. M. Hillman, "In vivo 3D morphology of astrocyte-vasculature interactions in the somatosensory cortex: implications for neurovascular coupling.," *Journal of cerebral blood flow & metabolism*, vol. 31, no. 3, pp. 795–806, 2011.

[78] M. M. Halassa, T. Fellin, H. Takano, J. H. Dong, and P. G. Haydon, "Synaptic islands defined by the territory of a single astrocyte.," *The Journal of neuroscience : the official journal of the Society for Neuroscience*, vol. 27, no. 24, pp. 6473–6477, 2007.

[79] S. J. Mulligan and M. B. A, "Calcium transients in astrocyte endfeet cause cerebrovascular constrictions.," *Nature*, vol. 431, no. 7005, pp. 195–199, 2004.

[80] H. Girouard, A. D. Bonev, R. M. Hannah, A. Meredith, R. W. Aldrich, and M. T. Nelson, "Astrocytic endfoot ca2+ and BK channels determine both arteriolar dilation and constriction.," *Proceedings of the National Academy of Sciences of the United States of America*, vol. 107, no. 8, pp. 3811–3816, 2010.

[81] D. Attwell, A. M. Buchan, S. Charpak, M. Lauritzen, B. A. MacVicar, and E. A. Newman, "Glial and neuronal control of brain blood flow," *Nature*, vol. 468, no. 7321, pp. 232–243, 2010.

[82] J. Fordsmann, R. Ko, H. Choi, K. Thomsen, B. Witgen, C. Mathiesen, M. Lønstrup, H. Piilgaard, M. Brian, and M. Lauritzen, "Increased 20-HETE synthesis explains reduced cerebral blood flow but not impaired neurovascular coupling after cortical spreading depression in rat cerebral cortex," *The Journal of Neuroscience*, vol. 33, no. 6, p. 2562–2570, 2013.

[83] J. Dreier, G. Petzold, K. Tille, U. Lindauer, G. Arnold, U. Heinemann, K. Einhäupl, and U. Dirnagl, "Ischaemia triggered by spreading neuronal activation is inhibited by vasodilators in rats," *Journal of Physiology*, vol. 531, no. 2, 2001.

[84] G. R. Gordon, H. B. Choi, R. L. Rungta, E. G. C, and M. B. A, "Brain metabolism dictates the polarity of astrocyte control over arterioles.," *Nature*, vol. 456, no. 7223, pp. 745–749, 2008.

[85] M. Bélanger, I. Allaman, and P. Magistretti, "Brain energy metabolism: Focus on Astrocyte-Neuron metabolic cooperation," *Cell Metabolism*, vol. 14, no. 6, pp. 724–738, 2011.

[86] L. Sokoloff, M. Reivich, C. Kennedy, M. Des Rosiers, C. Patlak, K. Pettigrew, O. Sakurada, and M. Shinohara, "The [14C]deoxyglucose method for the measurement of local cerebral glucose utilization: theory, procedure, and normal values in the conscious and anesthetized albino rat.," *Journal of neurochemistry*, vol. 28, no. 5, pp. 897–916, 1977.

[87] P. Magistretti and L. Pellerin, "Cellular bases of brain energy metabolism and their relevance to functional brain imaging: evidence for a prominent role of astrocytes.," *Cerebral cortex (New York, N.Y. : 1991)*, vol. 6, no. 1, pp. 50–61, 1996.

[88] P. Fox and M. Raichle, "Focal physiological uncoupling of cerebral blood flow and oxidative metabolism during somatosensory stimulation in human subjects.," *Proceedings of the National Academy of Sciences of the United States of America*, vol. 83, no. 4, pp. 1140–1144, 1986.

[89] P. Fox, M. Raichle, M. Mintun, and C. Dence, "Nonoxidative glucose consumption during focal physiologic neural activity.," *Science (New York, N.Y.)*, vol. 241, no. 4864, pp. 462–464, 1988.

[90] I. Simpson, A. Carruthers, and S. Vannucci, "Supply and demand in cerebral energy metabolism: the role of nutrient transporters," *Journal of Cerebral Blood Flow & Metabolism*, vol. 27, no. 11, pp. 1766–1791, 2007.

[91] G. Hamlin, I. Cernak, J. Wixey, and R. Vink, "Increased expression of neuronal glucose transporter 3 but not glial glucose transporter 1 following severe diffuse traumatic brain injury in rats.," *Journal of neurotrauma*, vol. 18, no. 10, pp. 1011–1018, 2001.

[92] T. Urabe, N. Hattori, S. Nagamatsu, H. Sawa, and Y. Mizuno, "Expression of glucose transporters in rat brain following transient focal ischemic injury.," *Journal of neurochemistry*, vol. 67, no. 1, pp. 265–271, 1996.

[93] E. Cornford, S. Hyman, M. Cornford, E. Landaw, and D. AV, "Interictal seizure resections show two configurations of endothelial glut1 glucose transporter in the human blood-brain barrier.," *Journal of cerebral blood flow and metabolism : official journal of the International Society of Cerebral Blood Flow and Metabolism*, vol. 18, no. 1, pp. 26–42, 1998.

[94] G. van Hall, M. Strømstad, P. Rasmussen, Ø. Jans, M. Zaar, C. Gam, B. Quistorff, N. H. Secher, and H. B. Nielsen, "Blood lactate is an important energy source for the human brain," *Journal of Cerebral Blood Flow & Metabolism*, vol. 29, pp. 1121–1129, 2009.

[95] G. Brooks, "Cell-cell and intracellular lactate shuttles," *The Journal of physiology*, vol. 587, no. 23, pp. 5591–5600, 2009.

[96] L. Pellerin, G. Pellegri, J. Martin, and P. Magistretti, "Expression of monocarboxylate transporter mrnas in mouse brain: support for a distinct role of lactate as an energy substrate for the neonatal vs. adult brain.," *Proceedings of the National Academy of Sciences of the United States of America*, vol. 95, no. 7, pp. 3990–3995, 1998.

[97] M. Prins and C. Giza, "Induction of monocarboxylate transporter 2 expression and ketone transport following traumatic brain injury in juvenile and adult rats.," *Developmental neuroscience*, vol. 28, no. 4-5, pp. 447–456, 2006.

[98] L. Pellerin and P. Magistretti, "Glutamate uptake into astrocytes stimulates aerobic glycolysis: a mechanism coupling neuronal activity to glucose utilization.," *Proceedings of the National Academy of Sciences of the United States of America*, vol. 91, no. 22, pp. 10625–10629, 1994.

[99] Y. Itoh, T. Esaki, K. Shimoji, M. Cook, M. J. Law, E. Kaufman, and L. Sokoloff, "Dichloroacetate effects on glucose and lactate oxidation by neurons and astroglia in vitro and on glucose utilization by brain in vivo," *Proceedings of the National Academy of Sciences*, vol. 100, no. 8, pp. 4879–4884, 2003.

[100] H. A, A. Almeida, and E. Fernández, "The bioenergetic and antioxidant status of neurons is controlled by continuous degradation of a key glycolytic enzyme by APC/C–Cdh1," *Nature Cell Biology*, vol. 11, no. 6, pp. 747–752, 2009.

[101] N. Cholet, L. Pellerin, E. Welker, P. Lacombe, J. Seylaz, P. Magistretti, and G. Bonvento, "Local injection of antisense oligonucleotides targeted to the glial glutamate transporter GLAST decreases the metabolic response to somatosensory activation," *Journal of Cerebral Blood Flow & Metabolism*, vol. 21, no. 4, pp. 404–412, 2001.

[102] S. Cerdán, T. B. Rodrigues, A. Sierra, M. Benito, L. L. Fonseca, C. P. Fonseca, and M. L. García-Martín, "The redox switch/redox coupling hypothesis," *Neurochemistry International*, vol. 48, no. 6-7, pp. 523–530, 2006.

[103] S. Mangia, I. A. Simpson, S. J. Vannucci, and A. Carruthers, "The in vivo neuron-to-astrocyte lactate shuttle in human brain: evidence from modeling of measured lactate levels during visual stimulation," *Journal of Neurochemistry*, vol. 109, no. s1, pp. 55–62, 2009.

[104] Y. Hu and G. Wilson, "A temporary local energy pool coupled to neuronal activity: fluctuations of extracellular lactate levels in rat brain monitored with rapid-response enzyme-based sensor.," *Journal of neurochemistry*, vol. 69, no. 4, pp. 1484–1490, 1997.

[105] A. Nehlig, W. Elisabeth, and C. D. Lam, "Selective uptake of [14C]2-deoxyglucose by neurons and astrocytes: high-resolution microautoradiographic imaging by cellular 14C-trajectography combined with immunohistochemistry.," *Journal of cerebral blood flow and metabolism : official journal of the International Society of Cerebral Blood Flow and Metabolism*, vol. 24, no. 9, pp. 1004–1014, 2004.

[106] A. B. Patel, J. C. Lai, G. M. Chowdhury, F. Hyder, D. L. Rothman, R. G. Shulman, and K. L. Behar, "Direct evidence for activity-dependent glucose phosphorylation in neurons with implications for the astrocyte-to-neuron lactate shuttle.," *Proceedings of the National Academy of Sciences of the United States of America*, vol. 111, no. 14, pp. 5385–5390, 2014.

[107] I. Lundgaard, B. Li, L. Xie, H. Kang, S. Sanggaard, J. D. Haswell, W. Sun, S. Goldman, S. Blekot, M. Nielsen, T. Takano, R. Deane, and M. Nedergaard, "Direct neuronal glucose uptake heralds activity-dependent increases in cerebral metabolism.," *Nature communications*, vol. 6, 2015.

[108] K. Kasischke, H. Vishwasrao, P. Fisher, and W. Zipfel, "Neural activity triggers neuronal oxidative metabolism followed by astrocytic glycolysis," *Science*, vol. 305, pp. 99–103, 2004.

[109] F. Cruz, M. Villalba, and G. MA, "Intracellular compartmentation of pyruvate in primary cultures of cortical neurons as detected by 13C NMR spectroscopy with multiple 13C labels," *Journal of Neuroscience Research*, vol. 66, pp. 771–781, 2001.

[110] N. J. Allen, R. Káradóttir, and D. Attwell, "A preferential role for glycolysis in preventing the anoxic depolarization of rat hippocampal area CA1 pyramidal cells," *The Journal of Neuroscience*, vol. 25, no. 4, pp. 848–859, 2005.

[111] T. Takano, G. F. Tian, W. Peng, N. Lou, D. Lovatt, A. J. Hansen, K. A. Kasischke, and M. Nedergaard, "Cortical spreading depression causes and coincides with tissue hypoxia.," *Nature neuroscience*, vol. 10, no. 6, pp. 754–762, 2007.

[112] A. Monro, "Observations on the structure and functions of the nervous system," 1783.

[113] H. Cushing, "The third circulation in studies in intracranial physiology and surgery," 1926.

[114] A. Gjedde, P. Johannsen, G. Cold, and L. Østergaard, "Cerebral metabolic response to low blood flow: possible role of cytochrome oxidase inhibition," *Journal of Cerebral Blood Flow & Metabolism*, vol. 25, no. 9, pp. 1183–1196, 2005.

[115] T. Glenn, D. Kelly, W. Boscardin, D. McArthur, P. Vespa, M. Oertel, D. Hovda, M. Bergsneider, L. Hillered, and N. Martin, "Energy dysfunction as a predictor of outcome after moderate or severe head injury: Indices of oxygen, glucose, and lactate metabolism," *Journal of Cerebral Blood Flow & Metabolism*, pp. 1239–1250, 2003.

[116] A. S. Cunningham, R. Salvador, J. P. Coles, D. A. Chatfield, P. G. Bradley, A. J. Johnston, L. A. Steiner, T. D. Fryer, F. I. Aigbirhio, P. Smielewski, G. B. Williams, T. A. Carpenter, J. H. Gillard, J. D. Pickard, and D. K. Menon, "Physiological thresholds for irreversible tissue damage in contusional regions following traumatic brain injury," *Brain*, vol. 128, no. Pt 8, pp. 1931–1942, 2005.

[117] M. Botteri, E. Bandera, C. Minelli, and N. Latronico, "Cerebral blood flow thresholds for cerebral ischemia in traumatic brain injury. a systematic review*," *Critical Care Medicine*, vol. 36, no. 11, p. 3089, 2008.

[118] D. Kelly, N. Martin, R. Kordestani, G. Counelis, D. Hovda, M. Bergsneider, M. DQ, E. Shalmon, D. Herman, and D. Becker, "Cerebral blood flow as a predictor of outcome following traumatic brain injury.," *Journal of neurosurgery*, vol. 86, no. 4, pp. 633–641, 1997.

[119] P. Bouzat, P. Marques-Vidal, J. Zerlauth, N. Sala, T. Suys, P. Schoettker, J. Bloch, R. T. Daniel, M. Levivier, R. Meuli, and M. Oddo, "Accuracy of brain multimodal monitoring to detect cerebral hypoperfusion after traumatic brain injury*," *Critical Care Medicine*, vol. 43, no. 2, p. 445, 2015.

[120] M. J. Cipolla, "The cerebral circulation," *Morgan & Claypool Life Sciences*, 2009.

[121] M. J. H. Aries, M. Czosnyka, K. P. Budohoski, L. A. Steiner, A. Lavinio, A. G. Kolias, P. J. Hutchinson, K. M. Brady, D. K. Menon, J. D. Pickard, and P. Smielewski, "Continuous determination of optimal cerebral perfusion pressure in traumatic brain injury*," *Critical Care Medicine*, vol. 40, no. 8, p. 2456, 2012.

[122] L. A. Steiner, J. P. Coles, A. J. Johnston, D. A. Chatfield, P. Smielewski, T. D. Fryer, F. I. Aigbirhio, J. C. Clark, J. D. Pickard, D. K. Menon, and M. Czosnyka, "Assessment of cerebrovascular autoregulation in head-injured patients: a validation study.," *Stroke; a journal of cerebral circulation*, vol. 34, no. 10, pp. 2404–2409, 2003.

[123] M. Czosnyka, P. Smielewski, P. Kirkpatrick, R. Laing, D. Menon, and J. Pickard, "Continuous assessment of the cerebral vasomotor reactivity in head injury.," *Neurosurgery*, vol. 41, no. 1, pp. 11–7; discussion 17, 1997.

[124] B. Meldrum, "Glutamate as a neurotransmitter in the brain: review of physiology and pathology.," *The Journal of nutrition*, vol. 130, no. 4S Suppl, pp. 1007S–1015S, 2000.

[125] T. Papouin, L. Ladépêche, J. Ruel, S. Sacchi, M. Labasque, M. Hanini, L. Groc, L. Pollegioni, J. P. Mothet, and S. H. H. Oliet, "Synaptic and extrasynaptic NMDA receptors are gated by different endogenous coagonists.," *Cell*, vol. 150, no. 3, pp. 633–646, 2012.

[126] G. E. Hardingham and H. Bading, "Synaptic versus extrasynaptic NMDA receptor signalling: implications for neurodegenerative disorders," *Nature Reviews Neuroscience*, vol. 11, no. 10, pp. 682–696, 2010.

[127] G. E. Hardingham, Y. Fukunaga, and H. Bading, "Extrasynaptic NMDARs oppose synaptic NMDARs by triggering CREB shut-off and cell death pathways," *Nature Neuroscience*, 2002.

[128] P. Pernot, J. Mothet, O. Schuvailo, A. Soldatkin, L. Pollegioni, M. Pilone, M. Adeline, R. Cespuglio, and S. Marinesco, "Characterization of a yeast d-Amino acid oxidase microbiosensor for d-Serine detection in the central nervous system," *Analytical Chemistry*, vol. 80, no. 5, pp. 1589–1597, 2008.

[129] T. Matsui, M. Sekiguchi, A. Hashimoto, U. Tomita, T. Nishikawa, and K. Wada, "Functional comparison of d-serine and glycine in rodents: the effect on cloned NMDA receptors and the extracellular concentration.," *Journal of neurochemistry*, vol. 65, no. 1, pp. 454–458, 1995.

[130] B. Day, F. Pomerleau, J. Burmeister, P. Huettl, and G. Gerhardt, "Microelectrode array studies of basal and potassium-evoked release of l-glutamate in the anesthetized rat brain.," *Journal of neurochemistry*, vol. 96, no. 6, pp. 1626–1635, 2006.

[131] N. Vasylieva, C. Woeffler-Maucler, A. Meiller, H. Viscogliosi, T. Lieutaud, D. Barbier, and S. Marinesco, "Immobilization method to preserve enzyme specificity in biosensors: Consequences for brain glutamate detection," *Analytical Chemistry*, vol. 85, no. 4, pp. 2507–2515, 2013.

[132] M. A. Herman and C. E. Jahr, "Extracellular glutamate concentration in hippocampal slice.," *The Journal of neuroscience : the official journal of the Society for Neuroscience*, vol. 27, no. 36, pp. 9736–9741, 2007.

[133] M. C. Morganti-Kossmann, M. Rancan, P. F. Stahel, and T. Kossmann, "Inflammatory response in acute traumatic brain injury: a double-edged sword," *Current Opinion in Critical Care*, vol. 8, no. 2, p. 101, 2002.

[134] M. Gauberti, A. Montagne, O. A. Marcos-Contreras, A. L. Behot, E. Maubert, and D. Vivien, "Ultra-Sensitive molecular MRI of vascular cell adhesion molecule-1 reveals a dynamic inflammatory penumbra after strokes," *Stroke*, vol. 44, no. 7, pp. 1988–1996, 2013.

[135] L. Steinman, "Role reversal: infiltrating t cells protect the brain," *Journal of Clinical Investigation*, vol. 125, no. 2, p. 493494, 2015.

[136] T. L. Roth, D. Nayak, T. Atanasijevic, A. P. Koretsky, L. L. Latour, and D. B. McGavern, "Transcranial amelioration of inflammation and cell death after brain injury," *Nature*, vol. 505, no. 7482, pp. 223–228, 2014.

[137] L. Fialkow, Y. Wang, and G. P. Downey, "Reactive oxygen and nitrogen species as signaling molecules regulating neutrophil function.," *Free radical biology & medicine*, vol. 42, no. 2, pp. 153–164, 2007.

[138] H. Kettenmann, U. K. Hanisch, M. Noda, and A. Verkhratsky, "Physiology of microglia.," *Physiological reviews*, vol. 91, no. 2, pp. 461–553, 2011.

[139] A. Karperien, H. Ahammer, and H. F. Jelinek, "Quantitating the subtleties of microglial morphology with fractal analysis.," *Frontiers in cellular neuroscience*, vol. 7, p. 3, 2013.

[140] V. E. Johnson, J. E. Stewart, F. D. Begbie, J. Q. Trojanowski, D. H. Smith, and W. Stewart, "Inflammation and white matter degeneration persist for years after a single traumatic brain injury.," *Brain : a journal of neurology*, vol. 136, no. Pt 1, pp. 28–42, 2013.

[141] F. O. Martinez and S. Gordon, "The m1 and m2 paradigm of macrophage activation: time for reassessment.," *F1000prime reports*, vol. 6, p. 13, 2014.

[142] J. D. Cherry, J. A. Olschowka, and O. MK, "Neuroinflammation and m2 microglia: the good, the bad, and the inflamed.," *Journal of neuroinflammation*, vol. 11, p. 98, 2014.

[143] J. T. Walsh, S. Hendrix, F. Boato, I. Smirnov, J. Zheng, J. R. Lukens, S. Gadani, D. Hechler, G. Gölz, K. Rosenberger, T. Kammertöns, J. Vogt, C. Vogelaar, V. Siffrin, A. Radjavi, F. Anthony, A. Gaultier, R. Gold, T. D. Kanneganti, R. Nitsch, F. Zipp, and J. Kipnis, "MHCII-independent CD4+ t cells protect injured CNS neurons via IL-4.," *The Journal of clinical investigation*, vol. 125, no. 2, pp. 699–714, 2015.

[144] J. P. Dreier, T. Isele, C. Reiffurth, N. Offenhauser, S. A. Kirov, M. A. Dahlem, and O. Herreras, "Is spreading depolarization characterized by an abrupt, massive release of gibbs free energy from the human brain cortex?," *The Neuroscientist*, vol. 19, no. 1, pp. 25–42, 2013.

[145] P. Vespa, "Continuous EEG monitoring for the detection of seizures in traumatic brain injury, infarction, and intracerebral hemorrhage: "To detect and protect"," *Journal of Clinical Neurophysiology*, vol. 22, no. 2, p. 99, 2005.

[146] P. M. Vespa, C. Miller, M. David, M. Eliseo, M. Etchepare, D. Hirt, T. C. Glenn, N. Martin, and D. Hovda, "Nonconvulsive electrographic seizures after traumatic brain injury result in a delayed, prolonged increase in intracranial pressure and metabolic crisis.," *Critical care medicine*, vol. 35, no. 12, pp. 2830–2836, 2007.

[147] D. D. Binz, L. G. ToussaintIII, and J. A. Friedman, "Hemorrhagic complications of ventriculostomy placement: A Meta-Analysis," *Neurocritical Care*, vol. 10, pp. 253–256, 2009.

[148] R. Beer, P. Lackner, B. Pfausler, and E. Schmutzhard, "Nosocomial ventriculitis and meningitis in neurocritical care patients," *Journal of Neurology*, vol. 255, pp. 1617–1624, 2008.

[149] P. H. Raboel, J. B. Jr., M. Andresen, B. M. Bellander, and B. Romner, "Intracranial pressure monitoring: Invasive versus Non-Invasive Methods—A review," *Critical Care Research and Practice*, vol. 2012, 2012.

[150] I. Chambers, P. Kane, D. Signorini, A. Jenkins, and A. Mendelow, "Bilateral ICP monitoring: its importance in detecting the severity of secondary insults.," *Acta neurochirurgica. Supplement*, vol. 71, pp. 42–43, 1998.

[151] L. Steiner and P. Andrews, "Monitoring the injured brain: ICP and CBF.," *British journal of anaesthesia*, vol. 97, no. 1, pp. 26–38, 2006.

[152] M. Smith, "Monitoring intracranial pressure in traumatic brain injury," *Anesthesia & Analgesia*, vol. 106, no. 1, pp. 240–248, 2008.

[153] S. Badri, J. Chen, J. Barber, N. R. Temkin, S. S. Dikmen, R. M. Chesnut, S. Deem, N. Yanez, and M. M. Treggiari, "Mortality and long-term functional outcome associated with intracranial pressure after traumatic brain injury.," *Intensive care medicine*, vol. 38, no. 11, pp. 1800–1809, 2012.

[154] F. Güiza, B. Depreitere, I. Piper, G. Citerio, I. Chambers, P. A. Jones, T. M. Y. Lo, P. Enblad, P. Nillson, B. Feyen, P. Jorens, A. Maas, M. U. Schuhmann, R. Donald, L. Moss, G. Van den Berghe, and G. Meyfroidt, "Visualizing the pressure and time burden of intracranial hypertension in adult and paediatric traumatic brain injury.," *Intensive care medicine*, vol. 41, no. 6, pp. 1067–1076, 2015.

[155] N. Lundberg, H. Troupp, and H. Lorin, "Continuous recording of the ventricular-fluid pressure in patients with severe acute traumatic brain injury. a preliminary report.," *Journal of neurosurgery*, vol. 22, no. 6, pp. 581–590, 1965.

[156] E. Sorrentino, J. Diedler, M. Kasprowicz, K. Budohoski, C. Haubrich, P. Smielewski, J. Outtrim, A. Manktelow, P. Hutchinson, J. Pickard, D. Menon, and M. Czosnyka, "Critical thresholds for cerebrovascular reactivity after traumatic brain injury.," *Neurocritical care*, vol. 16, no. 2, pp. 258–266, 2012.

[157] L. A. Steiner, M. Czosnyka, S. K. Piechnik, P. Smielewski, D. Chatfield, D. K. Menon, and J. D. Pickard, "Continuous monitoring of cerebrovascular pressure reactivity allows determination of optimal cerebral perfusion pressure in patients with traumatic brain injury.," *Critical care medicine*, vol. 30, no. 4, pp. 733–738, 2002.

[158] K. Tazarourte, A. Atchabahian, J. P. Tourtier, J. S. David, C. Ract, D. Savary, M. Monchi, and B. Vigué, "Pre-hospital transcranial doppler in severe traumatic brain injury: a pilot study.," *Acta anaesthesiologica Scandinavica*, vol. 55, no. 4, pp. 422–428, 2011.

[159] M. Müller, R. Esser, K. Kötter, J. Voss, A. Müller, and P. Stellmes, "Width of 3. ventricle: reference values and clinical relevance in a cohort of patients with relapsing remitting multiple sclerosis.," *The open neurology journal*, vol. 7, pp. 11–16, 2013.

[160] G. Seidel, M. Kaps, T. Gerriets, and A. Hutzelmann, "Evaluation of the ventricular system in adults by transcranial duplex sonography.," *Journal of neuroimaging : official journal of the American Society of Neuroimaging*, vol. 5, no. 2, pp. 105–108, 1995.

[161] I. Kiphuth, H. Huttner, T. Struffert, S. Schwab, and M. Köhrmann, "Sonographic monitoring of ventricle enlargement in posthemorrhagic hydrocephalus.," *Neurology*, vol. 76, no. 10, pp. 858–862, 2011.

[162] J. A. Llompart Pou, J. M. Abadal Centellas, M. Palmer Sans, J. Pérez Bárcena, M. Casares Vivas, J. Homar Ramírez, and J. Ibáñez Juvé, "Monitoring midline shift by transcranial color-coded sonography in traumatic brain injury. a comparison with cranial computerized tomography.," *Intensive care medicine*, vol. 30, no. 8, pp. 1672–1675, 2004.

[163] A. Caricato, V. Mignani, C. Sandroni, and D. Pietrini, "Bedside detection of acute epidural hematoma by transcranial sonography in a head-injured patient.," *Intensive care medicine*, vol. 36, no. 6, pp. 1091–1092, 2010.

[164] P. Bouzat, M. Oddo, and J. Payen, "Transcranial doppler after traumatic brain injury: is there a role?," *Current Opinion in Critical Care*, vol. 20, no. 2, p. 153, 2014.

[165] J. Klingelhöfer, B. Conrad, R. Benecke, D. Sander, and E. Markakis, "Evaluation of intracranial pressure from transcranial doppler studies in cerebral disease.," *Journal of neurology*, vol. 235, no. 3, pp. 159–162, 1988.

[166] M. Czosnyka, H. Richards, H. Whitehouse, and J. Pickard, "Relationship between transcranial doppler-determined pulsatility index and cerebrovascular resistance: an experimental study.," *Journal of neurosurgery*, vol. 84, no. 1, pp. 79–84, 1996.

[167] P. Bouzat, G. Francony, P. Declety, C. Genty, A. Kaddour, P. Bessou, J. Brun, C. Jacquot, S. Chabardes, J. L. Bosson, and J. F. Payen, "Transcranial doppler to screen on admission patients with mild to moderate traumatic brain injury.," *Neurosurgery*, vol. 68, no. 6, pp. 1603–9; discussion 1609, 2011.

[168] C. Ract, S. Le Moigno, N. Bruder, and B. Vigué, "Transcranial doppler ultrasound goal-directed therapy for the early management of severe traumatic brain injury.," *Intensive care medicine*, vol. 33, no. 4, pp. 645–651, 2007.

[169] H. van Santbrink, J. W. Schouten, E. W. Steyerberg, C. J. J. Avezaat, and A. I. R. Maas, "Serial transcranial doppler measurements in traumatic brain injury with special focus on the early posttraumatic period," *Acta Neurochirurgica*, 2002.

[170] T. Suys, P. Bouzat, M. Pedro, N. Sala, J. F. Payen, A. O. Rossetti, and M. Oddo, "Automated quantitative pupillometry for the prognostication of coma after cardiac arrest.," *Neurocritical care*, vol. 21, no. 2, pp. 300–308, 2014.

[171] T. B. Rodrigues, J. Valette, and A. Bouzier-Sore, "13C NMR spectroscopy applications to brain energy metabolism," *Frontiers in Neuroenergetics*, vol. 5, pp. 1–16, 2013.

[172] A. Bankier, D. Fleischmann, A. Windisch, P. Germann, W. Petritschek, M. Wiesmayr, and P. Hübsch, "Position of jugular oxygen saturation catheter in patients with head trauma: assessment by use of plain films.," *AJR. American journal of roentgenology*, vol. 164, no. 2, pp. 437–441, 1995.

[173] H. White and A. Baker, "Continuous jugular venous oximetry in the neurointensive care unit–a brief review.," *Canadian journal of anaesthesia = Journal canadien d'anesthésie*, vol. 49, no. 6, pp. 623–629, 2002.

[174] K. Kiening, A. Unterberg, T. Bardt, G. Schneider, and W. Lanksch, "Monitoring of cerebral oxygenation in patients with severe head injuries: brain tissue PO2 versus jugular vein oxygen saturation.," *Journal of neurosurgery*, vol. 85, no. 5, pp. 751–757, 1996.

[175] B. Matta and A. Lam, "The rate of blood withdrawal affects the accuracy of jugular venous bulb. oxygen saturation measurements.," *Anesthesiology*, vol. 86, no. 4, pp. 806–808, 1997.

[176] D. K. Sandsmark, M. A. Kumar, S. Park, and J. M. Levine, "Multimodal monitoring in subarachnoid hemorrhage.," *Stroke; a journal of cerebral circulation*, vol. 43, no. 5, pp. 1440–1445, 2012.

[177] S. Y. Cho, S. J. Kim, C. W. Jeong, C. Y. Jeong, S. S. Chung, J. Lee, and K. Y. Yoo, "Under general anesthesia arginine vasopressin prevents hypotension but impairs cerebral oxygenation during arthroscopic shoulder surgery in the beach chair position.," *Anesthesia and analgesia*, vol. 117, no. 6, pp. 1436–1443, 2013.

[178] M. Struchen, H. Hannay, C. Contant, and C. Robertson, "The relation between acute physiological variables and outcome on the glasgow outcome scale and disability rating scale following severe traumatic brain injury.," *Journal of neurotrauma*, vol. 18, no. 2, pp. 115–125, 2001.

[179] B. T. Foundation, A. A. of Neurological Surgeons, and C. of Neurological Surgeons, "Acknowledgments," *Journal of Neurotrauma*, vol. 24, no. supplement 1, p. ivi, 2007.

[180] C. Patet, H. Quintard, T. Suys, J. Bloch, R. Daniel, L. Pellerin, P. Magistretti, and M. Oddo, "Neuroenergetic response to prolonged cerebral glucose depletion after severe brain injury and the role of lactate.," *Journal of neurotrauma*, 2015.

[181] J. Cruz, O. Hoffstad, and J. Jaggi, "Cerebral lactate-oxygen index in acute brain injury with acute anemia: assessment of false versus true ischemia.," *Critical care medicine*, vol. 22, no. 9, pp. 1465–1470, 1994.

[182] M. Bergsneider, D. Hovda, E. Shalmon, D. Kelly, P. Vespa, N. Martin, M. Phelps, M. DL, M. Caron, J. Kraus, and D. Becker, "Cerebral hyperglycolysis following severe traumatic brain injury in humans: a positron emission tomography study.," *Journal of neurosurgery*, vol. 86, no. 2, pp. 241–251, 1997.

[183] S. Moritz, P. Kasprzak, C. Woertgen, K. Taeger, and C. Metz, "The accuracy of jugular bulb venous monitoring in detecting cerebral ischemia in awake patients undergoing carotid endarterectomy.," *Journal of neurosurgical anesthesiology*, vol. 20, no. 1, pp. 8–14, 2008.

[184] M. A. Poca, J. Sahuquillo, A. Vilalta, and A. Garnacho, "Lack of utility of arteriojugular venous differences of lactate as a reliable indicator of increased brain anaerobic metabolism in traumatic brain injury.," *Journal of neurosurgery*, vol. 106, no. 4, pp. 530–537, 2007.

[185] C. Metz, M. Holzschuh, T. Bein, C. Woertgen, R. Rothoerl, B. Kallenbach, K. Taeger, and A. Brawanski, "Monitoring of cerebral oxygen metabolism in the jugular bulb: Reliability of unilateral measurements in severe head injury," *Journal of Cerebral Blood Flow & Metabolism*, vol. 18, no. 3, pp. 332–343, 1998.

[186] F. Charbel, W. Hoffman, M. Misra, K. Hannigan, and J. Ausman, "Cerebral interstitial tissue oxygen tension, pH, HCO3, CO2.," *Surgical neurology*, vol. 48, no. 4, pp. 414–417, 1997.

[187] M. Roberts and G. Owens, "Direct mass spectrographic measurement of regional intracerebral oxygen, carbon dioxide, and argon.," *Journal of neurosurgery*, vol. 37, no. 6, pp. 706–710, 1972.

[188] C. LC, M. G, and F. RP, "Chronically implanted polarographic electrodes.," *Journal of applied physiology*, vol. 13, no. 1, pp. 85–91, 1958.

[189] S. Sakadzić, E. Roussakis, M. A. Yaseen, E. T. Mandeville, V. J. Srinivasan, K. Arai, S. Ruvinskaya, A. Devor, E. H. Lo, S. A. Vinogradov, and D. A. Boas, "Two-photon high-resolution measurement of partial pressure of oxygen in cerebral vasculature and tissue.," *Nature methods*, vol. 7, no. 9, pp. 755–759, 2010.

[190] O. Ndubuizu and L. J. C, "Brain tissue oxygen concentration measurements.," *Antioxidants & redox signaling*, vol. 9, no. 8, pp. 1207–1219, 2007.

[191] A. Parpaleix, Y. Goulam Houssen, and S. Charpak, "Imaging local neuronal activity by monitoring po2 transients in capillaries.," *Nature medicine*, vol. 19, no. 2, pp. 241–246, 2013.

[192] D. Lyons, *Mapping oxygen in the awake mouse brain.* Phd thesis, Universitée Pierre et Marie Curie - Paris VI, 2015.

[193] F. A. Pennings, P. Schuurman, P. van den Munckhof, and G. J. Bouma, "Brain tissue oxygen pressure monitoring in awake patients during functional neurosurgery: the assessment of normal values.," *Journal of neurotrauma*, vol. 25, no. 10, pp. 1173–1177, 2008.

[194] A. J. Johnston, L. A. Steiner, J. P. Coles, D. A. Chatfield, T. D. Fryer, P. Smielewski, P. J. Hutchinson, M. T. O'Connell, P. G. Al-Rawi, F. I. Aigbirihio, J. C. Clark, J. D. Pickard, A. K. Gupta, and D. K. Menon, "Effect of cerebral perfusion pressure augmentation on regional oxygenation and metabolism after head injury," *Critical Care Medicine*, vol. 33, no. 1, p. 189, 2005.

[195] A. Valadka, S. Gopinath, C. Contant, M. Uzura, and C. Robertson, "Relationship of brain tissue PO2 to outcome after severe head injury.," *Critical care medicine*, vol. 26, no. 9, pp. 1576–1581, 1998.

[196] U. Ungerstedt and C. Pycock, "Functional correlates of dopamine neurotransmission.," *Bulletin der Schweizerischen Akademie der Medizinischen Wissenschaften*, vol. 30, no. 1-3, pp. 44–55, 1974.

[197] U. Ungerstedt, "Microdialysis–principles and applications for studies in animals and man.," *Journal of internal medicine*, vol. 230, no. 4, pp. 365–373, 1991.

[198] B. M. Bellander, E. Cantais, P. Enblad, P. Hutchinson, C. H. Nordström, C. Robertson, J. Sahuquillo, M. Smith, N. Stocchetti, U. Ungerstedt, A. Unterberg, and N. V. Olsen, "Consensus meeting on microdialysis in neurointensive care.," *Intensive care medicine*, vol. 30, no. 12, pp. 2166–2169, 2004.

[199] Y. Tholance, G. Barcelos, I. Quadrio, B. Renaud, F. Dailler, and P. Armand, "Analytical validation of microdialysis analyzer for monitoring glucose, lactate and pyruvate in cerebral microdialysates.," *Clinica chimica acta; international journal of clinical chemistry*, vol. 412, no. 7-8, pp. 647–654, 2011.

[200] M. Schulz, L. Wang, M. Tange, and P. Bjerre, "Cerebral microdialysis monitoring: determination of normal and ischemic cerebral metabolisms in patients with aneurysmal subarachnoid hemorrhage.," *Journal of neurosurgery*, vol. 93, no. 5, pp. 808–814, 2000.

[201] P. Reinstrup, N. Ståhl, P. Mellergård, T. Uski, U. Ungerstedt, and C. Nordström, "Intracerebral microdialysis in clinical practice: baseline values for chemical markers during wakefulness, anesthesia, and neurosurgery.," *Neurosurgery*, vol. 47, no. 3, pp. 701–9; discussion 709, 2000.

[202] P. Vespa, M. Bergsneider, N. Hattori, H. M. Wu, S. C. Huang, N. A. Martin, T. C. Glenn, M. D. L, and D. A. Hovda, "Metabolic crisis without brain ischemia is common after traumatic brain injury: a combined microdialysis and positron emission tomography study.," *Journal of cerebral blood flow and metabolism : official journal of the International Society of Cerebral Blood Flow and Metabolism*, vol. 25, no. 6, pp. 763–774, 2005.

[203] J. Sahuquillo, M. Merino, A. Sánchez-Guerrero, F. Arikan, M. Vidal-Jorge, T. Martínez-Valverde, A. Rey, M. Riveiro, and M. Poca, "Lactate and the Lactate-to-Pyruvate molar ratio cannot be used as independent biomarkers for monitoring brain energetic metabolism: A microdialysis study in patients with traumatic brain injuries," *PLoS ONE*, vol. 9, no. 7, p. e102540, 2014.

[204] J. Marcoux, D. A. McArthur, C. Miller, T. C. Glenn, P. Villablanca, N. A. Martin, D. A. Hovda, J. R. Alger, and P. M. Vespa, "Persistent metabolic crisis as measured by elevated cerebral microdialysis lactate-pyruvate ratio predicts chronic frontal lobe brain atrophy after traumatic brain injury*," *Critical Care Medicine*, vol. 36, no. 10, pp. 2871–2877, 2008.

[205] I. Timofeev, K. L. H. Carpenter, J. Nortje, P. G. Al-Rawi, M. T. O'Connell, M. Czosnyka, P. Smielewski, J. D. Pickard, D. K. Menon, P. J. Kirkpatrick, A. K. Gupta, and P. J. Hutchinson, "Cerebral extracellular chemistry and outcome following traumatic brain injury: a microdialysis study of 223 patients," *Brain*, 2011.

[206] R. Hlatky, A. B. Valadka, J. Goodman, C. F. Contant, and C. S. Robertson, "Patterns of energy substrates during ischemia measured in the brain by microdialysis.," *Journal of neurotrauma*, vol. 21, no. 7, pp. 894–906, 2004.

[207] L. Hillered, L. Persson, P. Nilsson, R. Elisabeth, and P. Enblad, "Continuous monitoring of cerebral metabolism in traumatic brain injury: a focus on cerebral microdialysis.," *Current opinion in critical care*, vol. 12, no. 2, pp. 112–118, 2006.

[208] K. G. Cesarini, P. Enblad, E. Ronne-Engström, N. Marklund, K. Salci, P. Nilsson, H. Hårdemark, L. Hillered, and L. Persson, "Early cerebral hyperglycolysis after subarachnoid haemorrhage correlates with favourable outcome," *Acta Neurochirurgica*, 2002.

[209] M. Oddo, J. M. Levine, S. Frangos, E. Maloney-Wilensky, E. Carrera, R. T. Daniel, M. Levivier, P. J. Magistretti, and P. D. LeRoux, "Brain lactate metabolism in humans with subarachnoid hemorrhage.," *Stroke; a journal of cerebral circulation*, vol. 43, no. 5, pp. 1418–1421, 2012.

[210] J. M. Schmidt, S. Ko, R. Helbok, P. Kurtz, R. M. Stuart, M. Presciutti, L. Fernandez, K. Lee, N. Badjatia, E. S. Connolly, J. Claassen, and S. A. Mayer, "Cerebral perfusion pressure thresholds for brain tissue hypoxia and metabolic crisis after Poor-Grade subarachnoid hemorrhage," *Stroke*, vol. 42, no. 5, pp. 1351–1356, 2011.

[211] J. M. Guérit, A. Amantini, P. Amodio, K. V. Andersen, S. Butler, A. de Weerd, E. Facco, C. Fischer, P. Hantson, V. Jäntti, M. D. Lamblin, G. Litscher, and Y. Péréon, "Consensus on the use of neurophysiological tests in the intensive care unit (ICU): electroencephalogram (EEG), evoked potentials (EP), and electroneuromyography (ENMG)," *Neurophysiologie Clinique/Clinical Neurophysiology*, vol. 39, no. 2, pp. 71–83, 2009.

[212] J. Claassen, L. J. Hirsch, K. T. Kreiter, E. Y. Du, E. Connolly, R. G. Emerson, and S. A. Mayer, "Quantitative continuous EEG for detecting delayed cerebral ischemia in patients with poor-grade subarachnoid hemorrhage.," *Clinical neurophysiology : official journal of*

the International Federation of Clinical Neurophysiology, vol. 115, no. 12, pp. 2699–2710, 2004.

[213] C. Fischer, D. Morlet, P. Bouchet, J. Luaute, C. Jourdan, and F. Salord, "Mismatch negativity and late auditory evoked potentials in comatose patients.," *Clinical neurophysiology : official journal of the International Federation of Clinical Neurophysiology*, vol. 110, no. 9, pp. 1601–1610, 1999.

[214] I. Holeckova, C. Fischer, D. Morlet, C. Delpuech, N. Costes, and F. Mauguière, "Subject's own name as a novel in a MMN design: a combined ERP and PET study.," *Brain research*, vol. 1189, pp. 152–165, 2008.

[215] C. Fischer, F. Dailler, and D. Morlet, "Novelty p3 elicited by the subject's own name in comatose patients.," *Clinical neurophysiology : official journal of the International Federation of Clinical Neurophysiology*, vol. 119, no. 10, pp. 2224–2230, 2008.

[216] J. Guérit, "Evoked potentials in severe brain injury," *Progress in Brain Research*, vol. 150, pp. 415–426, 2005.

[217] B. Carter and W. Butt, "Are somatosensory evoked potentials the best predictor of outcome after severe brain injury? a systematic review," *Intensive Care Med*, vol. 31, 2005.

[218] A. Amantini, A. Grippo, S. Fossi, and C. Cesaretti, "Prediction of 'awakening'and outcome in prolonged acute coma from severe traumatic brain injury: evidence for validity of short latency SEPs," *Clinical Neurophysiology*, vol. 116, p. 229–235, 2005.

[219] L. AA, "Spreading depression of activity in the cerebral cortex," 1944.

[220] L. AA, "Further observations on the spreading depression of activity in the cerebral cortex.," vol. 10, no. 6, 1947.

[221] J. P. Dreier, "The role of spreading depression, spreading depolarization and spreading ischemia in neurological disease," *Nature Medicine*, vol. 17, no. 4, pp. 439–447, 2011.

[222] M. Sramka, G. Brozek, J. Bures, and P. Nádvorník, "Functional ablation by spreading depression: possible use in human stereotactic neurosurgery.," *Applied neurophysiology*, vol. 40, no. 1, pp. 48–61, 1977.

[223] A. Mayevsky, A. Doron, T. Manor, S. Meilin, N. Zarchin, and G. Ouaknine, "Cortical spreading depression recorded from the human brain using a multiparametric monitoring system.," *Brain research*, vol. 740, no. 1-2, pp. 268–274, 1996.

[224] A. Strong, M. Fabricius, M. Boutelle, S. Hibbins, S. Hopwood, R. Jones, M. Parkin, and M. Lauritzen, "Spreading and synchronous depressions of cortical activity in acutely injured human brain," *Stroke*, vol. 33, no. 12, 2002.

[225] J. Hartings, M. Bullock, D. Okonkwo, L. Murray, G. Murray, M. Fabricius, A. Maas, J. Woitzik, O. Sakowitz, B. Mathern, B. Roozenbeek, H. Lingsma, J. Dreier, A. Puccio, L. Shutter, C. Pahl, and A. Strong, "Spreading depolarisations and outcome after traumatic brain injury: a prospective observational study," *Lancet neurology*, vol. 10, no. 12, p. 1058–64, 2011.

[226] J. Dreier, S. Major, A. Manning, J. Woitzik, C. Drenckhahn, J. Steinbrink, C. Tolias, O. Ana, M. Fabricius, J. Hartings, P. Vajkoczy, M. Lauritzen, U. Dirnagl, G. Bohner, and A. Strong, "Cortical spreading ischaemia is a novel process involved in ischaemic damage in patients with aneurysmal subarachnoid haemorrhage," *Brain*, vol. 132, no. 7, pp. 1866–1881, 2009.

[227] J. P. Dreier, J. Woitzik, M. Fabricius, R. Bhatia, S. Major, C. Drenckhahn, T. N. Lehmann, A. Sarrafzadeh, L. Willumsen, J. A. Hartings, O. W. Sakowitz, J. H. H. Seemann, A. Thieme, M. Lauritzen, and A. J. Strong, "Delayed ischaemic neurological deficits after subarachnoid haemorrhage are associated with clusters of spreading depolarizations.," *Brain : a journal of neurology*, vol. 129, no. Pt 12, pp. 3224–3237, 2006.

[228] H. K. Shin, A. K. Dunn, P. B. Jones, D. A. Boas, M. A. Moskowitz, and C. Ayata, "Vasoconstrictive neurovascular coupling during focal ischemic depolarizations.," *Journal of cerebral blood flow and metabolism*, vol. 26, no. 8, pp. 1018–1030, 2006.

[229] A. J. Strong, P. J. Anderson, H. R. Watts, D. J. Virley, A. Lloyd, E. A. Irving, T. Nagafuji, M. Ninomiya, H. Nakamura, A. K. Dunn, and R. Graf, "Peri-infarct depolarizations lead to loss of perfusion in ischaemic gyrencephalic cerebral cortex.," *Brain : a journal of neurology*, vol. 130, no. Pt 4, pp. 995–991008, 2007.

[230] M. Lauritzen, J. Dreier, M. Fabricius, J. Hartings, R. Graf, and A. Strong, "Clinical relevance of cortical spreading depression in neurological disorders: migraine, malignant stroke, subarachnoid and intracranial hemorrhage, and traumatic brain injury," *Journal of cerebral blood flow and metabolism*, vol. 31, no. 1, 2011.

[231] R. Saito, R. Graf, K. Hübel, T. Fujita, G. Rosner, and W. Heiss, "Reduction of infarct volume by halothane: effect on cerebral blood flow or perifocal spreading depression-like depolarizations.," *Journal of cerebral blood flow and metabolism : official journal of the International Society of Cerebral Blood Flow and Metabolism*, vol. 17, no. 8, pp. 857–864, 1997.

[232] A. Douen, K. Akiyama, M. Hogan, F. Wang, L. Dong, A. Chow, and A. Hakim, "Preconditioning with cortical spreading depression decreases intraischemic cerebral glutamate levels and Down-Regulates excitatory amino acid transporters EAAT1 and EAAT2 from rat cerebal cortex plasma membranes," *Journal of Neurochemistry*, vol. 75, no. 2, pp. 812–818, 2000.

[233] D. Attwell and S. Laughlin, "An energy budget for signaling in the grey matter of the brain.," *Journal of cerebral blood flow and metabolism : official journal of the International Society of Cerebral Blood Flow and Metabolism*, vol. 21, no. 10, pp. 1133–1145, 2001.

[234] R. Kraig and C. Nicholson, "Extracellular ionic variations during spreading depression.," *Neuroscience*, vol. 3, no. 11, pp. 1045–1059, 1978.

[235] J. Makarova, G. Marta, and O. Herreras, "Variations in tissue resistivity and in the extension of activated neuron domains shape the voltage signal during spreading depression in the CA1 in vivo.," *The European journal of neuroscience*, vol. 27, no. 2, pp. 444–456, 2008.

[236] W. Risher, D. Ard, and J. Yuan, "Recurrent spontaneous spreading depolarizations facilitate acute dendritic injury in the ischemic penumbra," *The Journal of Neuroscience*, vol. 30, pp. 9859–9868, 2010.

[237] X. Lian and J. L. Stringer, "Energy failure in astrocytes increases the vulnerability of neurons to spreading depression," *European Journal of Neuroscience*, vol. 19, no. 9, pp. 2446–2454, 2004.

[238] V. H. A, "Compounds in brain extracts causing spreading depression of cerebral cortical activity and contraction of crustacean muscle.," *Journal of neurochemistry*, vol. 3, no. 4, pp. 300–315, 1959.

[239] M. L. Rogers, D. Feuerstein, C. Leong, M. Takagaki, X. Niu, R. Graf, and M. G. Boutelle, "Continuous online microdialysis using microfluidic sensors: Dynamic neurometabolic changes during spreading depolarization," *ACS Chemical Neuroscience*, vol. 4, no. 5, pp. 799–807, 2013.

[240] J. M. Hinzman, V. A. DiNapoli, E. J. Mahoney, G. A. Gerhardt, and J. A. Hartings, "Spreading depolarizations mediate excitotoxicity in the development of acute cortical lesions.," *Experimental neurology*, vol. 267, pp. 243–253, 2015.

[241] G. AR, "A study of the mechanisms by which potassium moves through brain tissue in the rat.," *The Journal of physiology*, vol. 335, pp. 353–374, 1983.

[242] R. Enger, W. Tang, G. F. Vindedal, V. Jensen, P. J. Helm, R. Sprengel, L. L. Looger, and E. A. Nagelhus, "Dynamics of ionic shifts in cortical spreading depression," *Cerebral Cortex*, vol. Epub ahead of print, p. bhv054, 2015.

[243] B. Shapiro, "Osmotic forces and gap junctions in spreading depression: a computational model.," *Journal of computational neuroscience*, vol. 10, no. 1, pp. 99–9120, 2001.

[244] N. J. Willmott, K. Wong, and A. J. Strong, "Intercellular ca2+ waves in rat hippocampal slice and dissociated glial–neuron cultures mediated by nitric oxide," *FEBS Letters*, vol. 487, no. 2, 2001.

[245] J. D. Pickard, N. Akalan, C. D. Rocco, V. Dolenc, R. Fahlbusch, J. L. Antunes, M. Sindou, N. de Tribolet, C. A. F. Tulleken, A. J. Strong, and R. Dardis, "Advances and technical standards in neurosurgery," *Advances and technical standards in neurosurgery*, 2005.

[246] R. Harris, L. Symon, N. Branston, and M. Bayhan, "Changes in extracellular calcium activity in cerebral ischaemia.," *Journal of cerebral blood flow and metabolism : official journal of the International Society of Cerebral Blood Flow and Metabolism*, vol. 1, no. 2, pp. 203–209, 1981.

[247] A. Hansen, "The extracellular potassium concentration in brain cortex following ischemia in hypo- and hyperglycemic rats.," *Acta physiologica Scandinavica*, vol. 102, no. 3, pp. 324–329, 1978.

[248] D. von Bornstädt, T. Houben, J. L. Seidel, Y. Zheng, E. Dilekoz, T. Qin, N. Sandow, S. Kura, K. Eikermann-Haerter, M. Endres, D. A. Boas, M. A. Moskowitz, E. H. Lo, J. P. Dreier, J. Woitzik, S. Sakadžić, and C. Ayata, "Supply-Demand mismatch transients in susceptible peri-infarct hot zones explain the origins of spreading injury depolarizations.," *Neuron*, vol. 85, no. 5, pp. 1117–1131, 2015.

[249] L. AA, "Pial circulatiuon and spreading depression of activity in the cerebral cortex," 1944.

[250] Y. Kao, W. Li, H. Lai, E. Oyarzabal, W. Lin, and Y. Shih, "Dynamic perfusion and diffusion MRI of cortical spreading depolarization in photothrombotic ischemia," *Neurobiology of Disease*, pp. 131–139, 2014.

[251] I. Sukhotinsky, E. Dilekoz, M. Moskowitz, and C. Ayata, "Hypoxia and hypotension transform the blood flow response to cortical spreading depression from hyperemia into hypoperfusion in the rat," *Journal of Cerebral Blood Flow & Metabolism*, vol. 28, no. 7, p. 1369–1376, 2008.

[252] D. Feuerstein, M. Takagaki, M. Gramer, A. Manning, H. Endepols, S. Vollmar, T. Yoshimine, A. Strong, R. Graf, and H. Backes, "Detecting tissue deterioration after brain injury: regional blood flow level versus capacity to raise blood flow," *Journal of Cerebral Blood Flow & metabolism*, vol. 34, no. 7, pp. 1117–1127, 2014.

[253] Z. Bere, T. P. Obrenovitch, G. Kozák, F. Bari, and E. Farkas, "Imaging reveals the focal area of spreading depolarizations and a variety of hemodynamic responses in a rat microembolic stroke model," *Journal of Cerebral Blood Flow & Metabolism*, vol. 34, no. 10, pp. 1695–1705, 2014.

[254] J. M. Hinzman, N. Andaluz, L. A. Shutter, D. O. Okonkwo, C. Pahl, A. J. Strong, J. P. Dreier, and J. A. Hartings, "Inverse neurovascular coupling to cortical spreading depolarizations in severe brain trauma.," *Brain : a journal of neurology*, vol. 137, no. Pt 11, pp. 2960–2972, 2014.

[255] J. Dreier, K. Körner, N. Ebert, A. Görner, I. Rubin, T. Back, U. Lindauer, T. Wolf, A. Villringer, K. Einhäupl, M. Lauritzen, and U. Dirnagl, "Nitric oxide scavenging by hemoglobin or nitric oxide synthase inhibition by N-Nitro-L-Arginine induces cortical spreading ischemia when k+ is increased in the subarachnoid space," *Jounal of Cerebral Blood Flow & metabolism*, vol. 18, no. 9, pp. 978–990, 1998.

[256] A. Leão and R. Morison, "Propagation of spreading cortical depression.," *The Journal of Nervous and Mental Disease*, vol. 102, no. 5, p. 512, 1945.

[257] A. Mayevsky, S. Lebourdais, and B. Chance, "The interrelation between brain PO2 and NADH oxidation-reduction state in the gerbil.," *Journal of neuroscience research*, vol. 5, no. 3, pp. 173–182, 1980.

[258] H. Piilgaard and M. Lauritzen, "Persistent increase in oxygen consumption and impaired neurovascular coupling after spreading depression in rat neocortex," *Journal of Cerebral Blood Flow & Metabolism*, vol. 29, no. 9, p. 1517–1527, 2009.

[259] B. Bosche, R. Graf, R. Ernestus, C. Dohmen, T. Reithmeier, G. Brinker, A. Strong, J. Dreier, and J. Woitzik, "Recurrent spreading depolarizations after subarachnoid hemorrhage decreases oxygen availability in human cerebral cortex," *Annals of Neurology*, vol. 67, no. 5, 2010.

[260] M. C. Parkin, S. E. Hopwood, M. G. Boutelle, and A. J. Strong, "Resolving dynamic changes in brain metabolism using biosensors and on-line microdialysis," *TrAC Trends in Analytical Chemistry*, vol. 22, no. 8, pp. 487–497, 2003.

[261] P. Hashemi, R. Bhatia, H. Nakamura, J. Dreier, R. Graf, A. Strong, and M. Boutelle, "Persisting depletion of brain glucose following cortical spreading depression, despite apparent hyperaemia: evidence for risk of an adverse effect of leão's spreading depression," *Journal of Cerebral Blood Flow & Metabolism*, vol. 29, no. 1, 2009.

[262] M. Parkin, S. Hopwood, D. Jones, P. Hashemi, H. Landolt, M. Fabricius, M. Lauritzen, M. Boutelle, and A. Strong, "Dynamic changes in brain glucose and lactate in pericontusional areas of the human cerebral cortex, monitored with rapid sampling on-line microdialysis: relationship with depolarisation-like events," *Journal of Cerebral Blood Flow & Metabolism*, vol. 25, no. 3, p. 402–413, 2005.

[263] S. Hopwood, M. Parkin, E. Bezzina, M. Boutelle, and A. Strong, "Transient changes in cortical glucose and lactate levels associated with peri-infarct depolarisations, studied with rapid-sampling microdialysis," *Journal of Cerebral Blood Flow & Metabolism*, vol. 25, no. 3, 2005.

[264] D. Feuerstein, A. Manning, P. Hashemi, R. Bhatia, M. Fabricius, C. Tolias, C. Pahl, M. Ervine, A. J. Strong, and M. G. Boutelle, "Dynamic metabolic response to multiple spreading depolarizations in patients with acute brain injury: an online microdialysis study," *Journal of Cerebral Blood Flow & Metabolism*, vol. 30, no. 7, pp. 1343–1355, 2010.

[265] A. V. Harreveld and E. Fifková, "Glutamate release from the retina during spreading depression," *Journal of Neurobiology*, vol. 2, no. 1, pp. 13–29, 1970.

[266] M. Fabricius, L. Jensen, and M. Lauritzen, "Microdialysis of interstitial amino acids during spreading depression and anoxic depolarization in rat neocortex.," *Brain research*, vol. 612, no. 1-2, pp. 61–69, 1993.

[267] R. A., M. Z., and J. Bures, "Tolerance to ketamine-induced blockade of cortical spreading depression transfers to MK-801 but not to AP5 in rats," *Brain Research*, vol. 693, no. 1-2, pp. 64–69, 1995.

[268] M. Lauritzen and A. Hansen, "The effect of glutamate receptor blockade on anoxic depolarization and cortical spreading depression," *Journal of Cerebral Blood Flow & Metabolism*, vol. 12, no. 2, pp. 223–229, 1992.

[269] D. N. Hertle, J. P. Dreier, J. Woitzik, J. A. Hartings, R. Bullock, D. O. Okonkwo, L. A. Shutter, S. Vidgeon, A. J. Strong, C. Kowoll, C. Dohmen, J. Diedler, R. Veltkamp, T. Bruckner, A. W. Unterberg, O. W. Sakowitz, and C. S. of Brain Injury Depolarizations (COSBID), "Effect of analgesics and sedatives on the occurrence of spreading depolarizations accompanying acute brain injury," *Brain*, vol. 135, no. 8, pp. 2390–2398, 2012.

[270] A. Marmarou, M. Foda, W. van den Brink, J. Campbell, H. Kita, and K. Demetriadou, "A new model of diffuse brain injury in rats. part i: Pathophysiology and biomechanics.," *Journal of neurosurgery*, vol. 80, no. 2, pp. 291–300, 1994.

[271] Y. Xiong, A. Mahmood, and M. Chopp, "Animal models of traumatic brain injury," *Nature Reviews Neuroscience*, vol. 14, no. 2, pp. 128–142, 2013.

[272] R. P. Fares, A. Belmeguenai, P. E. Sanchez, H. Y. Kouchi, J. Bodennec, A. Morales, B. Georges, C. Bonnet, S. Bouvard, R. S. Sloviter, and L. Bezin, "Standardized environmental enrichment supports enhanced brain plasticity in healthy rats and prevents cognitive impairment in epileptic rats.," *PloS one*, vol. 8, no. 1, p. e53888, 2013.

[273] I. Yatsiv, N. Grigoriadis, C. Simeonidou, P. Stahel, O. Schmidt, A. Alexandrovitch, J. Tsenter, and E. Shohami, "Erythropoietin is neuroprotective, improves functional recovery, and reduces neuronal apoptosis and inflammation in a rodent model of experimental closed head injury.," *FASEB journal : official publication of the Federation of American Societies for Experimental Biology*, vol. 19, no. 12, pp. 1701–1703, 2005.

[274] Y. van de Looij, F. Mauconduit, M. Beaumont, S. Valable, R. Farion, G. Francony, J. F. Payen, and H. Lahrech, "Diffusion tensor imaging of diffuse axonal injury in a rat brain trauma model.," *NMR in biomedicine*, vol. 25, no. 1, pp. 93–9103, 2012.

[275] A. Christiane, C. Várrallyay, F. Raslan, C. Kleinschnitz, and A. L. Sirén, "An experimental protocol for mimicking pathomechanisms of traumatic brain injury in mice.," *Experimental & translational stroke medicine*, vol. 4, p. 1, 2012.

[276] C. Schilte, P. Bouzat, A. Millet, P. Boucheix, P. Karin, B. Lemasson, E. L. Barbier, and J. F. Payen, "Mannitol improves brain tissue oxygenation in a model of diffuse traumatic brain injury.," *Critical care medicine*, 2015.

[277] I. Cernak and N. L. J, "Traumatic brain injury: an overview of pathobiology with emphasis on military populations.," *Journal of cerebral blood flow and metabolism : official journal of the International Society of Cerebral Blood Flow and Metabolism*, vol. 30, no. 2, pp. 255–266, 2010.

[278] H. Thompson, J. Lifshitz, N. Marklund, M. Grady, D. Graham, D. Hovda, and T. McIntosh, "Lateral fluid percussion brain injury: A 15-Year review and evaluation," *Journal of Neurotrauma*, vol. 22, no. 1, pp. 42–75, 2005.

[279] M. TK, R. Vink, L. Noble, I. Yamakami, S. Fernyak, H. Soares, and A. Faden, "Traumatic brain injury in the rat: characterization of a lateral fluid-percussion model.," *Neuroscience*, vol. 28, no. 1, pp. 233–244, 1989.

[280] R. Hicks, H. Soares, D. Smith, and T. McIntosh, "Temporal and spatial characterization of neuronal injury following lateral fluid-percussion brain injury in the rat.," *Acta neuropathologica*, vol. 91, no. 3, pp. 236–246, 1996.

[281] S. V. Kabadi, G. D. Hilton, B. A. Stoica, D. N. Zapple, and A. I. Faden, "Fluid-percussion-induced traumatic brain injury model in rats," *Nature Protocols*, vol. 5, no. 9, pp. 1552–1563, 2010.

[282] M. Sato, E. Chang, T. Igarashi, and L. J. Noble, "Neuronal injury and loss after traumatic brain injury: time course and regional variability.," *Brain research*, vol. 917, no. 1, pp. 45–54, 2001.

[283] S. V. Kabadi, B. A. Stoica, D. J. Loane, T. Luo, and A. I. Faden, "CR8, a novel inhibitor of CDK, limits microglial activation, astrocytosis, neuronal loss, and neurologic dysfunction after experimental traumatic brain injury," *Journal of Cerebral Blood Flow & Metabolism*, vol. 34, no. 3, pp. 502–513, 2014.

[284] R. Hamm, "Neurobehavioral assessment of outcome following traumatic brain injury in rats: an evaluation of selected measures.," *Journal of neurotrauma*, vol. 18, no. 11, pp. 1207–1216, 2001.

[285] J. Pierce, D. Smith, J. Trojanowski, and M. TK, "Enduring cognitive, neurobehavioral and histopathological changes persist for up to one year following severe experimental brain injury in rats.," *Neuroscience*, vol. 87, no. 2, pp. 359–369, 1998.

[286] H. H. Li, S. M. Lee, Y. Cai, R. L. Sutton, and D. A. Hovda, "Differential gene expression in hippocampus following experimental brain trauma reveals distinct features of moderate and severe injuries," *Journal of Neurotrauma*, vol. 21, no. 9, pp. 1141–1153, 2004.

[287] G. Fox, L. Fan, R. Levasseur, and A. Faden, "Sustained sensory/motor and cognitive deficits with neuronal apoptosis following controlled cortical impact brain injury in the mouse.," *Journal of neurotrauma*, vol. 15, no. 8, pp. 599–614, 1998.

[288] P. M. Washington, P. A. Forcelli, T. Wilkins, D. N. Zapple, M. Parsadanian, and M. P. Burns, "The effect of injury severity on behavior: a phenotypic study of cognitive and emotional deficits after mild, moderate, and severe controlled cortical impact injury in mice.," *Journal of neurotrauma*, vol. 29, no. 13, pp. 2283–2296, 2012.

[289] A. Obenaus, M. Robbins, G. Blanco, N. R. Galloway, E. Snissarenko, E. Gillard, S. Lee, and C. Margarita, "Multi-modal magnetic resonance imaging alterations in two rat models of mild neurotrauma.," *Journal of neurotrauma*, vol. 24, no. 7, pp. 1147–1160, 2007.

[290] D. L. Brody and D. M. Holtzman, "Morris water maze search strategy analysis in PDAPP mice before and after experimental traumatic brain injury.," *Experimental neurology*, vol. 197, no. 2, pp. 330–340, 2006.

[291] D. Feeney, M. Boyeson, R. Linn, H. Murray, and W. Dail, "Responses to cortical injury: I. methodology and local effects of contusions in the rat.," *Brain research*, vol. 211, no. 1, pp. 67–77, 1981.

[292] A. J. Williams, J. A. Hartings, X. M. C. Lu, M. L. Rolli, J. R. Dave, and F. C. Tortella, "Characterization of a new rat model of penetrating ballistic brain injury.," *Journal of neurotrauma*, vol. 22, no. 2, pp. 313–331, 2005.

[293] M. S. Grady, J. S. Charleston, D. Maris, B. M. Witgen, and J. Lifshitz, "Neuronal and glial cell number in the hippocampus after experimental traumatic brain injury: Analysis by stereological estimation," *Journal of Neurotrauma*, vol. 20, no. 10, p. 929941, 2003.

[294] G. Rogatsky, J. Sonn, and Y. Kamenir, "Relationship between intracranial pressure and cortical spreading depression following fluid percussion brain injury in rats," *Journal of Neurotrauma*, vol. 20, pp. 1315–1325, 2004.

[295] L. Baumgarten, R. Trabold, S. Thal, T. Back, and N. Plesnila, "Role of cortical spreading depressions for secondary brain damage after traumatic brain injury in mice," *Journal of Cerebral Blood Flow & Metabolism*, vol. 28, no. 7, p. 1353–1360, 2008.

[296] L. Y. Leung, G. Wei, D. A. Shear, and F. C. Tortella, "The acute effects of hemorrhagic shock on cerebral blood flow, brain tissue oxygen tension, and spreading depolarization following penetrating Ballistic-Like brain injury," *Journal of Neurotrauma*, vol. 30, no. 14, 2013.

[297] P. Bentzer, G. Mattiasson, M. TK, T. Wieloch, and P. Grande, "Infusion of prostacyclin following experimental brain injury in the rat reduces cortical lesion volume.," *Journal of neurotrauma*, vol. 18, no. 3, pp. 275–285, 2001.

[298] C. Zhang, R. Raghupathi, K. Saatman, D. Smith, J. Stutzmann, F. Wahl, and M. TK, "Riluzole attenuates cortical lesion size, but not hippocampal neuronal loss, following traumatic brain injury in the rat.," *Journal of neuroscience research*, vol. 52, no. 3, pp. 342–349, 1998.

[299] L. Schmued, C. Albertson, and W. Slikker, "Fluoro-Jade: a novel fluorochrome for the sensitive and reliable histochemical localization of neuronal degeneration.," *Brain research*, vol. 751, no. 1, pp. 37–46, 1997.

[300] R. Auer, H. Kalimo, Y. Olsson, and B. Siesjö, "The temporal evolution of hypoglycemic brain damage. i. light- and electron-microscopic findings in the rat cerebral cortex.," *Acta neuropathologica*, vol. 67, no. 1-2, pp. 13–24, 1985.

[301] R. Raghupathi, A. C. Conti, D. I. Graham, S. Krajewski, J. C. Reed, M. S. Grady, J. Q. Trojanowski, and T. K. McIntosh, "Mild traumatic brain injury induces apoptotic cell death in the cortex that is preceded by decreases in cellular bcl-2 immunoreactivity.," *Neuroscience*, vol. 110, no. 4, pp. 605–616, 2002.

[302] L. C. Schmued, C. C. Stowers, A. C. Scallet, and L. Xu, "Fluoro-Jade c results in ultra high resolution and contrast labeling of degenerating neurons.," *Brain research*, vol. 1035, no. 1, pp. 24–31, 2005.

[303] K. L. Sanderson, R. Raghupathi, K. E. Saatman, D. Martin, G. Miller, and T. K. McIntosh, "Interleukin-1 receptor antagonist attenuates regional neuronal cell death and cognitive dysfunction after experimental brain injury," *Journal of Cerebral Blood Flow & Metabolism*, vol. 19, no. 10, pp. 1118–1125, 1999.

[304] J. A. Cheney, A. L. Brown, F. M. Bareyre, A. B. Russ, J. D. Weisser, H. A. Ensinger, A. Leusch, R. Raghupathi, and K. E. Saatman, "The novel compound LOE 908 attenuates acute neuromotor dysfunction but not cognitive impairment or cortical tissue loss following traumatic brain injury in rats.," *Journal of neurotrauma*, vol. 17, no. 1, pp. 83–91, 2000.

[305] T. Enomoto, T. Osugi, H. Satoh, T. K. McIntosh, and T. Nabeshima, "Pre-Injury magnesium treatment prevents traumatic brain injury-induced hippocampal ERK activation, neuronal loss, and cognitive dysfunction in the radial-arm maze test.," *Journal of neurotrauma*, vol. 22, no. 7, pp. 783–792, 2005.

[306] B. M. Witgen, J. Lifshitz, M. L. Smith, E. Schwarzbach, S. Liang, M. S. Grady, and A. S. Cohen, "Regional hippocampal alteration associated with cognitive deficit following experimental brain injury: a systems, network and cellular evaluation.," *Neuroscience*, vol. 133, no. 1, p. 115, 2005.

[307] R. Selwyn, N. Hockenbury, S. Jaiswal, S. Mathur, R. C. Armstrong, and K. R. Byrnes, "Mild traumatic brain injury results in depressed cerebral glucose uptake: An (18)FDG PET study.," *Journal of neurotrauma*, vol. 30, no. 23, pp. 1943–1953, 2013.

[308] T. Luo, J. Wu, S. V. Kabadi, B. Sabirzhanov, K. Guanciale, M. Hanscom, J. Faden, K. Cardiff, C. J. Bengson, and A. I. Faden, "Propofol limits microglial activation after experimental brain trauma through inhibition of nicotinamide adenine dinucleotide phosphate oxidase," *Anesthesiology*, vol. 119, no. 6, pp. 1370–1388, 2013.

[309] C. Woeffler-Maucler, A. Beghin, D. Ressnikoff, L. Bezin, and S. Marinesco, "Automated immunohistochemical method to quantify neuronal density in brain sections: Application to neuronal loss after status epilepticus," *Journal of neuroscience methods*, vol. 225, p. 32–41, 2014.

[310] K. K. Kim, R. S. Adelstein, and S. Kawamoto, "Identification of neuronal nuclei (NeuN) as fox-3, a new member of the fox-1 gene family of splicing factors.," *The Journal of biological chemistry*, vol. 284, no. 45, pp. 31052–31061, 2009.

[311] S. Maxeiner, A. Glassmann, H. T. Kao, and K. Schilling, "The molecular basis of the specificity and cross-reactivity of the NeuN epitope of the neuron-specific splicing regulator, rbfox3.," *Histochemistry and cell biology*, vol. 141, no. 1, pp. 43–55, 2014.

[312] M. V. Sofroniew and H. V. Vinters, "Astrocytes: biology and pathology.," *Acta neuropathologica*, vol. 119, no. 1, pp. 7–35, 2010.

[313] J. Collombet, C. Masqueliez, E. Four, M. Burckhart, D. Bernabé, D. Baubichon, and G. Lallement, "Early reduction of NeuN antigenicity induced by soman poisoning in mice can be used to predict delayed neuronal degeneration in the hippocampus," *Neuroscience letters*, vol. 398, no. 3, pp. 337–342, 2006.

[314] R. Caton, "Electrical currents of the brain.," *Chicago Journal of Nervous and Mental Disease*, vol. 2, p. 610, 1875.

[315] G. Buzsáki, C. A. Anastassiou, and C. Koch, "The origin of extracellular fields and currents–EEG, ECoG, LFP and spikes.," *Nature reviews. Neuroscience*, vol. 13, no. 6, pp. 407–420, 2012.

[316] J. Kang, L. Jiang, S. Goldman, and M. Nedergaard, "Astrocyte-mediated potentiation of inhibitory synaptic transmission," *nature neuroscience*, vol. 1, pp. 683–692, 1998.

[317] A. Viggiano, S. Marinesco, F. Pain, A. Meiller, and H. Gurden, "Reconstruction of field excitatory post-synaptic potentials in the dentate gyrus from amperometric biosensor signals.," *Journal of neuroscience methods*, vol. 206, no. 1, pp. 1–6, 2012.

[318] N. Hayward, P. Tuunanen, R. Immonen, X. Ndode-Ekane, A. Pitkänen, and O. Gröhn, "Magnetic resonance imaging of regional hemodynamic and cerebrovascular recovery after lateral fluid-percussion brain injury in rats.," *Journal of cerebral blood flow & metabolism*, vol. 31, no. 1, pp. 166–177, 2011.

[319] Z. Xiao-Hong, Z. Yi, T. Run-Xia, L. Hao, Z. Nanyin, Z. Xiaoliang, M. Hellmut, U. Kamil, and C. Wei, "Development of 17O NMR approach for fast imaging of cerebral metabolic rate of oxygen in rat brain at high field," *Proceedings of the National Academy of Sciences*, vol. 99, no. 20, pp. 13194–13199, 2002.

[320] D. Jones, M. Parkin, H. Langemann, H. Landolt, S. Hopwood, A. Strong, and M. Boutelle, "On-line monitoring in neurointensive care: enzyme-based electrochemical assay for simultaneous, continuous monitoring of glucose and lactate from critical care patients," *Journal of Electroanalytical Chemistry*, vol. 538, pp. 243–252, 2002.

[321] A. Khan and A. Michael, "Invasive consequences of using micro-electrodes and microdialysis probes in the brain," *TrAC Trends in Analytical Chemistry*, pp. 503–508, 2003.

[322] M. Morgan, D. Singhal, and B. Anderson, "Quantitative assessment of blood-brain barrier damage during microdialysis.," *The Journal of pharmacology and experimental therapeutics*, vol. 277, no. 2, pp. 1167–1176, 1996.

[323] S. Marinesco and N. Dale, *Microelectrode Biosensors*, vol. 80 of *Neuromethods*. Humana Press, 2013.

[324] M. Vafaee and A. Gjedde, "Model of Blood-Brain transfer of oxygen explains nonlinear Flow-Metabolism coupling during stimulation of visual cortex," *Journal of Cerebral Blood Flow & Metabolism*, pp. 747–754, 2000.

[325] H. Grocott, R. Bart, H. Sheng, Y. Miura, R. Steffen, R. Pearlstein, and D. Warner, "Effects of a synthetic allosteric modifier of hemoglobin oxygen affinity on outcome from global cerebral ischemia in the rat.," *Stroke*, vol. 29, no. 8, pp. 1650–1655, 1998.

[326] V. Baughman, W. Hoffman, C. Thomas, D. Miletich, and R. Albrecht, "Comparison of methohexital and isoflurane on neurologic outcome and histopathology following incomplete ischemia in rats.," *Anesthesiology*, vol. 72, no. 1, pp. 85–94, 1990.

[327] L. Nilsson and B. Siesjö, "The effect of phenobarbitone anaesthesia on blood flow and oxygen consumption in the rat brain.," *Acta anaesthesiologica Scandinavica. Supplementum*, vol. 57, pp. 18–24, 1975.

[328] J. Harp, L. Nilsson, and B. Siesjö, "The effect of halothane anaesthesia upon cerebral oxygen consumption in the rat," *Acta Anaesthesiologica Scandinavica*, vol. 20, no. 1, pp. 83–90, 1976.

[329] L. Berntman, N. Dahlgren, and B. Siesjö, "Cerebral blood flow and oxygen consumption in the rat brain during extreme hypercarbia.," *Anesthesiology*, vol. 50, no. 4, pp. 299–305, 1979.

[330] P. Poulsen, D. Smith, L. Østergaard, E. Danielsen, A. Gee, S. Hansen, J. Astrup, and A. Gjedde, "In vivo estimation of cerebral blood flow, oxygen consumption and glucose metabolism in the pig by [15O]water injection, [15O]oxygen inhalation and dual injections of [18F]fluorodeoxyglucose," *Journal of Neuroscience Methods*, vol. 77, no. 2, p. 199–209, 1997.

[331] F. Hyder, R. Kennan, I. Kida, G. Mason, K. Behar, and D. Rothman, "Dependence of oxygen delivery on blood flow in rat brain: a 7 tesla nuclear magnetic resonance study.," *Journal of cerebral blood flow and metabolism : official journal of the International Society of Cerebral Blood Flow and Metabolism*, vol. 20, no. 3, pp. 485–498, 2000.

[332] F. Beckmann, K. Heise, B. Kölsch, U. Bonse, M. Rajewsky, M. Bartscher, and T. Biermann, "Three-dimensional imaging of nerve tissue by x-ray phase-contrast microtomography.," *Biophysical journal*, vol. 76, no. 1.1, pp. 98–9102, 1999.

[333] R. Gruetter, K. Ugurbil, and E. Seaquist, "Steady-state cerebral glucose concentrations and transport in the human brain.," *Journal of neurochemistry*, vol. 70, no. 1, pp. 397–408, 1998.

[334] J. Pfeuffer, I. Tkác, and R. Gruetter, "Extracellular-intracellular distribution of glucose and lactate in the rat brain assessed noninvasively by diffusion-weighted 1H nuclear magnetic resonance spectroscopy in vivo.," *Journal of cerebral blood flow and metabolism : official journal of the International Society of Cerebral Blood Flow and Metabolism*, vol. 20, no. 4, pp. 736–746, 2000.

[335] R. A. de Graaf, J. W. Pan, F. Telang, J. Lee, P. Brown, E. J. Novotny, H. P. Hetherington, and D. L. Rothman, "Differentiation of glucose transport in human brain gray and white matter," *Journal of Cerebral Blood Flow & Metabolism*, vol. 21, no. 5, pp. 483–492, 2001.

[336] J. M. N. Duarte, F. D. Morgenthaler, H. Lei, C. Poitry-Yamate, and R. Gruetter, "Steady-state brain glucose transport kinetics re-evaluated with a four-state conformational model," *Frontiers in Neuroenergetics*, vol. 1, p. 6, 2009.

[337] L. Barros, C. X. Bittner, A. Loaiza, and O. H. Porras, "A quantitative overview of glucose dynamics in the gliovascular unit.," *Glia*, vol. 55, no. 12, pp. 1222–1237, 2007.

[338] R. A. de Graaf, J. W. Pan, F. Telang, J. Lee, P. Brown, E. J. Novotny, H. P. Hetherington, and D. L. Rothman, "Differentiation of glucose transport in human brain gray and white matter," *Journal of Cerebral Blood Flow & Metabolism*, vol. 21, no. 5, pp. 483–492, 2001.

[339] I. Y. Choi, H. Lei, and R. Gruetter, "Effect of deep pentobarbital anesthesia on neurotransmitter metabolism in vivo: on the correlation of total glucose consumption with glutamatergic action.," *Journal of cerebral blood flow and metabolism : official journal of the International Society of Cerebral Blood Flow and Metabolism*, vol. 22, no. 11, pp. 1343–1351, 2002.

[340] I. Choi, S. Lee, S. Kim, and R. Gruetter, "In vivo measurements of brain glucose transport using the reversible Michaelis-Menten model and simultaneous measurements of cerebral blood flow changes during hypoglycemia.," *Journal of cerebral blood flow and metabolism : official journal of the International Society of Cerebral Blood Flow and Metabolism*, vol. 21, no. 6, pp. 653–663, 2001.

[341] F. D. Morgenthaler, D. M. Koski, R. Kraftsik, P. G. Henry, and R. Gruetter, "Biochemical quantification of total brain glycogen concentration in rats under different glycemic states.," *Neurochemistry international*, vol. 48, no. 6-7, pp. 616–622, 2006.

[342] J. M. M. Duarte, H. Lei, V. Mlynárik, and R. Gruetter, "The neurochemical profile quantified by in vivo 1H NMR spectroscopy.," *NeuroImage*, vol. 61, no. 2, pp. 342–362, 2012.

[343] L. Netchiporouk, N. Shram, D. Salvert, and R. Cespuglio, "Brain extracellular glucose assessed by voltammetry throughout the rat sleep-wake cycle.," *The European journal of neuroscience*, vol. 13, no. 7, pp. 1429–1434, 2001.

[344] H. Lei and R. Gruetter, "Effect of chronic hypoglycaemia on glucose concentration and glycogen content in rat brain: A localized 13C NMR study.," *Journal of neurochemistry*, vol. 99, no. 1, pp. 260–268, 2006.

[345] F. Du, Y. Zhang, X. Zhu, and W. Chen, "Simultaneous measurement of glucose blood–brain transport constants and metabolic rate in rat brain using in-vivo 1H MRS," *Journal of Cerebral Blood Flow & Metabolism*, vol. 32, no. 9, pp. 1778–1787, 2012.

[346] C. Ori, M. Dam, G. Pizzolato, L. Battistin, and G. Giron, "Effects of isoflurane anesthesia on local cerebral glucose utilization in the rat.," *Anesthesiology*, vol. 65, no. 2, pp. 152–156, 1986.

[347] W. Streit, "Microglial response to brain injury: a brief synopsis.," *Toxicologic pathology*, vol. 28, no. 1, pp. 28–30, 2000.

[348] A. C. Conti, R. Raghupathi, J. Q. Trojanowski, and M. T. K, "Experimental brain injury induces regionally distinct apoptosis during the acute and delayed post-traumatic period," *The Journal of neuroscience*, vol. 18, no. 15, pp. 5663–5672, 1998.

[349] Y. Sakamoto and M. Ishiguro, "Akaike information criterion statistics," 1986.

[350] B. Stephens, E. Spessert, G. Knaysi, M. Cota, and L. Latour, "Volumetric measurements of cytotoxic and vasogenic edema following traumatic brain injury using magnetic resonance imaging," *Neurology*, vol. 84, no. 14 Suppl, p. 7.156, 2015.

[351] I. Loubinoux, A. Volk, J. Borredon, S. Guirimand, B. Tiffon, J. Seylaz, and P. Méric, "Spreading of vasogenic edema and cytotoxic edema assessed by quantitative diffusion and t2 magnetic resonance imaging.," *Stroke; a journal of cerebral circulation*, vol. 28, no. 2, pp. 419–26; discussion 426, 1997.

[352] J. Dreier, J. K, G. Petzold, O. Tomkins, R. Klingebiel, U. Kopp, L. F, A. Friedman, and M. Dichgans, "Opening of the blood-brain barrier preceding cortical edema in a severe attack of FHM type II.," *Neurology*, vol. 64, no. 12, pp. 2145–2147, 2005.

[353] A. Schiefecker, R. Beer, B. Pfausler, and P. Lackner, "Clusters of cortical spreading depolarizations in a patient with intracerebral hemorrhage: A multimodal neuromonitoring study," *Neurocritical care*, vol. 22, no. 2, pp. 293–298, 2015.

[354] G. AR and V. N. Bruggen, "Magnetic resonance imaging of propagating waves of spreading depression in the anaesthetised rat," *Journal of Cerebral Blood Flow & Metabolism*, vol. 14, no. 1, pp. 7–11, 1994.

[355] R. Meierhans, M. Béchir, S. Ludwig, J. Sommerfeld, G. Brandi, C. Haberthür, R. Stocker, and J. F. Stover, "Brain metabolism is significantly impaired at blood glucose below 6 mM and brain glucose below 1 mM in patients with severe traumatic brain injury.," *Critical care (London, England)*, vol. 14, no. 1, p. R13, 2010.

[356] J. Goodman, A. Valadka, S. Gopinath, M. Uzura, and C. Robertson, "Extracellular lactate and glucose alterations in the brain after head injury measured by microdialysis.," *Critical care medicine*, vol. 27, no. 9, pp. 1965–1973, 1999.

[357] J. Korf, "Is brain lactate metabolized immediately after neuronal activity through the oxidative pathway?," *Journal of Cerebral Blood Flow & Metabolism*, vol. 26, no. 12, pp. 1584–1586, 2006.

[358] H. Krugers, D. Jaarsma, and J. Korf, "Rat hippocampal lactate efflux during electroconvulsive shock or stress is differently dependent on entorhinal cortex and adrenal integrity.," *Journal of neurochemistry*, vol. 58, no. 3, pp. 826–830, 1992.

[359] W. Kuhr, C. van den Berg, and J. Korf, "In vivo identification and quantitative evaluation of carrier-mediated transport of lactate at the cellular level in the striatum of conscious, freely moving rats.," *Journal of cerebral blood flow and metabolism : official journal of the International Society of Cerebral Blood Flow and Metabolism*, vol. 8, no. 6, pp. 848–856, 1988.

[360] C. Deby and R. Goutier, "New perspectives on the biochemistry of superoxide anion and the efficiency of superoxide dismutases," *Biochemical Pharmacology*, vol. 39, no. 3, pp. 399–405, 1990.

[361] M. Saran, C. Michel, and W. Bors, "Reaction of NO with o2-. implications for the action of endothelium-derived relaxing factor (EDRF).," *Free radical research communications*, vol. 10, no. 4-5, pp. 221–226, 1990.

[362] D. Green and G. Kroemer, "The central executioners of apoptosis: caspases or mitochondria?," *Science*, vol. 281, p. 1309, 1998.

[363] U. M and R. Alexander, "Reactive oxygen species as mediators of angiogenesis signaling. role of NAD (P) h oxidase," *Molecular and Cellular Biochemistry*, vol. 264, no. 1, pp. 85–87, 2004.

[364] C. Colton, L. Fagni, and D. Gilberts, "The action of hydrogen peroxide on paired pulse and long-term potentiation in the hippocampus," *Free radical Biology & Medicine*, vol. 7, pp. 3–8, 1989.

[365] A. Viggiano, E. Viggiano, and M. Monda, "Intracerebroventricular injection of oxidant and antioxidant molecules affects long-term potentiation in urethane anaesthetized rats," *Physiological Research*, vol. 57, pp. 269–273, 2008.

[366] T. Pellmar, "Peroxide alters neuronal excitability in the CA1 region of guinea-pig hippocampus in vitro," *Neuroscience*, vol. 23, no. 2, pp. 447–456, 1987.

[367] J. Auerbach and M. Segal, "Peroxide modulation of slow onset potentiation in rat hippocampus," *The journal of neuroscience*, vol. 17, no. 21, pp. 8695–8701, 1997.

[368] B. Ames, "Endogenous DNA damage as related to cancer and aging," *Mutation research*, vol. 214, pp. 41–46, 1989.

[369] B. Halliwell and S. Chirico, "Lipid peroxidation: its mechanism, measurement, and significance.," *The American Journal of Clinical Nutrition*, vol. 57, no. Suppl, pp. 715–725, 1993.

[370] A. Viggiano, E. Viggiano, I. Valentino, M. Monda, A. Viggiano, and B. Luca, "Cortical spreading depression affects reactive oxygen species production," *Brain research*, vol. 1368, pp. 11–18, 2011.

[371] J. H. Shin, B. J. Privett, J. M. Kita, R. Wightman, and M. H. Schoenfisch, "Fluorinated xerogel-derived microelectrodes for amperometric nitric oxide sensing.," *Analytical chemistry*, vol. 80, no. 18, pp. 6850–6859, 2008.

[372] A. J. Wells, R. Vink, P. C. Blumbergs, B. P. Brophy, S. C. Helps, S. J. Knox, and R. J. Turner, "A surgical model of permanent and transient middle cerebral artery stroke in the sheep," *PloS one*, vol. 7, no. 7, p. e42157, 2012.

[373] T. C. Glenn, N. A. Martin, M. A. Horning, D. L. McArthur, D. A. Hovda, P. Vespa, and G. A. Brooks, "Lactate: brain fuel in human traumatic brain injury: a comparison with normal healthy control subjects.," *Journal of neurotrauma*, vol. 32, no. 11, pp. 820–832, 2015.

[374] P. Bouzat, N. Sala, T. Suys, J. B. Zerlauth, M. Pedro, F. Feihl, J. Bloch, M. Messerer, M. Levivier, R. Meuli, P. J. Magistretti, and M. Oddo, "Cerebral metabolic effects of exogenous lactate supplementation on the injured human brain.," *Intensive care medicine*, vol. 40, no. 3, pp. 412–421, 2014.